ABSTRACT

OLSEN, CHRISTIAN HAARGAARD. Modeling Heart Rate Regulation by the Baroreflex. (Under the direction of Mette Olufsen and Hien Tran.)

The baroreceptor reflex is responsible for short term regulation of blood pressure. During orthostatic stress, such as posture changes, the baroreflex maintains constant blood pressure by regulating (among others) venous volume, systemic resistance and heart rate through the sympathetic and parasympathetic nervous system. This dissertation aims to develop a model for the baroreflex regulation of heart rate during head-up-tilt (HUT) considering blood pressure and respiration as input to the model. The model includes description of the strain of the arterial wall and the enclosed stretch-sensitivity baroreceptor neurons, the afferent neuron firing, sympathetic and parasympathetic activity, neurotransmitter concentrations at the synapse of the pacemaker cells of the heart, and a lumped description of intracellular pathways of the pacemaker cell and it's depolarization. The model is shown to exhibit positivity of solution under correct parametrization.

A correct mathematical description of the regulation of heart rate during orthostatic stress would make it possible to learn about system configuration not immediately measurable, through fitting of model output to experimental data. While this idea is simple, it posses several mathematical challenges, such as the question whether model parameters can be estimated, and what uncertainties follow such estimates and accompanying model predictions. The first question is answered through sensitivity and identifiability analysis, while the other is related to uncertainty quantification.

This dissertation provides a discussion of Sobol Indices and Morris elementary effects for global sensitivity analysis, and of structural correlation matrix method (SCM) and orthogonal sensitivities method (OSM) for identifiability analysis. The methods are applied to multiple examples of increasing complexity to present the underlying properties of each method, and possible forces and shortcomings of the methods.

Using the presented methods for identifiability analysis different subsets of parameters are constructed, and the model is fitted to experimental data for each subset, allowing only the chosen parameters to vary, while keeping the remaining fixed. Finally Delay-rejection adaptive Metropolis (DRAM) is used to determine parameter densities and model prediction intervals. Simulation results suggests that the model is able to produce an increase in heart rate following HUT, but that the implementation of respiration in it's current form do not increase the predictive power of the model, as it is unable to reproduce some of the faster dynamics. Furthermore, as an optimization where all parameters were allowed to vary produced the best fit, it is possible that the strategies used for building parameter subsets may be too restrictive in deeming parameters unidentifiable.

Modeling Heart Rate Regulation by the Baroreflex

by
Christian Haargaard Olsen

A dissertation submitted to the Graduate Faculty of
North Carolina State University
in partial fulfillment of the
requirements for the Degree of
Doctor of Philosophy

Biomathematics

Raleigh, North Carolina

2014

APPROVED BY:

_____
Mette Olufsen
Co-chair of Advisory Committee

_____
Hien Tran
Co-chair of Advisory Committee

_____
Johnny Ottesen

_____
Ralph Smith

_____
Jesper Mehlsen

BIOGRAPHY

Christian Haargaard Olsen was born in Copenhagen in 1984. He received his masters degree in Mathematics and Physics from Roskilde University in the spring of 2011, before attending North Carolina State University from the fall 2011 to the fall 2014.

ACKNOWLEDGEMENTS

TABLE OF CONTENTS

LIST OF TABLES

LIST OF FIGURES

Chapter 1

Introduction

The cardiovascular system is important for the health and well-being of all humans. It is responsible for the transport of nutrients and waste products, hormones used for signaling across the body, as well as the removal of excessive heat from the internal tissue to the skin (Burton 1966). One specific important role of the cardiovascular system is the supply of oxygen to organs, among which the brain is the most prominent recipient. Insufficient perfusion of the brain and subsequent deficiency of oxygen may cause light-headedness or syncope.

It is estimated that 35% of all people experience syncope during their lifetime (Van Dijk et al. 2006). In the emergency departments in Europe approximately 1% of all visits are due to syncope. Of these visits, approximately 40% are hospitalized with a median stay of 5.5 days (Abe et al. 2009). The total cost of syncope related hospitalizations was an estimated $2.4 billion in 2000 in the US alone (Sun, Emond, and Camargo Jr 2005). In addition, recurrent syncope has a large impact on the affected individual's quality of life, comparable to those of chronic illnesses such as chronic arthritis and end-stage renal disease, with levels of somatization, anxiety and depression comparable to those of psychiatric disorders (Abe et al. 2009; Linzer et al. 1991; Van Dijk et al. 2006). However, syncope is not just one syndrome but covers a numbers of conditions. The most common type of syncope is *reflex syncope*, which refers to a specific group of conditions, including:

- *Vasovagal* syncope (common fainting) induced by emotion or orthostatic stress.

- *Situational* syncope often occurring in young athletes or in the middle-aged/elderly as a precondition to orthostatic intolerance.

- *Carotid sinus* syncope triggered by mechanical stimulation of the carotid sinus.

- *Atypical* syncope describing occurrences that do not fit the other categories.

Reflex syncope occurs when a normally helpful control mechanism causes an inappropriate response that triggers vasodilation or bradycardia, which leads to a decrease in blood pressure and cerebral

perfusion (Abe et al. 2009). While cerebral regulation is the mechanism responsible for regulating blood flow to the brain locally, it depends on an adequate systemic blood pressure and cardiac output controlled by the autonomic nervous system.

The baroreceptor reflex, which is a mechanism of the autonomic nervous system, is associated with maintaining homeostasis of the cardiovascular system. The reflex is initiated when sensory neurons located in the carotid sinus and aortic arch, called baroreceptors, sense changes in arterial wall strain imposed by changes in blood pressure. In response strain sensitive baroreceptors innervate the cardiovascular control center in the nucleus tractus solitarius (NTS). Here different responses are initiated via activation or deactivation of sympathetic and parasympathetic pathways. An increase in sympathetic activity causes a release of noradrenaline onto smooth muscle cells lining the wall of the systemic arteries, as well as on the pacemaker cells and cardiac muscle of the heart inducing increased force and rate of heart contractions. All are effects that leads to an increase in blood pressure and cardiac output. Parasympathetic activation works in opposition to sympathetic activation. It releases the neurotransmitter acetylcholine onto the pacemaker cells, which slows heart rate and reduces cardiac output (Burton 1966; Hall 2011). Inefficient or faulty regulation by the baroreceptor reflex may lead to inadequate perfusion and syncope.

To asses the baroreceptor reflex many diagnostics tests exists including *carotid sinus massage*, *active standing*, *tilt table test*, *electrocardiographic monitoring*, etc. (Abe et al. 2009). Classically the use of data from these experiments rely on statistical analysis or qualitative interpretation of measurements by a health professional, and may therefore ignore information hidden in the dynamics of responses. It has been suggested that the use of mathematical models in life sciences can facilitate better development and tests of hypothesis (Beard and Kushmerick 2009), and for analysis of otherwise unobservable dynamics (Ottesen 2011).

William Harvey (1578-1657) was a pioneer in the field of mathematical modeling in physiology. He combined clinical observations of blood flow with a simple mathematical model to infer the circulatory system, predicting the existence of the capillaries, turning over a 1500 year old view of the cardiac system (Harvey and Ginsberg 1995). At the same time the application of mathematics in physics exploded after Newton (1642-1726) invented calculus and stated his famous laws of motion. One of the many insights brought by Newton was that the natural laws governing the motion of planets is equivalent to the ones governing the behavior on the surface of the earth. These advances made it possible to determine the distance and weights of planets, which was otherwise out of reach through the observation of the encapsulating system.

While physiological systems are accessible, it is typically impossible to measure system components through controlled experiments due to the complex and fragile nature of the system. However, with a mathematical description of the physiological system, equivalent to Newtons laws of motion for the planetary system, it is possible to infer information about different parts of the system merely by observing the system behavior. The development of cheap and accessible computers, and the

accompanying development of numerical methods, has increased the use of mathematical models in physiology.

While some fields of mathematical modeling make use of *system identification* (Ljung 1987), models in physiology are typically build from first principles to allow for a physical interpretation of components and parameters. An example of such efforts are the models developed by Ursino 1998 predicting blood pressure control in response to hemorrhage. Other efforts characterizing parts of the system include studies by Landgren 1952 Taher et al. 1988 and Ottesen 1997b, who developed mathematical models for the response of baroreceptors to pressure changes, and by Warner and Cox 1962 who presented a model for the relationship between autonomic nervous activity and heart rate. More recent models with similar goals for active stand and tilt table tests have been developed by Ottesen 1997a ,Olufsen, Tran, et al. 2006 and Ottesen and Olufsen 2013.

It is important to distinguish these modeling efforts from the more classical statistical investigations such as the study by Smyth, Sleight, and Pickering 1969 who investigated the baroreflex sensitivity through statistical analysis of clinical data from 20 individuals. Statistical analysis can reveal correlations between observations and provide valueable information about the observed data, but ignores knowledge of the structure of the observed system. Mathematical models on the other hand, provide a precise description of behavior of different parts of the system, and determine system configuration from experimental data (Tarantola 2005). The practical goal for using mathematical models in this setting is to be able to identify biomarkers in the form of parameters in the mathematical model that can point to physiological dysfunctionalities and guide the planning of treatment.

While this idea is simple, the mission contains an element of mathematical challenge. First, there is no guarantee that a solution fitting experimental data exists, or if it does, that the configuration that leads to this solution is easily found and that it has physiological meaningful values for parameters and substates. These problems increases as models become more complex and involve more parameters. *Sensitivity* and *identifiability analysis* are branches of mathematical modeling related to *experimental design* that are concerned with questions if model parameters have an influence on the model output and if their values can be identified (Miao et al. 2011; Saltelli, Ratto, et al. 2008).

Identifiability and numerical challenges are not the only important challenges. If model parameters can be estimated that enables the model to reproduce experimental data, it is now thought that the estimated parameter values give insight into the state of the real system. Moreover, it is important to consider the uncertainties associated with using a model and numerical approximations. *Uncertainty quantification* is the branch of mathematical modeling addressing the reliability of the model output and parameter estimates (R. C. Smith 2014). For practical use, it is important that parameter and model prediction uncertainties be calculated and presented as part of the results.

1.1 Overview of dissertation

The goal of this study is to develop a baroreflex model predicting heart rate regulation during postural change from sitting to standing. The model is investigated using dynamical systems analysis to show positivity of solutions, and through the use of numerical methods for estimating parameter sensitivities and identifiability. Finally parameter uncertainties will be quantified by computing parameter densities using a Bayesian framework, and these densities will be used to estimate prediction intervals for model output.

- Chapter 2 gives an introduction to the cardiovascular system and its control mechanisms. Specific attention is given to the baroreceptor reflex and the regulation of heart rate.

- Chapter 3 gives a description of the experimental data used for modeling.

- Chapter 4 describes the baroreflex model.

- In Chapter 5 the developed model is analyzed predicting behavior in terms of positivity of solutions and stability.

- Chapter 6 introduces identifiability. Local and global methods are used analysing the identifiability of models. The use of these methods are demonstrated by a number of examples.

- Chapter 7 gives a short introduction to uncertainty quantification and one method to calculate and propagate parameter uncertainties.

- Chapter 8 shows results from numerical simulations, fitting the model to experimental and simulated data.

- Chapter 9 contains concluding remarks.

Chapter 2

Physiological Background

This chapter gives an introduction to the cardiovascular system and the general mechanisms involved in regulating blood flow and blood pressure, as well as a more thorough description of how heart rate is regulated by the baroreceptor reflex system. The chapter is based on the texts by Burton 1966, Boron and Boulpaep 2012 and Hall 2011. Section 2.1 contains a brief introduction to the cardiovascular system, Section 2.2 provides a description of the mechanisms regulating the cardiovascular system, and Section 2.3 gives a more in-depth description of baroreflex regulation of the heart rate.

2.1   Cardiovascular system

The cardiovascular system consists of the blood, the heart pumping the blood and the vessels carrying it around the body. It is a transport system, ensuring efficient exchange and transport of

- oxygen and carbon dioxide,

- nutrients and waste materials,

- hormones, and

- thermal energy.

The cardiovascular system consists of two circuits originating from the heart: The systemic circuit transports blood around the body while the pulmonary circuit transports blood through the lungs. The two circuits are connected such that the blood returning from the systemic circuit, is directed into the pulmonary circuit, from where it is, again, directed to the systemic circuit, completing the cardiovascular cycle. In each of the two circuits the blood travel through arteries to the capillaries where the exchange of oxygen for carbon dioxide occurs. Subsequently, de-oxygenated blood is transported back to the hearth through a network of veins.

While the two circuits follow the same simple layout, the conditions they work under are quite different. On the systemic side the pressure generated by the heart has to be higher to facilitate the flow of blood to the furthest extremities of the body, while the blood pressure in the pulmonary circuit only needs to facilitate the transport through the lungs. Since the exchange is most efficient at low velocity, it is desirable that the blood flow is kept close to constant. Near constant flow is achieved by the large compliance of the large arteries that receive the blood from the heart, and the large volume of the veins. On the systemic side the large compliance of the large arteries is responsible for keeping the pressure approximately constant, typically oscillating between 80-120 mmHg. As the blood vessels bifurcate the pressure drops gradually to near 20-30 mmHg at the capillary level. Past the capillaries, the large volume of the venous side ensures that the pressure does not increase significantly as blood arrives from the capillaries. The blood pressure in the largest veins are as low as 2-5 mmHg. This configuration allows for near constant pressure gradient across the systemic circuit, and thereby a near constant flow.

Figure 2.1 shows an outline of the circulation, while Figure 2.2 shows how blood flow and oxygen consumption is distributed in the systemic circuit. Considering the distribution of blood flow between different organs, one should remember that 100% of the blood flows through the lungs on every cycle, as that is the sole purpose of the pulmonary circulation. Using the blood supply distribution as marker, it is clear that the supply of oxygen and removal of carbon dioxide is of highest importance for the well being of the person.

It is interesting to look at the disparity between the distribution of blood flow and oxygen consumption of the different organs. For most of the organs the flow corresponds fairly well to the oxygen consumption, except for the kidney, skeletal muscle and to some degree the skin. From the chart in Figure 2.2 it is clear that muscles consume huge amounts of oxygen, extracting more oxygen per volume blood than any other organ. The kidneys, on the other hand, is heavily perfused not caused they need oxygen, but rather by the need of the blood to be filtered for removal of waste products. Finally, the perfusion of the skin is due to thermal regulation, as the skin is used to deposit excess heat from the body.

Before beginning the discussion of regulation, it is important to emphasize that while all functions of the cardiovascular system is important for survival, the supply of oxygen and removal of carbon dioxide is the most critical function.
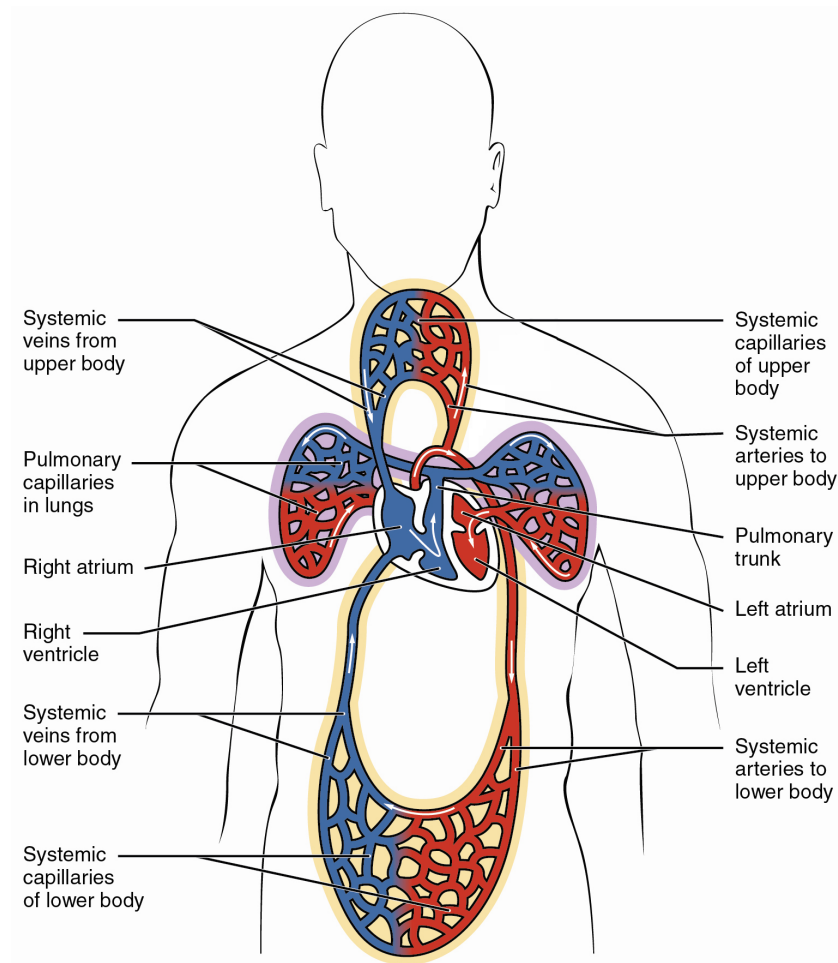
Figure 2.1: Overview of the cardiovascular circulation. Blood is pumped at high pressure from the left heart into the systemic arteries, from where it flows slowly at almost constant velocity through the capillaries to the veins. From the systemic veins, it flow into the right side of the heart, from where it is pumped into the pulmonary arteries. In the pulmonary circuit the blood flows from the arteries, through the capillaries and into the veins to return to the left side half of the heart. While the mechanism is similar, the pressure is lower on the pulmonary than on the systemic side. (Figure adapted from (*"2003 Dual System of Human Circulation" by OpenStax College - Anatomy & Physiology* n.d.) under Creative Commons Attribution 3.0 Unported license.)
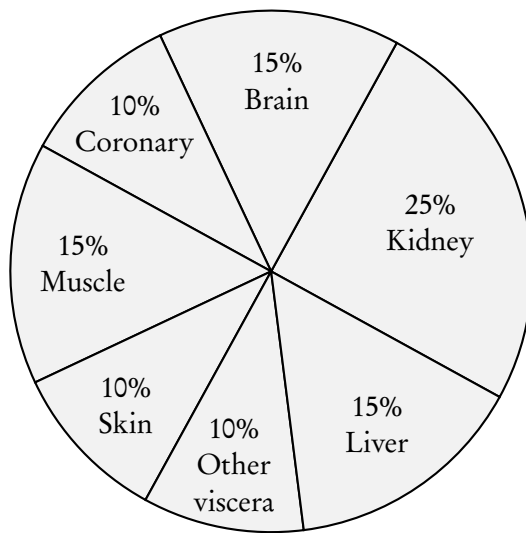
(a) Cardiac output distribution   (b) Oxygen consumption
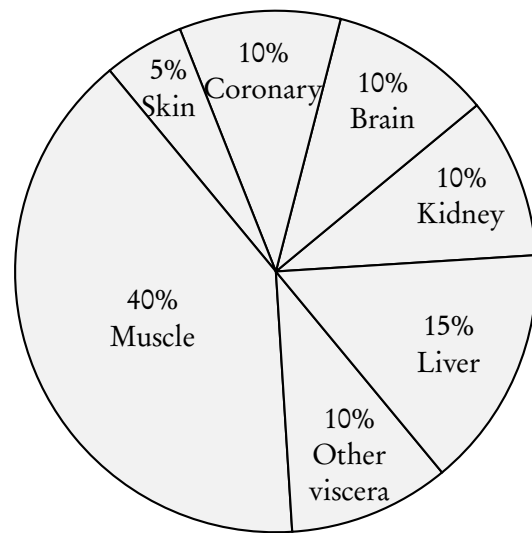
Figure 2.2: Distribution of cardiac output and oxygen consumption to different organs at rest. Based on numbers from Burton 1966.

2.2 Regulation of the cardiovascular system

As stated in the introduction the cardiovascular system is responsible for transport of oxygen, carbon dioxide, nutrients, waste, hormones and heat. Not only is it important that the entities are transported, but also that the right amounts reaches (or are removed from) the parts of the systems where they are required (or in excess) at the right times. This require system regulation, the topic of this section.

2.2.1 Cardiac output

As the different parts of the cardiovascular system and it's regulation is complex and intertwined, the description given here will take cardiac output (CO - the volume of blood pumped by the heart per unit time) as the basis. It can be calculated as the product of the stroke volume of the heart (SV) and the heart rate (HR)

$$CO = SV \times HR. \tag{2.1}$$

Both SV and HR may vary. SV can be determined by the return of blood to the heart due to what is known as the *Frank Starling mechanism*, which refers to an empirical law stating that the stroke volume increases with the volume of blood that is returned to the heart (Burton 1966). The existence of this mechanism implies that SV is determined mainly by the venous return, in turn making it dependent on the systemic resistance to flow and the pressure drop from the arterial to the venous side of the circuit.

Local blood flow regulation refers to the mechanism ensuring that blood flow in the arteries near tissue cells, called arterioles, is restricted or increased to supply the needed perfusion. This local blood flow regulation will increase the cross-sectional area of the arterioles when oxygen or nutrients are needed through dilation of smooth muscle surrounding the arterioles. Likewise, if the oxygen concentration of the surrounding tissue is higher than necessary, constriction of the smooth muscle will decrease the flow of blood through the arterioles. Figure 2.3 shows how the local control increases blood flow when the oxygen concentration of the supplied blood is low, and decrease blood flow when the concentration is high. It is believed that the degree of smooth muscle contraction is determined primarily by the oxygen concentration, as oxygen is necessary for the contraction. It is however speculated that other factors might affect the degree of restriction as well.

In addition to ensuring adequate perfusion of the local tissue local blood flow regulation direct the blood flow to where the resistance is smallest and blood is needed the most. If several parts of the circuit requires increased perfusion, local control of each part will reduce it's resistance to flow by dilating arterioles. The cumulative effect if local controls of large parts of the circuit decrease resistance to flow, is that the systemic resistance is decreased. A decrease in systemic resistance causes the blood to flow through faster, and for more blood to return to the heart, increasing the stroke volume and cardiac output. Hence the local tissue needs, expressed through the local blood flow regulation, also
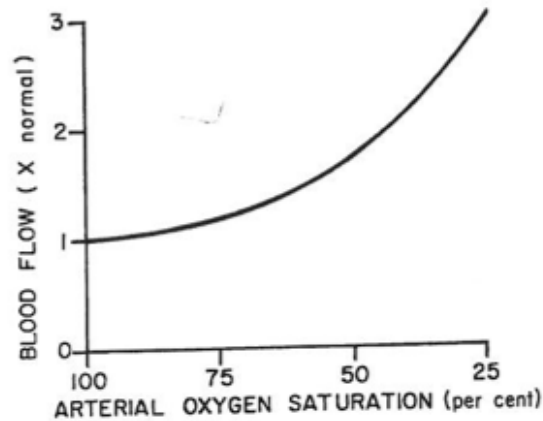
Figure 2.3: Effect of arterial oxygen saturation on blood flow through an isolated dog leg. Reprinted with permission from A.C. Guyton 1971.

regulates the cardiac output. The only requirement for the local blood flow regulation to determine the blood flow is the presence of blood and adequate arterial pressure, which in turn depends on the total *blood volume*. Hence, *long term regulation* of blood volume through digestion and excretion is also a requirement for proper function.

While the intrinsic control of the cardiovascular system in general ensures correct cardiac output, it can be helpful to simultaneously regulate the entire system at once. Such system wide regulation is achieved through hormonal and nervous control by the autonomic nervous system, for example during exercise or other activities that stress the system.

Long term intrinsic regulation of blood volume

The regulation of blood volume (and thereby pressure) is very complex. A simple explanation is given based on the diagram in Figure 2.4 describing the system that regulates arterial blood pressure and the cardiac output over longer time scales. Starting in the top left corner and following the outer edge of the diagram the parts involved are:

1. The relationship between the arterial blood pressure and the decrease in extra cellular fluid (ECF - the amount of body fluids outside of cells) through output in the Kidneys. Increased arterial blood pressure (ABP) will increase the amount of liquid excreted, $\frac{dE}{dt}(o)$ (o for out).

2. The total change in ECF volume is given by the sum of negative (through kidneys) and

10
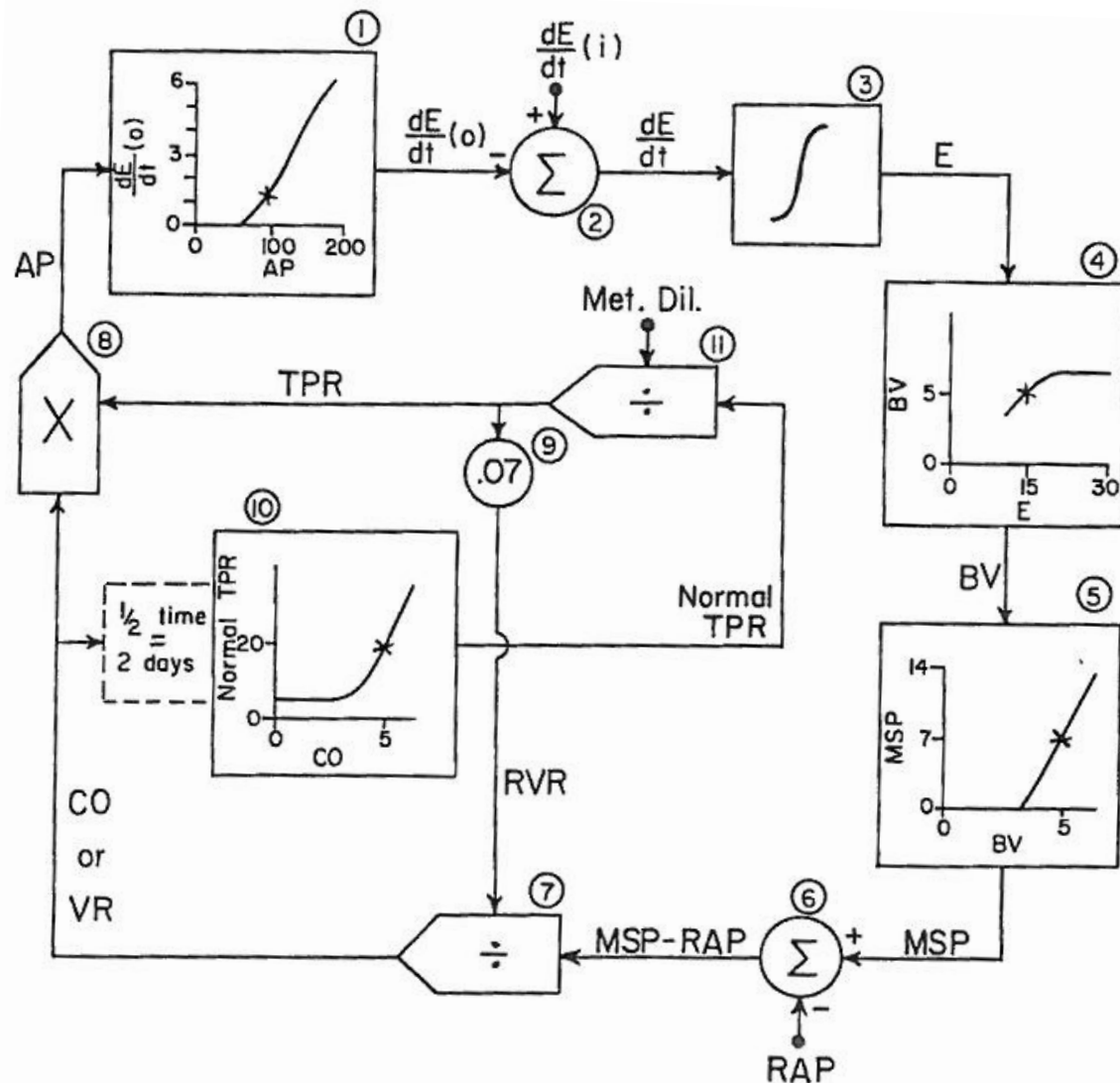
Figure 2.4: The intrinsic regulation of arterial pressure (AP) and cardiac output (CA). (1) The amount of excreted fluid volume is determined from ABP. (2) Total change in ECF. (3) Current ECF is the integrated changes. (4) BV is determined from ECF. (5) BV determines MSP. (6) BRP is determined from MSP and RAP. (7) CO determined by BRP and RVR. (8) AP determined by CO and TPR. (9) RVR is considered to be a praction of TPR. (10) On a longer timescale (2 days) TPR is regulated to match CO. (11) TPR is affected by metabolic activity. Reprinted with permission from A.C. Guyton 1971.

positive (through intake of fluids) changes in the ECF

$$\frac{\mathrm{d}E}{\mathrm{d}t} = \frac{\mathrm{d}E}{\mathrm{d}t}(i) - \frac{\mathrm{d}E}{\mathrm{d}t}(o). \tag{2.2}$$

3. The current level of ECF volume is given by the complete history of changes, or in a mathematical term integration of the changes.

$$E(t) = \int_{-\infty}^{t} \frac{\mathrm{d}E}{\mathrm{d}t}\,\mathrm{d}t. \tag{2.3}$$

4. Blood volume (BV) is determined from the current ECF.

5. The BV will determine the mean systemic pressure (MSP).

6. The pressure difference driving blood into the heart (blood return pressure BRP) depends on the MSP and the pressure in the heart, the right atrial pressure (RAP)

$$BRP = MSP - RAP. \tag{2.4}$$

7. The flow of blood into the heart, is also the flow of blood leaving the heart and thus the cardiac output (CO). It is dependent on the BRP and on the resistance to venous return (RVR)

$$CO = \frac{BRP}{RVR}. \tag{2.5}$$

8. Completing the cycle, the arterial pressure is given as CO divided by the total peripheral resistance (TPR)

$$AP = \frac{CO}{TPR}. \tag{2.6}$$

The remaining 3 parts of the regulation of the system describes the impact of the local blood flow regulation on the total blood flow.

9. In step 7 the cardiac output (CO) depend on the resistance to venous return (RVR). Resistance to venous return (RVR) is usually considered to be a set fraction of the total peripheral resistance(TPR)

$$RVR = 0.07\,TPR. \tag{2.7}$$

10. The long term local blood flow regulation will increase the resistance to flow if the tissue is experiencing excess perfusion. This regulation however happens exponentially with a 1/2 time of approximately 2 days. Thus the total peripheral resistance (TPR) will gradually move

towards the value corresponding to the current cardiac output (CO) as shown in Figure 2.4 at (10).

11. In addition to the long term regulation of the local blood flow regulation the TPR is also sensitive to the metabolic rate - primarily determined by the activity of the muscles. Metabolic activity will lead to a dilation of the vessels adjacent to the active tissue, to ensure increased perfusion. This increased perfusion will lead to an overall decrease in TPR given by,

$$\text{TPR} = \frac{\text{Normal TPR}}{\text{Metabolic dilation}}. \tag{2.8}$$

Regulation through the autonomic nervous system

The intrinsic regulation presented above operates with no direct neural input. However, in certain situations it is advantageous for the body to change the function of the cardiovascular circulation quickly. The autonomic nervous system, consisting of the sympathetic and parasympathetic nervous system, does exactly this.

Sympathetic nervous system

With regards to the regulation of the cardiovascular system the sympathetic nervous system is the one with the larger effect. The main effect of the sympathetic nervous system is to increase the arterial pressure and cardiac output - usually in situations where large amount of nutrients is required for the muscles.

The sympathetic nervous system innervates almost every blood vessel in the body - allowing for quick effects on the local resistance to blood flow - as well as the heart. Figure 2.5 shows how the sympathetic nerves innervates the different parts of the blood circulation on either side of the capillaries. Depending on the tissue and the type of stimuli of the vasomotor center, the sympathetic activation might cause vasoconstriction for both arteries, arterioles, venules and veins. Tissue where all vessels are constricted by sympathetic activation is usually found in kidneys, stomach, and other tissue that can do without perfusion if additional nutrients are required in the muscles for physical work. For muscle tissue the effect is different. Here sympathetic activation typically induces vasodilation, to accommodate the increase in required perfusion. The overall effect of sympathetic activation is increased arterial pressure and cardiac output.

Parasympathetic nervous system

The impact of the parasympathetic nervous system is smaller than that of the sympathetic nervous system. The parasympathetic tone is mediated through the vagus nerve and innervate the heart. At the heart the effect of the parasympathetic activation is to decrease heart rate and the force of contraction.
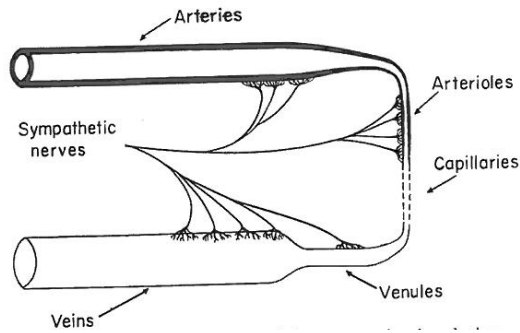
Figure 2.5: Innervation of the systemic circulation of the sympathetic nervous system. Reprinted with permission from A.C. Guyton 1971.

It does not affect blood vessels like the sympathetic nervous system does. Since, cardiac output is the product of stroke volume and heart rate

$$CO = SV \times HR, \tag{2.9}$$

activation of the parasympathetic nervous system leads to a decrease in cardiac output.

2.2.2 Determinants of arterial blood pressure

During a cardiac cycle the blood pressure changes between high pressure during the contraction called the *systolic* blood pressure and a low pressure before the contraction, called the *diastolic* blood pressure. This pressure difference between the systolic and diastolic value is the dynamic component, while the level is called the static component.

Static component of arterial blood pressure

Control of the static component of the arterial blood pressure is achieved by multiple regulation mechanisms that work on different timescales.

Short timescale

On the shortest timescale (seconds to minutes) the autonomic nervous system will be activated through the baroreceptor (pressure/stretch sensitive) reflex, the chemoreceptor (chemical sensitive) or the ischemic response (low oxygen) reflex depending on the change that needs adoption to.

The regulation of these systems is through the autonomic nervous system with the signal being mediated through the concentration of the neurotransmitters acetylcholine and noradrenaline. The

effectors of these systems are the smooth muscle lining blood vessels and the pacemaker cells of the heart. Acetylcholine concentration is regulated from the activity of the parasympathetic nervous system and it's primary effect regarding blood pressure is on the pacemaker cells of the heart. Increased amounts of acetylcholine will slow the heart rate while a decreased concentration will increase the heart rate. Noradrenaline concentration on the other hand is regulated from the activity of the sympathetic nervous system. Like acetylcholine noradrenaline also affects the pacemaker cells of the heart, but with an opposite effect. An increased concentration of noradrenaline will increase heart rate and decreased concentration will decrease heart rate. Noradrenaline also affects the cardiac muscle of the heart increasing the contractility of the heart. Finally the sympathetic nervous system innervates smooth muscles lining the arterial wall, as described in subsection 2.2.1, allowing constriction of blood vessels.

It is worth noting that increased tone of the smooth muscle cells lining blood vessels not only leads to increased arterial resistance, which leads to increased arterial pressure, but also to a decrease in the volume of blood pooled in peripheral limbs (Burton 1966, p. 180). Hence, the immediate regulation of blood pressure is primarily done by regulation of peripheral resistance and heart rate, while a constriction of vessel volume plays a role as well, as it increase the rate at which the blood returns to the heart, and thereby increases the cardiac filling and stroke volume.

Intermediate timescale

On the intermediate timescale (hours) the capillary fluid shift will counteract changes in blood pressure by shifting fluid volume between blood and interstitial fluid at the capillaries from high pressure to low pressure. On the same timescale the stress-relaxation will change the volume available for storage of the blood in vessels throughout the body.

Long timescale

On the longer timescale (hours to days) the kidney will regulate the arterial blood pressure by controlling the retention of salts and water and thereby controlling the total volume of fluid in the body. The complete feedback system for this regulation was described in Section 2.2.1.

Dynamic component

The dynamic component of the arterial blood pressure is the pulse pressure - the difference between systolic and diastolic pressure. This difference is determined by the vessel compliance. The pressure increases as the heart contracts, leading up to systole. Due to the large resistance to flow, most of the force/pressure expelled by the heart goes towards distending the wall of the large arteries. This increases the volume of the arteries, as the ejected blood is pooled in the arteries. The distensibility

of the wall is described by the *compliance C* of the arterial wall, defined as the volume change per pressure change,

$$C = \frac{\Delta V}{\Delta P}. \tag{2.10}$$

Hence a vessel with large compliance will expand greatly as pressure increase, while a vessel with small compliance will require a large pressure to distend. Note that qualitative nature of compliance is the inverse of elasticity, which is a measure of the change in force generated by displacement.
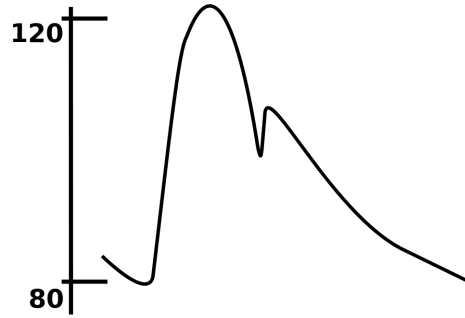
Figure 2.6:   A typical pulse pressure profile. Figure from Wikimedia Commons (`http://commons.wikimedia.org/wiki/File:Arterial-blood-pressure-curve.svg`).

After the heart valve is shut at the end of the contraction, the difference between the pressure exerted by the distended wall in the aorta and the pressure in the systemic veins, will drive a steady flow of blood through the circulation. As the blood leaves the aorta, the driving pressure difference between arterial and venous side decreases exponentially towards 0. The discharge is analogous to that of a charged capacitor in an electric RC circuit.

Since the blood causing the distention of the wall is the volume of one heart contraction and the compliance is a characteristic of the wall, one can relate the pulse pressure ΔP to the physiologically defined stroke volume $\text{SV} = \Delta V$

$$\text{SV} = C \Delta P. \tag{2.11}$$

Hence, for situations where the compliance can be considered constant measurements of the pulse pressure can be used as an indicator of the stroke volume. Equation (2.1) stated that cardiac output is the product of stroke volume and heart rate. Thus, combining the pulse pressure with a measurement of the heart rate gives an indicator for the cardiac output

$$\text{CO} = \text{SV} \times \text{HR} = C \Delta P \text{HR}. \tag{2.12}$$
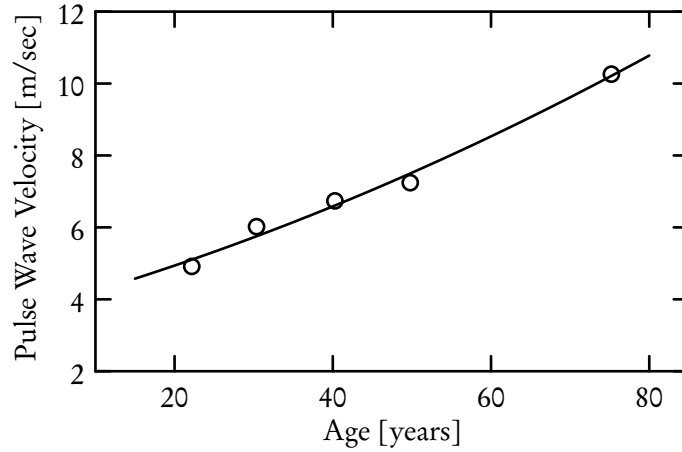
Figure 2.7: Aortic Pulse-wave velocity versus age. Graph is produced from digitized data from Burton 1966.

Pulse pressure velocity

Simultaneous measurements of the pulse pressure different distances from the heart shows that the pulse propagation is not instantaneous. The pulse pressure velocity can be determined by dividing the distance between measurement points by the delay of the pulse pressure profile. Experimental measurements (Hallock 1934) has shown that the velocity increases with age, as is demonstrated in Figure 2.7. This increase in pulse-wave velocity with age is due to a decrease in arterial compliance. This relation is build on classical derivation for the velocity of propagation of transverse elastic waves (Burton 1966). The relation states that,

$$v = \frac{3.57}{\sqrt{D}}, \quad \text{or} \quad D = \left(\frac{3.57}{v}\right)^2, \tag{2.13}$$

where v is the pulse-wave velocity and $D = \frac{\Delta V / V}{\Delta P}$ is the distensibility (or relative compliance). Using this formula the pulse wave velocity data in Figure 2.7 can be related to distensibility. A velocity of $10\,\text{m/s}$ is recorded for the eldest group and corresponds to a distensibility of $0.13\,1/\text{mmHg}$. Meanwhile a velocity of $5\,\text{m/s}$ is recorded for the youngest group and correspond to a distensibility of $0.51\,1/\text{mmHg}$. The graph is a clear indicator that the arterial wall stiffens as we age.

Another interesting effect of this relationship is that the pulse-wave profile changes as it propagates. Figure 2.8 shows the pulse pressure profile at different points in the arteries of the systemic circulation. Looking at the first two frames showing the profile at Proximal aorta and the femoral aorta we see that the inclining slope initiating the pressure wave is steeper in the femoral artery. Figure 2.9 shows

17
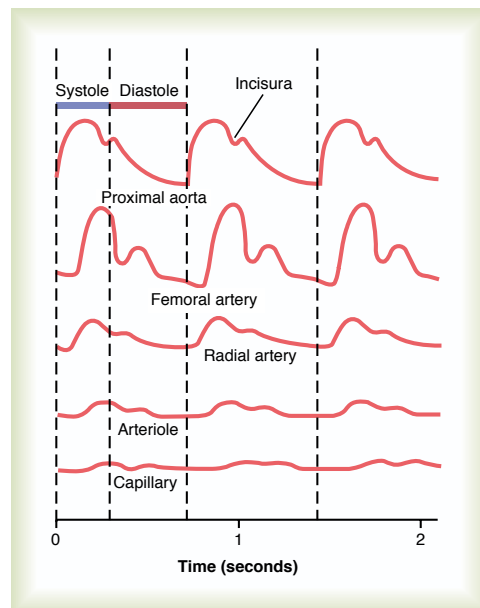
Figure 2.8: The pulse pressure profile recorded at different locations of the arterial system. Note the delay of the signal in the femoral artery as well as the increased initial slope. The delay enables the calculation of the pulse-wave velocity. The change in slope is due to higher wave speed at higher pressure, causing the top of the wave to overtake the initial incline. Reprinted with permission from Hall 2011.
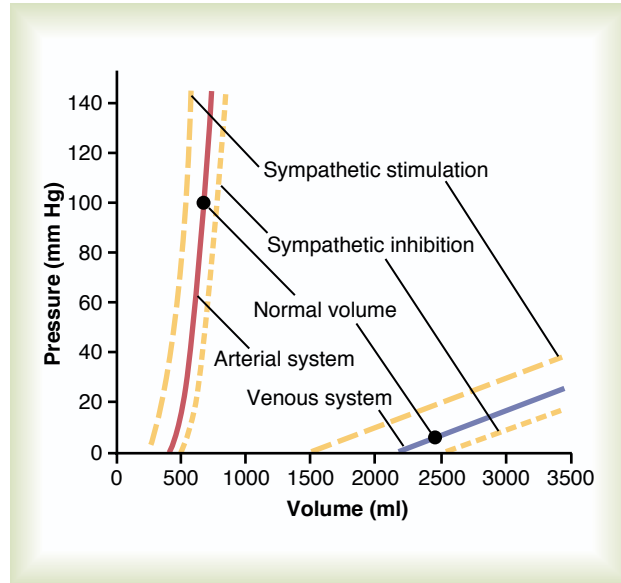
Figure 2.9: Pressure of arterial and venous system as a function of volume. Note that the arterial side reaches a maximum volume as pressure increases. As the volume approaches this maximum value the slope goes to infinity, corresponding to the compliance approaching zero. Reprinted with permission from Hall 2011.

the pressure plotted against volume of the arterial and venous systems. As the volume of the arteries goes to their maximum, the slope of the curve goes to infinity. Since the slope is given by $\frac{dP}{dV}$, it is the inverse of compliance, and the vertical curve reflects the compliance approaching zero. This effect is revealed in Figure 2.10 where the data for the arterial system from Figure 2.9 is plotted with the axis swapped along with the derivative - the compliance. We saw earlier that lower compliance results in increased wave propagation speed. This means that the top of the pressure wave travels faster than the rest of the wave, resulting in the top "catching up" to the initial rise in pressure, increasing the slope.

To summarize, the pulse pressure is determined primarily by the compliance of the arterial wall. The compliance of the arterial wall can be determined by the pulse-wave velocity and decreases with age. In addition the compliance is subject to the regulation through the sympathetic activation of the smooth muscle cells lining the arterial wall, as described earlier. In addition to causing constriction sympathetic stimulation will also decrease arterial compliance. Likewise, sympathetic inhibition will increase compliance of the smooth muscle cells.
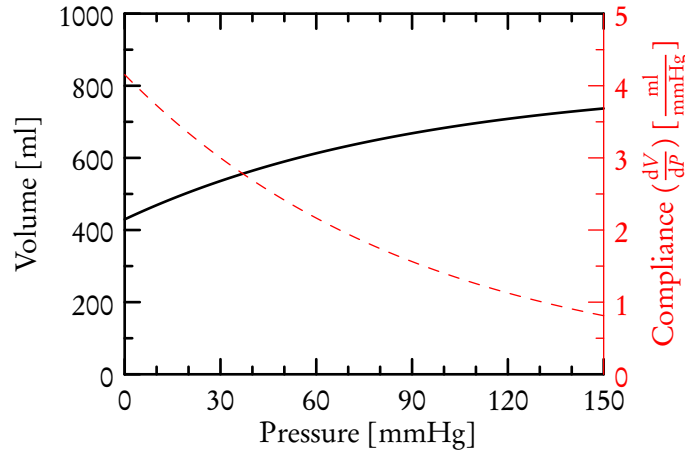
Figure 2.10: Arterial volume and compliance plotted against pressure. The volume curve is a sigmoidal plotted from digitized data from Figure 2.9 and the compliance is the derivative of the sigmoidal.

2.2.3 Blood flow regulation

The overall purpose of the blood circulation is the transport of nutrients, waste products and heat. In general tissue uses nutrients and produces waste products and heat. Depending on the state of the body different kinds of tissue/areas of the body are prioritized by the cardiovascular circulation. When high physical activity is required skeletal muscles are prioritized, when resting and digesting, intestines are prioritized. When temperature of the body is high flow to the skin is increased, when it is low, blood flow to the skin is decreased and mechanisms to produce heat activated.

A few local regulatory mechanisms are worth considering to give representative examples of local regulation specific for different organs: Blood flow in the brain, in the skin and to skeletal muscle.

Blood flow regulation in the brain

Proper function of the brain requires constant supply of oxygen and removal of carbon dioxide. This means that the regulation of blood flow to the brain primarily has the purpose of maintaining constant blood flow. The local control will respond to carbon dioxide and ischemia.

Increased carbon dioxide concentration in the blood is a very strong inhibitor of the vasoconstrictor mechanism of the vasomotor center. Exactly how the CO_2 concentration stimulates the vasomotor center is unknown, but it is presumed that carbon dioxide acts directly on the neuronal cells.

Ischemia is when blood flow to the brain is insufficient to maintain regular metabolism. Ischemia induces a response very similar to that of the high carbon dioxide concentrations - it activates the sympathetic nervous system vasoconstriction through the vasomotor center. This ischemic reaction

is useful if, for example, the pressure in the cerebral spinal fluid increases. If the pressure in the cerebrospinal fluid increases to that of the arteries in the cranial vault, the arteries will start to contract, and thus decrease blood flow to the brain. This decrease triggers an ischemic response through the vasomotor center increasing the arterial pressure. When the arterial pressure is increased sufficiently, blood will again flow to the brain.

Blood flow regulation in the skin

The main function of the circulation of blood through the skin is ensuring correct internal temperature of the body. Thermosensitive sensors are located in the thermal control center of the hypothalamus, in the skin, spinal chord and larger veins in the upper body. The hypothalamus contains both heat and cold sensitive sensors, whereas the skin and the deep body sensors in the spinal chord and larger veins in the upper body are primarily sensitive to cold. The nervous signals for these different sensors are integrated in the posterior hypothalamus, which then initiates the appropriate actions of the body to regulate the temperature.

Vasoconstriction of the blood vessels in the skin decreases blood flow to the skin retaining heat in the body. This works in cooperation with an increased heat production to maintain proper temperature in the body. Another effect is *piloerrection*, which causes contraction of the muscles surrounding the hair follicles on the skin resulting in the hair standing up. This has no real effect on humans due to our furless skin, but on other animals this leads to a thicker insulating layer of air around the skin. Vasodilation has the opposite effect as it increases the blood flow to the skin and thus help cool the body. Vasodilation works in cooperation with sweating and decrement of heat production.

Blood flow regulation skeletal muscle

The primary purpose of blood flow to the skeletal muscle is to supply adequate nutrients corresponding to the current level of activity and to remove excess heat. When the muscles are active the demand for nutrients increases, and the flow of blood should be adjusted accordingly.

Locally the blood flow is regulated intrinsically at the arteriolar level. As described in Section 2.2.1 this regulation is done through dilation of arterioles when oxygen levels of the tissue surrounding the capillaries are low and constricting them when oxygen levels are high.

Intensive and extensive activation of skeletal muscle usually follows sympathetic activation. This means that as the demand for oxygen increases, the cardiovascular system is already prepared to increase perfusion of the skeletal muscles. Preparation involves increased cardiac output and arterial pressure via an increase in systemic resistance and systemic venous volume.

2.3 Baroreceptor Reflex

While many organs of the human body are considered essential for survival, the brain and the heart are critical (Burton 1966). The health of the brain is reliant on sufficient supply of nutrients and removal of waste. Local regulation can increase resistance to reduce flow in case of high blood pressure, but no local mechanism can compensate for insufficient blood supply due to low arterial blood pressure. It is therefore vital for the brain that the system-wide blood pressure regulation, the *baroreceptor reflex* or simply the *baroreflex*, is functioning properly.

One should understand the baroreflex as a feedback loop with sensors, an integrator and several effectors - not unlike a thermostat. For a thermostat, changes in temperature away from the set point is registered by a thermometer that signals some kind of integrating unit, which in turns activate the effectors, thereby either heating or cooling to drive the temperature back to the set point. For the baroreceptor reflex, the baroreceptors are the sensors, that reads the level of and changes in blood pressure, the *Nucleus Tractus Solitarius* (NTS) works as the integrator, integrating the different sensory inputs, and signals the effectors that drives the blood pressure back towards the desired range of function. A well functioning baroreflex have several effectors to activate in response to a drop in blood pressure (Hall 2011):

- Increased system resistance to blood flow by contraction of smooth muscles lining arterioles. An increased resistance means that it will be harder to push blood through the vessels, increasing the arterial pressure (in front of the arterioles).

- Decreased venous volume through contraction of smooth muscles lining the veins. In addition to increasing systemic resistance slightly, the decreased venous volume increases cardiac return, which in turn increase cardiac output through the effect of the Frank-Starling mechanism, and thereby increase arterial blood pressure.

- Increased heart rate and contractile force of the heart, increasing the rate at which blood is moved from the venous to the arterial side of the circulation, increasing arterial blood pressure.

Figure 2.11 sketches the components involved in the baroreceptor reflex and the responses described above. While all of these effects are important for an effective regulation, this study focuses on the latter mechanism regulating heart rate in response to changes in blood pressure. The following will therefore describe only the parts of the system related to heart rate control.

2.3.1 Baroreceptors

The baroreceptors are pressure sensitive neurons originating in the wall in the large arteries with the highest densities being in the aortic and carotid arches as shown in Figure 2.11. Just as other neurons,
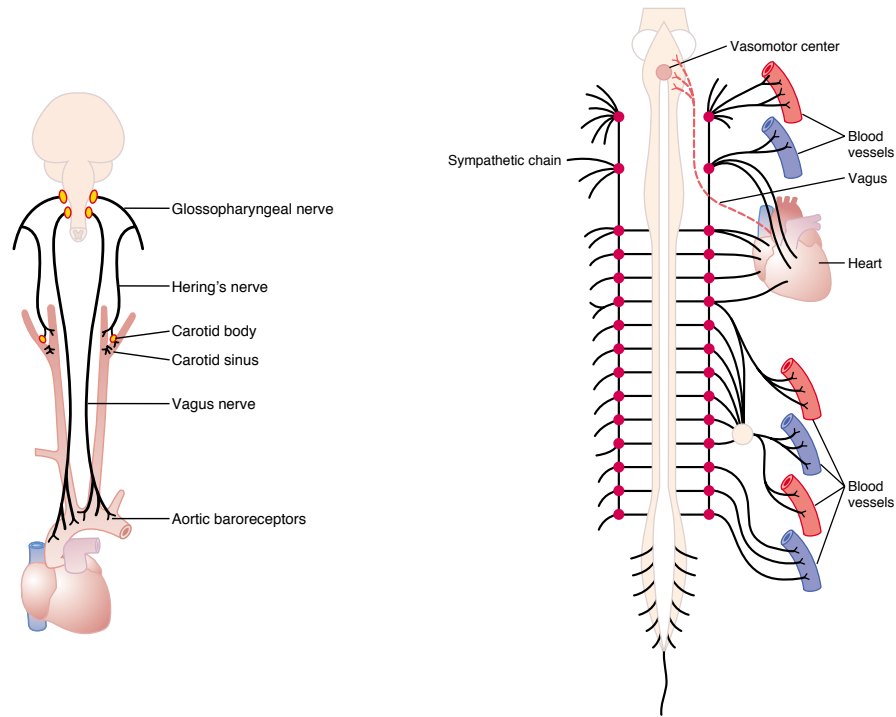
Figure 2.11: An overview of the components involved in the baroreflex. Left: Changes in arterial blood pressure are sensed by pressure sensitive neurons called baroreceptors in wall of arterial wall in the aortic arch and at carotid. Baroreceptors induces a nerve signal mediated by the vagus or Hering's nerve respectively, both terminating in *Tractus Solitarius* of the Medulla. Reprinted with permission from Hall 2011. Right: The black lines reflect the sympathetic nerves, while the dashed red line represent the vagus nerve that transmits the parasympathetic signal. Upon drop in pressure the vasoconstrictor center is activated causing an increase in sympathetic tone that leads to contraction of smooth muscles in arterioles and veins and an increase in rate and force of heart contractions. Meanwhile the vasomotor center withdraws parasympathetic tone in the vagus nerve, thereby increasing heart rate. Reprinted with permission from Hall 2011.

baroreceptors have a resting membrane potential of approximately −65mV. The negative potential is generated by the so called *sodium-potassium pump* that exchanges three Na^+ ions from the inside to the outside of the cell in exchange for two K^+ ions. At −65mV, the electrical potential and concentration gradients across the membrane are so large that an amount of ions equivalent to the one pumped leaks through the cell membrane, thereby reaching a constant level of polarization.

When the pressure sensitive end of the baroreceptor neuron is stimulated it causes a flow of positive ions into the neuron thereby depolarizing it (becoming less negative). As the membrane potential is increased to approximately −45mV voltage-gated sodium channels opens, allowing a large influx

of positive ions into the neuron. When the potential is close to zero the sodium-gated channels are deactivated, and voltage-gated potassium channels are activated, which will eventually start building up the membrane potential again. Since the depolarization happens at the end of the neuron, naturally, the excess amount of positive ions will begin to flow towards the remainder of the neuron, which is still highly polarized. This flux of positive ions will depolarize the membrane further, illustrated in Figure 2.12, causing voltage-gated sodium channels further down the neuron to open as the potential spreads, thereby starting a chain of depolarization along the neuron. This travelling wave of electrical potential is called an action potential, and works analogous in all nerve cells. It is important to note that the electrical potentials are always of the same magnitude and that large stimulation leads to a higher frequency rather than larger electrical "waves".
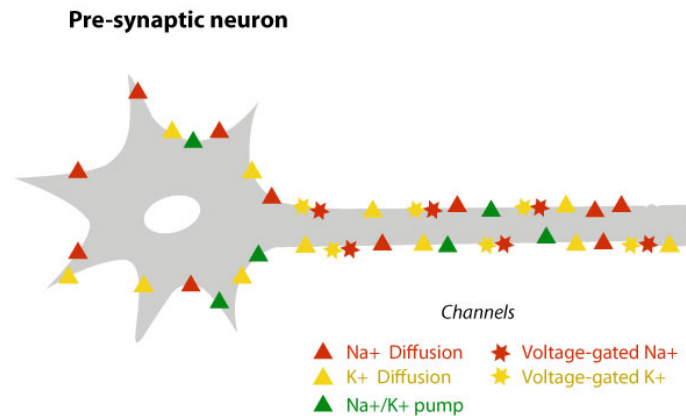
Figure 2.12: A schematic of a baroreceptor neuron with Na^+ and K^+ channels. Notice that the voltage gated channels are primarily placed along the axon to facilitate the propagation of action potentials.

2.3.2 Afferent firing

The baroreceptors are sensitive to pressure level and to changes in pressure, but mostly so at the typical operating pressure (Boron and Boulpaep 2012). Figure 2.13 shows the generated firing rate from the carotid baroreceptors for different levels of arterial blood pressure. It should be noted that:

- Firing at normal blood pressure is not zero. This means that the baroreceptors are able to

signal both positive and negative changes in blood pressure.

- Firing goes to zero for a healthy adult as the blood pressure drops near 50 mmHg, and reaches a maximum as blood pressure increases above 180 mmHg.

- The gradient of the curve is largest at normal blood pressure values around 100 mmHg. This means that the largest changes in the signal is sensed when blood pressure moves away from the set point at the normal value. This allows for quick and precise regulation by the baroreflex.

- The generated firing depends greatly on how fast the pressure changes. If blood pressure suddenly increases rapidly the response from the baroreceptors will be much larger than if it increases slowly. This is due to the graded generator potential from the sensory receptor causing larger depolarization, and thus causing more action potentials, for fast pressure changes.
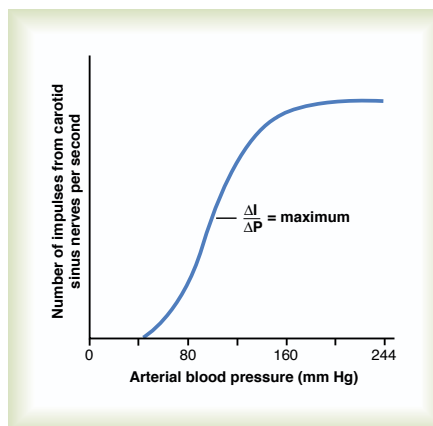
Figure 2.13: Firing of carotid baroreceptors as a function of arterial blood pressure. Note that firing rate for typical blood pressure is not zero, hence allowing for both positive and negative changes to be sensed by the baroreflex. Reprinted with permission from Hall 2011.

2.3.3 Autonomic Nervous System

The *Autonomic Nervous System* (ANS) is the part of the nervous system that works autonomous, without conscient direction from the brain. The signals from the baroreceptors are integrated in the area of the medulla called *Nucleus Tractus Solitarius* (NTS). Figure 2.14 contains a schematic of the

brain that shows the location of the medulla. For blood pressure control these signals are used to activate the *vasoconstrictor* and *vasodilator* centers of the vasomotor center when necessary. Control
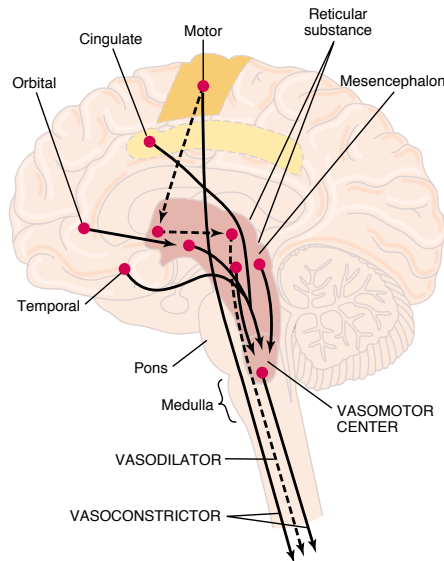
Figure 2.14: Schematic of parts of the brain important for circulatory regulation. Reprinted with permission from Hall 2011.

of heart rate is done through the *sympathetic* and *parasympathetic nervous system* which are respectively activated through the *lateral* and *medial* portion of the vasomotor center. An increased sympathetic signal generally leads to an increase in heart rate, while an increased parasympathetic signal leads to a decrease in heart rate. Mostly a decrease in parasympathetic tone will be accompanied by an increase in sympathetic tone, and vice versa, but not always. The two systems act differently on the heart, and complex behavior may arise where they are not inversely related. Simultaneous stimulation might for example lead to a decrease in heart rate, which usually leads to a decrease in cardiac output, and an increase in contractile force of the heart, usually leading to increased cardiac output. As shown in Figure 2.11 the sympathetic signal is mediated to the heart in an indirect manner through an interconnected network of neurons. At the termination of the sympathetic neurons at the synaptic junction at the pacemaker cells at the heart, the sympathetic neurons release the neurotransmitter *noradrenaline*. As is also shown in the figure, the parasympathetic signal is mediated directly via the vagus nerve to the heart, where the neurotransmitter *acetylcholine* is released onto the pacemaker cells.

2.3.4 Neurotransmitters, sinus node pacemaker and heart

At the synapse at the pacemaker cells of the heart the sympathetic and parasympathetic neurons release the neurotransmitters noradrenaline and acetylcholine.

Acetylcholine is synthesized in the terminal nerve ending where it is stored in large vesicles in highly concentrated form until release. Upon release acetylcholine exists for a few milliseconds before it is broken down to an *acetate ion* and *choline* catalyzed by the enzyme *acetylcholinesterase*. The formed choline is reabsorbed into the terminal ending and used to synthesize new acetylcholine.

The synthesis of noradrenalin begins in the terminal endings and in the storage vesicles where *dopamine* is hydroxylated to noradrenaline. After secretion into the synaptic junction noradrenaline is removed in different ways, usually after 1-2 seconds. 50-80% of the noradrenaline is reuptaken into the terminal ending, while the main part of the remaining noradrenaline is removed by diffusion into the surrounding body fluids. Through the blood it usually makes way to the liver where it is broken down.

The *sinus node* is a strip of cardiac muscle that has no contractile properties, but is able to autonomously generate action potentials. The sinus node is connected to the atrial muscle of the atrium such that any action potential generated in the sinus node spreads to the atrial muscle and causes contraction. The resting membrane potential of the sines nodal fiber is similar to that of the neurons explained earlier, but with a significant constant influx of sodium ions that works to depolarize the membrane. This leak is illustrated in Figure 2.15 as the lower part of the potential profile with a constant gradient. As the potential reaches approximately -40mV, slow acting sodium-calcium channels open and initiate the action potential. For the ventricular muscles, the dynamics are different which is illustrated by the different shapes of the potential profile. The resting potential is significantly lower, -90mV, and the spike is initiated by the activation of fast sodium channels when the potential is larger than approximately -85mV. Due to these fast channels, the potential can change faster than for the sinus nodal fibers causing the almost discrete behavior of the action potential.

Note that the primary determinant of the heart rate is the depolarization caused by diffusion. As soon as the potential hits -40mV, the action potential starts and the contraction of the heart is initiated. When acetylcholine is released at the synapse it causes a change in membrane permeability to potassium K^+, as illustrated in Figure 2.16. This causes potassium to leak out of the cell due to the concentration gradient, thereby hyperpolarizing the membrane potential and decreasing the action potential and heart contraction frequency. While the mechanism is not fully understood the release of noradrenaline increases the membrane permeability to sodium and calcium ions Na^+ and Ca^{2+}. This allows Na^+ and Ca^{2+} to enter the cell faster, increasing the rate of depolarization, leading to shorter time between action potentials and heart contractions. Figure 2.16 gives an overview of the synapse and the effect on the pacemaker cells.
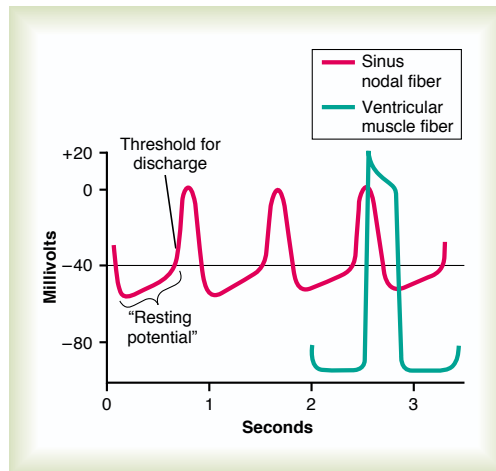
Figure 2.15: Electrical potential of a sinus nodal fibers as it generates action potentials that initiate heart contraction. Continuous leaking of Na^+ and Ca^{2+} depolarizes the membrane until the discharge potential is reached and the action potential is initiated. For the ventricular fibers the action potential is initiated as soon as any depolarization happens as it is driven by fast voltage gated sodium channels. Reprinted with permission from Hall 2011. It should be noted that *resting potential* refers to the lowest potential value, not the depolarization shown in the figure.
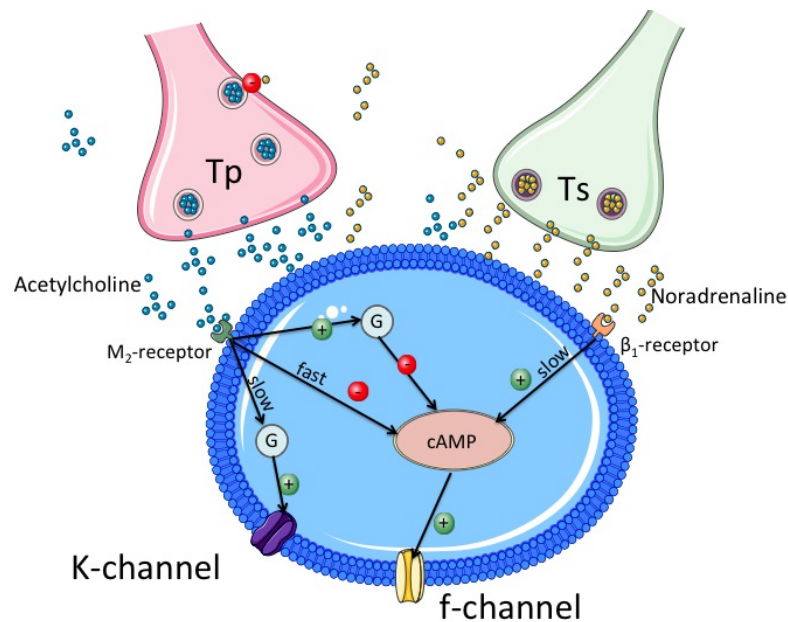
Figure 2.16: A schematic overview of the pacemaker cell synapse.

Chapter 3

Data

Typical experiments for testing the baroreceptor reflex includes postural challenges such as *active stand* or *tilt-table tests*, manipulation of systemic blood pressure such as *lower body negative pressure*, or respiratory challenges, including *valsalva*, *forced breathing* and *CO_2-rebreathing*. The modeling efforts of this study are based around experimental tilt table data obtained by MD. Jesper Mehlsen at Frederiksberg Hospital, Copenhagen, Denmark. This section describes the experimental procedure, what data are collected, and how the data are prepared for use in the mathematical model.

3.1   Experiment

To induce a response from the baroreflex the head-up-tilt (HUT) test changes the posture of the test subject by tilting the subject from supine to standing position. Initially the test subject is lying horizontally on a table, before being tilted to a 60° upright angle, as illustrated in Figure 3.1. As illustrated, the tilt causes pooling of the blood in the lower extremities, decreasing blood pressure for all points above center of gravity. This drop in pressure activates the baroreflex, and the response can be observed.

During the tilt, electrocardiogram (ECG) and blood pressure (BP) is measured. ECG is monitored using a five-electrode system, and blood pressure is monitored using a photoplethysmography (Finapres Medical Systems B.V) device mounted on the finger sampling at 1 kHz. To obtain an estimate of the blood pressure at the heart level, the test subject's hand is placed in a sling and held at the level of the heart. Figure 3.1 shows the experimental setup, with a test subject in upright position.

The procedure for atypical experiment is as follows:

- ECG and finapres is mounted on the test subject.

- The test subject is placed in supine position until breathing, heart rate and blood pressure are steady, typically 5-10 minutes.

29
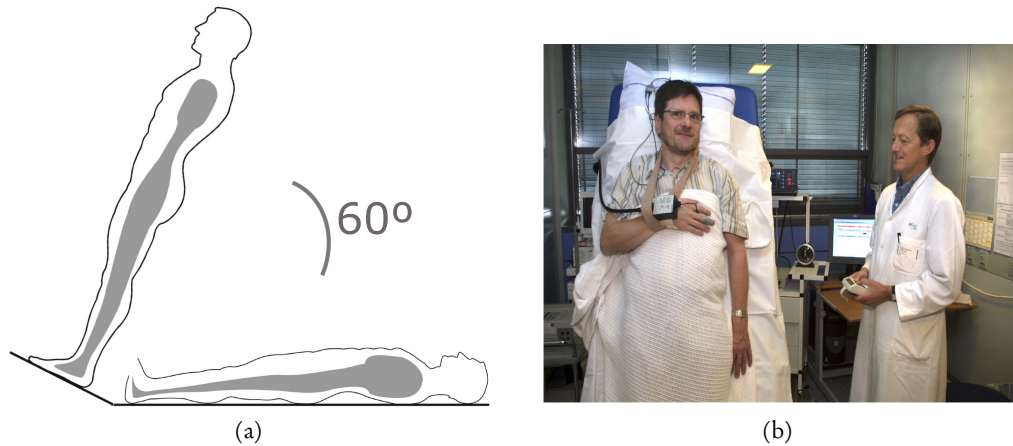
Figure 3.1: (a) When the test subject is tilted during HUT, the distribution of the blood volume is changed due to gravitational pull. This causes a decrease in blood pressure in the upper body, which activates the baroreflex. (b) Experimental setup for the HUT experiment, with the test subject in upright position. ECG is measured using five electrodes and BP is measured using a finapres device on the finger, with the hand located at heart level.

- The test subject is informed that the tilt is about to be initiated, and the table tilts 60° over a period of approximately 14 seconds.

- The test subject is left standing for approximately 10 minutes.

- The subject is tilted down.

The data used for this study are from tests performed on young healthy male individuals in their mid twenties believed to have perfectly functioning baroreflex regulation.

3.2   Blood pressure

Blood pressure is measured using photoplethysmography (Finapres Medical Systems B.V) mounted on the index finger, with the hand placed at heart level with the help of a closed loop sling around the neck.

Figure 3.2 shows blood pressure data from two different individuals.
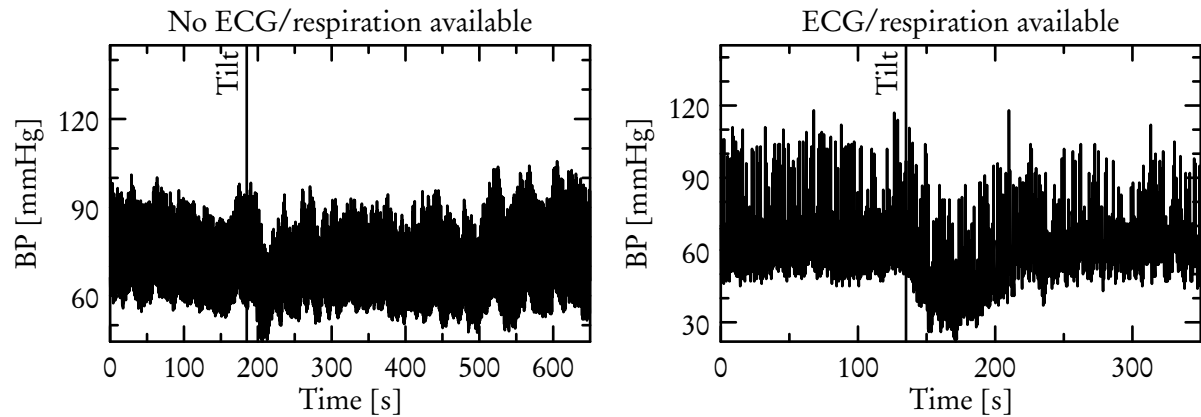
Figure 3.2: Blood pressure for two individuals. Left: only blood pressure available. Right: blood pressure and ECG available.

3.3 Calculation of heart rate

During the test blood pressure (BP) and electrocardiogram (ECG) are recorded. Due to the nature of the machines, different disturbances may occur. ECG is quite sensitive to movements of the chest such a coughing, while BP is sensitive to movement of the finger where the sensor is attached. In addition, the machinery measuring BP has a built-in calibration tool that might trigger during experiments to cause disturbances of measurements. Since the periodicity of the heart is seen in both the ECG and BP, both can be used to calculate heart rate (HR).

Figure 3.3 shows HR calculated from ECG and from BP. It is clear that there are some small deviations, but that the agreement between the two is very good in general. Since the heart rate calculated from blood pressure in general has more noise than that calculated from the ECG, I will be using the heart rate extracted from the ECG.

Electrocardiogram (ECG)

Extraction of heart rate from ECG is done using the software LabChart version 7.2.4 from AD Instruments. The software has built-in algorithms for recognising periods in an ECG curve[1]. Figure 3.4 illustrates how LabChart identifies the maximum of the QRS-complex.

---

[1]The settings used for Labchart are: ECG mode with QRS-width= .06s, normalization with a window of 5 seconds, minimum peak height of 0.9 S.D., Two-sided height detector, with maximum as trigger and a minimum period of 0.4 seconds.
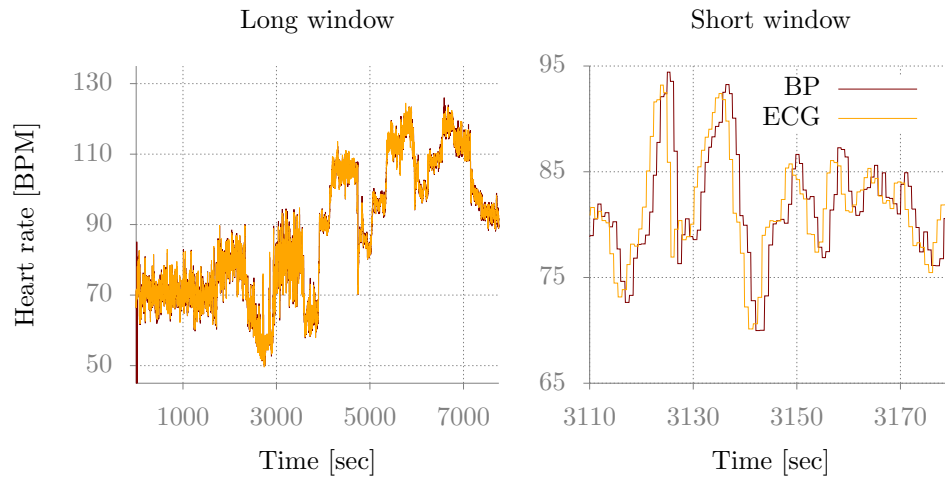
Figure 3.3: Heart rate calculated from electrocardiogram and blood pressure. Left: Agreement on a large timescale, with deviations from disturbances in blood pressure data. Right: Agreement on short timescale, with a small delay, $\sim$ 1sec, on the BP curve due timing of markers of periods in BP and ECG data.
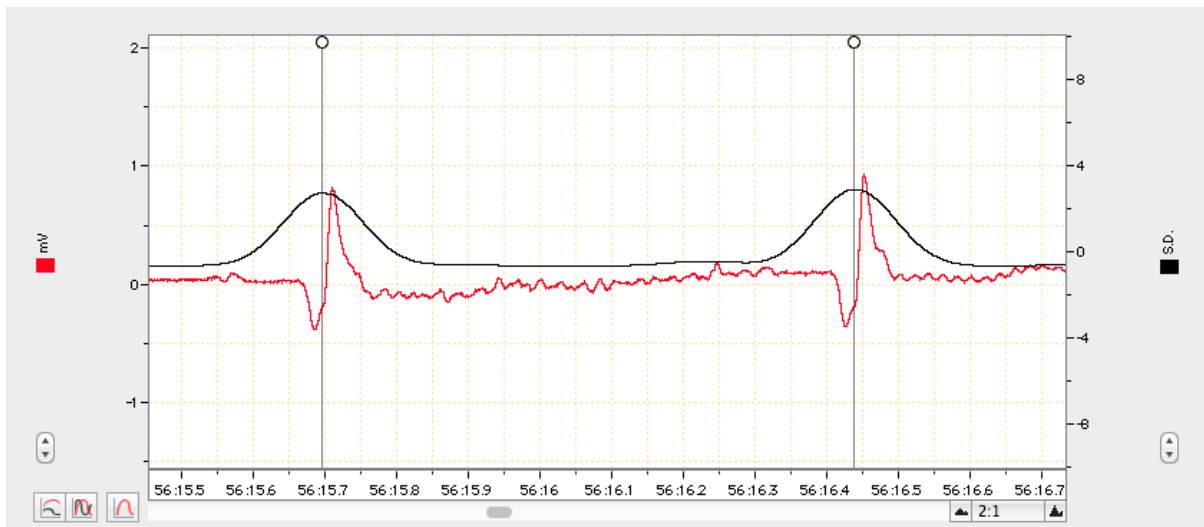
Figure 3.4: `LabChart`'s builtin algorithm identifies the peaks of QRS-complex for calculating heart rate.

3.4 Hydrostatic contribution to blood pressure

During the experiment blood pressure is measured using a finapres mounted on the finger, with the hand and finger held at heart level. In supine position this gives a good representation of the blood pressure at the carotid sinus baroreceptors. In the upright position, the blood pressure at heart level will have a larger hydrostatic component than the blood pressure at the carotid sinus baroreceptors. Assuming that the blood vessels of the measurement point and the baroreceptor is well connected, the only difference in blood pressure will be the difference in hydrostatic pressure. This contribution can be estimated as (Williams et al. 2013),

$$P = h\rho g \tag{3.1}$$

where h is the height difference, ρ is the density of the liquid, and g is the gravitational constant. Alternatively, assuming the density of blood is similar to the density of water, one can use the units described by (Thompson and Taylor 2008),

$$1 \text{ mmH}_2\text{O} = 9.80665 \text{ Pa}, \qquad 1 \text{ mmHg} = 133.3224 \text{ Pa}, \tag{3.2}$$

to translate the blood column height directly to mmHg through the ratio,

$$r = \frac{9.80665 \, {}^{\text{Pa}}/_{\text{mmH}_2\text{O}}}{133.3224 \, {}^{\text{Pa}}/_{\text{mmHg}}} \approx 0.074 \, {}^{\text{mmHg}}/_{\text{mmH}_2\text{O}}. \tag{3.3}$$

If we let d denote the distance from the heart to the baroreceptor, the vertical height difference between the heart and the carotid sinus can be determined from the tilt angle ϕ as,

$$h(\phi) = \sin(\phi)d. \tag{3.4}$$

Hence, the blood pressure at the carotid sinus can be modeled as the blood pressure at heart level minus the hydrostatic contribution,

$$P_{\text{CS}} = P_{\text{heart}} - h \times 0.074 \, {}^{\text{mmHg}}/_{\text{mmH}_2\text{O}}.$$

The tilt table operates with a constant angle velocity, $\omega = {}^{\pi}/_{(3 \times 14)}$, and the height during the tilt can be modelled as

$$h_\phi(t) = \sin\left(\frac{\pi}{3}\frac{1}{14}t\right)d. \tag{3.5}$$

Hence the model of the carotid sinus blood pressure is,

$$
P_{cs} = \begin{cases} P_{\text{heart}} & \text{if } t \leq t_{\text{tilt}} \\ P_{\text{heart}} - r h_{\omega} \left(t - t_{\text{tilt}} \right) & \text{if } t_{\text{tilt}} t \leq t_{\text{tilt}} + 14 \\ P_{\text{heart}} - r \sin\left(\frac{\pi}{3}\right) d & \text{if } t_{\text{tilt}} + 14 < t. \end{cases} \tag{3.6}
$$

Figure 3.5 shows blood pressure measured at heart level and the modeled pressure at carotid sinus.
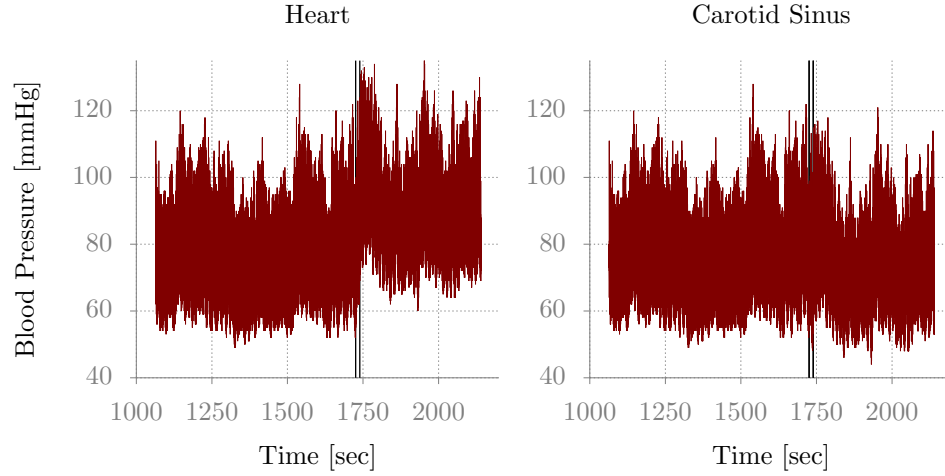
Figure 3.5: Blood pressure measured at heart level, and the blood pressure at carotid sinus as modelled by equation (3.6). Vertical lines marks the line of beginning and end of tilt from supine to upright position.

3.5 Respiration

While experimental methods exist for monitoring respiration, no such measurements were made while collecting data for this study. However, good approximations can be obtained by analysing ECG data. The electrodes of the ECG measures impedances and direction of electrical current through the upper body. As the lungs are filled with air during inspiration, the distances between electrodes change due to changes in volume, and as a result the impedance changes due to change in conductivity of the thoracic volume.

In the ECG signal the changes induced by respiration is reflected in the potential difference between the Q- and the R-peaks. The method used for extracting the respiration signal from the ECG follows

suggestion by Thomas et al. 2005 and Widjaja et al. 2010:

1. Identify Q- and R-wave peaks, and use potential differences as discrete measurements of respiration signal. See Figure 3.6.

2. Interpolate between points using a cubic spline, to obtain a continuous respiratory signal. See Figure 3.7.

3. Investigate reliability of amplitude and frequency of respiratory signal and extract frequency.

Amplitude detection and interpolation

Because the impedance of the breast is different when the lungs are filled with air, the difference in potential between the peaks of the Q and R waves varies over the respiratory cycle. Hence, information about the respiratory cycle can be obtained from the potential difference for each cycle.

Figure 3.6 shows the located peaks of Q and R waves for a small interval. The detected amplitudes should be such that the amplitude does not deviate more than 20% of the average of Q-R-amplitudes in a window of 41 cycles centered around the cycle in question (Thomas et al. 2005). Q-R pairs that do not satisfy this condition are removed.
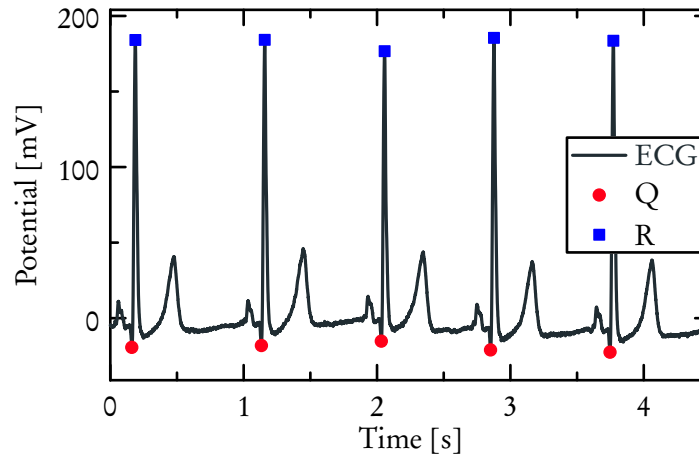
Figure 3.6: The located Q- and R-peaks of the ECG.

The left panel of Figure 3.7 shows the amplitudes plotted against the time precisely between the Q and R peaks, and the signal interpolated using a cubic spline. This cubic spline approximates the respiratory signal.
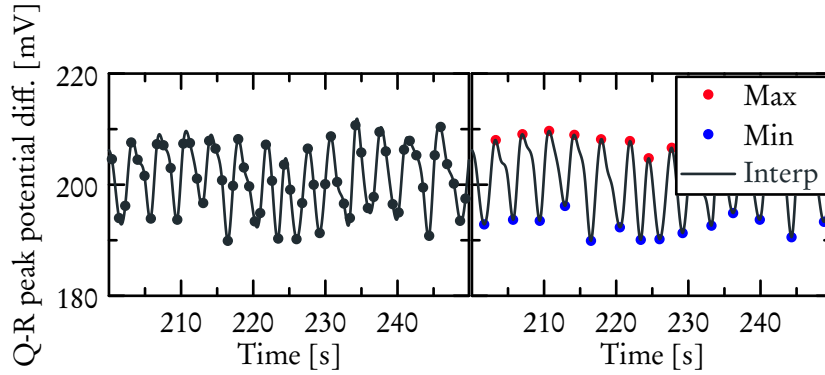
Figure 3.7: Left: The calculated amplitude difference between the Q- and R-eaks of the ECG, and the corresponding cubic spline interpolation, used as an approximation to respiration. Right: Located peaks and valleys of the respiratory signal.

Verification of respiratory signal

To ensure that the extracted respiratory signal are realistic, peaks and valleys are detected, as illustrated in Figure 3.7, and are used to check the respiratory signal for the following two conditions given by Widjaja et al. 2010.

Duration: The duration of a respiratory cycle should be at least 1.5 second. Shorter respiratory cycles are eliminated by removal of a peak and a valley such that the amplitude difference between the surrounding valley and peaks are maximal.

Amplitude: The amplitude difference between a peak and a valley should be at least 15% of the previous and the following amplitude. If it is not, a peak and a valley is removed such that the amplitude difference between surrounding peaks and valleys are maximal.

Respiratory frequency

The respiratory frequency is calculated using both the peaks and the valleys of the respiratory signal, as the inverse of the time between the previous and current time point. Calculated frequency data points and their cubic interpolations for peaks and valleys are plotted in the left panel of Figure 3.8, together with the approximated respiratory frequency calculated as the mean of the two splines. The right panel of the figure shows the entire respiratory frequency series.
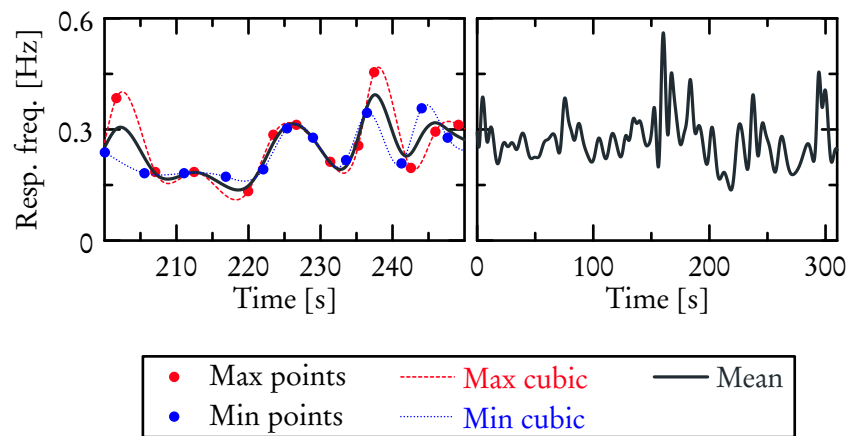
Figure 3.8: Left: Respiratory frequencies found using minimum and maximum values of the respiratory signal, their cubic spline interpolations, and the mean of the cubic splines consider the best approximation to the respiratory frequency. Right: The approximated respiratory frequency for the entire time series.

4

Chapter

Mathematical modeling of the baroreceptor reflex

Numerous modeling studies have addressed baroreflex regulation (e.g. Bannister 1993,Mosqueda-Garcia et al. 2000,Heusden et al. 2006), however, most of these only analyzed some aspects of the system, and most were validated against literature and/or animal data. To our knowledge, only a few models have described the complete system from blood pressure to heart rate regulation (Olufsen, Tran, et al. 2006; Bugenhagen, Cowley, and Beard 2010; Ottesen and Olufsen 2011). One obstacle in designing patient specific models is that human data are only available at the ends of the chain: blood pressure, which serves as an input to the system, and heart rate, the model output.

The mathematical model investigated in this chapter describes the negative baroreflex feedback system, that modulates heart rate, and respiration. The latter is believed to explain low frequency variation in heart rate (Yasuma and Hayano 2004). The model describes short-term regulation of heart rate as a function of arterial blood pressure and respiratory frequency. The dependence on these inputs reflects two mechanisms: baroreflex regulation and respiratory sinus arrhythmia (RSA).

The model, shown in Figure 4.1, includes the following components: A nonlinear elastic model describing total arterial wall strain in response to blood pressure changes, a viscoelastic model describing the arterial wall deformation, a linear model describing the afferent firing rate of the baroreceptor neurons in response to deformation of baroreceptor neurons, models describing the sympathetic and parasympathetic nervous outflows, models describing synaptic concentrations of acetylcholine and noradrenaline, and models describing intracellular compounds modulated via β_1 and M_2 receptors, and finally a model predicting heart rate. Below each model component is described in detail.
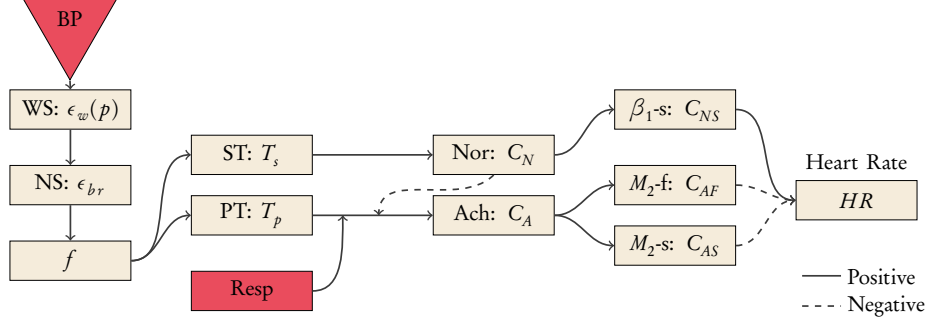
Figure 4.1: Overview of heart rate model. Model components include: Input blood pressure (BP) and respiratory frequency (Resp), arterial wall strain (WS), neuron strain (NS), firing rate (f), sympathetic (ST) and parasympathetic tone (PT), noradrenaline (Nor) and acetylcholine (Ach) concentration, pacemaker cell pathways β_1 slow ($\beta_1 - s$), M_2 slow ($M_2 - s$) and fast ($M_2 - f$), and heart rate (HR).

4.1 Model input

4.1.1 Blood pressure

Pulsatile continuous measurements of arterial blood pressure comprises the input to the model. To test whether the proposed model can predict known static and dynamic responses, it is tested against three stimuli shown in Figure 4.2: A step pressure change, an oscillating ramp down pressure, and experimental pulsatile blood pressure measured using a CNAP device during head-up-tilt (HUT).

4.1.2 Respiration

As respiratory frequency is hypothesized to influence the heart rate, and the model includes a description of the possible mechanism, respiratory frequency data is required as a model input.

As the available experimental data contains no measurements of respiration, an approximation is extracted from ECG using the method described in Section 3.5. When no ECG is available the model is parameterized to ignore respiratory input. For the data set presented earlier that does include ECG, the extracted respiratory signal is shown in Figure 4.3.
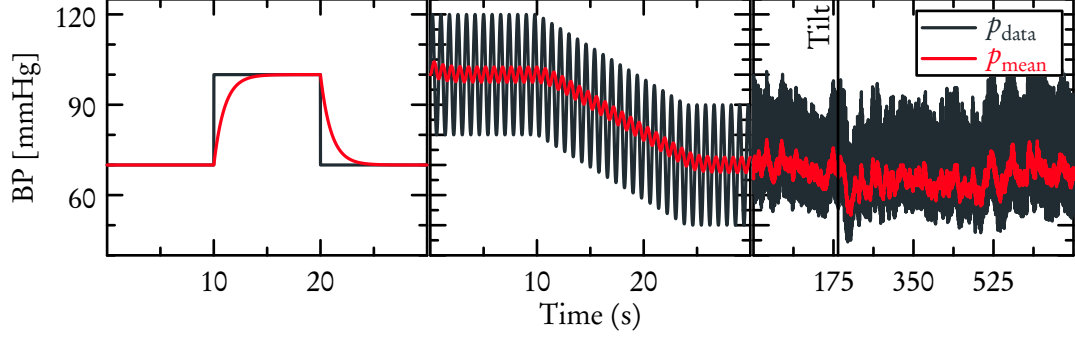
Figure 4.2: Input pressure signal used to investigate the qualitative behavior of the model. Left: a step input. The pressure increases from 70 to 100 mmHg, stays at the increased pressure for 10 sec, then returns to 70 mmHg. Middle: pressure oscillating with an amplitude of 20 mmHg and a period of 0.8 seconds. Initially the offset is 100 mmHg, but is decreased to 70 mmHg over 14 seconds (corresponding to the tilt duration in the experimental data). Right: measurements from a HUT experiment.
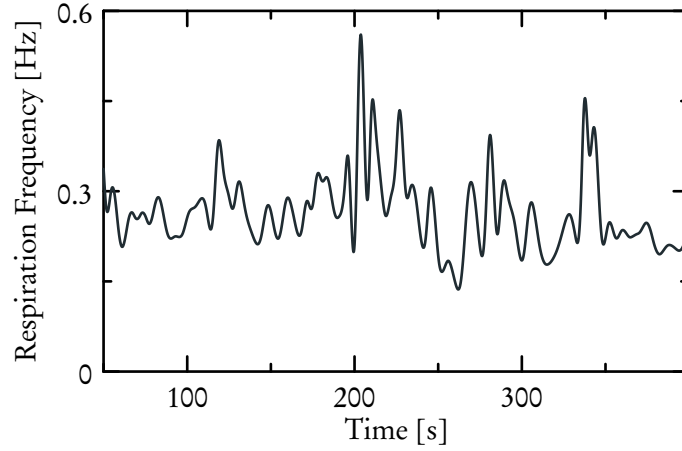
Figure 4.3: Example of data for respiration frequency used as model input.

4.2 Pressure-wall strain relation

It is known that the pressure-area relationship of the arterial wall is nonlinear and viscoelastic (Valdez-Jasso et al. 2011), and that the relation between arterial wall strain and nerve firing is viscoelastic (Katona and Barnett 1969; Coleridge et al. 1981; Valdez-Jasso et al. 2011). Given that two viscoelastic components in series are not distinguishable, the wall deformation is assumed elastic, while deformation of nerve ending is viscoelastic.

The nonlinear pressure-area relation observed for arteries during steady-state experiments (Laurent et al. 1994; Atienza et al. 2007), can be modelled using a sigmoidal function that saturate of the form,

$$A(p) = A_0 + (A_M - A_0)\frac{p^k}{p_0^k + p^k} \tag{4.1}$$

where p denotes the applied blood pressure, A_M, A_0 the maximum and unstressed cross-sectional area, while k and p_0 determine the steepness of the sigmoidal function and the pressure at which the transition from minimum to maximum area is centered around. A general principle, often observed in physiological systems, is that the largest response to changes in input happens at the typical functioning value (Burton 1966). Assuming this principle is correct, it is included in the model by setting p_0, the pressure at which the area is most sensitive, equal to the mean pressure at rest, i.e. $p_0 = \bar{p}$. In reality the arteries are distended at the typical pressure of operation, but the cross sectional at this pressure is lower than the midpoint between maximum and minimum cross-sectional area (Burton 1966).

The vessel strain ϵ_w can be related to deformation by,

$$\epsilon_w = \frac{r - r_0}{r}, \tag{4.2}$$

where r and r_0 denote the stressed and unstressed vessel radius. Using (4.1) the strain, (as illustrated in Figure 4.4) can be expressed as

$$\epsilon_w = 1 - \sqrt{\frac{p_0^k + p^k}{p_0^k + A_{M0}p^k}}, \quad A_{M0} = \frac{A_M}{A_0}. \tag{4.3}$$

Further assuming that the initial pressure is at equilibrium at rest (i.e. $p(0) = \bar{p}$), the initial strain of the arterial wall is given by

$$\epsilon_w(0) = 1 - \sqrt{\frac{2}{1 + A_{M0}}}. \tag{4.4}$$

Figure 4.4 shows a plot of the sigmoid function describing the wall strain.

Parameters.

The parameters needed to predict the wall strain are: the ratio of maximum to unstressed cross-sectional area A_{M0} and the parameter determining the rate of change of the sigmoid function k. In addition the constant $p_0 = \bar{p}$ is set as described above.

Using literature data and a few assumptions (outlined below) initial estimates of A_{M0} and k can be calculated. Arndt, Klauske, and Mersch 1968 measured carotid artery diameter during the regular cardiac cycle in vivo for 9 humans in supine position using ultra sound. Table 4.1 lists the data recorded

Table 4.1: Data recorded from Arndt, Klauske, and Mersch 1968 from in vivo human subjects using ultra sound.

Sub	Sex	Age	H-CA cm	BP cm H$_2$O (mmHg)		Δp cm H$_2$O (mmHg)	R diast. cm	Δr cm
				systol.	diastol.			
AR	m	34	26	177 (130)	122 (90)	55 (40)	0.36	+0.04
BE	m	23	26	177 (130)	106 (78)	71 (52)	0.40	+0.05
BO	m	24	26	177 (130)	95 (70)	82 (60)	0.35	+0.06
KE	m	31	23	143 (105)	88 (65)	55 (40)	0.39	+0.04
KO	m	28	27	147 (108)	86 (63)	61 (45)	0.38	+0.06
LE	m	28	27	170 (125)	109 (80)	61 (45)	0.43	+0.06
ME	m	28	27	170 (125)	113 (83)	57 (42)	0.39	+0.06
SC	f	27	22	160 (118)	109 (80)	51 (38)	0.37	+0.06
VO	f	28	26	163 (120)	109 (80)	54 (40)	0.36	+0.06
AV	M	28	26	166 (122)	103 (76)	63 (46)	0.39	+0.053

for the 7 male and 2 female subjects[1].

Assuming that under normal conditions the variations in blood pressure causes the crosssectional area of the artery to vary in the interval of 35% and 65% of the difference between unstressed and the maximum areas, k and A_{M0} is predicted using mean values from Table 4.1. The mean pressure is estimated as the mean of systolic and diastolic pressure,

$$p_0 = \frac{122 \text{ mmHg} + 76 \text{mmHg}}{2} = 99 \text{ mmHg}.$$

Assuming the mean systolic pressure causes a distension of 65%, and that the diastolic pressure causes a distension of 35%, can be formulated as

$$0.65 = \frac{(122 \text{ mmHg})^k}{(122 \text{ mmHg})^k + p_0^k}, \qquad 0.35 = \frac{(76 \text{ mmHg})^k}{(76 \text{ mmHg})^k + p_0^k},$$

---

[1]Note: 1 cmH$_2$O $= .736$mmHg.

Isolating and equating p_0 from the two expressions allows the calculation of an initial estimate for k

$$p_0^k = (122 \text{ mmHg})^k \frac{0.35}{0.65} = (76 \text{ mmHg})^k \frac{0.65}{0.35}$$

$$k = 2 \frac{\log\left(\frac{0.65}{0.35}\right)}{\log\left(\frac{122}{76}\right)} \approx 2.62.$$

For the parameter A_{M0} an estimate can be obtained by assuming that at the smallest cross-sectional area is obtained at diastole and the maximum value at systole. For example, if at diastole $p = 76$ mmHg the corresponding area is $A(76) = (0.39\text{cm})^2 \pi = 0.478\text{cm}^2$, and if at systole $p = 122$ mmHg, the corresponding area is $A(122) = (0.39\text{cm} + 0.053\text{cm})^2 \pi = 0.617\text{cm}^2$. This leads to an estimate of A_{M0}

$$0.478\text{cm}^2 = A_0 + (A_M - A_0)0.35$$
$$0.617\text{cm}^2 = A_0 + (A_M - A_0)0.65$$
$$A_0 = 0.316\text{cm}^2$$
$$A_M = 0.780\text{cm}^2$$
$$\rightarrow$$
$$A_{M0} = 2.47.$$

$$(4.5)$$

Figure 4.4 shows model fit to the experimental data, with parameters determined as described above and with values of k half and twice the nominal value.
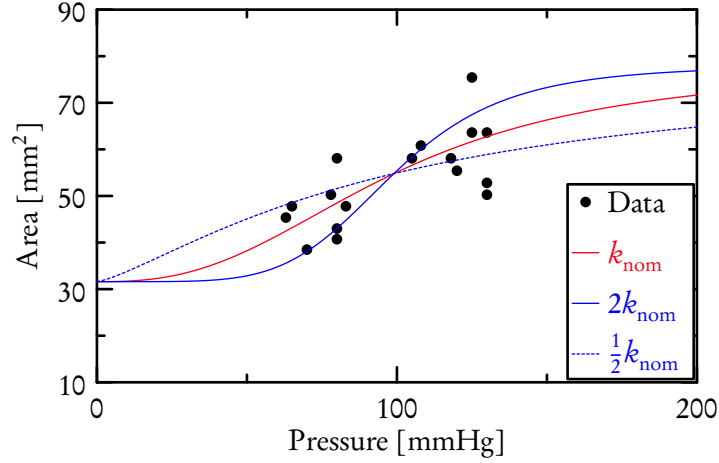
Figure 4.4: Fit of wall strain model (k_{nom}) with nominal parameter values obtained from average values of data from Arndt, Klauske, and Mersch 1968 (See Table 4.1), plotted together with the curves produced using a twice as large k ($2k_{nom}$) and half as large k ($1/2k_{nom}$).

4.3 Baroreceptor strain

The baroreceptor nerve endings are embedded within the arterial wall. It is not known exactly how these nerve endings stretch relative to the strain of the arterial wall, but certain features of the firing of the baroreceptors indicates that the strain of the baroreceptors relaxes viscoelastically. In this study, the approach proposed by (Bugenhagen, Cowley, and Beard 2010; Mahdi, Sturdy, et al. 2013) is followed, assuming that the baroreceptor nerve endings are elastic, but that the remaining part of the arterial wall is viscoelastic, i.e. in response to strain, it exhibits both elastic and viscous behavior.

One of the simplest viscoelastic models is the so-called *Voigt body*, which can be depicted as a dashpot and a spring in parallel (Alfrey 1997; Bugenhagen, Cowley, and Beard 2010; Fung 1990). The Voigt body model exhibits stress relaxation at a given rate in response to an applied strain. To account for more relaxation time scales, Voigt bodies are often placed in series. This study follows suggestions by Bugenhagen, Cowley, and Beard 2010 and Mahdi, Sturdy, et al. 2013 who analyzed how many Voigt bodies is needed to describe the deformation of the baroreceptor neurons in response to strain of the arterial wall. While Bugenhagen, Cowley, and Beard 2010 included three time-scales (using three voigt bodies in series), the later study by Mahdi, Sturdy, et al. 2013 showed that to account for known qualitative experimental responses such as overshoot, adaptation, and hysteresis, it is adequate to include two Voigt bodies.

44
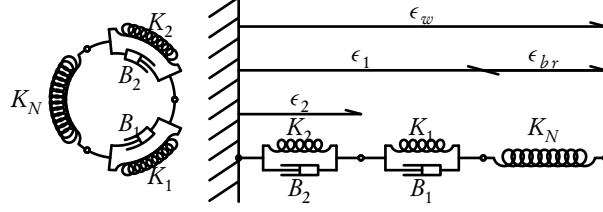
Figure 4.5: Right: Voigt body schematic. ϵ_{br} reflects the elastic part of the strain by a spring, K_N. ϵ_2 represents the strain on the left Voigt body, while ϵ_1 reflects the total strain over both Voigt bodies, illustrated by the lines above. Left: the model can be interpreted as the arterial wall consisting of three different kinds of tissue, that are connected in serial, forming a loop around the circumference of the artery.

The deformation displayed by the two Voigt bodies can be predicted by

$$
\begin{aligned}
\frac{d\epsilon_1}{dt} &= -(\alpha_1 + \alpha_2 + \beta_1)\epsilon_1 + (\beta_1 - \beta_2)\epsilon_2 + (\alpha_1 + \alpha_2)\epsilon_w, \\
\frac{d\epsilon_2}{dt} &= -\alpha_2\epsilon_1 - \beta_2\epsilon_2 + \alpha_2\epsilon_w, \\
\epsilon_{br} &= \epsilon_w - \epsilon_1,
\end{aligned}
\tag{4.6}
$$

where $\alpha_i = K_N/B_i$, $\beta_i = K_i/B_i$ and ϵ_{br} denotes the strain of the baroreceptor neuron, ϵ_2 the strain of the second Voigt body and ϵ_1 is the sum of the strain of both Voigt bodies, as shown in Figure 4.5.

Initial conditions for the differential equations are obtained by assuming that at rest the system is in equilibrium, ie. $\frac{d\epsilon_1}{dt} = \frac{d\epsilon_1}{dt} = 0$.

$$
\begin{aligned}
\epsilon_1(0) &= \varkappa\epsilon_w, \quad \varkappa = \frac{\alpha_1\beta_2 + \alpha_2\beta_1}{\alpha_1\beta_2 + \alpha_2\beta_1 + \beta_1\beta_2}, \\
\epsilon_2(0) &= \frac{\alpha_2}{\beta_2}(1-\varkappa)\epsilon_w, \\
\epsilon_{br}(0) &= \epsilon_w(1-\varkappa) = \epsilon_w\frac{\beta_1\beta_2}{\alpha_1\beta_2 + \alpha_2\beta_1 + \beta_1\beta_2}.
\end{aligned}
\tag{4.7}
$$

Figure 4.6 shows the response generated when combining the elastic wall deformation model with the two Voigt body viscoelastic model for the two types of input presented earlier: a step increase followed by a step decrease and data from a tilt table experiment.
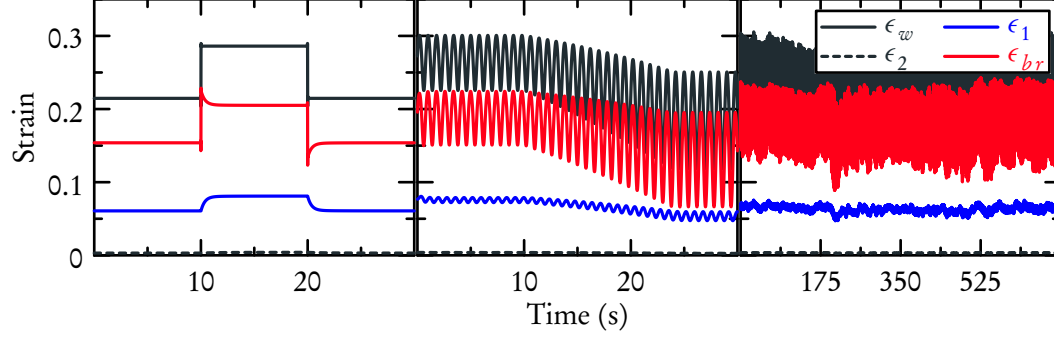
Figure 4.6: Strains of the viscoelastic components in response to, Left: a step in pressure. Middle: an oscillating ramp-down pressure signal. Right: experimental pressure data.

Parameters.

K_N represents the spring constant of the baroreceptor neuron, K_1 and K_2 the spring constants of the two Voigt bodies, and B_1 and B_2 the dampening effect from the dashpots in the two Voigt body model. The scaled parameters $\alpha_1, \alpha_2, \beta_1, \beta_2$ represents the spring constants scaled by the dampening from the dashpots.

To distinguish the two dashpots, the time scales of the viscoelastic components should be different, $\alpha_1 \neq \alpha_2$. Nominal parameter values are: $\alpha_1 = 0.75, \alpha_2 = 0.1, \beta_1 = 2, \beta_2 = 0.5$. The time scales for this configuration are $\tau_2 = 0.566$ and $\tau_1 = 2.784 \text{ sec}^{-1}$.

4.4 Baroreceptor neuron firing

As noted in Chapter 2, afferent firing of baroreceptor neurons originates when action potentials are initiated by strain of stretch-sensitive ion channels. This can be modeled using a Hodgkin Huxley type model (Schild et al. 1994), which in its simplest form can be reduced to an integrate and fire model (Abbott 1999; Lapicque 1907; Koch and Segev 1998). (Mahdi, Sturdy, et al. 2013) compared the integrate and fire model with a simple linear model, and noted that except for situations where the pressure is decreased discretely, baroreceptor firing does not cease and that a simple linear model is adequate. As such sudden drops in blood pressure are not expected to happen in vivo, it is assumed hat firing rate f can be predicted by

$$f = \epsilon_{br} s_1 + s_2, \tag{4.8}$$

where s_1 and s_2 denotes the gain and shift respectively (Bugenhagen, Cowley, and Beard 2010). Realizations of this model is shown in Figure 4.7 for both a step increase in pressure and experimental pressure data.
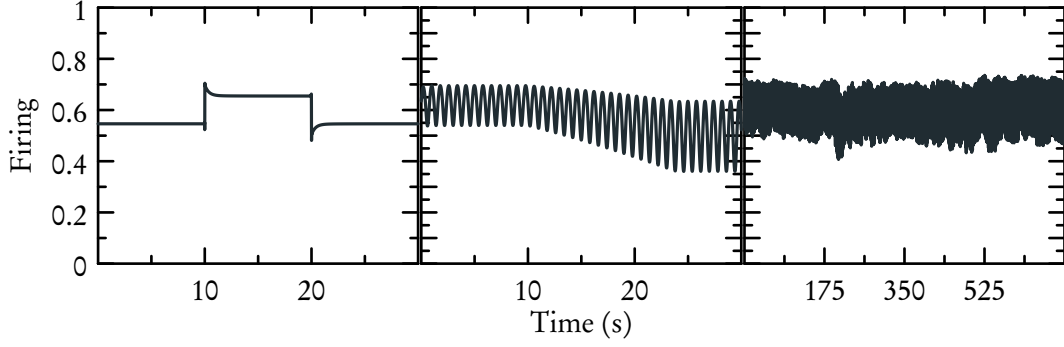
Figure 4.7: Left: Afferent neuron firing in response to step pressure increase. Middle: Response to oscillating ramp-down signal. Right: Baroreceptor firing for the experimental pressure input data.

Parameters.

Assuming the smallest and largest possible firing rates are 0 and 1, set

$$
\begin{aligned}
s_1 &= \frac{1}{x+1} \frac{\sqrt{A_{M0}}}{\sqrt{A_{M0}} - 1} \approx 2.0, \\
s_2 &= \frac{x}{x+1} \approx 0.27.
\end{aligned}
\tag{4.9}
$$

The origin of these expressions are discussed in Section 5.2.3.

4.5 Parasympathetic and sympathetic outflow

The baroreceptor firing is integrated in the nucleus tractus solitarius (NTS), from which efferent signals are generated along sympathetic and parasympathetic pathways. The parasympathetic outflow is transmitted via the vagus nerve, while the sympathetic outflow is transmitted via the sympathetic ganglia. An increase in afferent baroreceptor firing (corresponding to an increase in pressure) leads to an increase in the parasympathetic outflow (or tone), whereas a decrease in afferent baroreceptor firing (corresponding to a decrease in pressure) leads to an increase in sympathetic outflow. Moreover, the response saturates at high and low pressure.

Similar to Olufsen, Tran, et al. 2006, these responses are modeled using Hill functions of the form

$$T_{\text{p,br}}(f) = T_{p_m} + \left(1 - T_{p_m}\right) \frac{f^\xi}{f^\xi + f_p^\xi},$$

$$T_s(f) = 1 - \left(1 - T_{s_m}\right) \frac{f^\eta}{f^\eta + f_s^\eta},$$

(4.10)

where $T_{\text{p,br}}$ and T_s denote the contributions from the baroreflex (br) to parasympathetic (p) and sympathetic (s) tone. T_{p_m} and T_{s_m} denote the minimum values of the non-dimensional parasympathetic and sympathetic tone. The maximum value is 1. f_s and f_p determines the firing at which the system is most sensitive to changes and the value denoting the transition from minimum to maximum value. η and ξ are not shown on the figure but determines the slope of the curve during the transition between the minimum and maximum value. Figure 4.8 illustrates the qualitative behavior of these functions, while Figure 4.9 shows the tones corresponding to the model input.
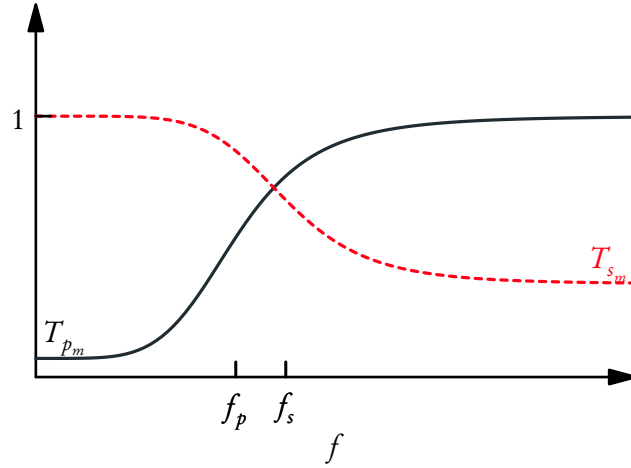
Figure 4.8: Hill functions used to model the contribution of the baroreflex to the parasympathetic and sympathetic outflows.

Parameters.

Assuming that the smallest and largest possible afferent firing rates lead to a values 10% and 90% between the minimum and maximum value of the parasympathetic tone, a nominal value for ξ can be
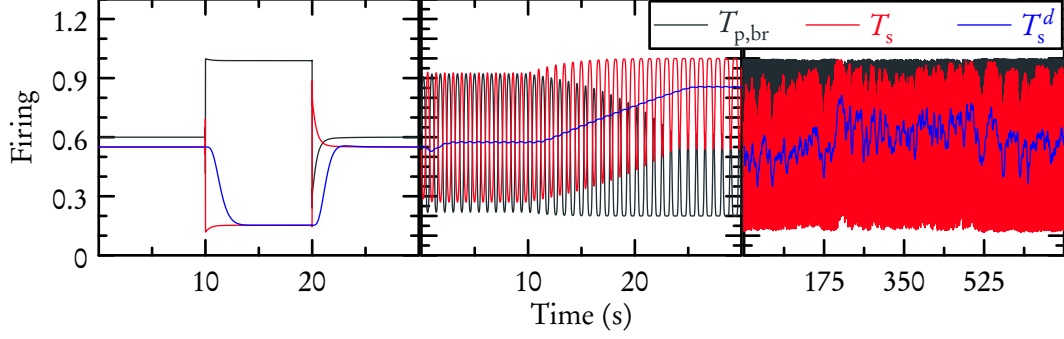
Figure 4.9: Parasympathetic, sympathetic and delayed sympathetic tone for: Left: Step input. Middle: Oscillating ramp down signal. Right: Experimental data.

estimated.

$$\frac{f_m^\xi}{f_m^\xi + f_0^\xi} = 0.1, \quad \frac{f_M^\xi}{f_M^\xi + f_0^\xi} = 0.9,$$

$$\xi = 2\frac{\log(9)}{\log\left(\frac{f_M}{f_m}\right)}. \tag{4.11}$$

It should be noted that the larger the ratio between f_m and f_M, the smaller the value of ξ. This is reasonable as a larger proportional difference means that the change from minimum to maximum happens over a longer interval, and therefore the gradient is smaller. The analysis for the sympathetic expression is analogous.

Parameters f_p and f_s describe the point with the maximum gradient of the Hill functions, and thereby the firing rate where the system is most sensitive to changes. By setting these equal to the firing rate at the initial steady state pressure $p = p_0$, it is ensured that the parasympathetic and sympathetic tone are most sensitive to changes at their typical operation value. For an initial estimate of the nominal value, $f_s = f_p$ are given by

$$\begin{aligned}
f_p = f_s &= \epsilon_b r(p_0)s_1 + s_2 = (\epsilon_w(p_0) - \epsilon_1(p_0))s_1 + s_2 \\
&= \epsilon_w(p_0)(1-x)s_1 + s_2 \\
&= \left(1 - \sqrt{\frac{2}{1+A_{M0}}}\right)(1-x)s_1 + s_2,
\end{aligned} \tag{4.12}$$

using the expressions found for initial conditions of ϵ_{br} and the value of ϵ_w at $p = p_0$ from (4.4). Though this lead to reasonable estimate, one might also choose $f_s = 0.65$ and $f_p = 0.35$ to reflect the different levels of afferent firing where the activity level of the sympathetic and parasympathetic

system changes. $\eta = \xi = 6$ are set to reflect and expectation of maximum to minimum neuron firing ratio of approximately 2.

4.5.1 Parasympathetic contribution from respiration

Earlier efforts of modeling the baroreceptor reflex regulation were not able to predict the fast fluctuations happening at around 0.3 Hz (Olufsen, Tran, et al. 2006; Olufsen and Ottesen 2013). These oscillations are also seen in blood pressure and ECG. They originate in the respiratory control center, which, in addition to controlling breathing, also stimulate the pacemaker cells of the heart directly via the vagus nerve (Mehlsen et al. 1987).

To account for respiration the total parasympathetic tone T_p is predicted as the sum of two weighted terms corresponding to baroreceptor input, $T_{p,br}$ and respiratory input, $T_{p,resp}$

$$T_p = \alpha T_{p,br} + \beta T_{p,resp}. \tag{4.13}$$

It has been found that the effect of respiration on the heart rate depends on posture (Kobayashi 1996). This is modelled by letting α and β change with posture, represented by the angle ϕ,

$$\begin{aligned}
\alpha(\phi) &= \alpha_m + (\alpha_M - \alpha_m) \frac{\phi^{k_\alpha}}{\phi^{k_\alpha} + \phi_\alpha^{k_\alpha}}, \\
\beta(\phi) &= \beta_M - (\beta_M - \beta_m) \frac{\phi^{k_\beta}}{\phi^{k_\beta} + \phi_\beta^{k_\beta}}.
\end{aligned} \tag{4.14}$$

In supine position ($\phi = 0$), the respiratory input is the primary source of parasympathetic activity, while the baroreceptor induced signal is the primary source in vertical position ($\phi = 60° = \pi/3$). In addition, it is believed that the total parasympathetic tone should be stronger in supine than upright position , ie. $\alpha_m + \beta_M > \alpha_M + \beta_m$.

Figure 4.10 shows a qualitative example of how the weighting of the two components can shift, and at the same time increase or decrease the total effect.

A high respiration frequency will increase heart rate to accommodate the increased rate of carbon dioxide and oxygen exchange in the lungs (Mehlsen et al. 1987). The respiratory signal itself $T_{p,resp}$ is predicted by a Hill function dependent on the respiration frequency $f_{r,t}$,

$$T_{p,resp} = 1 - \frac{f_r^{k_r}}{f_r^{k_r} + f_{r,t}^{k_r}}, \tag{4.15}$$

where $f_{r,t} = 0.25$ is the set point for the respiration frequency, and $k_r = 5$ determines the slope of the transition from no to full effect of the respiratory input. The Hill function ensures that high
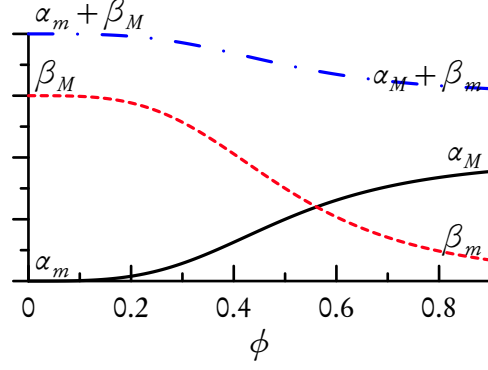
Figure 4.10: Hill functions describing the weighting of the contributions to the parasympathetic tone by the baroreflex and by respiration.

respiratory frequencies leads to a decrease in parasympathetic tone, in turn, increasing heart rate and cardiac output.

Parameters.

Nominal parameter values are chosen to be $\alpha_m = 0.4, \alpha_M = 0.6, \beta_m = 0.3, \beta_M = 0.6$ based on the hypothesis that the weighting of the two inputs changes with tilt angle. The chosen parameter values gives, $\alpha_m + \beta_M > \alpha_M + \beta_m$, ensuring that the total parasympathetic signal is smaller in upright position, and that the sum is on the order of 1. Parameters determining the slope of the weighting functions are set at $k_\alpha = k_\beta = 5$, localizing the changes around the correct angle, while also avoiding that the change is discrete.

4.5.2 Sympathetic delay

The sympathetic signal is modeled as a distributed delay, such that the signal at the synapse at the heart is described as a convolution of the ANS sympathetic tone with a gamma distribution,

$$T_{s,d} = \int_{-\infty}^{t} T_s(\eta) g_\alpha^\rho(t-\eta)\,\mathrm{d}\eta, \quad g_\alpha^\rho(u) = \frac{\alpha^\rho u^{\rho-1} e^{-\alpha u}}{(\rho-1)!}, \tag{4.16}$$

where α and ρ are integers that determines the shape of the gamma distribution. The gamma distributions for different values of ρ with mean delay $t_d = \rho/\alpha = 5$ are plotted in Figure 4.11.

Equation (4.16) can be rewritten as

$$T_{s,d} = k T_d^\rho, \quad k = \frac{\alpha^\rho}{(\rho-1)!}, \quad T_d^\rho = \int_{-\infty}^{t} T_s(\eta)(t-\eta)^{(\rho-1)} e^{-\alpha(t-\eta)}\,\mathrm{d}\eta, \tag{4.17}$$

51
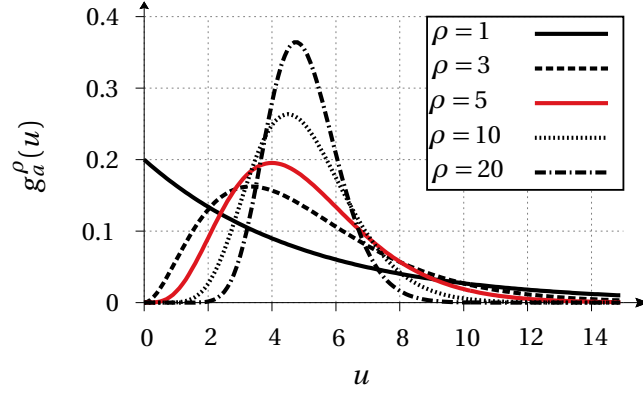
Figure 4.11: Shape of the weighting function $g_\alpha^\rho(u)$ for different values of ρ, all with same mean delay $t_d = \rho/\alpha = 5$ and $\alpha = 1$. The weighting function with $\rho = 5$ is used for the delay of the sympathetic pathway.

which can be written as a system of ode's using the *linear chain trick* (H. Smith 2010; MacDonald 1978)

$$
\begin{aligned}
\frac{\mathrm{d}\, T_d^\rho}{\mathrm{d}\,t} &= (\rho-1)\, T_d^{\rho-1} - \alpha T_d^\rho, \\
&\;\;\vdots \\
\frac{\mathrm{d}\, T_d^2}{\mathrm{d}\,t} &= T_d^1 - \alpha T_d^2, \\
\frac{\mathrm{d}\, T_d^1}{\mathrm{d}\,t} &= T_s(t) - \alpha T_d^1.
\end{aligned}
\tag{4.18}
$$

The initial conditions are set to reflect equilibrium,

$$
\begin{aligned}
\frac{\mathrm{d}\, T_d^\rho}{\mathrm{d}\,t} &= \frac{\mathrm{d}\, T_d^{\rho-1}}{\mathrm{d}\,t} = \cdots = \frac{\mathrm{d}\, T_d^1}{\mathrm{d}\,t} = 0, \\
&\Rightarrow \\
T_d^1(0) &= \frac{T_s(0)}{\alpha} \\
T_d^2(0) &= \frac{T_d^1(0)}{\alpha} \\
&\;\;\vdots \\
T_d^\rho(0) &= \frac{(\rho-1)T_d^{\rho-1}(0)}{\alpha}.
\end{aligned}
\tag{4.19}
$$

Parameters.

The mean time delay t_d is the only parameter associated with this model of the sympathetic delay. The degree of the gamma distribution is chosen as $\rho = 5$ as a trade-off between the width of the distribution and the number of differential equations required for the implementation. The size of the delay is

ambiguous as different sources report different values. Hammer and Saul 2005 suggest $t_d < 1$ second, Warner et al. 1969 2-2.5 seconds (modeling of the response for dogs), Ottesen 1997b suggests 4-7 seconds, and A.C Guyton and Harris 1951 13 seconds. For this study, the nominal value is set in the low end of the span of suggested values, at $t_d = 1.5$ seconds.

4.6 Neurotransmitter concentrations

The neurotransmitter concentrations are predicted assuming first order kinetics as described by Ottesen and Olufsen 2013, but with an added term for the release of acetylcholine reflecting the inhibitory effect of noradrenaline

$$\begin{aligned}
\frac{d C_A}{d t} &= -\frac{C_A}{\tau_A} + q_p T_p - k_{iN} C_N T_p = -\frac{C_A}{\tau_A} + \left(q_p - k_{iN} C_N\right) T_p, \\
\frac{d C_N}{d t} &= -\frac{C_N}{\tau_N} + q_s T_{s,d}.
\end{aligned}$$

(4.20)

Here, the concentrations of acetylcholine and noradrenaline are denoted by C_A and C_N, respectively, T_p and $T_{s,d}$ are the parasympathetic and delayed sympathetic tone, τ_A and τ_N are time constants describing the rate at which the neurotransmitters are removed, q_p and q_s are parameters describing the sensitivity to parasympathetic and sympathetic tone, and k_{iN} is a parameter describing the inhibitory effect of noradrenaline on the release of acetylcholine. Since parasympathetic and sympathetic tones are nondimensionalized, the neurotransmitters are nondimensionalized similarly. Figure 4.12 shows concentrations predicted by the equations above for step input pressure and for experimental input pressure.

The initial concentrations are determined by assuming equilibrium with the initial sympathetic and parasympathetic tones, $T_p(p_0), T_{s,d}(p_0)$. This gives the expressions

$$\begin{aligned}
C_N(0) &= q_s \tau_N T_{s,d}(0) \\
C_A(0) &= \tau_A \left(q_p - k_{iN} C_N(0) T_p(0)\right).
\end{aligned}$$

(4.21)

Parameters.

The parameters are the time constants for removal of free neurotransmitter τ_A and τ_N, the sensitivity to the parasympathetic and sympathetic signals q_p and q_s and the inhibitory effect of noradrenaline on the release of acetylcholine k_{iN}. Nominal values are $q_p = 5, q_s = 0.11$. Nominal values of the time scales are set as the inverse of the sensitivities $\tau_A = 0.2, \tau_N = 9.1, k_{iN} = 0.5$. It should be noted that the parameters are selected such that $q_p > k_{iN} C_N$, because if not, this term will increase removal, not
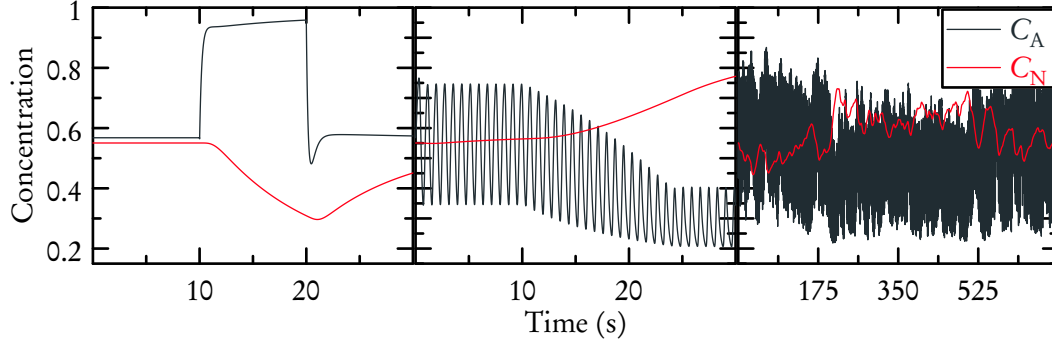
Figure 4.12: Neurotransmitter concentrations for Acetylcholine C_A and Noradrenaline C_N. Left: using step input. Middle: oscillating ramp-down signal. Right: using experimental data as model input. Both modeled with no respiratory input.

just inhibit release. In addition, this requirement guarantees that the initial condition for $C_A > 0$ as can be seen from (4.21).

4.7 Cell pathways

As described in Section 2.3.4 noradrenaline affects the depolarization rate of the pacemaker cells while acetylcholine affect both the depolarization rate and the resting potential. Ottesen and Olufsen 2013 lump the mechanisms initiated by acetylcholine into a fast and a slow component, while the mechanism initiated by noradrenaline has only one slow component. The description is based on simple assumptions about the mechanisms of how the neurotransmitters activate the receptors. Since the effect saturate at high concentrations, the effects are modeled by

$$
\begin{aligned}
\frac{\mathrm{d}\,C_{AF}}{\mathrm{d}\,t} &= \frac{1}{\tau_{AF}}\left(\mu \frac{C_A^2}{C_A^2 + K_A^2} - C_{AF}\right), \\
\frac{\mathrm{d}\,C_{AS}}{\mathrm{d}\,t} &= \frac{1}{\tau_{AS}}\left((1-\mu)\frac{C_A^2}{C_A^2 + K_A^2} - C_{AS}\right) \\
C_{AT} &= C_{AS} + C_{AF} \\
\frac{\mathrm{d}\,C_{NS}}{\mathrm{d}\,t} &= \frac{1}{\tau_{NS}}\left(\frac{C_N^2}{C_N^2 + K_N^2} - C_{NS}\right).
\end{aligned}
\tag{4.22}
$$

Here C_{AF} and C_{AS} represent the fast and slow pathways of acetylcholine, and C_{NS} the effect noradrenaline, $\tau_{AF}, \tau_{AS}, \tau_{NS}$ the decay rates of the effective quantities, K_A and K_N one half of the max responses of acetylcholine and noradrenaline, and μ describes the weighting of fast versus slow pathway

for acetylcholine.

Assuming that the fast effect for acetylcholine is instantaneous, C_{AF} can be predicted by a quasi-steady-state assumption as

$$C_{AF} = \mu \frac{C_A^2}{C_A^2 + K_A^2}. \tag{4.23}$$

Figure 4.13 shows the mediated signals through the different pathways for the step input pressure and the experimental input pressure.

Initial values for C_{AS} and C_{NS} are determined from steady state using the initial values of neurotransmitter concentrations $C_A(0)$ and $C_N(0)$,

$$C_{AS}(0) = (1-\mu) \frac{C_A(0)^2}{C_A(0)^2 + K_A^2}$$

$$C_{NS}(0) = \frac{C_N(0)^2}{C_N(0)^2 + K_N^2}. \tag{4.24}$$
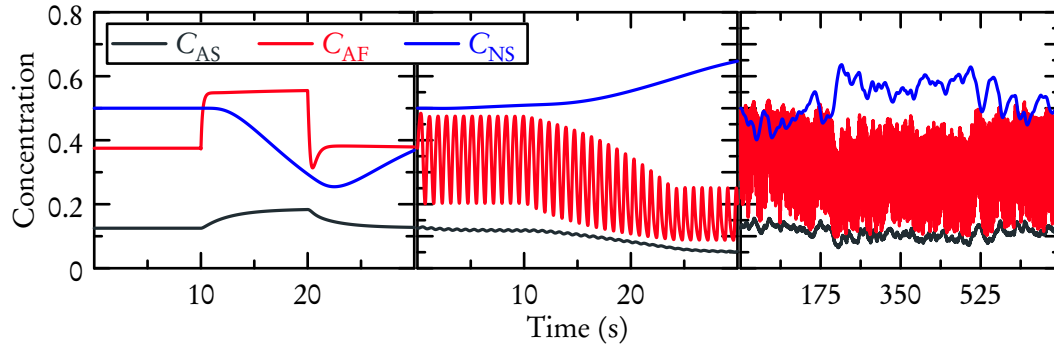
Figure 4.13: The fast C_{AF} and slow C_{AS} acetylcholine concentrations and the slow C_{NS} noradrenaline concentration. Left: using step input. Middle: Using an oscillating ramp-down signal. Right: using experimental data as model input. Both modeled with no respiratory input.

Parameters.

The nominal values of the time scales are $\tau_{AS} = 2$ and $\tau_{NS} = 2.5$, the values for one half of the maximum responses are set at the initial neurotransmitter concentrations $K_A = C_A(0)$ and $K_N = C_N(0)$, and $\mu = 0.75$ (Ottesen and Olufsen 2013). Setting K_A, K_N from initial neurotransmitter concentrations

also means that $C_{\text{AS}}(0) = 1 - \mu/2$, $C_{\text{AF}} = \mu/2$ and $C_{\text{NS}}(0) = 1/2$.

4.8 Heart Rate

The heart rate is affected by all the three lumped pathways described above. The general effect of C_{NS} is to increase heart rate while the effect of C_{AS}, C_{AF} is to decrease heart rate. However, as illustrated in Figure 4.14 C_{AF} and C_{NS} interacts through their effect on cyclic AMP. The heart rate is predicted
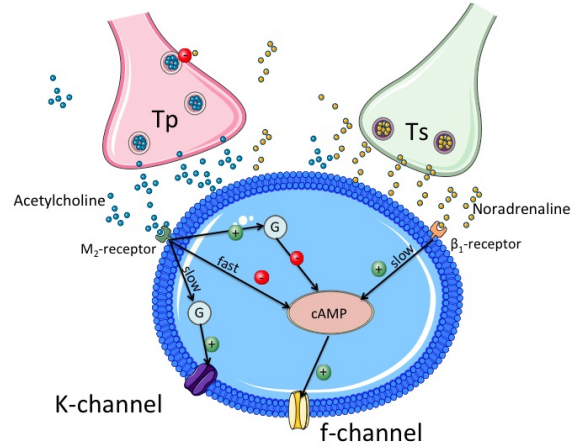
Figure 4.14:   Schematic of the synapse at the pacemaker cell.

following a similar model by Ottesen and Olufsen 2013 but alternated to reflect that only the fast acetylcholine activated pathway interact with the noradrenaline activated pathway. In addition, since the heart rate is a discrete signal, the expression below is used to describe the change in the cumulative number of heart beats

$$\frac{\mathrm{d}h}{\mathrm{d}t} = h_0 + h_M C_{NS} - h_m (C_{AS} + C_{AF}) - \frac{1}{h_0} h_M h_m C_{NS} C_{AF}, \quad h(t_0) = 0, \tag{4.25}$$

Here h_0 denote the base depolarization rate in the absence of ANS stimuli, and h_M and h_m denote the sensitivity to acetylcholine and noradrenaline activated pathways. The initial conditions just signifies that the count of heart beats will be started from 0. The mean heart rate for a period in time from t_a to t_b can then be calculated as

$$HR(t_a, t_b) = \frac{h(t_b) - h(t_a)}{t_b - t_a}. \tag{4.26}$$

If a continuous signal is required the heart rate is to be considered constant with value determined from the most recent contraction cycle.
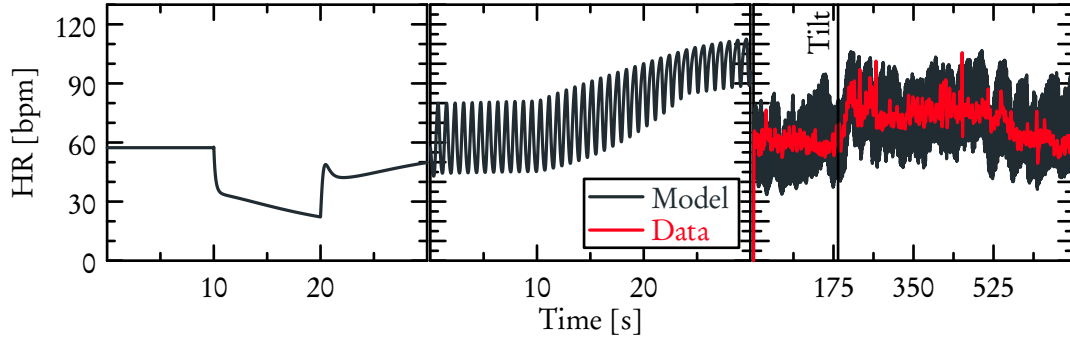
Figure 4.15: Output heart rate for the three different input signals. Note that for the right figure the parameter values used to generate the plot has not been optimized to fit the data.

Parameters.

Tanaka, Monahan, and Seals 2001 found that the maximum heart rate for healthy adults follows the expression $HR_{max} = 208 - 0.7 \times age$ [bpm]. For a 25 year old subject the maximum heart rate is approximately 190 bpm. It is assumed that the minimum heart rate is 20 bpm (resting heart rate lower than 30 bpm are often reported for top athletes), i.e. the model should cover a span in heart rate from 20 to 190 bpm.

Assuming that the minimum value occurs with full parasympathetic and no sympathetic activity, and that the maximum occurs with full sympathetic and no parasympathetic activity, $h_m + h_M = 170$ bpm. Assuming the intrinsic heart rate with no autonomic stimulation is approximately $h_0 = 100$ bpm, one get estimates for the nominal parameter values $h_m = 80$bpm and $h_M = 90$bpm.

4.9 Model discussion

4.9.1 Effect of sympathetic delay

While it has been physiologically observed that there is a delay associated with sympathetic pathways (Hall 2011), it is unclear if this delay has a significant impact on the heart rate. Previous mathematical models of the baroreceptor reflex have been divided on whether to include this delay or not, and none

have implemented the delay as distributed (Ottesen 1997a; Ottesen 1997b; Ottesen and Olufsen 2011; Olufsen and Ottesen 2013; Olsen, Gøtze, and Mosegaard 2011).

To decide whether or not the delay should be included in this mathematical model, the impact on model output of different values of mean delay $t_d = 0, 1, 5, 10, 15$ is investigated.
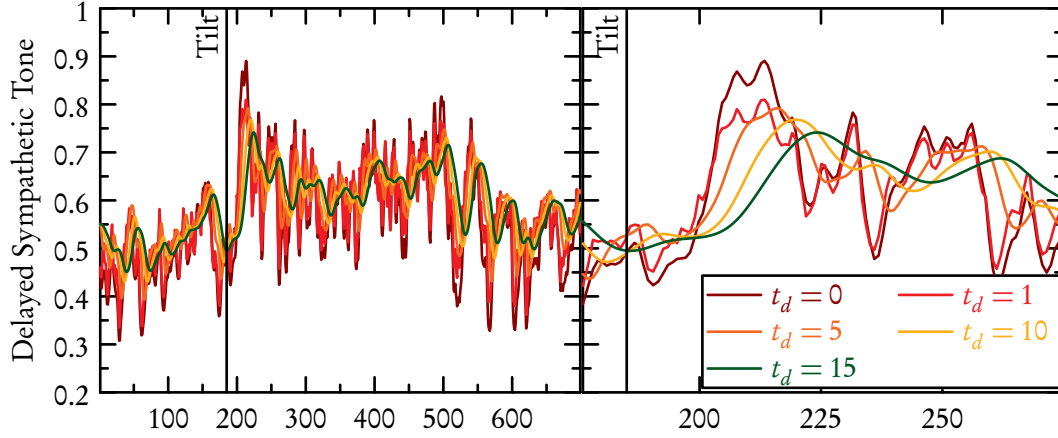
Figure 4.16: Delayed sympathetic outflow for different delays. Left: complete time series. Right: zoom around the tilt.

Figure 4.16 shows the delayed sympathetic signal for the different delays while Figure 4.17 shows the corresponding model output heart rate along with experimental data. This figure also includes a line showing the model output where the sympathetic signal is held constant to illustrate the effect of removing sympathetic dynamics. Note that no respiratory effect is included for these data.

Observations

Considering the two figures showing the delayed sympathetic signal, it is observed that:

- Increasing the value of the delay parameter t_d increases the delay. This is especially clear in the right panel of Figure 4.16 where the change in sympathetic tone following the tilt in the experiment shows an increase in delay with increased value of t_d.

- There is a smoothing and dampening effect associated with introducing the delay. This effect increases with the amount of delay.

Considering the two figures showing the model output heart rate, a couple of observations can be made as well:
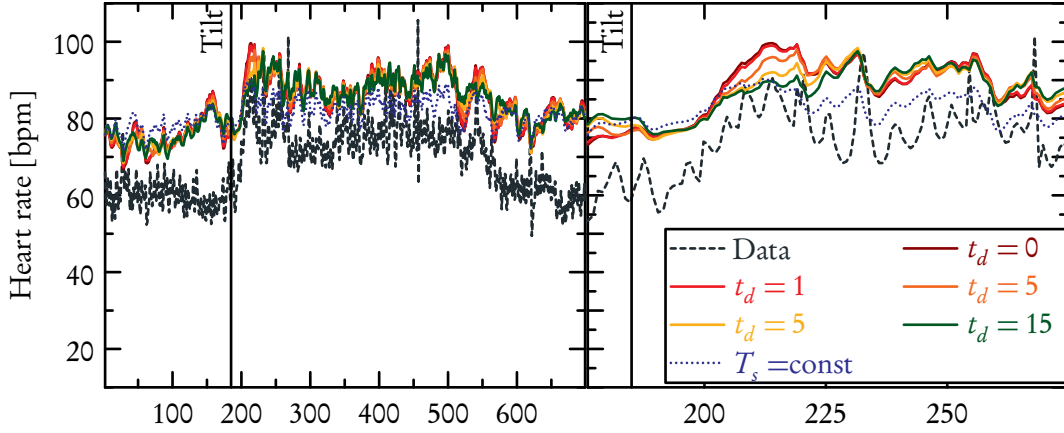
Figure 4.17: Model output heart rate calculated with different values of the delay and with constant sympathetic activity shown along with experimental heart rate data. Left: complete time series. Right: zoom around the tilt.

- The curves for different values of t_d are very similar. From the left panel of Figure 4.17 it is not possible to distinguish between the curves. Even when zooming in on the curves, right panel of Figure 4.17, the curves are very similar.

- The curves corresponding to a larger delay tend to have smaller amplitude on oscillations. This is visible on the interval 200-220 seconds on the zoomed graph in the right panel of Figure 4.17.

- The peak of oscillations does not appear to be shifted with the delay. Even when the levels are shifted, the curves corresponding to the model output have peaks at the same points in time.

- Using a constant value for the delayed sympathetic tone does not lead to a signal qualitatively different when considering the entire time series. Looking at the zoomed graph, it is clear that the graph for constant sympathetic tone is different and shows less oscillations than the other configurations.

Discussion

From the observations made on the delayed sympathetic signal, it is clear that a distributed delay can be implemented using the suggested method. The result is a signal that is both delayed and smoothed/damped as suggested by the convolution equation, (4.16).

From the observations made on the heart rate, it appears that the primary effect of introducing a distributed delay on the sympathetic pathway is that the peak values are dampened. As the signals

59

have not been fitted, it is not possible to say which of the delay configuration would be able to match the experimental data better, but it is clear that the quality of such fits would be very similar.

One would expect that a delay on the sympathetic pathway might lead to a delay in peak values of heart rate following stimulation of the baroreceptors during HUT, but the data suggests that, at least for this model, fast changes in heart rate is primarily due to the effects of the parasympathetic system.

It is also worth noting that other parts of the model contain transients that might account mechanistically for the physiological sympathetic delay. These transients include the model for the concentration of the neurotransmitter noradrenaline associated with the sympathetic system, as well as the model of intracellular pathway effects of the pacemaker cells associated with noradrenaline.

Constant value of the sympathetic delay leads to a model output heart rate qualitatively similar to other configurations when looking at the overall graph. When zooming in it is clear that oscillations in heart rate are smaller in amplitude, making the heart rate for the constant sympathetic signal look like it could be an extrapolation of increasing the mean delay t_d to larger values.

Conclusion

The method used for implementing a distributed delay works very well. The sympathetic signal is both smoothed/damped and delayed. While the sympathetic delay exists and it is possible to model it, the results of this simple investigation suggests that it is unnecessary to include it in this model. Note that this may be due to the effect not being important for heart rate regulation during HUT, or to the effect being included in other parts of the model.

4.9.2   Effect of respiration

The model reflects the hypothesis that the respiratory frequency affects the parasympathetic part of the autonomic nervous system, as discussed in Section 4.5.1. Since this mechanism has not been included in previous modeling attempts for the baroreceptor reflex, it is relevant to perform a simple investigation of the effect of the implementation on the model output heart rate.

Respiration can be measured experimentally or extracted approximately from ECG data. As the data set considered during the development of the model consist solely of blood pressure data, it is impossible to extract respiratory data from it. Figure 4.18 shows blood pressure, heart rate and respiratory frequency for another healthy subject. The extraction of respiratory frequency was discussed in Section 3.5, but the data set is used here for evaluating the effect of including respiration in the model.

The left panel of Figure 4.19 shows total parasympathetic tone as predicted by the model using three different configurations, one that gives no weight to the respiratory input (a), and two that do (b,c).

a) $\alpha_m = 1.0, \quad \alpha_M = 1.0, \quad \beta_m = 0.0, \quad \beta_M = 0.0,$
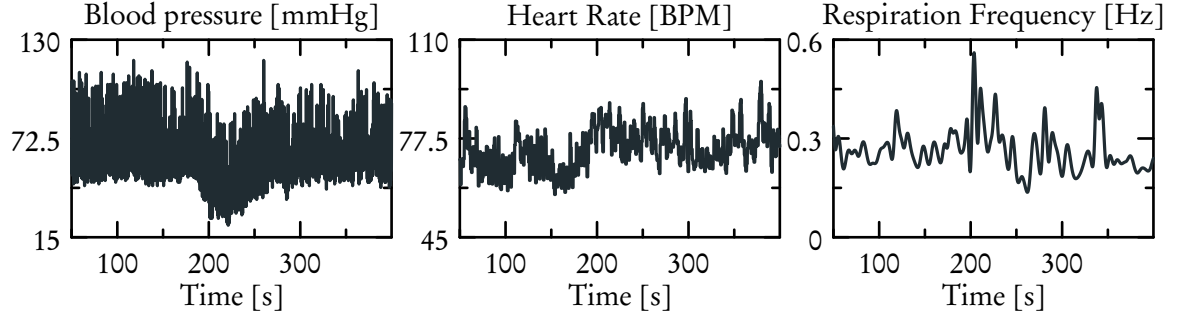
Figure 4.18: An experimental data set with respiration extracted from ECG.

b) $\alpha_m = 0.4$, $\alpha_M = 0.6$, $\beta_m = 0.4$, $\beta_M = 0.6$,

c) $\alpha_m = 0.2$, $\alpha_M = 0.8$, $\beta_m = 0.2$, $\beta_M = 0.8$.

The right panel of Figure 4.19 shows the model output heart rate for the three configurations along with experimental data.
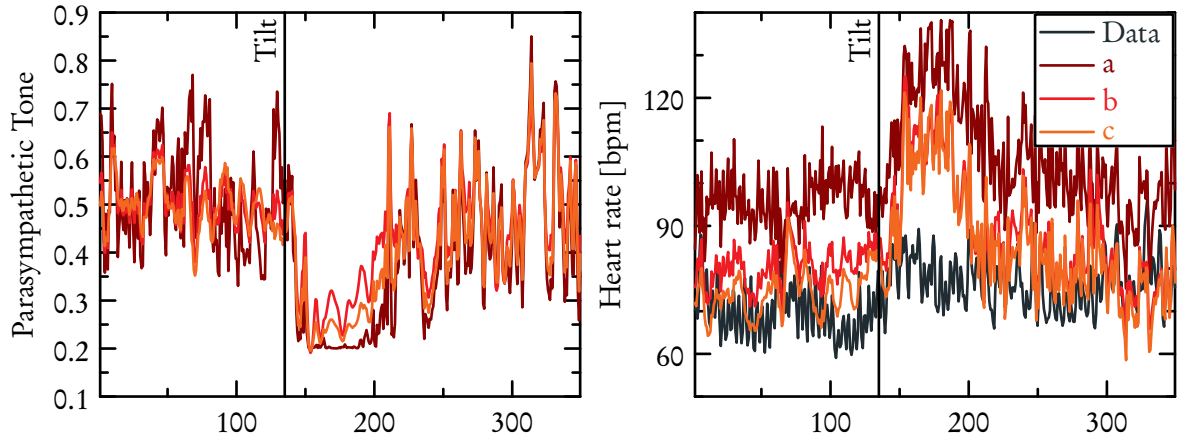
Figure 4.19: Left: Example of model total parasympathetic tone with (b,c) and without (a) effect of respiration. Right: Corresponding model output heart rate plotted along experimental data. Note that model output has not been fitted against experimental data.

61

Observations

Considering the total parasympathetic signal in Figure 4.19 the following observations are made.

- The parasympathetic tone falls dramatically following the tilt.

- Inclusion of the respiratory signal dampens some fast fluctuations in the signal before the tilt, reflecting respiratory input dominating the faster oscillations in blood pressure.

- The level of parasympathetic activity is similar with and without input from respiration. It should be noted that the configurations have been made such that $\alpha_m + \beta_M = \alpha_M + \beta_m$. Other configurations are possible.

Likewise, respiratory effect on model output heart rate is considered and the following observations are made.

- The baseline heart rate is lower when the respiratory signal is included (with the current configurations), even though the parasympathetic signals are of similar magnitude.

- Varying parameter values for the weighting results in different model output heart rates.

Conclusion

The total parasympathetic signal is a weighted sum of the contributions from the baroreceptors and the respiration with weights changing from favoring respiration to baroreceptors at the time of the tilt. It is therefore not surprising that including the respiratory input has an impact on the total parasympathetic signal. As desired, the effect of the respiration appears to be largest before the tilt indicated by the dampening of the fluctuations otherwise carried from the oscillations in blood pressure.

It is notable how different the model output is between the different configurations given the very similar, in terms of magnitude, parasympathetic signals. It is not possible from the current simple investigation to say if including the respiration or not provides a more accurate description of heart rate, only that the respiration allows for different dynamics. For this reason the respiratory input will be kept as part of the model.

5

Model analysis

The model description from the previous chapter does not mention restrictions on values of modeled quantities. However, for the physiological system it is clear that the model description of quantities such as physical length, frequencies and concentrations, should be restricted to positive values. This chapter introduces terminology from dynamical systems analysis, discusses the heart rate model under this framework to determine if it can be guaranteed that the model show proper behaviour.

5.1 Desired properties

5.1.1 Positivity

Positivity of solutions guarantees that state variables $\mathbf{x}$ defined on $\mathbb{R}^n, n \in \mathbb{Z}$ of a system of ordinary differential equations (ode) with positive initial conditions remains positive at all times. For such a system the first orthant is left invariant with respect to the flow related to the differential operator $\mathrm{d}/\mathrm{d}t$. L. Allen 2007 describes what she defines as *persistence* which is a bit more strict.

Definition 1 (Persistence) *Given a system of differential equations $dX/dt = F(X, t)$, $X(0) = X_0$, where $X(t) = (x_1(t), x_2(t), \ldots, x_n(t))^T \in \mathbb{R}^n, n \in \mathbb{Z}$, the system is said to be persistent if for any positive initial condition, $X_0 > 0$, i.e. all coordinates are strictly positive, the solution $X(t)$, fulfill*

$$\lim_{t \to \infty} \inf x_i(t) > 0$$

for $i = 1, 2, \ldots, n$.

5.1.2 Trapping region

A trapping region $\mathbf{R}$ is a compact (closed and bounded) connected region in the phase space $\mathbb{R}^n$ for which it is true that if $\mathbf{x}(t_0) \in \mathbf{R}$, then $\forall\, t_+ : t_+ > t_0 \,|\, \mathbf{x}(t_+) \in \mathbf{R}$. That is a trajectory located in $\mathbf{R}$ at time t_0 will remain in $\mathbf{R}$ for all times following. Consequently $\mathbf{R}$ is left invariant with respect to the flow determined by the ode. In some contexts the existence of a trapping region can help guarantee a closed orbit within the trapping region. In two dimension the existence of such a closed orbit is guaranteed in the trapping region $\mathbf{R}$ by the Poincare-Bendixson theorem provided no fixed point exists in $\mathbf{R}$ (Strogatz 1994). For the context of this study, a trapping region located in the first orthant can guarantee that trajectories originating in the region remain positive.

5.1.3 Stable fixed point

For an equilibrium point, $(\hat{x}, \hat{y})$, for the dynamical system

$$\frac{\mathrm{d}}{\mathrm{d}t}\begin{pmatrix} x \\ y \end{pmatrix} = \begin{pmatrix} f(x,y) \\ g(x,y) \end{pmatrix}, \tag{5.1}$$

the Jacobian is given by

$$\begin{aligned} a &= \frac{\partial f}{\partial x}(\hat{x}, \hat{y}), & b &= \frac{\partial f}{\partial y}(\hat{x}, \hat{y}) \\ c &= \frac{\partial g}{\partial x}(\hat{x}, \hat{y}), & d &= \frac{\partial g}{\partial y}(\hat{x}, \hat{y}). \end{aligned} \tag{5.2}$$

Any small perturbation around the fixed point

$$\begin{pmatrix} u \\ v \end{pmatrix} = \begin{pmatrix} x - \hat{x} \\ y - \hat{y} \end{pmatrix} \tag{5.3}$$

can be approximated by a linearization that involves the entries of the Jacobian plus higher order terms (Strogatz 1994)

$$
\begin{aligned}
\dot{u} = \dot{x} &= f\left(\hat{x}+u,\hat{y}+v\right) \\
&= f\left(\hat{x},\hat{y}\right)+u\frac{\partial f}{\partial x}\left(\hat{x},\hat{y}\right)+v\frac{\partial f}{\partial y}\left(\hat{x},\hat{y}\right)+\mathcal{O}\left(u^2,v^2,uv\right) \\
&= u\frac{\partial f}{\partial x}\left(\hat{x},\hat{y}\right)+v\frac{\partial f}{\partial y}\left(\hat{x},\hat{y}\right)+\mathcal{O}\left(u^2,v^2,uv\right) \\
&= au+bv+\mathcal{O}\left(u^2,v^2,uv\right), \\
\dot{v} = \dot{y} &= g\left(\hat{x}+u,\hat{y}+v\right) \\
&= g\left(\hat{x},\hat{y}\right)+u\frac{\partial g}{\partial x}\left(\hat{x},\hat{y}\right)+v\frac{\partial g}{\partial y}\left(\hat{x},\hat{y}\right)+\mathcal{O}\left(u^2,v^2,uv\right) \\
&= u\frac{\partial g}{\partial x}\left(\hat{x},\hat{y}\right)+v\frac{\partial g}{\partial y}\left(\hat{x},\hat{y}\right)+\mathcal{O}\left(u^2,v^2,uv\right) \\
&= cu+dv+\mathcal{O}\left(u^2,v^2,uv\right).
\end{aligned}
\tag{5.4}
$$

Ignoring higher order terms, the behavior of perturbations can be described by

$$
\begin{pmatrix} \dot{u} \\ \dot{v} \end{pmatrix} = \begin{pmatrix} a & b \\ c & d \end{pmatrix}\begin{pmatrix} u \\ v \end{pmatrix}.
\tag{5.5}
$$

The behavior of trajectories around the fixed point can be determined by considering the eigenvalues λ_n and corresponding eigenvectors w_n of the Jacobian matrix A

$$
Aw_n = \lambda_n w_n, \quad A = \begin{pmatrix} a & b \\ c & d \end{pmatrix}.
\tag{5.6}
$$

For the linear system real negative eigenvalues guarantees that the perturbation will decay in the direction of the corresponding eigenvector. For Real positive eigenvalues perturbations will increase in the direction of the corresponding eigenvector. Complex eigenvalues gives rise to spiraling trajectories with direction towards the fixed point if $\mathrm{Re}(\lambda_n) < 0$ and direction away from the fixed point if $\mathrm{Re}(\lambda_n) > 0$. If $\mathrm{Re}(\lambda_n) = 0$, one will see oscillations around the fixed point.

The stability of the linearized system is relevant because of the *Hartman-Grobman theorem*, which states that if $\mathrm{Re}(\lambda_i) \neq 0, \forall i$, then a homeomorphism exists between the non-linear and the linearized system near the equilibrium point (Strogatz 1994). Hence if $\mathrm{Re}(\lambda) \neq 0$, the stability of the linearized system determines the properties of the fixed point in the nonlinear system.

As a side note, when determining stability, it is often useful to remember that the sum of the

eigenvalues of an $N \times N$ matrix is given by the trace,

$$\text{Tr}(\mathbf{A}) = \lambda_1 + \cdots + \lambda_N, \tag{5.7}$$

and that the product of the eigenvalues is equal to the determinant,

$$\text{Det}(\mathbf{A}) = \prod_{i=1}^{N} \lambda_i. \tag{5.8}$$

5.2 Model analysis

5.2.1 Wall Strain

The wall strain of the heart rate model is given by (4.3)

$$\epsilon_w = 1 - \sqrt{\frac{p_0^k + p^k}{p_0^k + A_{M0} p^k}}, \quad A_{M0} = \frac{A_M}{A_0}.$$

Since the wall strain is a relative measure of the radial strain of the blood vessel, it should be positive and bounded. From the derivation in Valdez-Jasso 2011 it is clear that it should be bounded between 0 and 1. Analyzing ϵ_w gives insight into the limits,

$$\lim_{p \to 0} \epsilon_w = 1 - \lim_{p \to 0} \left(\sqrt{\frac{\alpha^k + p^k}{\alpha^k + A_{M0} p^k}} \right) = 1 - \sqrt{\frac{\alpha^k}{\alpha^k}} = 0,$$

$$\lim_{p \to \infty} \epsilon_w = 1 - \lim_{p \to \infty} \left(\sqrt{\frac{\alpha^k + p^k}{\alpha^k + A_{M0} p^k}} \right) = 1 - \sqrt{\frac{\lim_{p \to \infty} \left(p^k \right)}{A_{M0} \lim_{p \to \infty} \left(p^k \right)}} = 1 - (A_{M0})^{-\frac{1}{2}},$$

$$\tag{5.9}$$

$$\frac{d\epsilon_w}{dp} = \frac{1}{2} \left(\alpha^k + A_{M0} p^k \right)^{-\frac{1}{2}} k p^{k-1}$$

$$\times \left[A_{M0} \left(\alpha^k + p^k \right)^{\frac{1}{2}} \left(\alpha^k + A_{M0} p^k \right)^{-1} - \left(\alpha^k + p^k \right)^{-\frac{1}{2}} \right].$$

Since $A_{M0} > 1$,

$$\frac{A_{M0} \alpha^k + A_{M0} p^k}{\alpha^k + A_{M0} p^k} > 1,$$

$$\tag{5.10}$$

$$A_{M0} \left(\alpha^k + p^k \right)^{\frac{1}{2}} \left(\alpha^k + A_{M0} p^k \right)^{-1} > \left(\alpha^k + p^k \right)^{-\frac{1}{2}},$$

which ensures that $\frac{d\epsilon_w}{dp} > 0$ for all $p > 0$. Hence for $0 < p_m \leq p \leq p_M < \infty$, the wall strain is restricted to some interval $\epsilon_w \in \left(\epsilon_{w_m}, \epsilon_{w_M}\right)$ with $0 < \epsilon_{w_m}$ and $\epsilon_{w_M} < 1 - (A_{M0})^{-\frac{1}{2}}$. This interval ensures a positive wall strain for feasible input.

5.2.2 Baroreceptor strain

The strain of the baroreceptor nerve ending ϵ_{br} is given by (4.6),

$$\epsilon_{br} = \epsilon_w - \epsilon_1.$$

The physical model shown in Figure 4.5 imposes the restriction,

$$\epsilon_2 < \epsilon_1 < \epsilon_w, \tag{5.11}$$

where the strains ϵ_1, ϵ_2 are determined by the ode

$$\frac{d\epsilon_1}{dt} = -(\alpha_1 + \alpha_2 + \beta_1)\epsilon_1 + (\beta_1 - \beta_2)\epsilon_2 + (\alpha_1 + \alpha_2)\epsilon_w,$$

$$\frac{d\epsilon_2}{dt} = -\alpha_2\epsilon_1 - \beta_2\epsilon_2 + \alpha_2\epsilon_w.$$

This is a linear and inhomogeneous dynamical system. Assuming a constant wall strain ϵ_w, the system is homogeneous and it is possible to further investigate it. Calculating the Jacobian yields

$$J = \begin{bmatrix} -(\alpha_1 + \alpha_2 + \beta_1) & (\beta_1 - \beta_2) \\ -\alpha_2 & -\beta_2 \end{bmatrix}, \tag{5.12}$$

from which the trace and determinant can be obtained,

$$\begin{aligned} \mathrm{Tr}(J) = \lambda_1 + \lambda_2 &= -(\alpha_1 + \alpha_2 + \beta_1) - \beta_2 < 0, \\ \mathrm{Det}(J) = \lambda_1 \lambda_2 &= \beta_2(\alpha_1 + \alpha_2 + \beta_1) + \alpha_2(\beta_1 - \beta_2) \\ &= \beta_2(\alpha_1 + \beta_1) + \alpha_2\beta_1 > 0. \end{aligned} \tag{5.13}$$

Since all parameters are positive, if any equilibrium point exists it will be stable.

If $\beta_1 = \beta_2$, the equation describing the strain does not depend on ϵ_2, essentially reducing the model to one voigt body. Assuming therefore a choice of $\beta_1 \neq \beta_2$ calculating the nullclines yields,

$$\begin{aligned} \epsilon_2 &= \frac{\alpha_1 + \alpha_2 + \beta_1}{\beta_1 - \beta_2}\epsilon_1 - \frac{\alpha_1 + \alpha_2}{\beta_1 - \beta_2}\epsilon_w, \\ \epsilon_2 &= -\frac{\alpha_2}{\beta_2}\epsilon_1 + \frac{\alpha_2}{\beta_2}\epsilon_w. \end{aligned} \tag{5.14}$$

For positive parameter values these two straight lines have different slopes, they will intersect exactly once, and the Voigt-body model will have exactly one fixed point.

The analysis of the Jacobian shows that any fixed point will be stable, but does not guarantee that it exists in the first orthant. Equating the two nullclines gives an expression for ϵ_1 for the fixed point,

$$\epsilon_1 = \frac{\alpha_1\beta_2 + \alpha_2\beta_1}{\alpha_1\beta_2 + \alpha_2\beta_1 + \beta_1\beta_2}\epsilon_w$$
$$= x\epsilon_w,$$
(5.15)

for $x = \frac{\alpha_1\beta_2 + \alpha_2\beta_1}{\alpha_1\beta_2 + \alpha_2\beta_1 + \beta_1\beta_2}$. Since all parameters are strictly positive, both numerator and denominator are strictly positive, and since the denominator is larger, $0 < x < 1$. The fixed point will be on the interval $(x\epsilon_m, x\epsilon_M) \subset (0, \epsilon_M)$. Inserting the expression for ϵ_1 for the fixed point into the expression for the ϵ_2-nullcline, gives

$$\epsilon_2 = \frac{\alpha_2}{\beta_2}(\epsilon_w - x\epsilon_w)$$
$$= \frac{\alpha_2}{\beta_2}(1 - x)\epsilon_w$$
(5.16)

for the fixed point. Expanding

$$\frac{\alpha_2}{\beta_2}(1 - k) = \frac{\alpha_2}{\beta_2}\left(\frac{\beta_1\beta_2}{\alpha_1\beta_2 + \alpha_2\beta_1 + \beta_1\beta_2}\right)$$
$$= \frac{\alpha_2\beta_1}{\alpha_1\beta_2 + \alpha_2\beta_1 + \beta_1\beta_2}$$
$$< x < 1,$$
(5.17)

guarantees that the fixed point $(\epsilon_1, \epsilon_2) \in (0, \epsilon_M) \times (0, \epsilon_M)$. Also, since $\epsilon_2 < x\epsilon_w$, then $\epsilon_2 < \epsilon_1$, which satisfy the restriction from the physical interpretation of the model in (5.11).

To guarantee positivity for ϵ_2 it is required that

$$\lim_{\epsilon_2 \to 0} \dot{\epsilon}_2 = (\epsilon_w - \epsilon_1) > 0.$$

which implies that it is required and sufficient that $\epsilon_w > \epsilon_1$. For ϵ_1 the requirement is,

$$\lim_{\epsilon_1 \to 0} \dot{\epsilon}_1 = (\beta_1 - \beta_2)\epsilon_2 + (\alpha_1 + \alpha_2)\epsilon_w > 0,$$

which is always true if $\beta_1 > \beta_2$ which is the configuration described earlier. Hence positivity is guaranteed if $\epsilon_w > \epsilon_1$, which is also the constraint from the physical model.

Figure 5.1 shows a sketch of the phase plane for this system, with parameters $\alpha_1 = \alpha_2 = \beta_2 = 1, \beta_1 = 2$ and $\epsilon_w = 0.5$. It shows ϵ_1- and ϵ_2-nullclines, the fixed point and the physical boundaries
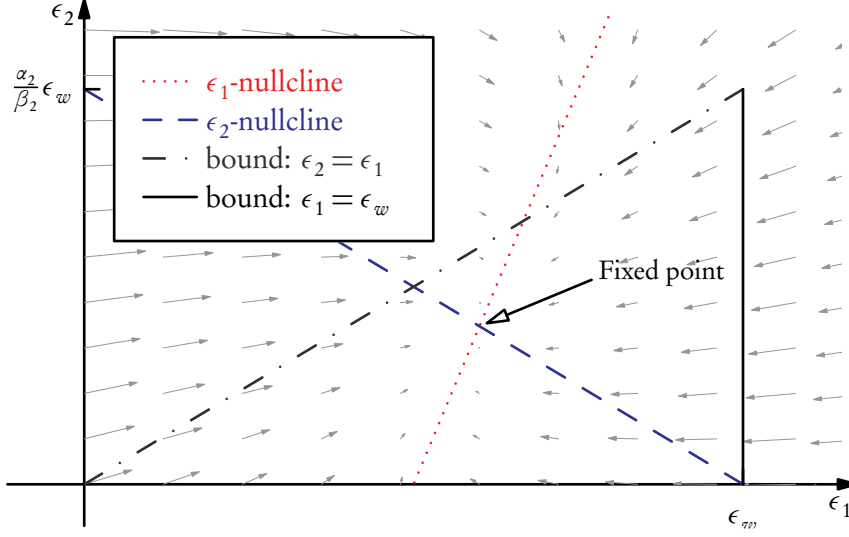
Figure 5.1: A sketch of the ϵ_1- and ϵ_2-nullclines in the (ϵ_1, ϵ_2)-phase plane, as well as a trapping region (black line). Below the ϵ_2-nullcline, $\dot{\epsilon}_2 > 0$, and above $\dot{\epsilon}_2 < 0$. Likewise, left of the ϵ_1-nullcline, $\dot{\epsilon}_1 > 0$ and right of it, $\dot{\epsilon}_1 < 0$.

$\epsilon_2 = \epsilon_1, \epsilon_1 = \epsilon_w$. In addition to guaranteeing positivity, the physical boundaries also gives a trapping region.

The vertical and horizontal boundaries have already been discussed. For the inclined boundary $\epsilon_2 = \epsilon_1$ it is required that the flow in the vertical direction is smaller than the flow in the horizontal direction

$$\lim_{\epsilon_2 \to \epsilon_1^-} \dot{\epsilon}_2 < \lim_{\epsilon_2 \to \epsilon_1^-} \dot{\epsilon}_1. \tag{5.18}$$

Evaluating the flow gives

$$\lim_{\epsilon_2 \to \epsilon_1^-} \dot{\epsilon}_1 = -(\alpha_1 + \alpha_2 + \beta_2)\epsilon_1 + (\alpha_1 + \alpha_2)\epsilon_w$$

$$\lim_{\epsilon_2 \to \epsilon_1^-} \dot{\epsilon}_2 = -(\alpha_2 + \beta_2)\epsilon_1 + \alpha_2\epsilon_w. \tag{5.19}$$

Inserting these two expressions into the inequality,

$$-(\alpha_2 + \beta_2)\epsilon_1 + \alpha_2\epsilon_w < -(\alpha_1 + \alpha_2 + \beta_2)\epsilon_1 + (\alpha_1 + \alpha_2)\epsilon_w$$

$$0 < -\alpha_1\epsilon_1 + \alpha_1\epsilon_w \tag{5.20}$$

$$\epsilon_1 < \epsilon_w,$$

which is the requirement for positivity as well. Hence when approaching any part of the boundary of the trapping region, the flow points into the region.

Since the baroreceptor strain is given by $\epsilon_{br} = \epsilon_w - \epsilon_1$ and $\epsilon_1 \in \left(0, \epsilon_{w_M}\right)$, it is guaranteed that $\epsilon_{br} \in \left(0, \epsilon_{w_M}\right)$. By assuming a constant input ϵ_w it has been shown that under such conditions, the model has a trapping region given by the physical constraints of the model with a stable fixed point in the first orthant. Furthermore it was shown, that $\epsilon_1 < \epsilon_w$ guarantees positivity of solution.

Dynamical wall strain

Since ϵ_w is changing dynamically, the trapping region found above will not be static. This can cause problems if $\dot{\epsilon}_w < \dot{\epsilon}_1$ as the boundary of the trapping region might overtake the ϵ_1 value, causing $\epsilon_1 > \epsilon_w$. If this happens, it will result in an unphysical configuration where the strain of the two viscoelastic components is larger than the total strain of the wall. Hence, to prevent unphysical behavior the restrictions $\epsilon_2 < \epsilon_1 < \epsilon_w$ can be checked when solving the model.

Alternatively, assuming that the time scale of the fluctuations of the trapping region is so much faster than the time scales of the system, that any violations against the constraints are quickly rectified, keeping $\epsilon_1 > 0, \epsilon_2 > 0$, one can choose to ignore the violation of the physical model and focus on ensuring positive neuron firing. Choosing this approach the maximum and minimum neuron strain ϵ_{br} can be calculated. Given that the trajectory started with an ϵ_1 value lower than that of the fixed point for maximum arterial wall strain, $\epsilon_1 < \varkappa\epsilon_{wM}$, the maximum value the first component can take is at the fixed point $\epsilon_1 = \varkappa\epsilon_{wM}$. Assuming the wall strain drops to 0 instantaneously, the strain of the neuron will be

$$\epsilon_{br,min} = 0 - \varkappa\epsilon_{wM} = -\varkappa\epsilon_{wM}.$$

Likewise, if an instantaneous change goes the other way, $\epsilon_1 = 0$ and $\epsilon_w = \epsilon_{wM}$ and the maximum strain will be

$$\epsilon_{br,max} = \epsilon_{wM} - 0 = \epsilon_{wM}.$$

5.2.3 Baroreceptor neuron firing

The nondimensionalized neuron firing,

$$f = \epsilon_{br}s_1 + s_2,$$

should be limited to values on the interval $[0, 1]$.

If the solution is checked to ensure the constraint $\epsilon_2 < \epsilon_1 < \epsilon_w$ is satisfied, the minimum strain

possible is $\epsilon_{br,min} = 0$, and the maximum strain is $\epsilon_{br,max} = \varkappa \epsilon_{wM}$. This gives the expressions

$$
\begin{aligned}
0 &= s_1(0) + s_2, \\
1 &= s_1(\epsilon_{wM}) + s_2,
\end{aligned}
\tag{5.21}
$$

and the nominal values $s_2 = 0$ and $s_1 = \dfrac{1}{\epsilon_{wM}} = \dfrac{\sqrt{A_{M0}}}{\sqrt{A_{M0}} - 1}$, since $\epsilon_{wM} = 1 - \dfrac{1}{\sqrt{A_{M0}}}$.

Alternatively, if temporary negative neuron strain is allowed, and the constraints relaxed, one can determine the minimum neuron strain is $\epsilon_{br,min} = -\varkappa \epsilon_{wM}$ and the maximum strain is $\epsilon_{br,max} = \epsilon_{wM}$. This gives the expressions

$$
\begin{aligned}
0 &= s_1(-\varkappa \epsilon_{wM}) + s_2 \\
1 &= s_1(\epsilon_{wM}) + s_2.
\end{aligned}
\tag{5.22}
$$

Solving yields,

$$
\begin{aligned}
s_1 &= \frac{1}{\varkappa + 1} \frac{1}{\epsilon_{wM}} = \frac{1}{\varkappa + 1} \frac{\sqrt{A_{M0}}}{\sqrt{A_{M0}} - 1}, \\
s_2 &= s_1 \varkappa \epsilon_{wM} = \frac{\varkappa}{\varkappa + 1}.
\end{aligned}
\tag{5.23}
$$

In summary, it is possible to select the parameters such that firing rate is guaranteed to be positive. However, it should be noted, that these values may not guarantee a physiological response, as it is based on the assumption on very rapid changes in the strain of the arterial wall.

5.2.4 Parasympathetic and sympathetic outflow

Since (4.10) describing the sympathetic and parasympathetic activity are simple Hill functions

$$
\begin{aligned}
T_{p,br}(f) &= T_{p_m} + \left(1 - T_{p_m}\right) \frac{f^\xi}{f^\xi + f_p^\xi}, \\
T_s(f) &= 1 - \left(1 - T_{s_m}\right) \frac{f^\eta}{f^\eta + f_s^\eta},
\end{aligned}
$$

they are bounded between

$$
\begin{aligned}
\lim_{f \to \infty} T_p &= 1, \\
\lim_{f \to 0} T_p &= T_{p_m}, \\
\lim_{f \to \infty} T_s &= T_{s_m}, \\
\lim_{f \to 0} T_s &= 1,
\end{aligned}
\tag{5.24}
$$

71

guaranteeing positive solutions for the parasympathetic and sympathetic tone for positive values T_{p_m}, T_{s_m}.

5.2.5 Neurotransmitter concentrations

Equation (4.20) describes the concentration of free neurotransmitters with synapse inhibition,

$$\frac{d\,C_A}{d\,t} = -\frac{C_A}{\tau_A} + q_p T_p - k_{iN} C_N T_p = -\frac{C_A}{\tau_A} + \left(q_p - k_{iN} C_N\right) T_p,$$

$$\frac{d\,C_N}{d\,t} = -\frac{C_N}{\tau_N} + q_s T_s.$$

Consider first the concentration of noradrenaline. If the concentration approaches 0, the change in concentration is positive

$$\lim_{C_N \to 0^+} \dot{C}_N = q_s T_s > 0,$$

since $q_s > 0, T_s \in (0, 1)$. In addition, due to this restriction on T_s

$$\lim_{C_N \to C_N^*} \dot{C}_N < 0$$

for any $C_N^* \geq q_s \tau_N$, since $0 < T_s < 1$. Hence, one upper bound for C_N is $C_N^* = q_s \tau_N$. Since the initial value is $C_N(0) = \tau_N q_s T_s \in (0, q_s \tau_N)$, the solution will remain within this trapping region and thereby remain positive.

For the concentration of acetylcholine to remain positive for positive initial conditions it is required that

$$\lim_{C_A \to 0^+} \dot{C}_A = \left(q_p - k_{iN} C_N\right) T_p > 0.$$

This is satisfied if $\left(q_p - k_{iN} C_N^*\right) T_p > 0$, which means that C_A remains positive for positive initial conditions if

$$C_N^* < \frac{q_p}{k_{iN}}.$$

Hence the requirement for positive solutions for noradrenaline and acetylcholine is

$$q_s \tau_N < \frac{q_p}{k_{iN}}.$$

5.2.6 Cell pathways

The cell pathway concentrations are given by Equation (4.22),

$$C_{AF} = \mu \frac{C_A^2}{C_A^2 + K_A^2}$$

$$\frac{\mathrm{d}\, C_{AS}}{\mathrm{d}\, t} = \frac{1}{\tau_{AS}} \left((1 - \mu) \frac{C_A^2}{C_A^2 + K_A^2} - C_{AS} \right)$$

$$C_{AT} = C_{AS} + C_{AF}$$

$$\frac{\mathrm{d}\, C_{NS}}{\mathrm{d}\, t} = \frac{1}{\tau_{NS}} \left(\frac{C_N^2}{C_N^2 + K_N^2} - C_{NS} \right),$$

Since $C_A > 0, C_N > 0$ acetylcholine and noradrenaline concentration has a lower bound $C_A > \check{C}_A > 0, C_N > \check{C}_N > 0$.

For C_{AF} the positive solutions for C_A and C_N imply

$$C_{AF} > \mu \frac{\check{C}_A^2}{\check{C}_A^2 + K_A^2} > 0,$$

as $\mu \in (0, 1)$. Since

$$\lim_{C_A \to \infty} \frac{C_A^2}{C_A^2 + K_A^2} = 1,$$

C_{AF} is bounded from above as well by $C_{AF} < \mu$.

The two other concentrations will be bounded from below by

$$\lim_{C_A \to \check{C}_A} (1 - \mu) \frac{C_A^2}{C_A^2 + K_A^2} = \check{\tilde{C}}_{AS} \quad \text{and}$$

$$\lim_{C_N \to \check{C}_N} \frac{C_N^2}{C_N^2 + K_N^2} = \check{\tilde{C}}_{NS}$$

since then

$$\lim_{C_{AS} = \check{\tilde{C}}_{AS}} \dot{C}_{AS} = \frac{1}{\tau_{AS}} \left((1 - \mu) \frac{C_A^2}{C_A^2 + K_A^2} - \check{\tilde{C}}_{AS} \right) > 0,$$

$$\lim_{C_{NS} = \check{\tilde{C}}_{NS}} \dot{C}_{NS} = \frac{1}{\tau_{NS}} \left(\frac{C_N^2}{C_N^2 + K_N^2} - \check{\tilde{C}}_{NS} \right) > 0,$$

(5.25)

with $\mu \in (0, 1)$.

For large concentrations of acetylcholine and noradrenaline, C_{AS} and C_{NS} will be bounded from

above by

$$\lim_{C_A \to \infty} (1-\mu) \frac{C_A^2}{C_A^2 + K_A^2} = (1-\mu) \quad \text{and}$$

$$\lim_{C_N \to \infty} \frac{C_N^2}{C_N^2 + K_N^2} = 1,$$

sice

$$\lim_{C_{AS} \to (1-\mu)} \dot{C}_{AS} = \frac{(1-\mu)}{\tau_{AS}} \left(\frac{C_A^{*2}}{C_A^{*2} + K_A^2} - 1 \right) < 0,$$

$$\lim_{C_{NS} \to 1} \dot{C}_{NS} = \frac{1}{\tau_{NS}} \left(\frac{C_N^{*2}}{C_N^{*2} + K_N^2} - 1 \right) < 0.$$

Hence trapping regions for both concentrations exists: $C_{AS} \in \left(\tilde{C}_{AS}, (1-\mu) \right)$ and $C_{NS} \in \left(\tilde{C}_{NS}, 1 \right)$. Since the initial conditions are given by

$$C_{AS}(0) = (1-\mu) \frac{C_A(0)^2}{C_A(0)^2 + K_A^2} > (1-\mu) \frac{\tilde{C}_A^2}{C_A^2 + K_A^2} = \tilde{C}_{AS}$$

$$C_{NS}(0) = \frac{C_A(0)^2}{C_A(0)^2 + K_N^2} > \frac{\tilde{C}_N^2}{C_N^2 + K_N^2} = \tilde{C}_{NS}$$

the concentration will remain positive, and be bounded from above by $C_{AS} < (1-\mu)$ and $C_{NS} < 1$. Since the bounds on the fast pathway is $0 < C_{AF} < \mu$, the total activity of pathways activated by acetylcholine is $C_{AT} \in (0, 1)$.

5.2.7 Heart rate

The pace maker cell depolarization rate, and thus the cumulative depolarization, is predicted by Equation (4.25),

$$\frac{\mathrm{d}h}{\mathrm{d}t} = h_0 + h_N C_{NS} - h_A (C_{AS} + C_{AF}) - \frac{1}{h_0} h_N h_A C_{NS} C_{AF}, \quad h(t_0) = 0.$$

Due to the signs of the terms, the largest and smallest obtainable values of the derivative are obtained in the limits where

$$\lim_{C_{AT} \to 0, C_{NS} \to 1} \dot{h} = h + h_M,$$

$$\lim_{C_{AT} \to 1, C_{NS} \to 0} \dot{h} = h - h_m,$$

(5.26)

which shows that the smallest possible depolarization rate is $h - h_m$ and the largest is $h + h_M$.

5.2.8 Heart rate

Since the depolarization rate is always positive, the number of heart beats will be strictly increasing, which in turn guarantees that the numerator of (4.26) is positive. Therefore, evaluating the heart rate only for positive increments in time guarantees a positive heart rate.

5.2.9 Summary

The voigt body model might show negative values for the baroreceptor neuron strain, and therefore also possibly negative values for firing for some parameter configurations. Given the model formulation negative firing will be detected by most simulation software due to it being the base of the exponential in the expression describing the activity of the sympathetic and parasympathetic pathways.

For the concentration of acetylcholine the constraint

$$q_s \tau_N < \frac{q_p}{k_{iN}}$$

guarantees that the given initial condition will provide a solution that remains positive.

The remaining part of the model will be positive for the given initial conditions, and provide physical/physiological sound behavior. Whether or not the model is a good representation of the dynamics within these boundaries is another question.

6

Sensitivity and Identifiability Analysis

To solve *inverse problems* one relies on different numerical techniques to determine parameter values for which the model has the best fit experimental data The routines that exists to solve such problems are many and diverse, each with different niches of application. However, all routines depends on the mathematical structure of the model and associated data to allow for estimation of model parameters, as well as available data to do so.

This chapter will introduce terminology and analysis methods for discussing and determining whether model parameters can be estimated or not. The first part will be concerned with introducing the terms *identifiability* and *sensitivity*, along with simple examples for illustration. The second part will introduce numerical methods for sensitivity and identifiability analysis, and demonstrate the use of these methods using examples of increasing complexity.

6.1 Identifiability

Identifiability is a property that describes whether it is possible to uniquely determine parameter values. In this section two different types of identifiability will be introduced: *practical* and *structural identifiability*.

Concepts and methods will be presented with reference to the system of ordinary differential equations given by

$$\dot{x}(t) = f(t, x(t), u(t), \theta),$$
$$y(t_i) = h(x(t_i), u(t_i), \theta), \tag{6.1}$$

where x is the model state vector, t is the independent variable, $u(t)$ model input, θ the parameter vector, and $h(x, u, \theta)$ the observation function that relates the model states to the observable model output $y(t_i)$ at $t = t_i$.

Definition 2 *Practical Identifiability. The dynamical system (6.1) is said to be* practically identifiable *if θ can be uniquely determined given input u(t) and the measurable system output y(t).*

It should be emphasized that practical identifiability depends not only on the structure of the mathematical model, but also on available data. *Structural identifiability* on the other hand considers the structure of the mathematical model, not limited by the availability of data (Miao et al. 2011; Ljung and Glad 1994).

Definition 3 *Structural Identifiability. The system structure is said to be* structural (algebraically) identifiable *if a meromorphic function*

$$\Phi = \Phi\left(\theta, u, \dot{u}, \ldots, u^{(k)}, y, \dot{y}, \ldots, y^{(k)}\right), \Phi \in R^p \tag{6.2}$$

can be constructed based on algebraic equations of the system state x, the input u, and the output y in a finite number of algebraic or differentiation steps such that $\Phi = 0$ and $\det \frac{\partial \Phi}{\partial \theta} \neq 0$ hold in $[t_0, t_1]$ for any (θ, x_0, u) in an open and dense subset of $\Theta \times M \times C_u^N[t_0, t_1]$. Here k is a positive integer, $\dot{u}, \ldots, u^{(k)}$ are derivatives of u, and $\dot{y}, \ldots, y^{(k)}$ the derivatives of y, Θ the parameter space, M an open set of initial system states, and $\mathscr{C}_u^N$ the function space spanned by all input functions differentiable up to order N.

In short, this definition states that the system is structurally identifiable if and only if it is possible to uniquely determine parameter values given the model output for all possible input functions. Input data that properly elucidates the structure of the mathematical model and allows for identification of all parameters are called *persistently exciting* (Ljung and Glad 1994). Hence, for a model to be practical identifiable it must be structural identifiability and have a persistently exciting input. Two examples are presented to demonstrate the difference between structural and practical identifiability.

6.1.1 Example: Structural unidentifiability

The concentration of a chemical compound can be described by the differential equation,

$$\frac{dx}{dt} = -ax(t) + bu(t), \qquad x(0) = 0, \tag{6.3}$$

where $x(t)$ is the concentration, $u(t)$ represents the admission of the chemical compound into the system, while a and b are model parameters. Assume that the chemical concentration cannot be measured directly at time t_i, but only via the relation

$$y(t_i) = cx(t_i), \tag{6.4}$$

where c is another parameter. Now, given data for y, is it possible to uniquely determine the values of the parameters a, b, c?

Structural identifiability considers the question if it is possible to determine values for the parameters given any possible input $u(t)$ with a corresponding output $y(t)$ with infinite precision. On the other hand practical identifiability is concerned with the question whether it is possible to identify parameter values given the model and a specific input-output data set. For example, if the model is used to describe some chemical compound admitted to a patient at a hospital, restrictions exists on what input is allowed, and with what precision output data can be obtained. In other settings, measurements may only be available at certain times and with limited precision, or the model may only be a good description of reality in some range of the parameter space.

If the problem is written in algebraic form it's structure can be revealed,

$$\frac{1}{c}\frac{\mathrm{d}y}{\mathrm{d}t} = -a\frac{1}{c}y(t) + bu(t),$$
$$0 = bcu(t) - y'(t) - ay(t). \tag{6.5}$$

The identifiable coefficients in this relation are bc and a, i.e. several combinations of b and c may produce the same product bc and thereby the same input-output mapping. If initial conditions are known, it may be possible to use this extra information to determine the value of one parameter or parameter combination. For this example, the information gained about the system is

$$x(0) = x_0 \rightarrow y(0) = cx_0. \tag{6.6}$$

If x_0 is non-zero and known, it is possible to determine the value of c from this relation, in turn allowing for identification of parameter b. However, if $x_0 = 0$ no information about the value of c can be extracted from the initial condition. In summary, the structure of the problem makes it possible to identify two parameter components $\{bc, a\}$, under the assumption that available input/output data is persistent excitatory.

For a simple problem like this, the structural unidentifiability can be recognised in the solution,

$$y(t) = bc \int_0^t e^{-at^*} u(t - t^*) \mathrm{d}t^*, \tag{6.7}$$

as b and c only occur as the product bc.

6.1.2 Example: Practical unidentifiability

The heart rate model described in Chapter 4 uses Hill functions to describe saturating components of the baroreceptor reflex. The Hill function is given by

$$y(x) = b - (b - a)\frac{x^k}{x^k + x_*^k}, \tag{6.8}$$

with the parameters a, b, k, x_*. Here b and a represents the function value before and after the change, x_* the point at which the change happens and k determines how rapidly the change occurs.

There may however be restrictions in the data that makes it impossible to identify correct parameter values. If measurements are only available near the bounds, as illustrated in Figure 6.1, the values of a and b are identifiable, while the parameters associated with the transition, k and x_*, are not practical identifiable.

For this example it is obvious that the transition cannot be described with the presented data, but for more complicated models this effect might not be directly observable.
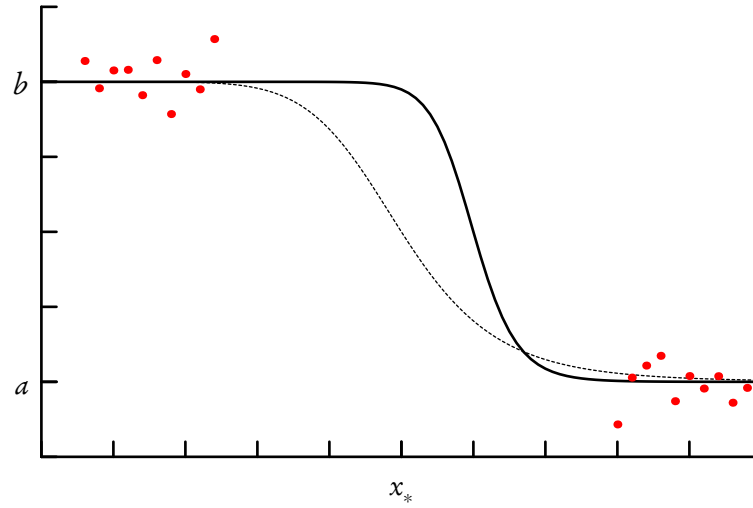
Figure 6.1: Two different parameter configurations of the Hill function match the data points (red dots) equally well. While the parameters y_a, y_b that describe the output levels at the ends of the intervals are identifiable, parameters k, x_* that describe the transition are not.

The two examples presented illustrates two different mechanisms for unidentifiability. In the first example, the relationship between the different parameters meant that different combinations could yield the same model output. Hence, unidentifiability was due to the relationship between the parameters. For the second example, unidentifiability was caused by not having persistently exciting data (missing information). Turning this description of the restriction upside down, the practical unidentifiability can be related to the insensitivity of the model output at the given measurement points to the parameters describing the transition.

As the heart rate model have large restrictions on available input (blood pressure) for which output measuremnts (heart rate) exists, the focus in this study will be on practical identifiability.

6.2 Sensitivities

Sensitivities describe the change in the model output due to changes in parameter values. Two different approach to sensitivity analysis will be presented here: *Local sensitivities* are calculated as the derivative of the model output with respect to the parameters at a given parameter configuration (local), and *global sensitivities* quantifying the effect of varying parameters over some subspace of the parameter space.

6.2.1 Derivative based sensitivities

Local derivative based sensitivities $S_\theta(t)$ are derivatives of the model output $y(t)$ with respect to the parameters θ,

$$S_\theta(t,\theta) = \frac{\mathrm{d}\, y(t,\theta)}{\mathrm{d}\theta}. \tag{6.9}$$

For simple problems these can be calculated analytically, but for more complex problems it is often advantageous to approximate these numerically. Three different computational methods exists for computing the derivatives: *Sensitivity equations*, *automatic differentiation*, and *finite differences approximation*.

Sensitivities of the model states to parameter values $S_\theta^{\mathrm{x}} = \frac{\partial x}{\partial \theta}$ can be computed using the sensitivity equations method as the solution to the ode

$$\begin{aligned}
\frac{\mathrm{d}}{\mathrm{d}t}\left(\frac{\partial x}{\partial \theta}\right) &= \frac{\mathrm{d}f}{\mathrm{d}\theta} + \frac{\mathrm{d}f}{\mathrm{d}x}\frac{\partial x}{\partial \theta} \\
\frac{\mathrm{d}S_\theta^{\mathrm{x}}}{\mathrm{d}t} &= J_\theta + J_x S_\theta^{\mathrm{x}},
\end{aligned} \tag{6.10}$$

obtained by differentiating the model ode $f(x,\theta,t)$ with respect to the parameter vector θ. Here $J_\theta = \frac{\mathrm{d}f}{\mathrm{d}\theta}$ is the *parameter Jacobian* and $J_x = \frac{\mathrm{d}f}{\mathrm{d}x}$ the model *Jacobian* which can be calculated analytically, using finite difference approximations, or by *automatic differentiation* (Griewank et al. 1989). Subsequently the state sensitivities S_θ^{x} can then be used to calculate the model output sensitivities S_θ by application of the chain rule on the output function $y = h(x,t,\theta)$.

Alternatively, the derivative with respect to θ_i can be calculated using the forward difference approximation

$$\hat{S}_{\theta_i}(t) = \frac{y(t,\theta + he_i) - y(t,\theta)}{h}, \tag{6.11}$$

where h is chosen appropriately to reflect the precision of the model output, and e_i is the unit vector in the i'th component direction. If the error in the model evaluation is on the order of ϵ, the step size should be $h = \sqrt{\epsilon}$ to get similar error on the sensitivities (Pope et al. 2009).

For the heart rate model the ode's are solved using the `Sundials` `CVODES` library, which has

included algorithms for calculating sensitivies via sensitivity equations with finite difference approximations of the jacobian and parameter jacobian (Serban and Hindmarsh 2005).

6.2.2   Global sensitivity analysis

Global sensitivity analysis measures how model output is affected by changes in parameter values over some interval or subspace of the parameter space.

In this study global sensitivities are calculated using two methods: *Sobol indices* and the *Morris method*. Sobol indices are computed by analyzing the model output variance over parameter space and decomposing it to contributions from the different parameters. The larger the impact on the variance, the more sensitive the parameter is. The Morris method calculate sensitivities by quantifying the effect of large changes parameter values one at the time, starting from different points in parameter space.

Sobol indices

The method was originally developed by Sobol 2001 but several variations exists, see Saltelli, Annoni, et al. 2010. The description of the Sobol indices and the algorithm for calculating first order effects follows the presentation by R. C. Smith 2014, but with modifications to reflect the algorithm presented by Jansen 1999.

Consider a scalar valued nonlinear model

$$Y = f(\Theta), \tag{6.12}$$

with parameters represented by the vector of random variables $\Theta = \left[\Theta_1, \ldots, \Theta_p\right], \Theta_i \in \Gamma_i \subset \mathbb{R}^n$ while $\rho_\Theta(\theta) = \prod_{k=1}^p \rho_{\Theta_k}(\theta_k)$, where Γ_i denotes the range of the random variable Θ_i and $\rho_\Theta(\theta)$ and $\rho_{\Theta_i}(\theta_i)$ are the joint and individual probability densities.

Consider the model decomposition Sobol 1993

$$f(\theta) = \sum_{\mathbf{i}' \subseteq \{1,2,\ldots,p\}} f_{\mathbf{i}'}(\theta_{\mathbf{i}'}), \tag{6.13}$$

where f is the model output, $\mathbf{i}' = \{i_1, \ldots, i_s\}$ is a set of parameters with cardinality s, $\theta_{\mathbf{i}'} = \left[\theta_{i_1}, \ldots, \theta_{i_s}\right]$ and $f_\emptyset = f_0$. Then if

$$\int_{\Gamma_k} f_{\mathbf{i}'}(\theta_{\mathbf{i}'}) \rho_k(\theta_k) \mathrm{d}\theta_k = 0$$

for any parameter θ_k and $\mathbf{i}' = \{1, \ldots, s\}$ that includes k, the decomposition is unique and the compo-

nent functions are given by

$$f_{\mathbf{i}'}(\theta_{\mathbf{i}'}) = \int_{\Gamma^{p-s}} f(\theta) \rho_\theta(\theta_{\sim \mathbf{i}'}) \, d\theta_{\sim \mathbf{i}'} - \sum_{\substack{l' \subset \mathbf{i}' \\ l' \neq \mathbf{i}'}} f_{l'}(\theta_{l'}).$$

To determine the effect of the parameter interaction in the set $\mathbf{i}'$, consider the conditional partial variance,

$$D_{\mathbf{i}'} = \int_{\Gamma^s} f_{\mathbf{i}'}^2(\theta_{\mathbf{i}'}) \rho_\theta(\theta_{\mathbf{i}'}) \, dq_{\mathbf{i}'} = \mathrm{var}[\mathbb{E}(Y|\theta_{\mathbf{i}'})] - \sum_{\substack{l' \subset \mathbf{i}' \\ l' \neq \mathbf{i}', l' \neq \emptyset}} D_{l'},$$

and the total variance

$$D = \int_\Gamma f^2(\theta) \rho_\Theta(\theta) \, d\theta - f_0^2 = \sum_{\substack{\mathbf{i}' \subseteq \{1,2,\dots,p\} \\ \mathbf{i}' \neq \emptyset}} D_{\mathbf{i}'}.$$

The Sobol indices are defined as

$$S_{\mathbf{i}'} = \frac{D_{\mathbf{i}'}}{D} \tag{6.14}$$

giving

$$\sum_{\substack{\mathbf{i}' \subseteq \{1,2,\dots,p\} \\ \mathbf{i}' \neq \emptyset}} S_{\mathbf{i}'} = 1.$$

The total sensitivity index

$$S_{T_{\mathbf{i}'}} \equiv \sum_{k, \mathbf{i}' \in k} S_k$$

describes the sensitivity of the model output variance to the parameter k, including the effects of interactions with other parameters.

Algorithm for estimating Sobol sensitivity indices.

A naive brute-force approach for estimating the first order indices S_i and S_{T_i} requires M^2 model evaluations for each parameter, where M is the number of points (in parameter space) used to evaluate the conditional mean $\mathbb{E}(Y|\theta_i)$, see Equation (6.14) and (R. C. Smith 2014). Saltelli, Annoni, et al. 2010 put forward an algorithm that reduces the number of model evaluations required to $M(p+2)$, while the algorithm used in our study is due to Jansen 1999 and requires $2M(p+2)$ evaluations for a better trade off between precision and cost. It should be noted that these algorithms truncate the variance decomposition after 2nd order. If higher order interactions are present in the model, these algorithms may give incorrect estimates.

Algorithm 1 *Sobol indices. Using M model evaluations and p parameters,*

1. Create two $M \times p$ sample matrices

$$
A = \begin{bmatrix} \theta_1^1 & \cdots & \theta_i^1 & \cdots & \theta_p^1 \\ \vdots & & & & \vdots \\ \theta_1^M & \cdots & \theta_i^M & \cdots & \theta_p^M \end{bmatrix}, \qquad
B = \begin{bmatrix} \hat{\theta}_1^1 & \cdots & \hat{\theta}_i^1 & \cdots & \hat{\theta}_p^1 \\ \vdots & & & & \vdots \\ \hat{\theta}_1^M & \cdots & \hat{\theta}_i^M & \cdots & \hat{\theta}_p^M \end{bmatrix},
$$

where θ_i^j and $\hat{\theta}_i^j$ are parameter samples drawn from the distribution corresponding to parameter i. In addition create the matrix

$$
C = \begin{bmatrix} A \\ B \end{bmatrix}.
$$

2. Create two $M \times p$ matrices

$$
A_B^i = \begin{bmatrix} \theta_1^1 & \cdots & \hat{\theta}_i^1 & \cdots & \theta_p^1 \\ \vdots & & & & \vdots \\ \theta_1^M & \cdots & \hat{\theta}_i^M & \cdots & \theta_p^M \end{bmatrix}, \qquad
B_A^i = \begin{bmatrix} \hat{\theta}_1^1 & \cdots & \theta_i^1 & \cdots & \hat{\theta}_p^1 \\ \vdots & & & & \vdots \\ \hat{\theta}_1^M & \cdots & \theta_i^M & \cdots & \hat{\theta}_p^M \end{bmatrix},
$$

that is, let $A_B^i = A$, but replace the i'th column with the i'th column from B. Likewise, let $B_A^i = B$, but replace the i'th column with the i'th column from A.

3. Compute the model output vectors

$$
y_A = f(A), \quad y_B = f(B), \quad y_{A_B^i} = f(A_B^i), \quad y_{B_A^i} = f(B_A^i), \tag{6.15}
$$

noting that

$$
y_C = \begin{bmatrix} y_A \\ y_B \end{bmatrix}. \tag{6.16}
$$

4. Estimates of the first order sensitivity indices can be computed by

$$
S_i^* = \frac{\frac{1}{M} \sum_{j=1}^{M} y_A^j y_{B_A^i}^j - y_A^j y_B^j}{\frac{1}{2M} \sum_{j=1}^{M} y_C^j y_C^j - \left(\frac{1}{M} \sum_{j=1}^{M} y_C^j \right)^2} = \frac{\frac{1}{M} y_A^T \left(y_{B_A^i} - y_B \right)}{\frac{1}{2M} y_C^T y_C - \left(\frac{1}{M} \sum_{j=1}^{M} y_C^j \right)^2}
$$

$$
S_{T_i}^* = \frac{\frac{1}{M} \sum_{j=1}^{M} \left(y_A^j y_{A_b^i}^j \right)^2}{\frac{1}{2M} \sum_{j=1}^{M} y_C^j y_C^j - \left(\frac{1}{M} \sum_{j=1}^{M} y_C^j \right)^2} = \frac{\frac{1}{M} \left(y_A - y_{A_B^i} \right)^T \left(y_A - y_{A_B^i} \right)}{\frac{1}{2M} y_C^T y_C - \left(\frac{1}{M} \sum_{j=1}^{M} y_C^j \right)^2}. \tag{6.17}
$$

Table 6.1: Analytical first order Sobol indices S_i, as well as estimated first order S_i^* and total effect $S_{T_i}^*$, for the Ishigami function using $M = 10,000$ evaluations. Values of coefficients used were $a = 7$, $b = 0.05$ and $q_i \sim \mathcal{U}(-\pi, \pi)$.

Measure	θ_1	θ_2	θ_3
S_i	$2.22 \cdot 10^{-1}$	$6.97 \cdot 10^{-1}$	$0.00 \cdot 10^{0}$
S_i^*	$2.12 \cdot 10^{-1}$	$6.87 \cdot 10^{-1}$	$9.64 \cdot 10^{-3}$
$S_{T_i}^*$	$2.93 \cdot 10^{-1}$	$6.87 \cdot 10^{-1}$	$6.19 \cdot 10^{-2}$

Test of implementation: Ishigami function.

The implementation of the Sobol algorithm was tested using the Ishigami function,

$$f(q) = \sin(\theta_1) + a \sin(\theta_2)^2 + b \theta_3^4 \sin(\theta_1), \tag{6.18}$$

with values $a = 7, b = .05$ as suggested by Sobol and Levitan 1999, and $\theta_i \sim \mathcal{U}(-\pi, \pi)$. In Table 6.1 first order estimates are compared with analytical values given by R. C. Smith 2014. Deviations of less than 5% indicates that the implementation correctly estimates the partial variances for $M = 10,000$.

Since S_{T_i} is the sum of all effects including θ_i, and S_i the first order effect, the difference $S_{T_i} - S_i$ is be the sum of interaction terms including θ_i. The degree of higher order interaction associated with parameter i may thus be observed through the different $S_{T_i}^* - S_i^*$. For θ_2 the difference is ≈ 0, suggesting that only first order effects are relevant. For θ_1 and θ_2 the difference is non-zero, suggesting that these parameters are involved in higher order effects. Both suggestions are confirmed from the analytical results where the only non-zero higher order variance is D_{13}.

Morris Screening

Morris screening describes the sensitivity of model output to each parameter q_i by sampling the *elementary effects* (Morris 1991; R. C. Smith 2014)

$$d_i(\theta) = \frac{f(\theta + \Delta e_i) - f(\theta)}{\Delta}, \tag{6.19}$$

from a grid of points Γ_l in the parameter distribution range Γ, and estimating the mean and variance of the distribution of $|d_i(\theta)|$,

$$u_i^* = \frac{1}{r} \sum_{j=1}^{r} \left| d_i^j(\theta) \right|$$

$$\sigma_i^{2*} = \frac{1}{r-1} \sum_{j=1}^{r} \left(d_i^j(\theta) - \mu_i \right)^2, \qquad \mu_i = \frac{1}{r} \sum_{j=1}^{r} d_i^j(\theta). \tag{6.20}$$

This provides an estimate of large scale local effects of sensitivity to the parameter θ_i.

The choice of the number of points (in each dimension) on the grid l and the value of Δ is important as they determine the sampling of the parameter space. By choosing l to be even and $\Delta = \frac{l}{2(l-1)}$ it is possible to ensure an even probability sampling from Γ_l, as this guarantees equal probability for all points on the grid (R. C. Smith 2014).

Implementation.

The implementation presented here creates a trajectory through the grid in the parameter space, such that for each step on the trajectory just one parameter is changed. Creating such a trajectory one *elementary effect* sampling can be obtained for each of the p parameters using $p+1$ function evaluations (R. C. Smith 2014).

Algorithm 2 *Morris Indices*

For each $j = 1, \ldots, r$:

1. *Sample an initial parameter vector θ^* from the uniform distribution $\mathcal{U}(0,1)$.*

2. *Create the $(p+1) \times p$ permutation matrix B^* where each row represents a parameter configuration. A completely deterministic permutation matrix is given by*

$$B_j^* = J_{p+1,p} \theta^* + \Delta B, \tag{6.21}$$

   where $J_{p+1,p}$ is a $(p+1) \times p$ matrix of ones, Δ is the chosen grid step size, and B is a lower triangular matrix of ones. Each row in B^* differs in exactly one column, corresponding to the parameter for which the step is made. A random permutation matrix can be obtained by applying the orientation matrix

$$B_j^* = \left(J_{p+1,p} \theta^* + \frac{\Delta}{2} \left[\left(2B - J_{p+1,p} \right) D^* + J_{p+1,p} \right] \right) P^*, \tag{6.22}$$

   where the $p \times p$ matrix D^* is diagonal with elements randomly chosen from the set $\{-1, 1\}$, and the $p \times p$ matrix P^* is created by perturbing the columns of a $p \times p$ identity matrix.

3. *Map the uniformly distributed values in B^* to the correct distributions using the mapping m. This is achieved using the inverse survival function, and the survival function for the uniform distribution $x \sim \mathcal{U}(0,1)$: $1-x$. Let $m_k(\theta_k)$ be this mapping for the k'th parameter. When applied a new matrix C_j is formed*

$$
C_j = \begin{bmatrix} m_1(B^*_{j(1,1)}) & \cdots & m_i(B^*_{j(1,i)}) & \cdots & m_p(B^*_{j(1,p)}) \\ \vdots & & & & \vdots \\ m_1(B^*_{j(p+1,1)}) & \cdots & m_i(B^*_{j(p+1,i)}) & \cdots & m_p(B^*_{j(p+1,p)}) \end{bmatrix} \tag{6.23}
$$

with values following the correct distributions.

4. *Evaluate the model output for each of these $p+1$ configurations, in the $p+1 \times 1$ vector*

$$
y_j = f(C_j). \tag{6.24}
$$

5. *Through analysis of B^* identify which two consecutive rows k and $k+1$ that corresponds to each parameter i, and calculate the corresponding elementary effect,*

$$
d_i^j = \frac{y_{j,k+1} - y_{j,k}}{\Delta}. \tag{6.25}
$$

Finally the sampling mean μ_i^* and variance σ_i^{2*} for each parameter i can be estimated by

$$
u_i^* = \frac{1}{r} \sum_{j=1}^{r} \left| d_i^j(\theta) \right|
$$
$$
\sigma_i^{2*} = \frac{1}{r-1} \sum_{j=1}^{r} \left(d_i^j(\theta) - \mu_i \right)^2, \qquad \mu_i = \frac{1}{r} \sum_{j=1}^{r} d_i^j(\theta). \tag{6.26}
$$

Example: Sobols' function.

The function

$$
Y = \prod_{i=1}^{p} g_i(\Theta_i), \quad g_i(\Theta_i) = \frac{|4\Theta_i - 2| + a_i}{1 + a_i} \tag{6.27}
$$

where $a_i \geq 0$ are fixed coefficients, is due to Sobol 2001, and often used as a test case for global sensitivity analysis since by construction it is highly nonlinear, non-monotonic and has non-zero interactions. Similar to R. C. Smith 2014 the values $l = 4$, $\Delta = \frac{2}{3}$, $p = 6$, $a_1 = 78, a_2 = 12, a_3 = 0.5, a_4 = 2, a_5 = 97, a_6 = 33$ and $\theta_i \sim \mathcal{U}(0,1), i = 1, \ldots, 6$ are used to compute the estimates listed in Table 6.2. The listed values μ_i^*, σ_i^* are obtained using an implementation of Algorithm 2. As the estimates are of the same order of magnitude the implementation is considered correct.

Table 6.2: μ_i^S, σ_i^S are numerical estimates from R. C. Smith 2014, μ_i^*, σ_i^* are obtained using my implementation of the naive algorithm for Morris measures.

Measure	θ_1	θ_2	θ_3	θ_4	θ_5	θ_6
μ_i^S	$5.60 \cdot 10^{-2}$	$2.77 \cdot 10^{-1}$	$1.76 \cdot 10^{0}$	$1.19 \cdot 10^{0}$	$3.50 \cdot 10^{-2}$	$9.90 \cdot 10^{-2}$
μ_i^*	$3.94 \cdot 10^{-2}$	$3.05 \cdot 10^{-1}$	$1.73 \cdot 10^{0}$	$7.44 \cdot 10^{-1}$	$2.59 \cdot 10^{-2}$	$8.68 \cdot 10^{-2}$
σ_i^S	$3.84 \cdot 10^{-2}$	$1.90 \cdot 10^{-1}$	$1.68 \cdot 10^{0}$	$1.13 \cdot 10^{0}$	$3.74 \cdot 10^{-2}$	$2.38 \cdot 10^{-2}$
σ_i^*	$3.34 \cdot 10^{-2}$	$3.32 \cdot 10^{-1}$	$2.02 \cdot 10^{0}$	$9.16 \cdot 10^{-1}$	$1.48 \cdot 10^{-2}$	$7.36 \cdot 10^{-2}$

Mapping uniformly distributed random variable to other distributions.

For some problems parameter values are known to follow certain distributions. Since the Morris algorithm is described for parameters following uniform distributions, one can interpret the grid as a division based on the percentile of the distribution. This interpretation makes it easy to translate the uniformly sampled point $\theta_{\mathcal{U}} \sim \mathcal{U}(0,1)$ to another distribution, given that the inverse survival distribution function (iSDF) or the inverse cumulative distribution function (iCDF) is available. The following describes how to use the iSDF to map between distributions.

For the random variable $\theta_{\mathcal{U}}$ first determine the survival distribution function (SDF) value of $\theta_{\mathcal{U}}$ for the uniform distribution $y = \text{SDF}_{\mathcal{U}}(\theta_{\mathcal{U}})$. For the uniform distribution $\mathcal{U}(0,1)$ the SDF is simple, $\text{SDF}_{\mathcal{U}}(x) = 1 - x$. Next, map this survival probability to the target distribution $\mathcal{T}$ using the iSDF of the target distribution $\text{iSDF}_{\mathcal{T}}(y)$. In conclusion: One can obtain a random variable $\theta_{\mathcal{T}}$ distributed according to $\mathcal{T}$ by

$$\theta_{\mathcal{T}} = \text{iSDF}_{\mathcal{T}}(1 - \theta_{\mathcal{U}}) \tag{6.28}$$

given that $\theta_{\mathcal{U}} \sim \mathcal{U}(0,1)$.

Figure 6.2 shows the probability density function and the survival distribution functions for the uniform distribution and the beta distribution with parameter values $a = 2, b = 7$.

Example: SIR-model

To illustrate the two methods consider an SIR model given by (R. C. Smith 2014)

$$
\begin{aligned}
\frac{dS}{dt} &= \delta N - \delta S - \gamma k I S, & S(0) &= S_0, \\
\frac{dI}{dt} &= \gamma k I S - (r + \delta) I, & I(0) &= I_0, \\
\frac{dR}{dt} &= r I - \delta R, & R(0) &= R_0.
\end{aligned}
\tag{6.29}
$$

Here, S represents the number of susceptible individuals, I the number of infected, and R the number of recovered. $N = S + I + R$ is the total number of individuals, the size of the population. The
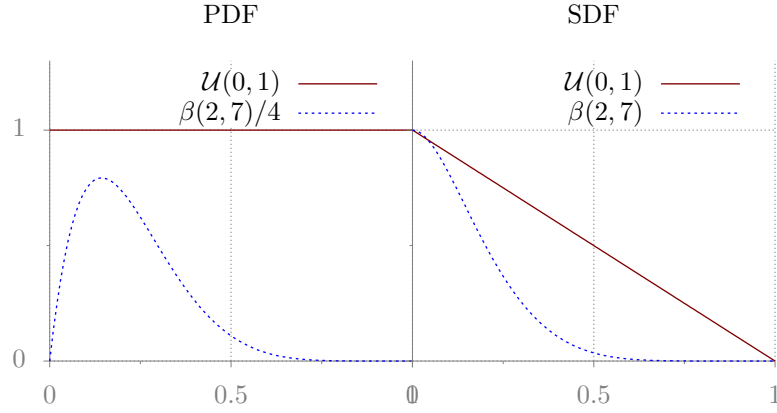
Figure 6.2: Probability density function and survival distribution function for the uniform distribution and beta distribution with parameters $a = 2, b = 7$.

parameters in the model represents:

γ: Infection coefficient. Describes how efficient an infection is transmitted by individuals in contact.

k: Interaction coefficient. Describes the degree of interaction between individuals.

r: Recovery rate.

δ: Death/birth rate. Describes the rate at which individuals, independently of the infection, are "reborn" into the susceptible group.

The parameters follows the distributions

$$\gamma \sim \mathcal{U}(0,1), \quad k \sim \beta(a,b), \quad r \sim \mathcal{U}(0,1), \quad \delta \sim \mathcal{U}(0,1).$$

The β-distribution is shown in Figure 6.3 for two different configurations: $\beta(2,7)$ and $\beta(0.2,15)$.

The SIR model was implemented in PYTHON and the differential equations solved using *lsoda* from the FORTRAN library *odepack* through a wrapper in the python package *SciPy*, *scipy.integrate.odeint* (Jones, T. Oliphant, P., et al. 2001–; T.E. Oliphant 2007).

As the algorithms for Sobol and Morris considers a scalar model output, consider the response function

$$y = \int_0^5 R(t,\theta)\,\mathrm{d}t. \tag{6.30}$$

Beta PDF
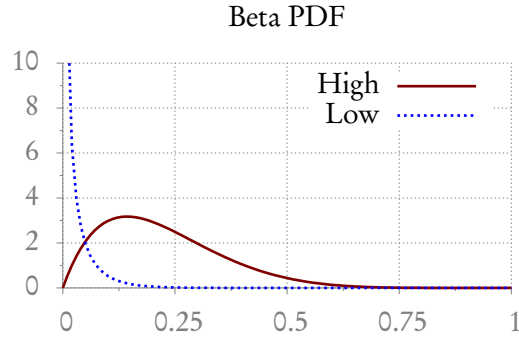
Figure 6.3: Beta probability distribution function (pdf) for high degree of interaction, $a = 2, b = 7$, and for low degree of interaction, $a = 0.2, b = 15$.

While this function can be evaluated using a quadrature rule, it may also be evaluated by adding an additional state y to system of differential equations

$$\frac{\mathrm{d}y}{\mathrm{d}t} = R, \qquad y(0) = 0. \tag{6.31}$$

Sampling of random variables was done using the library *numpy.random*, and the remapping of distributions was done using the library *scipy.stats*.

Figure 6.4 shows the result with the initial conditions $S_0 = 900, I_0 = 100, R_0 = 0$, with parameters set at the mean values for large degree of interaction, i.e. $\gamma = r = \delta = 0.5$ and $k = \frac{2}{2+7}$.
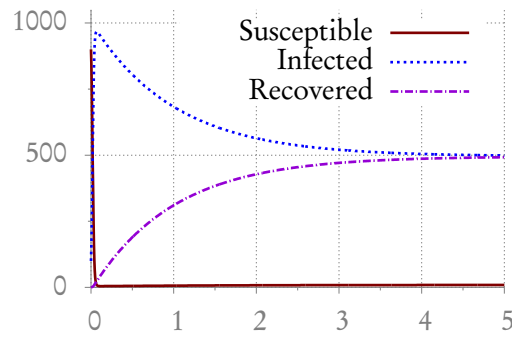
Figure 6.4: Solution of the model for mean parameter values for high degree of interaction.

Table 6.3: Measures obtained using different configurations for the distribution of k.

(a) $a = 2, b = 7$

Measure	γ	k	r	δ
S_i	$4.44 \cdot 10^{-2}$	$-8.30 \cdot 10^{-3}$	$7.79 \cdot 10^{-1}$	$1.12 \cdot 10^{-1}$
S_{T_i}	$-4.48 \cdot 10^{-2}$	$-1.07 \cdot 10^{-1}$	$6.38 \cdot 10^{-1}$	$1.93 \cdot 10^{-1}$
μ_i^*	$2.21 \cdot 10^{2}$	$6.16 \cdot 10^{2}$	$2.26 \cdot 10^{3}$	$1.36 \cdot 10^{3}$
σ_i	$3.37 \cdot 10^{2}$	$1.59 \cdot 10^{3}$	$9.52 \cdot 10^{2}$	$5.39 \cdot 10^{2}$

(b) $a = 0.2, b = 15$

Measure	γ	k	r	δ
S_i	$6.01 \cdot 10^{-2}$	$5 \cdot 10^{-1}$	$1.74 \cdot 10^{-1}$	$1.19 \cdot 10^{-1}$
S_{T_i}	$2.82 \cdot 10^{-1}$	$7.35 \cdot 10^{-1}$	$2.89 \cdot 10^{-1}$	$2.31 \cdot 10^{-1}$
μ_i^*	$5.15 \cdot 10^{2}$	$2 \cdot 10^{3}$	$1.08 \cdot 10^{3}$	$8.26 \cdot 10^{2}$
σ_i	$7.34 \cdot 10^{2}$	$2.23 \cdot 10^{3}$	$1.44 \cdot 10^{3}$	$8.69 \cdot 10^{2}$

High degree of interaction.

Results obtained for $a = 2$ and $b = 7$ are shown in Table 6.3a. From the Sobol indices the order of importance is r, δ, γ, k, with r and δ being one order of magnitude more important than γ, which is again one order of magnitude more important than k. The Morris measures tells a similar story, although they rank γ and k more evenly, one order of magnitude below r and δ. This suggests that the parameters γ and k does not contribute significantly to the model for this configuration. These suggestions are further supported by the scatter plots of parameter value against number of recovered individuals at time $t = 5$, shown in Figure 6.5. The figure shows that the expected value of $R(5)$ do not change with the value of parameters γ and k (uniform distribution of points), whereas it clearly depends on the value of r and δ.

Figure 6.3 shows the beta distribution for k. It is clear that for a large degree of interaction, $a = 2, b = 7$, the values obtained for k will have a median removed from both 0 and 1.

Figure 6.6 shows the estimated probability density function of $R(5)$ for the case where all parameters are allowed to vary and for the case where only r and δ are allowed to vary. Fixing γ and k is found to be unimportant to model output, as it does not change the statistical behavior of the model.

Low degree of interaction.

Results obtained for $a = 0.2$ and $b = 15$ are shown in Table 6.3b. The Sobol indices suggest the ordering k, r, δ, γ, with k being five times as significant as r, which is in turn approximately twice
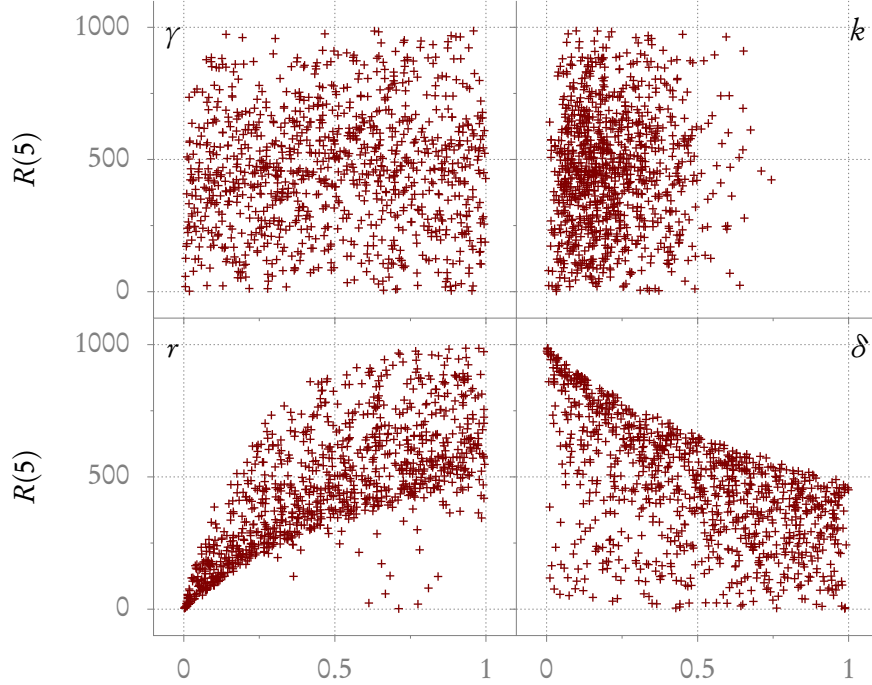
Figure 6.5: Scatter plots of parameter values vs. the number of recovered individuals R at time $t = 5$ for the configuration corresponding to a high degree of interaction.

as significant as γ and δ. The Morris indices suggest the ordering k, r, δ, γ. These suggestions are supported by the scatter plots in Figure 6.7 where the number of recovered individuals at time $t = 5$ is plotted against the value of the parameters. Note that the value of the parameter k has been remapped and plotted as the value on the uniform distribution $\mathcal{U}(0, 1)$ that has the same survival distribution function. Figure 6.3 shows the beta distribution. The plots reveal that the probability of experiencing an extreme low value of k is significant. Since the infection coefficient $\gamma < 1$ an extreme low value of k would lead to very slow disease dynamics, and may even cause the disease to go extinct, if the recovery rate r and the birth/death rate δ is large enough. This is illustrated in Figure 6.6, where the estimated probability density function of $R(5)$ is plotted for the case where all parameters are allowed to vary and for the case where only k, r and δ are allowed to vary, while γ and k are fixed at their mean values. Furthermore, to show the importance of k the estimate of the probability distribution
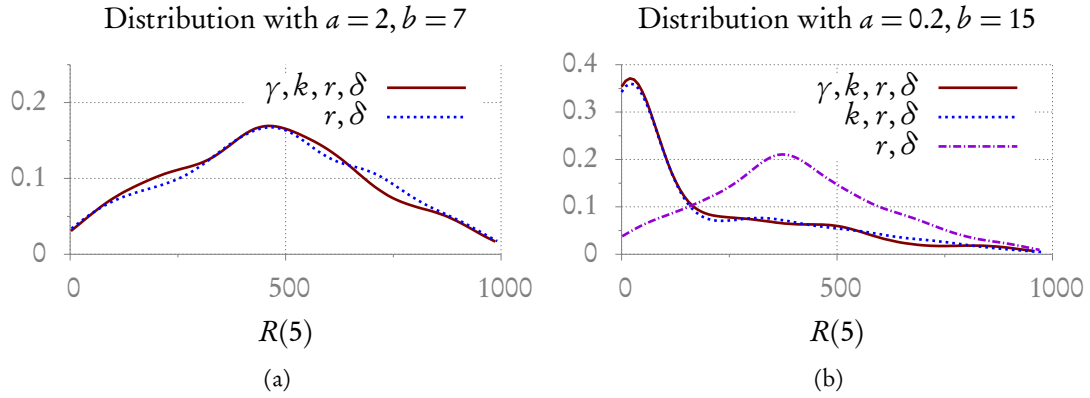
Figure 6.6: (a) Gaussian kernel density distribution of $R(5)$ obtained using 1,000 realizations of the model with parameter values drafted from their respective distributions. The two curves represents varying parameters $\{\gamma, k, r, \delta\}$ and $\{r, \delta\}$ respectively. Parameters not varied were set at the mean value of the associated distribution. (a) The parameters for the β-distribution for k was $a = 2$ and $b = 7$. (b) The parameters for the β-distribution for k was $a = 0.2$ and $b = 15$. The third curve is included to show the resulting distribution if k wrongly had been fixed at mean value.

with k set at the mean value has been included, corresponding to the reduced model configuration with high degree of interaction. Note that with this probability distribution, the value of k is quite significant for the disease dynamics.
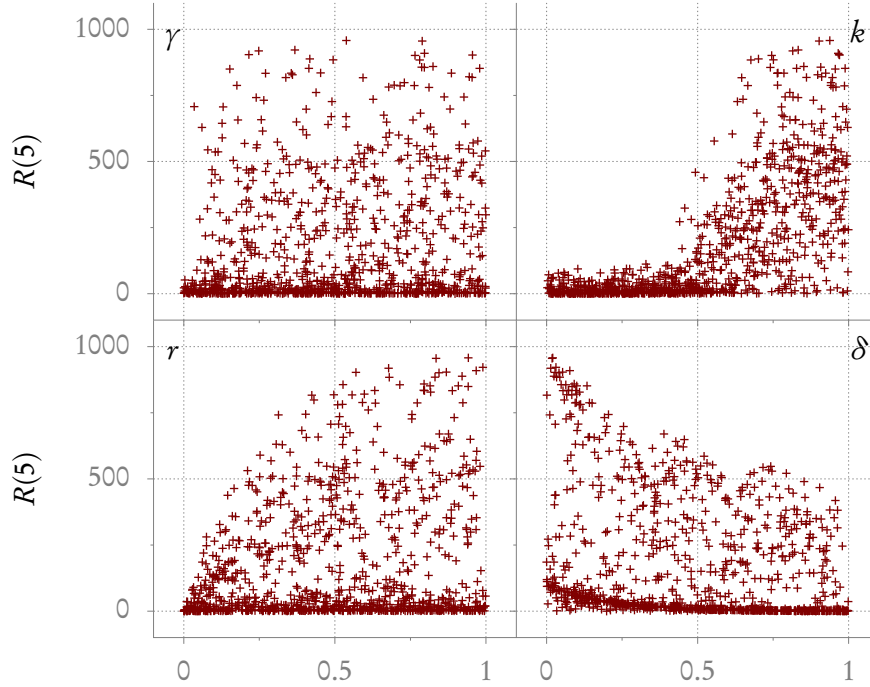
Figure 6.7: Scatter plots of parameter values vs. number of recovered individuals R at time $t = 5$ for the configuration corresponding to a low degree of interaction. Note: Values of parameter k has been mapped to the value on the uniform distribution with the same survival density function value to better show how the percentile of the random variable affects the model output.

6.3 Identifiability analysis/Subset selection

As discussed earlier in Section 6.1, unidentifiability can be due to the model output being insensitivity to the parameters in question, or to only a combination of parameters being identifiable. The first type of unidentifiability was illustrated with the Hill function example and the second by the linear input example where the parameters where structural unidentifiable.

While the sensitivity estimates introduced above will show if parameters affect the model output, it does not reveal parameter interactions or possible over-parametrisation. Attention will therefore now turn to methods for finding identifiable subsets of parameters, *subset selection*. The methods applied

in this study are based on local sensitivities and include both an element of the magnitude of model sensitivity to the parameters and parameter interactions.

Two methods are presented here: *The structural correlation method* (SCM) (Jacquez 1985; Miao et al. 2011; Ottesen and Olufsen 2013) and the *orthogonal sensitivities method* (OSM) (Li, Henson, and Kurtz 2004). SCM is based on identifying pairwise correlations between parameter estimates. A subset will be selected by first removing insensitive parameters, and then removing one parameter at the time until no correlations are left in the subset. OSM starts with an empty set and adds one parameter at the time based on the magnitude of sensitivity to the parameter and the linear independence between it and the existing subset. Numerous other methods for subset selection exists, including the *Eigenvalue* and the *SVD-QR* method. Miao et al. 2011 provides a good overview of available methods that are based on local sensitivities.

Before discussing the two methods it is relevant to discuss the *Fisher Information Matrix* as it is a core component of both methods.

Fisher Information Matrix

For Equation (6.1) the *Fisher information matrix* (FIM) is given by

$$F = \sigma^{-2} S^T S, \tag{6.32}$$

where S is given by (6.9) for some specific parameter configuration and σ^2 is the variance associated with the problem.

For a least-squares problem in general the objective is to minimize the cost function (sum of squares)

$$\text{SS} = \frac{1}{2} \sum_{i=0}^{n-1} r_i^2, \tag{6.33}$$

where

$$r_i = v_i - y_i$$

are the residuals where v_i is the measured data and y_i is the i'th output of the function. For the heart rate model, y_i would denote the model output (heart rate) at time t_i.

In optimization the goal is to find the parameter configuration θ^* that minimizes (6.33). For this optimum the gradient vector is zero, $g(\theta^*) = 0$. The Taylor expansion of the cost function around the optimum point θ^* in the parameter space is given by

$$\text{SS}(\theta) = \text{SS}(\theta^*) + g\Delta + \Delta^T H \Delta + \mathcal{O}\left(\Delta^3\right). \tag{6.34}$$

where $\Delta = (\theta - \theta^*)$, g is the gradient given by

$$g_j = \frac{\partial \mathrm{SS}}{\partial \theta_j} = \sum_{i=0}^{n-1} r_i \frac{\partial r_i}{\partial \theta_j}$$

and H is the Hessian (square matrix with second-order partial derivatives) of the cost function given by

$$H_{jk} = \frac{\partial g_j}{\partial \theta_k} = \sum_{i=0}^{n-1} \frac{\partial r_i}{\partial \theta_k} \frac{\partial r_i}{\partial \theta_j} + r_i \frac{\partial^2 r_i}{\partial \theta_j \partial \theta_k}.$$

Ignoring higher-order terms of the taylor expansion in (6.3), and re-arranging gives

$$\mathrm{SS}(\theta) = \mathrm{SS}(\theta^*) + \Delta^T H \Delta$$

since $g(\theta^*) = 0$. If H is singular there exists some $\Delta \neq 0$, such that $H\Delta = 0$, which in turn means that $\mathrm{SS}(\theta) = \mathrm{SS}(\theta^*)$, and thereby, that the minimizer of the cost function is not unique.

When r is small or when r varies nearly as a linear function near an minimum of (6.33), a good approximation to the Hessian is obtained by ignoring the second-order term (Wolfram 2013).

$$H_{jk} \approx \sum_{i=0}^{n-1} \frac{\partial r_i}{\partial \theta_k} \frac{\partial r_i}{\partial \theta_j}.$$

Since $r_i = v_i - y_i$ the derivative of the residual is given by

$$\frac{\partial r_i}{\partial \theta_j} = \frac{\partial}{\partial \theta_j}(v_i - y_i) = -\frac{\partial y_i}{\partial \theta_j} = -S_{ij}.$$

Hence the Hessian approximation can be written as a matrix product,

$$H \approx S^T S = F,$$

and analysis of FIM will show which parameters may cause unidentifiability.

While the presentation above is based on the absolute sensitivities, similar arguments can be made for the relative sensitivities. Define $\tilde{y}_i = \ln y_i$ and $\tilde{\theta}_j = \ln \theta_j$, then the Hessian of the relative cost function

$$\tilde{H} = \tilde{S}^T \tilde{S}$$

can be approximated by FIM using the relative sensitivities

$$\tilde{S}_{ij} = \frac{\partial \ln y_i}{\partial \ln \theta_j}.$$

Structural Correlation Method

In statistics, correlations between parameters can be determined by estimating parameter values by solving the inverse problem against different sets of data and calculate correlations on the resulting series of parameter estimates. A simple recipe for calculating correlations in this manner would be to (Miao et al. 2011)

1. Select nominal values for the parameters. Call this set θ_0.

2. Obtain the solution to the mathematical model $y(t_i, \theta_0)$ using the nominal parameter values.

3. Using the solution $y(t_i, \theta_0)$ generate n new data sets by adding iid. noise from a normal distribution
$$y_j(t_i) = y(t_i, \theta_0) + \mathcal{N}(0, \sigma^2), \quad \text{for } j = 0, \ldots, n-1$$

4. For each artificial data set y_j, determine the parameter set θ_j that minimizes the least squares cost
$$\text{SS}_j = \frac{1}{N} \sum_{i=0}^{N-1} \left(y_j(t_i) - y(t_i, \theta_j) \right)^2.$$

5. Calculate covariances of the obtained parameters by
$$\text{Cov}[a, b] = \text{E}\left[\left(a - \text{E}[a] \right) \left(b - \text{E}[b] \right) \right]$$
$$\approx \frac{1}{n} \sum_{j=0}^{n-1} \left(a_j - \frac{1}{n} \sum_{j=0}^{n-1} a_j \right) \left(b_j - \frac{1}{n} \sum_{j=0}^{n-1} b_j \right)$$

6. Here, the variance of the parameter a is given by
$$\text{Var}[a] = \text{Cov}[a, a].$$

7. Correlations are then calculated by scaling with the variance of each parameter
$$\text{Cor}(a, b) = \frac{\text{Cov}[a, b]}{\sqrt{\text{Var}[a] \text{Var}[b]}}.$$

   Often these correlations are presented in a matrix called the *correlation matrix*, where each parameter are represented by a row and a column. As covariances are independent of the order of the parameters, the covariance and correlation matrix are often depicted as triangular matrices.

While this method makes it clear how to understand what correlations are, the computational cost of this method is high. The covariance matrix C can also be approximated as the inverse of the Fisher

information matrix (FIM) - the first order approximation to the model Hessian. This covariance matrix will tell about the variances to expect for parameter estimates, and enable calculation of the correlations analogous to above. For problems with constant variance σ the parameter covariance is given as the inverse of the FIM, given in Equation (6.32), by

$$C = F^{-1}. \tag{6.35}$$

The idea behind the structural correlation method is that if a pair of parameters show a large correlation, that is, that their uncertainty is strongly coupled, it is not feasible to estimate both parameters. The correlations can be based on either absolute $S_j(t) = \frac{\partial y(t)}{\partial \theta_j}$ or relative sensitivities $\tilde{S}_j(t) = \frac{\partial y(t)}{\partial \theta_j} \frac{\theta_j}{y(t)}$. Often relative sensitivities are preferred since this enables one to compare different model output and parameters with values of different orders of magnitudes.

Algorithm 3 *Structural Correlation Method (Daun et al. 2008; Olufsen and Ottesen 2013)*

1. *For each parameter calculate the 2-norm of the sensitivity of the model output to this parameter*

$$\bar{S}_j = \sqrt{\sum_{i=0}^{N-1} S_j(t_i)^2}.$$

2. *Fix insensitive parameters for which $\bar{S}_j < \sqrt{\epsilon}$ where ϵ is the tolerance used when calculating the sensitivities.*

3. *Repeat through the following steps.*

   (a) *Calculate the covariance matrix by inverting the FIM, $C = (F)^{-1} = (S^T S)^{-1}$, and determine correlations as described above. If the largest correlation is smaller than some value γ, the subset reduction procedure is complete.*

   (b) *For the correlation with the largest absolute value, fix the parameter with the lowest overall sensitivity, determined by the 2-norm of the sensitivities $\bar{S}_j$.*

   (c) *The parameter to be fixed is noted, and the column of S corresponding to this parameter are removed from S, before correlations are calculated again, and the process is repeated.*

Orthogonal sensitivities

Contrary to the structural correlation method, this method builds a subset by selecting one parameter at the time and adding it to a subset of identifiable parameters. The method by Li, Henson, and Kurtz 2004 combines two of the methods presented by Miao et al. 2011, the principle component analysis (PCA) and the orthogonal method. For each parameter an importance index e is calculated using PCA and each time the subset of already selected parameters is updated the remaining parameters

have their orthogonality index d calculated. At each iteration the parameter with the highest product $I = ed$ is added to the subset.

Importance index/principle component analysis.

The name *principle components* refers to the *eigenvectors* v corresponding to *eigenvalues* λ of the matrix F

$$Fv = F\lambda. \tag{6.36}$$

For the OSM method the matrix of interest is

$$F = \tilde{S}^T \tilde{S},$$

where $\tilde{S} = \frac{\partial y}{\partial \theta} \frac{\theta}{y} = \frac{\partial \ln y}{\partial \ln \theta}$ is the relative sensitivities. Eigenvectors describe directions for which the matrix will only scale the vector.

For this particular context the eigenvectors of F will describe directions in the parameter space that change proportional to the corresponding eigenvalues. To find parameters that may cause a large impact on the model output, it is relevant to look for parameters for which the gradient can change when parameter values are changed, that is for eigenvectors with large eigenvalues. Hence to investigate the impact of parameter j on the gradient for the i'th eigenvalue-eigenvector combination, consider the product of the j'th component of the eigenvector and the eigenvalue from (6.36)

$$(\lambda_i v_i)_j.$$

Combining the eigenvectors into a matrix Q where the i'th column is the vector v_i, the *Importance index* e_j used in OSM is calculated by summing over all the eigenvalues, and normalizing by the sum of the eigenvalues

$$e_j = \frac{\sum_{i=0}^{m-1} \lambda_i Q_{ji}}{\sum_{i=0}^{m-1} \lambda_i}. \tag{6.37}$$

Orthogonality index / Linear independence.

While building the identifiable subset, the columns of the sensitivity matrix S corresponding to the already selected parameter $i = l_1, \dots, l_s$ span a space denoted by $\tilde{S}_s = \text{span}\left(\tilde{S}_{l_1}, \dots, \tilde{S}_{l_s}\right)$. For each of the remaining parameters, $i = k_1, \dots, k_{p-s}$ the projection of the corresponding column of the sensitivity matrix $\tilde{S}_i$ onto $\tilde{S}_s$ is found as

$$\tilde{s} = \sum_{i=l_1}^{l_s} \alpha_i \tilde{S}_i.$$

This is done by finding the coefficients α_i that solves

$$\min_{\alpha_i} \frac{1}{2}\left(\tilde{S}_j - \tilde{s}\right)^T \left(\tilde{S}_j - \tilde{s}\right),$$

which is equivalent to solving the linear system

$$\begin{bmatrix} \tilde{s}_{l_1}^T \tilde{s}_{l_1} & \cdots & \tilde{s}_{l_s}^T \tilde{s}_{l_1} \\ \vdots & \ddots & \vdots \\ \tilde{s}_{l_1}^T \tilde{s}_{l_s} & \cdots & \tilde{s}_{l_s}^T \tilde{s}_{l_s} \end{bmatrix} \alpha = \begin{bmatrix} \tilde{S}_j^T \tilde{s}_{l_1} \\ \vdots \\ \tilde{S}_j^T s_{l_s} \end{bmatrix}, \tag{6.38}$$

since the column corresponding to the already selected parameters are linearly independent[1]. $\tilde{s}$ is now the projection of $\tilde{S}_i$ onto $\tilde{S}_s$. If $\tilde{S}_i$ can be expressed in the basis of $\tilde{S}_s$ the two vectors will be equivalent (in direction), and the parameter i adds no dynamics to the model output (that has not already been included). In this case, the parameter is insignificant, and would be rejected for the subset. On the contrary, if $\tilde{s}$ is very different from $\tilde{S}_i$, S_i should be included in the subset.

The linear independence is determined by observing sine to the angle between the projection $\tilde{s}$ and $\tilde{S}_i$. This is called the *orthogonality index*,

$$d_i = \sin\left[\arccos\left(\frac{S_i^T \tilde{s}}{||\tilde{S}_i||\,||\tilde{s}||}\right)\right]. \tag{6.39}$$

Identifiability index.

After calculating the orthogonality index for all non-ranked parameters, their total identifiability index can be calculated as

$$I_i = d_i e_i \tag{6.40}$$

Now, select the parameter with the highest identifiability index, and repeat the process from calculating orthogonality indices.

Example: Structural unidentifiability revisited

To illustrate the ideas behind these two methods the example of structural unidentifiability from Section 6.1.1 will be revisited. For this example, the initial condition of x_0 is treated as a variable and sensitivities are analyzed for a specific input signal.

$$\dot{x}(x,t) = -ax + bu(t), \quad x(0) = x_0$$
$$y(x) = cx. \tag{6.41}$$

---

[1]If one seeks to continue ranking after building a full rank basis, one should then consider only the importance index.

where x is the state, $u(t)$ some input signal, $y(t)$ the model output and α, β, c, x_0 are parameters.

The solution to the differential equation and the model output is given by

$$x(t) = x_0 e^{-at} + \int_0^t e^{-a(t-s)} b u(s) \, ds,$$

$$y(t) = c x_0 e^{-at} + cb \int_0^t e^{-a(t-s)} u(s) \, ds. \tag{6.42}$$

Here the parameter c only appears in combination with the initial condition/parameter x_0 and in combination with the parameter b. Hence, as discussed earlier, there is not a one-to-one correspondence between parameters and the model output, as different configurations of parameter values can give an identical model output.

The sensitivities can be calculated analytically

$$\frac{\partial y}{\partial a}(t, \theta) = -c t x_0 e^{-at} - cb \int_0^t (t-s) e^{-a(t-s)} u(s) \, ds,$$

$$\frac{\partial y}{\partial b}(t, \theta) = c \int_0^t e^{-a(t-s)} u(s) \, ds,$$

$$\frac{\partial y}{\partial c}(t, \theta) = x_0 e^{-at} + b \int_0^t e^{-a(t-s)} u(s) \, ds, \tag{6.43}$$

$$\frac{\partial y}{\partial x_0}(t, \theta) = c e^{-at}.$$

Using input function $u(x) = \sin(x)$, parameters $a = 1.5, b = 2, c = 3$ and $x_0 = 1$ for $x_i \in [0, 7]$ the resulting sensitivities are as shown in Figure 6.8. From Equation (6.42) it can be seen that it is impossible to identify all of $\{b, c, x_0\}$ at the same time, as these parameters only occur two places in the solution, and only in combinations. From this analysis it should be possible only to identify two of these three parameters, due to the structural link between their roles.

Calculating the condition number (hints at the difficulty of inverting the matrix/degree of linear dependence/singularity) of $S^T S$ for different subsets of parameters gives the results shown in Table 6.4, which confirms this suspicion. The results reveal a very large condition number when all parameters are included, and when only a is excluded. On the other hand, removing parameter b, c or x_0 reduces the condition number to the order of 10^2.

Looking at the results from the sensitivity analysis with the condition numbers presented in Table 6.4 it is not surprising that letting parameters b or c be fixed reduces the condition number, as the sensitivity to these parameters are proportional. At the same time it is remarkable that fixing x_0 also reduces the condition number. This hints that slight differences at the beginning of the curves of the sensitivities for b and c is enough to distinguish these parameters.

Using the orthogonal sensitivities method (OSM) the ranking shown in Table 6.5 is found. Note:
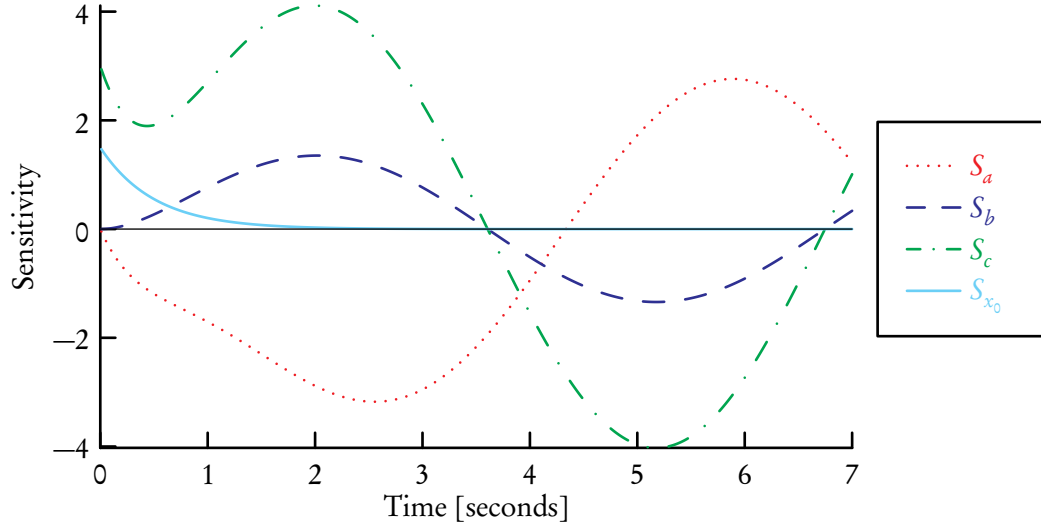
Figure 6.8:   Sensitivities for the linear input example.

Table 6.4:   Condition numbers for matrix $S^T S$ for different parameter subsets.

Subset	$\varkappa(S^T S)$
$\{a, b, c, x_0\}$	2.73×10^{17}
$\{b, c, x_0\}$	3.20×10^{16}
$\{a, c, x_0\}$	1.68×10^{2}
$\{a, b, x_0\}$	6.73×10^{1}
$\{a, b, c\}$	4.35×10^{2}

1. c is ranked as most important. This is not surprising when looking at the sensitivity plots.

2. a is ranked 2nd. The orthogonality of a is only .546 but this is still significantly larger than that of b which is .20. The sensitivity to x_0 is more orthogonal with $d = .95$, but since the sensitivity to x_0 is a lot smaller, the total identifiability index for a is still the largest.

3. b is ranked 3rd. The orthogonality of b is .196, a lot smaller than for x_0, which is .934. However because the importance index of b is .243 while that of x_0 only is .031, b is prioritized.

4. x_0 is ranked last. When a, b, c has already been chosen, the orthogonality index of x_0 is

Table 6.5: Ranking obtained using the orthogonal sensitivities method (OSM). Columns shown are Orthogonality (d), Importance (PCA) score (e) and total Importance ($I = de$).

Rank	Parameter	d	e	I
1	c	–	0.766	–
2	a	0.546	0.578	0.315
3	b	0.196	0.243	0.047
4	x_0	0.000	0.031	0.000

0.000. This confirms the suspicion that the sensitivities are linearly dependent.

Since there is a linear dependence in S, the FIM 6.32 is not invertible. Hence it is impossible to calculate statistical correlations of the parameters value using the Cramer-Rao bound (Miao et al. 2011). If however, one of the parameters b, c or x_0 is removed from S, the correlation matrix can be calculated (assuming normally distributed errors with standard deviation 1). Denoting the correlation matrix obtained without parameter b as C_b and likewise for the other parameters, the resulting matrices are

$$C_b = \begin{bmatrix} 1.000 & 0.027 & -0.006 \\ - & 1.000 & -0.008 \\ - & - & 1.000 \end{bmatrix},$$

$$C_c = \begin{bmatrix} 1.000 & 0.027 & 0.005 \\ - & 1.000 & 0.004 \\ - & - & 1.000 \end{bmatrix}, \tag{6.44}$$

$$C_{x_0} = \begin{bmatrix} 1.000 & 0.006 & 0.005 \\ - & 1.000 & -0.198 \\ - & - & 1.000 \end{bmatrix},$$

which suggests that all remaining parameters are identifiable when either b, c or x_0 is fixed.

One important final remark is that fixation of parameters reduces the degrees of freedom of the model and introduces a bias. For this example the relationship between b, c and x_0 makes it impossible to say which/that two parameters are identifiable. Since fixing one parameter effectively changes the model, it does not make sense to compare parameter values for x_0 for an optimization where a is fixed with another value obtained with b fixed. These two estimates of x_0 should not be expected to be similar as they are de facto parameters of different models.

6.4 Examples

To compare the performance of the local and global methods introduced in this chapter, they are applied to four different example problems of increasing complexity. The first three considers the effect called *aliasing* that occurs when oscillating signals are sampled at a low frequency, while the last example is the part of the heart rate model that describes the viscoelastic behavior of the arterial wall, the *Voigt-body model*.

6.4.1 Aliasing

Consider the function

$$f(t, \theta) = \sum_{k=1}^{p} \theta_k^2 \sin(2\pi k t). \tag{6.45}$$

If evaluation of the function is restricted to a certain rate, one may experience *aliasing*. Aliasing is when an oscillating signal is recorded at such a rate that the recorded signal appears to be oscillating at a lower frequency or not at all. While this example is nonlinear in the parameters θ_k, it is based on an example with linear aliasing in R. C. Smith 2014.

Assume that the function can be evaluated at n evenly spaced values $t_i = i\Delta t, i = 0, \ldots, n-1, \Delta t = \frac{1}{n-1}$ and that the parameters are restricted to the interval $(0, 1)$. It is clear that the parameters could be rescaled to obtain a system linear in the parameters. Using $n = 5$ means that the function can be observed/evaluated at the points $t = 0, 1/4, 1/2, 3/4, 1$. For $p = 4$ this results in the series shown in Figure 6.9. The figure shows that there is only two non-zero different basis functions with this resolution of evaluations, and hence it is unlikely that all four parameters can be identified. The other panels in Figure 6.9 shows the basis functions evaluated at resolutions $n-1 = \{8, 16\}$ and full resolution. From the figures it can be seen that only one parameter does not contribute to the model output for $n-1 = 8$ and that all parameters contribute for $n-1 = 16$. These three configurations will be analyzed using the methods presented in Section 6.3.

Local derivative based sensitivities.

The local sensitivities are given by

$$\frac{\partial f}{\partial \theta_k}(t, \theta) = 2\theta_k \sin(2\pi k t). \tag{6.46}$$

Since it has already been shown that the basis functions are linearly dependent if evaluated at $n = 5$ points, the sensitivities will also be linearly dependent. Therefore, it is known in advance that it is not possible to identify all parameters uniquely.
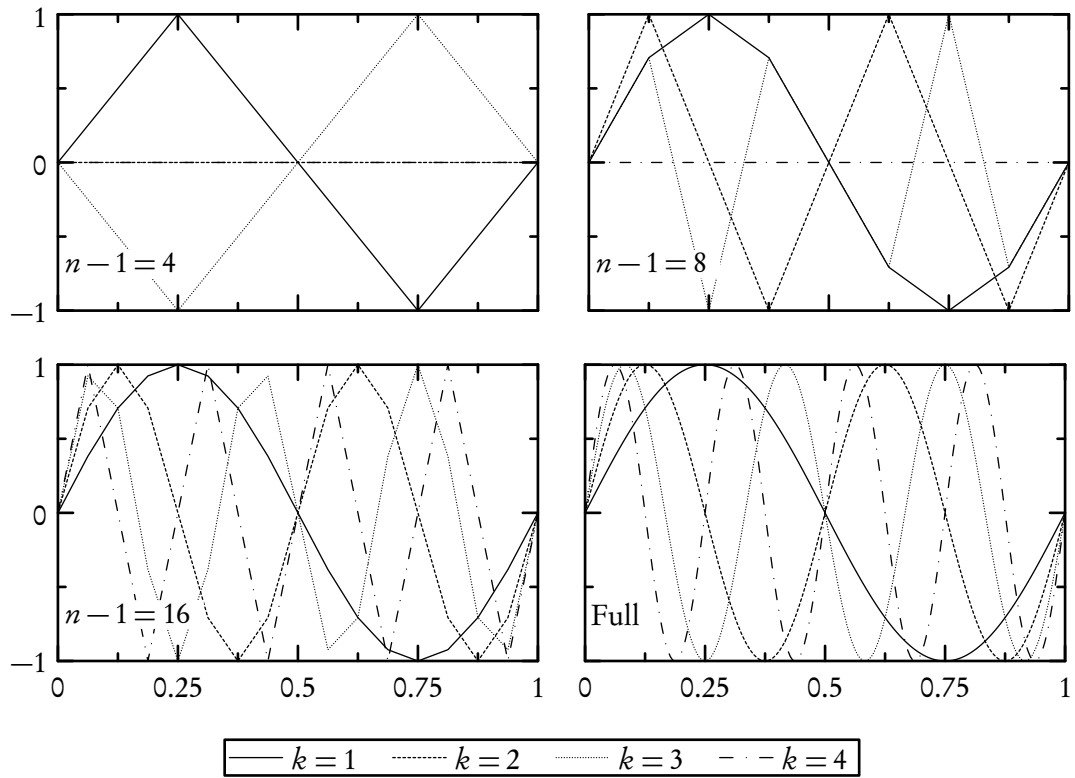
Figure 6.9: Basis function evaluated at $t = 0, 1/n, 2/n, \ldots, n-1/n, 1$ for the three measurement resolutions and full time series.

Table 6.6: Condition numbers for $S^T S$ for $n-1 = 4, 8, 16$. It is evident that the matrix is non-invertible unless $n-1 = 16$.

$n-1$	$\mathcal{K}\left(S^T S\right)$	Rank$\left(S^T S\right)$
4	2.7×10^{31}	1
8	1.5×10^{30}	3
16	1.0×10^{0}	4

Table 6.7: Correlation matrix for the system with $n-1 = 16$. No correlations are present, suggesting that there should be no problem with identifiability.

	θ_2	θ_3	θ_4
θ_1	-5.3×10^{-17}	-2.2×10^{-32}	-5.8×10^{-17}
θ_2		-8.6×10^{-17}	1.0×10^{-16}
θ_3			6.5×10^{-17}

Correlation method

Since there is a linear dependence between the four basis functions (two of them being zero), the Fisher information matrix $F = S^T S$ is not invertible, and therefore, the correlations cannot be calculated. Table 6.6 shows the condition numbers of the $F = S^T S$-matrix for different values of n. As the Fisher information matrix is invertible for $n-1 = 16$, the correlations can be calculated. They are shown in Table 6.7, and shows no correlations.

Orthogonal method.

Table 6.8 shows the rankings obtained using the orthogonal method for $n-1 = 4, 8, 16$. For $n-1 = 4$ only one parameter is found to be identifiable, while three are found identifiable for $n-1 = 8$, and all parameters are identifiable for $n-1 = 16$.

Global methods

Assume that parameters are uniformly distributed

$$\theta_i \sim \mathcal{U}(0, 1).$$

From the local analysis and arguments about the dimension of the spanned space, it is expected that

Table 6.8: Ranking obtained using the orthogonal method for $n-1=\{4,8,16\}$. For $n-1=4$ since the rank of the sensitivity matrix is 1, it is not meaningful to select more than one parameter. From the E-values, it is known that parameters θ_1 and θ_3 are identifiable, but not both at the same time. For $n-1=8$ the rank of the sensitivity matrix is 3, so it is sensible to choose only three parameters. The choice of $\theta_1, \theta_2, \theta_3$ is consistent with behavior of the basis functions. For $n-1=16$ the rank of the sensitivity matrix is 4, so all parameters are expected identifiable.

(a) $n-1=4$					(b) $n-1=8$					(c) $n-1=16$				
Rank	Par	d	e	I	Rank	Par	d	e	I	Rank	Par	d	e	I
1	θ_1	—	0.71	—	1	θ_1	—	0.47	—	1	θ_3	—	0.38	—
2	θ_3	0.00	0.71	0.00	2	θ_3	1.00	0.47	0.47	2	θ_2	1.00	0.37	0.37
3	θ_2	0.00	0.00	0.00	3	θ_2	1.00	0.33	0.33	3	θ_1	1.00	0.32	0.32
4	θ_4	0.00	0.00	0.00	4	θ_4	0.00	0.00	0.00	4	θ_4	1.00	0.29	0.29

parameters θ_2 and θ_4 are non-influential in the $n-1=4$ case, that θ_4 is non-influential for $n-1=8$, and that all parameters are influential for $n-1=16$. In addition it is expected that the effect of all influential parameters on the model output are similar in magnitude.

Sobol indices.

The estimated first order Sobol indices S_i^* and total effects S_{Ti}^* are listed in Table 6.9. As expected, for $n-1=4$ only θ_1 and θ_3 have an effect on the model output, while θ_2 and θ_4 have no effect. Also note that the total effect estimates S_{Ti}^* are similar for θ_1 and θ_3.

Likewise, for $n-1=8$ and $n-1=16$ the estimated indices match the expected behavior from the analysis of local sensitivities and the basis functions of the model.

Morris indices.

All parameters are expected to have equal sensitivities, due to equal weights and same mean value, and those that reduce to the same basis functions with the $n-1=4$ resolution to show some second or higher order effects. The resulting indices are shown in Table 6.9. The effects predicted by the two global methods are consistent.

6.4.2 Nonlinear aliasing revisited

Considering the aliasing example above but with $p=n=10$ results in global measures shown it Table 6.10. Both Sobol indices and Morris measures suggests that all parameters are equally sensitive except for θ_5 and θ_{10} that have no impact on the model output. This result is coherent with the

Table 6.9: Sobol and Morris indices for the parameters in example 1 with $m = 5$ and $n-1 = 4, 8, 16$ parameters. For $n-1 = 4$ both methods (correctly) estimates that parameters θ_2 and θ_4 are insignificant and that θ_1 and θ_3 have similar (actually equal) effect on the output. For $n-1 = 8$ both methods (correctly) estimates that θ_4 are insignificant and that θ_1, θ_2 and θ_3 have similar (actually equal) effect on the output. For $n-1 = 16$ both methods (correctly) estimates that all parameters are equally influential on model output.

$(n-1)$		θ_1	θ_2	θ_3	θ_4
4	S_i^*	0.22	−0.01	0.16	−0.01
	S_{Ti}^*	0.81	0.04	0.80	0.04
	μ_i^*	3.88	0.00	3.43	0.00
	σ_i^*	18.44	0.00	17.35	0.00
8	S_i^*	0.33	0.33	0.31	−0.02
	S_{Ti}^*	0.29	0.29	0.32	−0.06
	μ_i^*	9.92	10.83	10.52	0.00
	σ_i^*	83.73	90.08	87.42	0.00
16	S_i^*	0.24	0.24	0.25	0.25
	S_{Ti}^*	0.28	0.28	0.26	0.27
	μ_i^*	22.15	20.60	22.23	21.97
	σ_i^*	377.60	312.96	362.59	364.69

rankings obtained using OSM shown in Table 6.11. As indicated by these tables there are two parameters θ_5 and θ_{10} that does not contribute to the model output, and hence the Fisher information matrix is invertible, and correlations cannot be calculated using the SCM method.

6.4.3 Added interaction term

For the example with $p = 4, n-1 = 8$ the parameter θ_4 was non-influential, but $\theta_1, \theta_2, \theta_3$ were linearly independent, and should all be identifiable. Adding to the sum an interaction term $\theta_1\theta_4 \sin(2\pi t)$, gives the response-function

$$f(t, \theta) = \theta_1\theta_4 \sin(2\pi t) + \sum_{k=1}^{4} \theta_k^2 \sin(2\pi k t). \tag{6.47}$$

One would expect that θ_4 now has influence on the model output, but that a large part of the influence is through interaction. Sobol indices and Morris measures are shown in Table 6.12. Table 6.13 shows the ordering from OSM using parameter values $\theta_i = 1$. It is seen that the parameter θ_4 now has an impact ($E = 0.18$), but that it is does not contribute any dynamics that are not already represented by the other parameters (namely θ_1 that it is linearly dependent on). Again, since there is a linear

Table 6.10: Sobol indices obtained using Jansen's implementation and morris indices for $p = n - 1 = 10$.

	θ_1	θ_2	θ_3	θ_4	θ_5	θ_6	θ_7	θ_8	θ_9	θ_{10}
S_i^*	0.05	0.05	0.06	0.04	0.00	0.05	0.05	0.06	0.05	0.00
S_{Ti}^*	0.19	0.18	0.18	0.19	-0.02	0.17	0.18	0.17	0.20	-0.02
μ_i^*	9.78	8.83	9.25	8.90	0.00	8.82	9.96	8.88	9.22	0.00
σ_i^*	112.00	105.67	116.31	93.10	0.00	103.31	134.31	102.61	117.50	0.00

Table 6.11: Ratings obtained using OSM for $p = n - 1 = 10$.

Rank	Par	d	E	I
1	θ_2	—	0.36	—
2	θ_8	0.98	0.36	0.35
3	θ_4	1.00	0.30	0.30
4	θ_6	0.98	0.30	0.30
5	θ_1	0.97	0.25	0.24
6	θ_9	0.98	0.25	0.24
7	θ_7	0.92	0.23	0.21
8	θ_3	0.98	0.23	0.22
9	θ_{10}	0.00	0.00	0.00
10	θ_5	0.00	0.00	0.00

Table 6.12: Global measures obtained for linear aliasing with interaction term with $p = 4, n - 1 = 8$.

	θ_1	θ_2	θ_3	θ_4
S_i^*	0.61	0.09	0.09	0.08
S_{Ti}^*	0.73	0.13	0.13	0.20
μ_i^*	19.95	11.85	11.06	4.00
σ_i^*	298.03	87.54	93.07	18.81

Table 6.13: Ranking obtained for $p = 4, n - 1 = 8$ with interaction and parameter values $\theta_i = 1$. Compare to Table 6.8 for the same setup without interaction.

Rank	Par	d	E	I
1	θ_1	—	0.53	—
2	θ_3	1.00	0.22	0.22
3	θ_2	1.00	0.22	0.22
4	θ_4	0.00	0.18	0.00

dependence in the sensitivities, correlations cannot be calculated using the SCM method.

6.4.4 Viscoelastic Two-Voigt-body model

For the last example, consider the Two-Voigt-body model used to represent the viscoelastic strain of the baroreceptor neurons in the heart rate model. The model shown in Figure 4.5 consists of two Voigt-bodies in series with a spring, with each Voigt-body consisting of a dash-pot and a spring in parallel.

The model (4.6) is described by the two differential equations,

$$\frac{d\epsilon_1}{dt} = -(\alpha_1 + \alpha_2 + \beta_1)\epsilon_1 + (\beta_1 - \beta_2)\epsilon_2 + (\alpha_1 + \alpha_2)\epsilon_w$$
$$\frac{d\epsilon_2}{dt} = -\alpha_2\epsilon_1 - \beta_2\epsilon_2 + \alpha_2\epsilon_w. \tag{6.48}$$

Consider ϵ_2 as the model output, use the Heaviside function as the input $\epsilon_w = H$, and parameter values $\alpha_1 = 2, \alpha_2 = 1, \beta_1 = 2, \beta_2 = 0.4$. For the global methods, parameter values will be sampled on

Table 6.14: Sensitivity Indices for the two Voigt-body model. S_i^* and S_{Ti}^* are the first order and total Sobol indices, while μ and σ are the estimates for the mean and variance of the elementary effects of the Morris method.

	α_1	α_2	β_1	β_2
S_i^*	0.19	0.78	-0.16	-0.21
S_{Ti}^*	0.15	0.54	0.15	0.17
μ	0.05	0.09	0.05	0.05
σ_i	0.01	0.01	0.01	0.00

Table 6.15: Correlation matrix and OSM ranking for the two-Voigt body model.

(a) SCM correlations					(b) OSM ranking				
	α_1	α_2	β_1	β_2	Rank	Par	d	E	I
α_1	–	-0.90	-0.56	-0.91	1.00	β_2	–	0.97	–
α_2	-0.90	–	0.85	0.98	2.00	α_2	0.42	0.18	0.08
β_1	-0.56	0.85	–	0.75	3.00	α_1	0.23	0.04	0.01
β_2	-0.91	0.98	0.75	–	4.00	β_1	0.17	0.05	0.01

the intervals of $75-125\%$ of the nominal value, eg. $\alpha_1 \in 2 \times (0.75, 1.25)$ and so on. The model is solved for $t \in (0,5)$, with the heaviside function changing at $t = 0.5$. Parameters α_1, α_2 determine how the strain is distributed between the two Voigt bodies, while β_1, β_2 determine the relaxation time for each Voigt body.

The resulting sensitivities are depicted in Table 6.14, 6.15, and the local derivative based sensitivities are plotted in Figure 6.10. Results show that the different methods provide different results. While Mahdi, Meshkat, and Sullivant 2014 found that the model is structurally identifiable when regarding wall strain ϵ_w as model input and ϵ_1 as model output, the practical analysis suggests otherwise. Both the Sobol indices and OSM denotes β_1 as unidentifiable, while the Morris method finds that β_2 has the least influence on the model output and SCM finds a rather large correlation between α_1 and β_2.
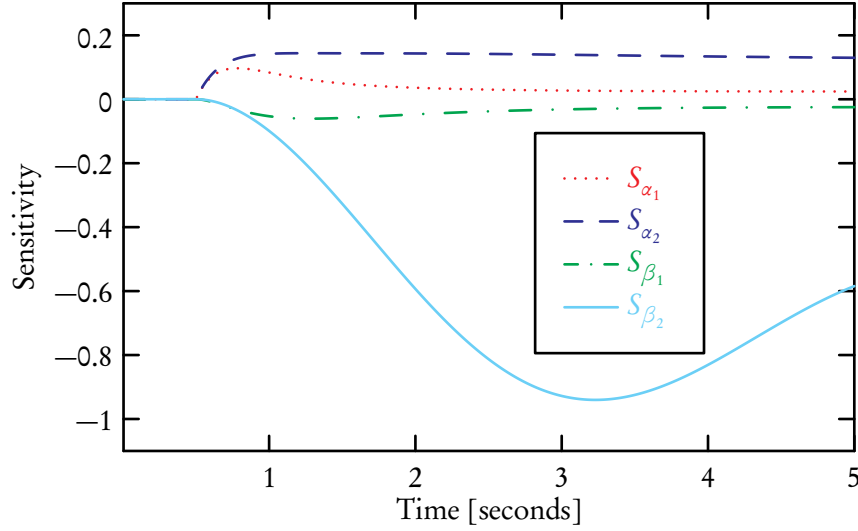
Figure 6.10: Sensitivities for the voigt body model.

6.5 Discussion

The concepts and differences of structural and practical identifiability have been introduced. Different methods for obtaining local sensitivity measures have been discussed, as well as two different methods for assessing global parameter influence on the model output. Namely, calculation of Sobol indices and the Morris method. For analysing local sensitivities and determine identifiability SCM and OSM has been introduced.

The different methods have been applied to examples of increasing complexity to study the feasibility of the methods and illustrate differences and similarities in the obtained results. For the most part the methods were found to have similar or comparable results, though with a few differences for the most complex example. From the examples investigated here it is not possible to decide which (combinations) of the four methods should be preferred, but a few differences can be highlighted. Sobol indices is considered to be very reliable, but the used algorithm assumes no interactions of degree higher than two (Saltelli, Annoni, et al. 2010), and still comes with a high computational cost. The Morris method provides comparable results for most of the examples considered here, but at a much smaller cost. The local methods approaches the subset selection procedure differently and deliver different results for the example where both can be applied. It is worth noting in this context that even though SCM will reveal the existence of correlations, it will not be able to do so for perfect correlations, as these will lead to linear dependent sensitivities and thereby a singular FIM. Therefore SCM might be challenged by over parametrized problems such as the example presented in Section 6.4.

Chapter 7

Uncertainty quantification

Uncertainty quantification is the process of determining parameter output uncertainties due to uncertainties in experimental measurements. Using a Bayesian framework, parameters can be described as random variables for which densities can be estimated and updated upon arrival of new information. Parameter densities can be used in the calculation of *credible intervals*, which can be propagated through the model to obtain uncertianty measurements in form of *prediction intervals*.

This is in opposition to parameter estimation in the frequentists framework where parameters are described by an estimate of the "true" value and a *confidence interval*. While the frequentists approach allows for calculation of confidence intervals for parameter estimates, confidence intervals does not represent the probability distribution of the parameter (Belia et al. 2005), and may not be viable as basis for estimation of model output uncertianties (R. C. Smith 2014).

When credible intervals have been found for parameters, these intervals can be propagated through the mathematical model to quantify uncertainties in model output. This process is known as *uncertainty propagation*. Several methods exist, but for problems with high dimensions and possible parameter interaction, sampling methods are usually preferred (R. C. Smith 2014). Sampling methods sample parameter configurations from the joint parameter density, find solutions for these configurations and build densities for the model output based on the results.

Using Markov Chain Monte Carlo methods parameter densities and model output densities can be computed simultaneously. The methods discussed here will be of this type.

This chapter gives a very brief introduction to Bayesian inference, motivates the use of Markov Chains to obtain estimate densities, and presents two Markov Chain Monte Carlo (MCMC) algorithms.

7.1 Bayesian inference

In the Bayesian framework, parameters are regarded as random variables $\Theta = \left[\Theta_1, \ldots, \Theta_p\right]$ and parameter estimation is thereby the process of estimating the distribution associated with the random variables. Given the observations $v = [v_1, \ldots, v_n]$, Bayes' formula,

$$\pi(\theta \mid v) = \frac{\pi(v \mid \theta)\,\pi_0(\theta)}{\pi_\Gamma(v)} \tag{7.1}$$

can be used to describe the relationship between the prior parameter density $\pi_0(\theta)$, the posterior density $\pi(\theta \mid v)$, the likelihood $\pi(v \mid \theta)$ of observing the data v for the model given θ, and the normalization factor (the marginal density) $\pi_\Gamma(v)$. Since $\pi_\Gamma(v)$ is a normalization constant it can be determined by $\pi_\Gamma(v) = \int \pi(v \mid \theta)\,\pi_0(\theta)\,\mathrm{d}\theta$. The result is often known as the *Bayes theorem for inverse problems*. For observations v_{obs}, the posterior density estimate is

$$\pi(\theta \mid v_{\mathrm{obs}}) = \frac{\pi(v_{\mathrm{obs}} \mid \theta)\,\pi_0(\theta)}{\int \pi(v_{\mathrm{obs}} \mid \theta)\,\pi_0(\theta)\,\mathrm{d}\theta}. \tag{7.2}$$

If the errors between the model output and measurements are normally and identically independently distributed (iid) random variables with mean $\mu = 0$ and variance σ^2, the likelihood function is

$$\pi(v \mid \theta) = L\left(v \mid \theta, \sigma^2\right) = \frac{1}{(2\pi\sigma^2)^{\frac{n}{2}}} e^{-\mathrm{SS}_\theta/2\sigma^2}, \quad \mathrm{SS}_\theta = \sum_{i=1}^{n} [v_i - f_i(\theta)]^2. \tag{7.3}$$

With the likelihood function given, it is possible to estimate the posterior density $\pi(\theta \mid v_{\mathrm{obs}})$ with the prior $\pi_0(\theta)$ if the integral in the denominator of (7.2) can be estimated. While this route is theoretically possible, the evaluation of high-dimensional integrals is a difficult and expensive task and methods for doing so is still an active research area including methods such as *sparse grids* (Smolyak 1963; Bungartz and Griebel 2004) and *quasi-Monte Carlo methods* (Halton 1960; Joe and Kuo 2003; Vandewoestyne and Cools 2006).

Another option for estimating the posterior density is by sampling directly from the density $\pi(v_{\mathrm{obs}} \mid \theta)\,\pi_0(\theta)$. Such sampling can be achieved using *Markov chain monte carlo* methods such as the *Metropolis algorithm* or the *Delayed Rejection Adaptive Metropolis* (DRAM).

7.2 Metropolis algorithm

If a chain of samples of a random variable is generated satisfying the Markov property such that the k'th value only depends on the $(k-1)$'th value, the sampled chain will follow the stationary distribution of the state space of the variable (in this application, the possible parameter configurations).

The method was originally developed by Metropolis et al. 1953 to describe the state of a physical system in the context of statistical mechanics.

Algorithm 4 *Metropolis Algorithm*

    1. Initialize the chain: Choose an initial value θ^0 that satisfies $\pi\left(\theta^0 \,|\, v\right) > 0$

    2. For $k = 2,\ldots,M$:

        (a) Sample $z \sim \mathcal{N}\left(0,1\right)$ and construct the new candidate

$$\theta^* = \theta^{k-1} + Rz, \tag{7.4}$$

        where R is the Cholesky decomposition of either the parameter covariance matrix estimator $V = \sigma^{-2}\left[S^T S\right]^{-1}$ (See Section 6.2.1), or a diagonal matrix D where each element denotes the scaling of the corresponding parameter. This guarantees that each component of the constructed candidate is normally distributed around the previous value,

$$\theta^* \sim \mathcal{N}\left(\theta^{k-1}, V\right).$$

        This also means that the proposal distribution is symmetric between the two states, such that the probability of proposing θ^* given θ^{k-1} is equal to the probability of proposing the value θ^{k-1} given a current value θ^*.

        (b) Compute the ratio of the likelihoods

$$r\left(\theta^* \,|\, \theta^{k-1}\right) = \frac{\pi\left(\theta^* \,|\, v\right)}{\pi\left(\theta^{k-1} \,|\, v\right)} = \frac{\pi\left(v \,|\, \theta^*\right)\pi_0\left(\theta^*\right)}{\pi\left(v \,|\, \theta^{k-1}\right)\pi_0\left(\theta^{k-1}\right)}. \tag{7.5}$$

        Note that the normalization constant $\int \pi\left(v \,|\, \theta\right)\pi_0\left(\theta\right) \mathrm{d}\theta$ is irrelevant.

        (c) Choose the next chain element

$$\theta^k = \begin{cases} \theta^* & \text{with probability } \alpha = \min\left(1, r\right), \\ \theta^{k-1} & \text{otherwise.} \end{cases} \tag{7.6}$$

        That is, if the likelihood of data given the new candidate is higher than for the current configuration, accept the candidate. Otherwise, accept the new candidate with a probability given by the ratio r.

Note: If a non-informative prior is chosen $\pi_0(\theta^*) = \pi_0(\theta^{k-1})$, and the assumption of normally

identical and independent distributed errors applied, the ratio is given by

$$r\left(\theta^* \mid \theta^{k-1}\right) = \frac{\pi(v \mid \theta^*)\pi_0(\theta^*)}{\pi(v \mid \theta^{k-1})\pi_0(\theta^{k-1})} = \frac{\pi(v \mid \theta^*)}{\pi(v \mid \theta^{k-1})} = \frac{e^{-\mathrm{SS}_{\theta^*}/2\sigma^2}}{e^{-\mathrm{SS}_{\theta k-1}/2\sigma^2}} = e^{-\left[\mathrm{SS}_{\theta^*}-\mathrm{SS}_{\theta k-1}\right]/2\sigma^2}. \quad (7.7)$$

7.3   Delayed rejection adaptive metropolis (DRAM)

DRAM combines two methods for improving efficiency of Metropolis-Hastings type (of which Metropolis algorithm is a simple variant) MCMC algorithms. These two ideas are delayed rejection and adaptive Metropolis. Delayed rejection allows the algorithm to try additional proposals per step if the initially proposed step is not accepted. This increases the acceptance rate and thereby mixing of the chain, which results in better estimates of the posterior densities. Adaptive metropolis allows the metropolis algorithm to update the covariance matrix based on the history of the chain. This helps the algorithm make better proposals, and move to the correct posterior distribution faster, reducing what is called the *burn-in* period.

Note that updating the proposal function using history of the chain breaks the Markov property, and other properties need to be established for guarantee sampling from the posterior distribution (Haario et al. 2006; R. C. Smith 2014). See Haario et al. 2006 for further information.

Haario et al. 2006 provide a `Matlab` toolbox for MCMC including DRAM at `http://helios.fmi.fi/~lainema/mcmc/`.

Algorithm 5 below introduces the algorithm except for the description of the delayed rejection step, which is is given in Algorithm 6.

Algorithm 5 *Delayed Rejection Adaptive Metropolis Algorithm (DRAM) with a uniform prior*

1. *Set design parameters $n_s, \sigma_s^2, k_0, s_d$ and wanted number of chain iterates M*

2. *Determine $\theta_0 = \arg\min_\theta \sum_{i=1}^N [v_i - f_i(\theta)]^2$*

3. *Compute the initial variance estimate: $s_0^2 = \frac{SS_{\theta 0}}{n-p}$*

4. *Construct covariance estimate $V = s_0^2 \left[S^T(\theta^0)S(\theta^0)\right]^{-1}$ and $R = chol(V)$*

5. *For $k = 1, \ldots, M$*

   (a) *Sample $z_k = \mathcal{N}(0,1)$*

   (b) *Construct candidate $\theta^* = \theta^{k-1} + Rz_k$*

   (c) *Sample $u_\alpha \sim \mathcal{U}(0,1)$*

   (d) *Compute the sum of squares $SS_{\theta^*} = \sum_{i=1}^N [v_i - f_i(\theta^*)]^2$*

(e) *Compute*

$$\alpha\left(\theta^*\mid\theta^{k-1}\right)=\min\left(1,e^{-\left[SS_{\theta^*}-SS_{\theta^{k-1}}\right]/2s_{k-1}^2}\right)$$

(f) *If $u_\alpha < \alpha$, Set*

$$\theta^k=\theta^*,SS_{\theta^k}=SS_{\theta^*}$$

Otherwise

Enter Delayed rejection algorithm

(g) *Update $s_k \sim$ Inv-Gamma (a_{val}, b_{val}), where*

$$a_{val}=\frac{1}{2}\left(n_s+n\right),b_{val}=\frac{1}{2}\left(n_s\sigma_s^2+SS_{\theta^k}\right).$$

(h) *if* $\mod(k,k_0)=1$ *then update*

$$V_k=s_d\,Cov\left[\theta^0,\theta^1,\ldots,\theta^k\right].$$

Otherwise

$$V_k=V_{k-1}.$$

(i) *Update $R_k = chol(V_k)$.*

Algorithm 6 *Delayed rejection algorithm for DRAM*

1. *Set the design parameter $\gamma_2 = \frac{1}{5}$*

2. *Sample $z_k \sim \mathcal{N}(0,1)$*

3. *Construct second-stage candidate $\theta^{*2}=\theta^{k-1}+\gamma_2 R_k z_k$*

4. *Sample $u_\alpha \sim \mathcal{U}(0,1)$*

5. *Compute $SS_{\theta^{*2}}=\sum_{i=1}^N\left[v_i-f_i\left(\theta^{*2}\right)\right]^2$*

6. *Compute*

$$\alpha_2\left(\theta^{*2}\mid\theta^{k-1},\theta^*\right)=\min\left(1,\frac{\pi\left(\theta^{*2}\mid v\right)J\left(\theta^*\mid\theta^{*2}\right)\left[I-\alpha\left(\theta^*\mid\theta^{*2}\right)\right]}{\pi\left(\theta^{k-1}\mid v\right)J\left(\theta^*\mid\theta^{k-1}\right)\left[I-\alpha\left(\theta^*\mid\theta^{k-1}\right)\right]}\right).$$

7. *If $u_a < \alpha$*

$$Set\ \theta^k=\theta^{*2},SS_{\theta^k}=SS_{\theta^{*2}}$$

otherwise

$$Set\ \theta^k=\theta^{k-1},SS_{\theta^k}=SS_{\theta^{k-1}}.$$

7.4 Practical challenges for MCMC

In application of the DRAM or other MCMC methods there are a few challenges that need to be addressed, specifically challenges related to the question of whether the chain has reached the target density and is sampling from the stationary distribution and how well it does so.

While the points sampled from a Markov chain will reflect the stationary distribution when the length approaches infinity, this creates some practical challenges. Usually the chain will take a while before converging and sampling from the correct areas of parameter space. The period for the chain to reach the range of the stationary distribution is typically called the *burn-in*, and samples from this period should be ignored to get a better estimate of the stationary distribution (Haario et al. 2006). The adaptive component of DRAM increases the speed at which the algorithm will reach the correct part of parameter space by dynamically adjusting the covariance matrix.

Another problem may arise due to incorrect or imprecise parameter variances, as they will greatly affect the rate of acceptance for the proposed steps. While the chain may be in the range of the stationary density, it may not sample well from it if proposed points are rejected due to incorrect large variances. An optimal acceptance rate should be around 30% (Haario et al. 2006). The delayed rejection component of DRAM helps in this regard, as it allows for generation of additional proposals with adjusted variances, in turn increasing the acceptance rate.

8

Simulations

The mathematical model presented in Chapter 4 has been implemented in *C* using the ode-solver Sundials Cvodes. Sundials is fast, able to solve stiff equations using backwards differentiation methods and provides built-in support for calculating local sensitivities using sensitivity equations with finite difference approximations to the Jacobian and the parameter Jacobian. While programming in C is cumbersome compared to Matlab or similar numerical methods, the gain in terms of computation time is significant. Calling and solving the ode using the C-code takes approximately 170ms, while an analogous implementation in Matlab takes over 30 seconds to solve the system using `ode15s`. The implementation in C thus allows for 150-200 times as many model evaluations in the same time frame as the corresponding implementation in Matlab.

The methods presented for identifiability analysis has been implemented as presented using `Python` with the libraries `Numpy` and `Scipy` for more advanced mathematical operations such as matrix operations, and linear algebra in general. For optimization the python library `lmfit` (`http://lmfit.github.io/lmfit-py/`) has been used, which include Levenberg-Marquardt and Nelder-Mead algorithms among others. For uncertainty quantification the MCMC toolbox for Matlab (`http://helios.fmi.fi/~lainema/mcmc/`), was used as it contains an implementation of the DRAM algorithm (Haario et al. 2006) discussed in Chapter 7. The same model implementations was used for all analysis by wrapping calls to the C-code in appropriate ways.

This chapter presents results for identifiability analysis, optimization and uncertainty quantification, as well as a brief discussion of the results. Methods for identifiability analysis discussed earlier, is used for subset selection for the heart rate model presented in Chapter 4. Found subsets are used for parameter optimization, and in turn uncertainty quantification.

8.1 Identifiability analysis

The goal is to find a subset of parameters that can be estimated given the model and available data. As discussed in Chapter 6 there is not "one" correct way to do this. Several methods exists, each with a set of advantages and disadvantages. However, good subsets should fulfill the following requirements:

Sensitivity: The model output should be sensitive to changes in model parameters. Non-influential parameters may cause problems for some optimization algorithms.

Identifiability: The model parameters should be identifiable, and contain no parameters for which the impact on model output caused by a change in one parameter, can be counteracted by a change in others.

Dynamics: The subset should restrict possible model output dynamics as little as possible. It is important that the model is still able to reflect the modeled dynamics.

First feasible parameter intervals will be determined for the global analysis. Next, two strategies will be applied for building identifiable parameter sets:

Strategy 1: Four sets will be build, one for each of OSM, SCM, the Morris and the Sobol method.

Strategy 2: The three sensitivity methods, two-norm of local derivative based sensitivities, Morris and Sobol methods, are used for removing insensitive parameters, and the remaining parameters are analyzed using OSM and SCM to build identifiable parameter sets.

Finally the different parameter sets will be tested by optimizing model output against synthetic data generated using the model with known parameter values. Section 8.2 will build on the results from this section by using suggested subsets for optimization against experimental data.

8.1.1 Parameters

Parameters of the heart rate model is listed in Table 8.1 with preliminary lower and upper bounds. The preliminary bounds are chosen such that the maximum allowed value is approximately double and the minimum value approximately half of the nominal values described in Chapter 4. As established in Chapter 5 model state positivity can be established by restrictions on parameters. Due to the formulation of model equations, unphysical behavior such as negative nerve firing frequency will lead to numerical problems, which in turn will prevent the ode solver from finding a solution. However, parameter constraints guaranteeing positive solutions are not trivial to include for the global sensitivity methods presented in Chapter 6.1. An alternative approach for guaranteeing proper model behavior is to adjust parameter intervals such that the model can be solved for any sampled parameter configuration.

To investigate the parameter intervals $30,000$ different parameter configurations was sampled using a uniform distribution over the parameter intervals. $2,714$ of these parameter configurations,

Table 8.1: Parameters for the heart rate model with unadjusted minimum and maximum bounds for global sensitivity analysis.

Name	Min	Max	Name	Min	Max
p_0	–	–	β_m	0.30	1.20
k	1.00	5.00	β_M	0.65	2.70
A_{m0}	1.00	5.00	β_k	5.00	5.00
α_1	0.35	1.50	$f_{r,t}$	0.15	0.60
α_2	0.05	0.20	k_r	5.00	5.00
β_1	1.00	4.00	t_d	–	–
β_2	0.25	1.00	τ_A	0.10	0.40
s_1	1.00	5.00	q_p	2.50	10.00
s_2	0.10	0.50	k_{iN}	0.25	1.00
T_{pm}	0.10	0.40	τ_N	4.00	20.00
ξ	1.00	15.00	q_s	0.05	0.25
f_p	0.2	0.75	μ	0.30	0.95
T_{sm}	0.10	0.50	K_A	–	–
η	1.00	15.00	τ_{AS}	1.00	4.00
f_s	0.2	0.75	τ_{NS}	1.20	5.00
ϕ_f	$\pi/6$	$\pi/6$	K_N	–	–
α_m	0.20	0.80	h_0	60.00	120.00
α_M	0.30	1.20	h_m	20.00	80.00
α_k	5.00	5.00	h_M	80.00	140.000

corresponding to 9% of tested configurations, leading to solver break down was recorded, and the distributions for each parameter in this set was investigated. Table 8.2 shows quartiles for each parameter, linearly scaled to the interval $[0, 1]$.

Values for parameters with no influence on breaking the solver should follow the underlying uniform distribution. Results in Table 8.2 show that parameters k, A_{M0}, α_1 and s_1 are overrepresented in the high end of their intervals, as their mean values (indicated by the blue bar) is significantly larger than $1/2$, while β_1, s_2 are overrepresented in the low end of the interval. α_2 and β_2 also deviates from the mean, but since their deviations are smaller, this could be an effect due to interaction with some of other mentioned parameters. To determine a better interval for these parameters it is beneficial to look at a histogram of the sampled points, such as the one shown in Figure 8.1 for s_2. Adjusting the
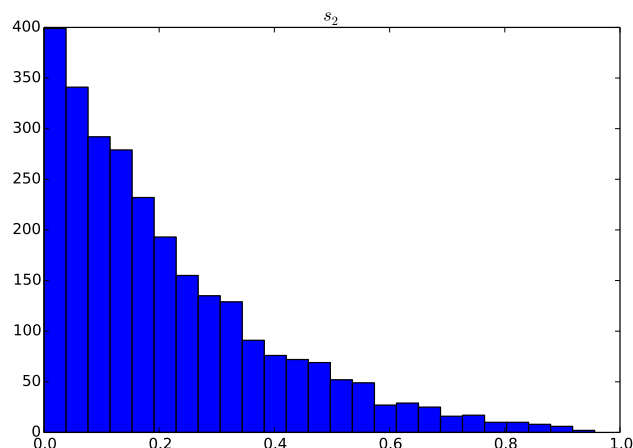
Figure 8.1: Histogram for failed values of s_2, scaled to the interval $[0, 1]$

parameter intervals leads to the intervals shown in Table 8.3. Running a similar test for the updated intervals reveals that 185 parameter configurations, corresponding to 0.6%, lead to the numerical solver breaking down.

8.1.2 Each method by itself

To facilitaty a comparisson of the different methods for subset selection a fixed size for subsets were set. The cut-off for the different methods are a bit different, but judging from the sensitivy rakings in Figure 8.2 the different rankings experienced a decline around 16-17 parameters, leading to the choice

Table 8.2: Distribution for each parameter for the configurations that caused the solver to fail, as well as new interval boundaries. The blue dot shows the median, while each end of the bar shows the 25% and 75% percentile respectively. The dashed lines shows the expected median and quartiles for parameter not influencing the outcome, while the dotted lines show the 37.5% and 62.5% percentile. Note that quartiles have been linearly scaled to the interval $[0, 1]$.

Parameter	Quartiles	Adjusted low	Adjusted high
k		1	4
A_{M0}		1	4
α_1		0.35	1.25
α_2		$5 \cdot 10^{-2}$	0.2
β_1		1.5	4
β_2		0.25	1
s_1		1	4
s_2		0.15	0.5
T_{pm}		0.1	0.4
ξ		1	15
f_p		0.2	0.75
T_{sm}		0.1	0.5
η		1	15
f_s		0.2	0.75
α_m		0.2	0.8
α_M		0.3	1.2
k_α		5	5
β_m		0.3	1.2
β_M		0.65	2.7
k_β		5	5
τ_A		0.1	0.4
q_p		2.5	10
k_{iN}		0.25	1
τ_N		4	20
q_s		$5 \cdot 10^{-2}$	0.25
μ		0.3	0.95
τ_{AS}		1	4
τ_{NS}		1.2	5
h_0		60	120
h_m		20	80
h_M		80	140
$f_{r,t}$		0.15	0.6
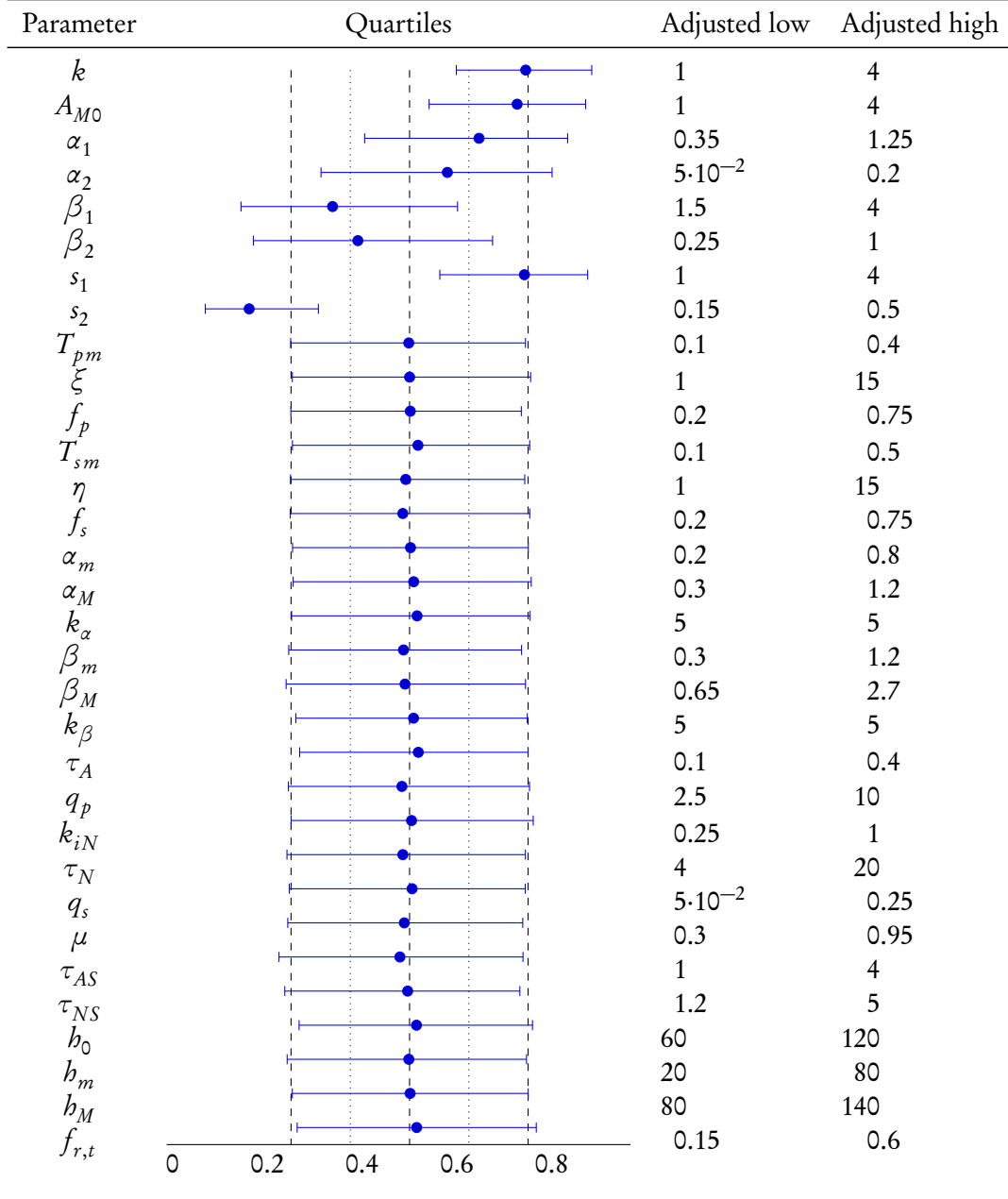
Table 8.3: Parameters for the heart rate model with adjusted bounds.

Name	Min	Max	Name	Min	Max
p_0	–	–	β_m	0.30	1.20
k	1.00	4.00	β_M	0.65	2.70
A_{m0}	1.00	4.00	β_k	5.00	5.00
α_1	0.35	1.25	$f_{r,t}$	0.15	0.60
α_2	0.05	0.20	k_r	5.00	5.00
β_1	1.50	4.00	t_d	–	–
β_2	0.25	1.00	τ_A	0.10	0.40
s_1	1.00	4.00	q_p	2.50	10.00
s_2	0.15	0.50	k_{iN}	0.25	1.00
T_{pm}	0.10	0.40	τ_N	4.00	20.00
ξ	1.00	15.00	q_s	0.05	0.25
f_p	0.2	0.75	μ	0.30	0.95
T_{sm}	0.10	0.50	K_A	–	–
η	1.00	15.00	τ_{AS}	1.00	4.00
f_s	0.2	0.75	τ_{NS}	1.20	5.00
ϕ_f	$\pi/6$	$\pi/6$	K_N	–	–
α_m	0.20	0.80	h_0	60.00	120.00
α_M	0.30	1.20	h_m	20.00	80.00
α_k	5.00	5.00	h_M	80.00	140.000

of subset size of 17.

Sobol Indices

Using the parameter intervals shown in Table 8.3 to calculate Sobol indices leads to the ranking shown in Table 8.4. Figure 8.2 shows a graphic illustration of the values. Parameter values with a ratio of Sobol Indice to the most influential parameter, h_0, lower than 1×10^{-2} is considered noninfluential, in accordance with the choice of subsets containing 17 parameters.

Morris Indices

Using the parameter intervals shown in Table 8.1 to calculate the Morris indices leads to the ranking shown in Table 8.4. Figure 8.2 shows a graphic illustration of the values.

SCM

Relative local sensitivities were calculated using the nominal parameters values given in Chapter 4. Figure 8.2 shows the two norms found for the relative sensitivities. The subset reduction process are given in Table 8.5. Choosing 17 parameters results in the subset

$$\theta_{SCM} = \left\{ k, A_{M0}, \alpha_1, \alpha_2, \beta_1, f_p, T_{sm}, \alpha_M, \beta_M, q_p, \tau_N, \mu, \tau_{AS}, \tau_{NS}, h_0, h_M, f_{r,t} \right\}. \tag{8.1}$$

The condition number of the FIM formed with the remaining parameters is $\sim 1.3 \times 10^7$.

OSM

The rankings obtained using the OSM method is shown in Table 8.6. Choosing 17 parameters results in the subset

$$\theta_{OSM} = \left\{ k, \beta_1, T_{pm}, f_p, f_s, \alpha_M, \beta_m, \beta_M, \tau_A, q_p, \tau_N, q_s, \mu, h_0, h_m, h_M, f_{r,t} \right\} \tag{8.2}$$

The condition number of the corresponding FIM matrix is $\sim 1.6 \times 10^6$. Note that even though this subset contains 17 parameters, the orthogonality index goes to 0 very quickly, suggesting that perhaps the subset should be even smaller.

Discussion

From Figure 8.2 it is clear that the ranking from the two global methods show similar tendencies in the ranking. While all methods rank the parameters, none of them suggests how big of a subset would be preferable. A few things are worth considering: A specific value of correlation for SCM will determine the size of a subset, as will a specific cut-off value for OSM. In addition Figure 8.2 shows

Table 8.4: Ordering of parameters using the four different methods. Parameters below the horizontal line were not selected by the corresponding method.

Rank	Morris	Sobol	OSM	SCM	Two-norm	S2value
1	h_0	h_0	h_0	h_0	h_0	1
2	h_m	h_m	$f_{r,t}$	τ_{NS}	h_m	0.65
3	h_M	$f_{r,t}$	f_p	τ_{AS}	A_{M0}	0.52
4	$f_{r,t}$	h_M	f_s	A_{M0}	q_p	0.48
5	β_M	s_1	α_M	τ_N	$f_{r,t}$	0.47
6	A_{M0}	α_M	h_m	q_p	f_p	0.47
7	k	s_2	β_m	h_M	s_1	0.46
8	α_M	A_{M0}	τ_N	k	τ_A	0.45
9	μ	β_M	μ	T_{sm}	s_2	0.44
10	s_2	β_1	τ_A	α_M	f_s	0.43
11	β_m	μ	k	α_1	h_M	0.34
12	α_m	β_2	q_p	α_2	τ_N	0.33
13	β_1	α_2	q_s	β_1	q_s	0.33
14	f_s	η	β_M	f_p	μ	0.23
15	s_1	k	h_M	β_M	α_M	0.2
16	β_2	f_s	β_1	μ	β_M	0.16
17	T_{sm}	α_m	T_{pm}	$f_{r,t}$	α_m	0.13
18	η	f_p	η	τ_A	β_m	0.11
19	α_2	β_m	A_{M0}	k_{iN}	α_1	0.11
20	f_p	τ_A	α_1	q_s	β_1	0.11
21	τ_N	τ_{NS}	τ_{AS}	T_{pm}	T_{pm}	$6.52 \cdot 10^{-2}$
22	ξ	τ_{AS}	β_2	β_2	α_2	$5.77 \cdot 10^{-2}$
23	α_1	ξ	ξ	ξ	β_2	$5.77 \cdot 10^{-2}$
24	T_{pm}	T_{pm}	T_{sm}	s_1	k	$5.56 \cdot 10^{-2}$
25	q_s	T_{sm}	k_{iN}	η	T_{sm}	$4.83 \cdot 10^{-2}$
26	k_{iN}	k_{iN}	α_2	α_m	ξ	$3.6 \cdot 10^{-2}$
27	τ_{AS}	α_1	s_2	f_s	k_{iN}	$3.35 \cdot 10^{-2}$
28	τ_A	q_s	τ_{NS}	s_2	η	$2.22 \cdot 10^{-2}$
29	q_p	q_p	s_1	h_m	τ_{AS}	$4.78 \cdot 10^{-3}$
30	τ_{NS}	τ_N	α_m	β_m	τ_{NS}	$2.18 \cdot 10^{-3}$

Table 8.5: Subset selection result from SCM. This table shows which parameter was removed fixed in each step.

SCM

Step	Correlation	Par A	Par B	Sens A	Sens B	Result
1	1	β_M	β_m	0.16	0.11	Fix β_m
2	0.99	h_0	h_m	1	0.65	Fix h_m
3	-0.99	s_1	s_2	0.46	0.44	Fix s_2
4	1	f_p	f_s	0.47	0.43	Fix f_s
5	0.98	α_M	α_m	0.2	0.13	Fix α_m
6	0.94	T_{sm}	η	$4.83 \cdot 10^{-2}$	$2.22 \cdot 10^{-2}$	Fix η
7	-0.96	A_{M0}	s_1	0.52	0.46	Fix s_1
8	-0.97	ξ	k	$3.6 \cdot 10^{-2}$	$5.56 \cdot 10^{-2}$	Fix ξ
9	0.92	β_2	α_2	$5.77 \cdot 10^{-2}$	$5.77 \cdot 10^{-2}$	Fix β_2
10	0.88	h_M	T_{pm}	0.34	$6.52 \cdot 10^{-2}$	Fix T_{pm}
11	-0.86	τ_N	q_s	0.33	0.33	Fix q_s
12	-0.9	τ_N	k_{iN}	0.33	$3.35 \cdot 10^{-2}$	Fix k_{iN}
13	-0.94	q_p	τ_A	0.48	0.45	Fix τ_A
14	-0.85	q_p	$f_{r,t}$	0.48	0.47	Fix $f_{r,t}$
15	0.85	h_0	μ	1	0.23	Fix μ
16	0.83	β_M	α_M	0.16	0.2	Fix β_M
17	0.82	f_p	A_{M0}	0.47	0.52	Fix f_p
18	0.73	α_1	β_1	0.11	0.11	Fix β_1
19	-0.81	α_2	α_1	$5.77 \cdot 10^{-2}$	0.11	Fix α_2
20	0.9	A_{M0}	α_1	0.52	0.11	Fix α_1
21	-0.89	α_M	A_{M0}	0.2	0.52	Fix α_M
22	-0.82	τ_N	T_{sm}	0.33	$4.83 \cdot 10^{-2}$	Fix T_{sm}
23	-0.7	h_M	k	0.34	$5.56 \cdot 10^{-2}$	Fix k
24	0.7	h_M	q_p	0.34	0.48	Fix h_M
25	0.78	h_0	q_p	1	0.48	Fix q_p
26	0.65	τ_N	A_{M0}	0.33	0.52	Fix τ_N
27	0.98	A_{M0}	h_0	0.52	1	Fix A_{M0}
28	-0.2	τ_{AS}	h_0	$4.78 \cdot 10^{-3}$	1	Fix τ_{AS}
29	$3 \cdot 10^{-2}$	h_0	τ_{NS}	1	$2.18 \cdot 10^{-3}$	Fix τ_{NS}
30	—			0	0	Last parameter h_0.

Table 8.6: Ranking of heart rate model parameters using OSM. The horizontal line denotes the cut off between identifiable and nonidentifiable parameters.

<div align="center">

OSM

Rank	Par	d	E	I
1	h_0	0	0.52	0
2	$f_{r,t}$	0.43	0.24	0.1
3	f_p	0.31	0.24	$7.45 \cdot 10^{-2}$
4	f_s	0.19	0.22	$4.17 \cdot 10^{-2}$
5	α_M	0.23	$8.77 \cdot 10^{-2}$	$2.04 \cdot 10^{-2}$
6	h_m	$5.58 \cdot 10^{-2}$	0.33	$1.86 \cdot 10^{-2}$
7	β_m	0.31	$4.87 \cdot 10^{-2}$	$1.52 \cdot 10^{-2}$
8	τ_N	$8.16 \cdot 10^{-2}$	0.17	$1.38 \cdot 10^{-2}$
9	μ	$9.63 \cdot 10^{-2}$	0.12	$1.16 \cdot 10^{-2}$
10	τ_A	$2.79 \cdot 10^{-2}$	0.23	$6.43 \cdot 10^{-3}$
11	k	0.21	$2.61 \cdot 10^{-2}$	$5.56 \cdot 10^{-3}$
12	q_p	$1.24 \cdot 10^{-2}$	0.25	$3.07 \cdot 10^{-3}$
13	q_s	$1.31 \cdot 10^{-2}$	0.17	$2.22 \cdot 10^{-3}$
14	β_M	$2.77 \cdot 10^{-2}$	$7.13 \cdot 10^{-2}$	$1.98 \cdot 10^{-3}$
15	h_M	$6.78 \cdot 10^{-3}$	0.18	$1.19 \cdot 10^{-3}$
16	β_1	$1.95 \cdot 10^{-2}$	$5.64 \cdot 10^{-2}$	$1.1 \cdot 10^{-3}$
17	T_{pm}	$2.75 \cdot 10^{-2}$	$3.29 \cdot 10^{-2}$	$9.03 \cdot 10^{-4}$
18	η	$7.21 \cdot 10^{-2}$	$1.12 \cdot 10^{-2}$	$8.1 \cdot 10^{-4}$
19	A_{M0}	$2.74 \cdot 10^{-3}$	0.27	$7.42 \cdot 10^{-4}$
20	α_1	$5.93 \cdot 10^{-3}$	$5.65 \cdot 10^{-2}$	$3.35 \cdot 10^{-4}$
21	τ_{AS}	0.43	$6.57 \cdot 10^{-4}$	$2.85 \cdot 10^{-4}$
22	β_2	$7.58 \cdot 10^{-3}$	$3 \cdot 10^{-2}$	$2.28 \cdot 10^{-4}$
23	ξ	$1.29 \cdot 10^{-2}$	$1.62 \cdot 10^{-2}$	$2.1 \cdot 10^{-4}$
24	T_{sm}	$4.03 \cdot 10^{-3}$	$2.48 \cdot 10^{-2}$	$1 \cdot 10^{-4}$
25	k_{iN}	$4.18 \cdot 10^{-3}$	$1.72 \cdot 10^{-2}$	$7.21 \cdot 10^{-5}$
26	α_2	$2.06 \cdot 10^{-3}$	$3 \cdot 10^{-2}$	$6.19 \cdot 10^{-5}$
27	s_2	$2.25 \cdot 10^{-4}$	0.23	$5.11 \cdot 10^{-5}$
28	τ_{NS}	0.22	$1.31 \cdot 10^{-4}$	$2.83 \cdot 10^{-5}$
29	s_1	$1.49 \cdot 10^{-8}$	0.24	$3.55 \cdot 10^{-9}$
30	α_m	$2.11 \cdot 10^{-8}$	$5.55 \cdot 10^{-2}$	$1.17 \cdot 10^{-9}$

</div>

Table 8.7: Ordering and relative change in sensitivity per step down the ordering ladder.

Sobol/Morris/2-norm ordering

Rank	Sobol	Si	Si_j/Si_{j-1}	Morris	μ	μ_j/μ_{j-1}	Par	$\bar{S}$	$\bar{S}_j/\bar{S}_{j-1}$
1	h_0	0.14	0	h_0	295.53	0	h_0	1	0
2	h_m	0.53	0.46	h_m	310.36	0.66	h_m	0.65	0.65
3	$f_{r,t}$	$2.73 \cdot 10^{-2}$	0.39	h_M	35.62	0.58	A_{M0}	0.52	0.81
4	h_M	0.18	0.83	$f_{r,t}$	84.81	0.91	q_p	0.48	0.92
5	s_1	0.33	0.56	β_M	202.27	0.71	$f_{r,t}$	0.47	0.99
6	α_M	0.23	0.87	A_{M0}	128.37	0.9	f_p	0.47	0.99
7	s_2	0.72	0.95	k	139.53	0.95	s_1	0.46	0.98
8	A_{M0}	0.6	0.88	α_M	218.31	0.88	τ_A	0.45	0.98
9	β_M	$4.42 \cdot 10^{-2}$	0.93	μ	21.96	0.89	s_2	0.44	0.97
10	β_1	$4.63 \cdot 10^{-2}$	0.67	s_2	37.11	0.94	f_s	0.43	1
11	μ	$8.12 \cdot 10^{-2}$	0.75	β_m	70.69	0.98	h_M	0.34	0.79
12	β_2	$3.86 \cdot 10^{-2}$	0.94	α_m	99.99	0.96	τ_N	0.33	0.96
13	α_2	0.14	0.78	β_1	90.06	0.99	q_s	0.33	1
14	η	0.14	0.77	f_s	195.76	0.97	μ	0.23	0.71
15	k	$8.85 \cdot 10^{-2}$	0.99	s_1	204.62	0.71	α_M	0.2	0.84
16	f_s	0.63	0.98	β_2	261.24	0.92	β_M	0.16	0.83
17	α_m	$8.04 \cdot 10^{-2}$	0.65	T_{sm}	213.13	0.78	α_m	0.13	0.78
18	f_p	0.49	0.92	η	343.36	0.9	β_m	0.11	0.86
19	β_m	$5.2 \cdot 10^{-2}$	0.99	α_2	10.03	0.94	α_1	0.11	0.99
20	τ_A	$1.82 \cdot 10^{-2}$	0.65	f_p	9.51	0.83	β_1	0.11	1
21	τ_{NS}	$3.09 \cdot 10^{-2}$	0.9	τ_N	15.9	0.66	T_{pm}	$6.52 \cdot 10^{-2}$	0.6
22	τ_{AS}	$1.69 \cdot 10^{-2}$	1	ξ	46.6	0.8	α_2	$5.77 \cdot 10^{-2}$	0.89
23	ξ	$1.86 \cdot 10^{-2}$	0.99	α_1	18.88	0.96	β_2	$5.77 \cdot 10^{-2}$	1
24	T_{pm}	0.25	0.95	T_{pm}	232.26	0.62	k	$5.56 \cdot 10^{-2}$	0.96
25	T_{sm}	$4.69 \cdot 10^{-2}$	0.87	q_s	10.2	0.86	T_{sm}	$4.83 \cdot 10^{-2}$	0.87
26	k_{iN}	$4.69 \cdot 10^{-2}$	0.8	k_{iN}	6.43	0.84	ξ	$3.6 \cdot 10^{-2}$	0.74
27	α_1	8.76	0.88	τ_{AS}	1,397.23	0.64	k_{iN}	$3.35 \cdot 10^{-2}$	0.93
28	q_s	4	0.68	τ_A	918.29	0.98	η	$2.22 \cdot 10^{-2}$	0.66
29	q_p	1.29	0.98	q_p	532.41	0.95	τ_{AS}	$4.78 \cdot 10^{-3}$	0.22
30	τ_N	1.55	0.93	τ_{NS}	483.69	0.68	τ_{NS}	$2.18 \cdot 10^{-3}$	0.46

that at certain points the value of the Sobol indices jump more than others. For example, choosing the cut-off at 13 parameters seems less than optimal for the ranking from Morris indices, a little better for the Sobol indices, and fine for the sensitivity two-norm.

Considering the first 17 parameters of the ranking from the Morris and Sobol methods, 15 parameters are chosen by both methods

$$\left\{k, A_{M0}, \beta_1, \beta_2, s_1, s_2, f_s, \alpha_m, \alpha_M, \beta_M, \mu, h_0, h_m, h_M, f_{r,t}\right\}. \tag{8.3}$$

The parameters that were chosen by one methods but not the other was $\{\alpha_2, \eta\}$ for Sobol and $\{\beta_m, T_{sm}\}$ for Morris.

Likewise, considering the first 17 parameters of the ranking from OSM and SCM, 11 parameters appear in both sets

$$\left\{k, \beta_1, f_p, \alpha_M, \beta_M, q_p, \tau_N, \mu, h_0, h_M, f_{r,t}\right\}. \tag{8.4}$$

The parameters that were chosen by only one of the two methods was for OSM $\left\{f_s, T_{pm}, \beta_m, \tau_A, q_s, h_m\right\}$ and for SCM $\{A_{M0}, \alpha_1, \alpha_2, T_{sm}, \tau_{AS}, \tau_{NS}\}$.

Comparing the two local methods we noted that parameters unique to one method compared to the other appear in similar parts of the model. For example, the parameter τ_A chosen by OSM likely have a similar effect on the model output as τ_{AS} chosen by SCM. However, if one fixes τ_A and runs OSM again, it does not select τ_{AS}. Likewise, fixing τ_{AS} and running SCM again does not result in a subset containing τ_A. For the remaining difference in the subsets there is no apparent connection. While SCM favors some parameters from the early parts of the model $\{A_{M0}, \alpha_1, \alpha_2\}$, OSM seems to favor parameters related to the respiratory input β_m and the sympathetic chain $\{f_s, q_s\}$.

Figure 8.3 shows how many times each parameter was selected by the four methods when prompted with the task of choosing the 17 most identifiable parameters. Subsets are created based on the frequency at which parameters were selected by the four methods. If $\theta_{n/4}$ describes the subset of parameters selected n times of the four methods, then

$$\begin{aligned} \theta_{4/4} &= \{k, \beta_1, \alpha_M, \beta_M, \mu, h_0, h_M\}, \\ \theta_{3/4} &= \left\{k, A_{M0}, \beta_1, f_s, \alpha_M, \beta_M, \mu, h_0, h_m, h_M, f_{r,t}\right\}, \\ \theta_{2/4} &= \left\{k, A_{M0}, \alpha_2, \beta_1, \beta_2, s_1, s_2, f_p, f_s, \alpha_M, \beta_m, \beta_M, q_p, \tau_N, \mu, h_0, h_m, h_M, f_{r,t}\right\}. \end{aligned} \tag{8.5}$$

These subsets have respectively 7, 12 and 20 parameters, and the condition numbers for FIM are 3.0×10^5 for $\theta_{4/4}$, 3.4×10^7 for $\theta_{3/4}$ and 5.5×10^9 for $\theta_{2/4}$.

Table 8.8: Ranking of heart rate model parameters using OSM for the Sobol ranking based subset.

		OSM		
Rank	Par	d	E	I
1	h_0	0	0.59	0
2	$f_{r,t}$	0.43	0.28	0.12
3	A_{M0}	0.22	0.31	$6.95 \cdot 10^{-2}$
4	α_M	0.37	0.1	$3.73 \cdot 10^{-2}$
5	f_s	$9.24 \cdot 10^{-2}$	0.26	$2.39 \cdot 10^{-2}$
6	h_m	$5.82 \cdot 10^{-2}$	0.38	$2.24 \cdot 10^{-2}$
7	β_M	0.16	$8.38 \cdot 10^{-2}$	$1.37 \cdot 10^{-2}$
8	μ	$9.53 \cdot 10^{-2}$	0.14	$1.32 \cdot 10^{-2}$
9	k	0.27	$2.96 \cdot 10^{-2}$	$8.06 \cdot 10^{-3}$
10	h_M	$2.39 \cdot 10^{-2}$	0.2	$4.86 \cdot 10^{-3}$
11	β_1	$3.03 \cdot 10^{-2}$	$6.52 \cdot 10^{-2}$	$1.98 \cdot 10^{-3}$
12	s_1	$4.53 \cdot 10^{-3}$	0.27	$1.25 \cdot 10^{-3}$
13	η	$8.07 \cdot 10^{-2}$	$1.29 \cdot 10^{-2}$	$1.04 \cdot 10^{-3}$
14	s_2	$2.21 \cdot 10^{-3}$	0.26	$5.79 \cdot 10^{-4}$
15	β_2	$1.14 \cdot 10^{-2}$	$3.47 \cdot 10^{-2}$	$3.94 \cdot 10^{-4}$
16	α_2	$3.07 \cdot 10^{-3}$	$3.47 \cdot 10^{-2}$	$1.07 \cdot 10^{-4}$

8.1.3 Combination of global and local methods

The next strategy involves using the different sensitivity ranking methods to select parameters that are influential and subsequently use the local methods OSM and SCM to determine an identifiable subset from this reduced set. The different ranking methods selects the parameters

$$\theta_{\text{sobol}} = \left\{ k, A_{M0}, \alpha_2, \beta_1, \beta_2, s_1, s_2, \eta, f_s, \alpha_M, \beta_M, \mu, h_0, h_m, h_M, f_{r,t} \right\},$$
$$\theta_{\text{morris}} = \left\{ k, A_{M0}, \beta_1, \beta_2, s_1, s_2, f_s, \alpha_m, \alpha_M, \beta_m, \beta_M, \mu, h_0, h_m, h_M, f_{r,t} \right\}, \tag{8.6}$$
$$\theta_{\bar{S}} = \left\{ A_{M0}, s_1, s_2, f_p, f_s, \alpha_M, \beta_M, \tau_A, q_p, \tau_N, q_s, \mu, h_0, h_m, h_M, f_{r,t} \right\}.$$

The OSM and SCM rankings are shown in Tables 8.8 and 8.9 for the Sobol method, in Table 8.10 and 8.11 for Morris method, and in Table 8.12 and 8.13 for the local 2-norm method. The vertical lines in the tables represents the threshold separating identifiable from non-identifiable. The limits are placed based on the subset size as well as relative changes in identifiability measures. Table 8.14 shows an overview of the identified subsets.

Table 8.9: Subset selection result from SCM for the Sobol ranking based subset. Note, this table shows which parameter was fixed in each per step.

SCM

Step	Correlation	Par A	Par B	Sens A	Sens B	Result
1	0.99	h_0	h_m	1	0.65	Fix h_m
2	0.95	s_2	k	0.44	$5.56 \cdot 10^{-2}$	Fix k
3	−0.98	s_1	A_{M0}	0.46	0.52	Fix s_1
4	0.9	α_2	β_1	$5.77 \cdot 10^{-2}$	0.11	Fix α_2
5	0.9	h_0	μ	1	0.23	Fix μ
6	−0.82	h_M	h_0	0.34	1	Fix h_M
7	−0.78	s_2	A_{M0}	0.44	0.52	Fix s_2
8	0.75	β_2	f_s	$5.77 \cdot 10^{-2}$	0.43	Fix β_2
9	−0.88	A_{M0}	β_1	0.52	0.11	Fix β_1
10	0.88	f_s	A_{M0}	0.43	0.52	Fix f_s
11	0.81	α_M	β_M	0.2	0.16	Fix β_M
12	0.78	$f_{r,t}$	α_M	0.47	0.2	Fix α_M
13	0.66	h_0	A_{M0}	1	0.52	Fix A_{M0}
14	−0.8	η	h_0	$2.22 \cdot 10^{-2}$	1	Fix η
15	0.9	h_0	$f_{r,t}$	1	0.47	Fix $f_{r,t}$
16	—			—	—	Last parameter h_0.

Table 8.10: Ranking of heart rate model parameters using OSM for the Morris ranking based subset.

		OSM		
Rank	Par	d	E	I
1	h_0	0	0.59	0
2	$f_{r,t}$	0.43	0.28	0.12
3	A_{M0}	0.22	0.31	$6.91 \cdot 10^{-2}$
4	α_M	0.37	0.1	$3.75 \cdot 10^{-2}$
5	f_s	$9.24 \cdot 10^{-2}$	0.26	$2.38 \cdot 10^{-2}$
6	h_m	$5.82 \cdot 10^{-2}$	0.38	$2.22 \cdot 10^{-2}$
7	β_m	0.31	$5.57 \cdot 10^{-2}$	$1.72 \cdot 10^{-2}$
8	μ	$9.62 \cdot 10^{-2}$	0.14	$1.32 \cdot 10^{-2}$
9	k	0.26	$2.96 \cdot 10^{-2}$	$7.66 \cdot 10^{-3}$
10	h_M	$2.39 \cdot 10^{-2}$	0.2	$4.82 \cdot 10^{-3}$
11	β_M	$4.47 \cdot 10^{-2}$	$8.45 \cdot 10^{-2}$	$3.77 \cdot 10^{-3}$
12	α_m	$5.25 \cdot 10^{-2}$	$6.42 \cdot 10^{-2}$	$3.37 \cdot 10^{-3}$
13	β_1	$2.94 \cdot 10^{-2}$	$6.48 \cdot 10^{-2}$	$1.91 \cdot 10^{-3}$
14	s_2	$3.66 \cdot 10^{-3}$	0.26	$9.53 \cdot 10^{-4}$
15	s_1	$1.62 \cdot 10^{-3}$	0.27	$4.43 \cdot 10^{-4}$
16	β_2	$1.03 \cdot 10^{-2}$	$3.45 \cdot 10^{-2}$	$3.56 \cdot 10^{-4}$

Table 8.11: Subset selection result from SCM for the Morris ranking based subset. Note, this table shows which parameter was fixed in each step.

<div align="center">SCM</div>

Step	Correlation	Par A	Par B	Sens A	Sens B	Result
1	0.97	k	s_2	$5.56 \cdot 10^{-2}$	0.44	Fix k
2	0.96	β_M	β_m	0.16	0.11	Fix β_m
3	0.97	α_M	α_m	0.2	0.13	Fix α_m
4	0.98	h_0	h_m	1	0.65	Fix h_m
5	−0.96	A_{M0}	s_1	0.52	0.46	Fix s_1
6	0.91	h_0	μ	1	0.23	Fix μ
7	0.84	h_M	s_2	0.34	0.44	Fix h_M
8	−0.81	A_{M0}	s_2	0.52	0.44	Fix s_2
9	−0.8	β_2	β_1	$5.77 \cdot 10^{-2}$	0.11	Fix β_2
10	−0.85	A_{M0}	β_1	0.52	0.11	Fix β_1
11	0.89	A_{M0}	f_s	0.52	0.43	Fix f_s
12	0.86	α_M	β_M	0.2	0.16	Fix β_M
13	0	$f_{r,t}$	$f_{r,t}$	0.47	0.47	Fix $f_{r,t}$
14	0.95	h_0	A_{M0}	1	0.52	Fix A_{M0}
15	0.74	h_0	α_M	1	0.2	Fix α_M
16	—			—	—	Last parameter h_0.
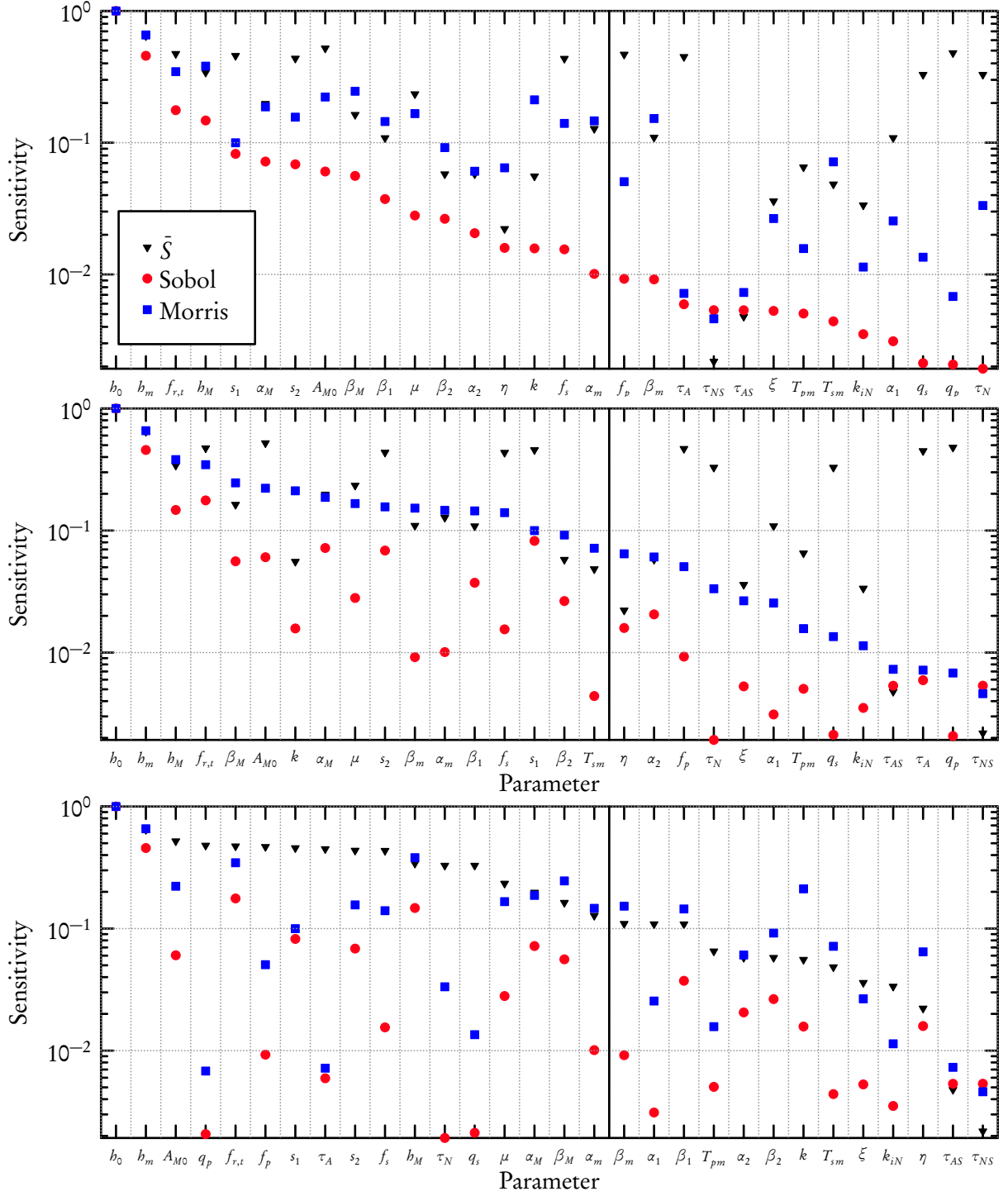
Figure 8.2: Two-norm of time series of local derivative based relative sensitivities and of global indices obtained using the Sobol and Morris methods. Top: ordered by the Sobol indices. Middle: ordered by Morris elementary effects. Bottom: ordered by local derivative based relative sensitivities.

134
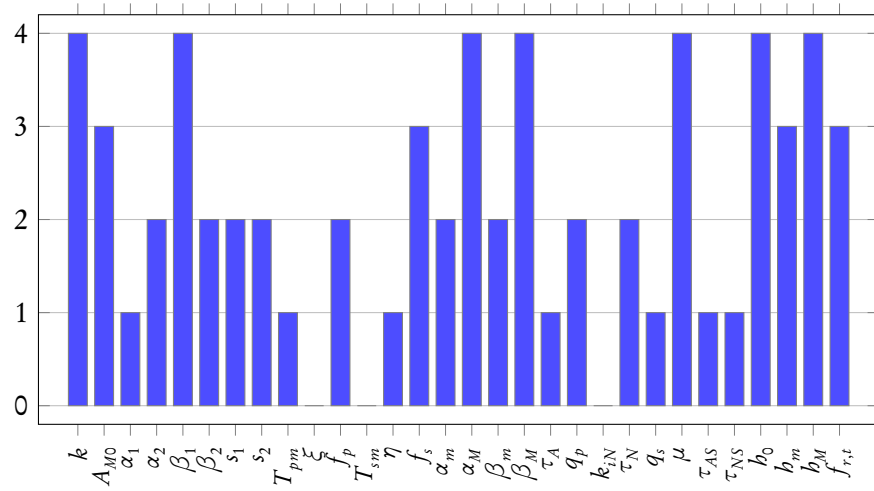
Figure 8.3: Histogram of parameter occurrence in subsets of size 16 generated by the four different methods.

Table 8.12: Ranking of parameters using OSM for the local method ranking based subset.

		OSM		
Rank	Par	d	E	I
1	h_0	0	0.52	0
2	$f_{r,t}$	0.43	0.24	0.1
3	f_p	0.31	0.25	$7.52 \cdot 10^{-2}$
4	f_s	0.19	0.23	$4.22 \cdot 10^{-2}$
5	α_M	0.23	$8.85 \cdot 10^{-2}$	$2.06 \cdot 10^{-2}$
6	h_m	$5.58 \cdot 10^{-2}$	0.34	$1.89 \cdot 10^{-2}$
7	τ_N	$8.35 \cdot 10^{-2}$	0.17	$1.43 \cdot 10^{-2}$
8	β_M	0.16	$7.22 \cdot 10^{-2}$	$1.18 \cdot 10^{-2}$
9	μ	$9.53 \cdot 10^{-2}$	0.12	$1.17 \cdot 10^{-2}$
10	τ_A	$3.31 \cdot 10^{-2}$	0.23	$7.72 \cdot 10^{-3}$
11	q_p	$1.31 \cdot 10^{-2}$	0.25	$3.25 \cdot 10^{-3}$
12	s_1	$1.2 \cdot 10^{-2}$	0.24	$2.9 \cdot 10^{-3}$
13	q_s	$1.31 \cdot 10^{-2}$	0.17	$2.25 \cdot 10^{-3}$
14	h_M	$6.76 \cdot 10^{-3}$	0.18	$1.2 \cdot 10^{-3}$
15	A_{M0}	$3.48 \cdot 10^{-3}$	0.27	$9.53 \cdot 10^{-4}$
16	s_2	0	0.23	0

Table 8.13: Subset selection result from SCM for the local method based subset. Note that the table shows what parameter was removed per step.

SCM

Step	Correlation	Par A	Par B	Sens A	Sens B	Result
1	0.99	h_0	h_m	1	0.65	Fix h_m
2	0.98	A_{M0}	f_p	0.52	0.47	Fix f_p
3	−0.97	s_1	A_{M0}	0.46	0.52	Fix s_1
4	−0.95	q_s	τ_N	0.33	0.33	Fix q_s
5	−0.93	s_2	A_{M0}	0.44	0.52	Fix s_2
6	−0.88	f_s	τ_N	0.43	0.33	Fix τ_N
7	−0.89	τ_A	q_p	0.45	0.48	Fix τ_A
8	0.82	f_s	A_{M0}	0.43	0.52	Fix f_s
9	−0.78	q_p	$f_{r,t}$	0.48	0.47	Fix $f_{r,t}$
10	0.93	α_M	β_M	0.2	0.16	Fix β_M
11	0.89	μ	h_0	0.23	1	Fix μ
12	0.78	q_p	h_M	0.48	0.34	Fix h_M
13	0.87	q_p	h_0	0.48	1	Fix q_p
14	0.95	h_0	A_{M0}	1	0.52	Fix A_{M0}
15	0.74	h_0	α_M	1	0.2	Fix α_M
16	—			—	—	Last parameter h_0.

Table 8.14: Overview of the created subsets.

Subset	Parameters	Size	Cond. FIM	χ^2_ν	AIC
4/4	$\{k,\beta_1,\alpha_M,\beta_M,\mu,h_0,h_M\}$	7	$3 \cdot 10^5$	26.49	1,420
3/4	$\{k,A_{M0},\beta_1,f_s,\alpha_M,\beta_M,\mu,h_0,h_m,h_M,f_{r,t}\}$	11	$3.4 \cdot 10^7$	25.55	1,409
2/4	$\{k,A_{M0},\alpha_2,\beta_1,\beta_2,s_1,s_2,f_p,f_s,\alpha_M,\beta_m,\beta_M,q_p,\tau_N,\mu,h_0,h_m,h_M,f_{r,t}\}$	19	$5.5 \cdot 10^9$	25.88	1,422
Sobol SCM	$\{A_{M0},\beta_1,\beta_2,s_2,\eta,f_s,\alpha_M,\beta_M,h_0,f_{r,t}\}$	10	$1.8 \cdot 10^6$	25.31	1,404
Sobol OSM	$\{k,A_{M0},f_s,\alpha_M,\beta_M,\mu,h_0,h_m,h_M,f_{r,t}\}$	10	$7.2 \cdot 10^4$	25.41	1,405
Sobol combined	$\{A_{M0},f_s,\alpha_M,\beta_M,h_0,f_{r,t}\}$	6	$3.9 \cdot 10^3$	29.63	1,468
Morris SCM	$\{A_{M0},\beta_1,\beta_2,f_s,\alpha_M,\beta_M,h_0,f_{r,t}\}$	8	$1.3 \cdot 10^6$	29.63	1,469
Morris OSM	$\{A_{M0},f_s,\alpha_M,\beta_m,\mu,h_0,h_m,f_{r,t}\}$	8	$6.1 \cdot 10^3$	26.47	1,421
Morris combined	$\{A_{M0},f_s,\alpha_M,h_0,f_{r,t}\}$	5	$2.7 \cdot 10^3$	31.16	1,488
Local SCM	$\{A_{M0},\alpha_M,\beta_M,q_p,\mu,h_0,h_M,f_{r,t}\}$	8	$1.1 \cdot 10^4$	26.85	1,427
Local OSM	$\{f_p,f_s,\alpha_M,\beta_M,\tau_A,\tau_N,\mu,h_0,h_m,f_{r,t}\}$	10	$1.7 \cdot 10^4$	28.08	1,448
Local combined	$\{\alpha_M,\beta_M,\mu,h_0,f_{r,t}\}$	5	$2.9 \cdot 10^3$	32.26	1,503

8.1.4 Subset tests using synthetic data

On one hand a large subset is more likely to lead to problems with identifiability. On the other, fixation of parameter values biases the model and reduces the range of the model dynamics.

To test the viability of the selected subsets, the following tests were performed.

- Create a synthetic data set using the model with nominal parameter values, with noise added. Noise is independent, identically normally distributed with mean $\mu = 0$ and standard deviation $\sigma = 5$.

- Change parameter values to 85% of the nominal value used to create synthetic data.

- Run optimization algorithm for each subset allowing only variation of the parameters in the subset.

- Compare quality of fits.

Using the method outlined above, and the model output f_i using p parameters to synthetic heart rate data f_i with n measurements, results in the least squares cost

$$\chi_\nu^2 = \frac{1}{n-p-1} \sum_{i=1}^{n} (y_i - f_i)^2 \tag{8.7}$$

values shown in Table 8.14. In addition the Akaike Information Criteria (IAC) (Akaike 1974) is calculated as well based on the expression,

$$\text{AIC} = n \ln \left(\frac{1}{n} \sum_{i=1}^{n} (y_i - f_i)^2 \right) + 2(p+1) \tag{8.8}$$

under the assumption that errors are independent, identically, normally distributed (Burnham and Anderson 2004).

Discussion

All tested methods gives reasonable results, with χ_ν^2 very close to $\sigma^2 = 25$. For the first strategy all three parameters sets give comparable results in terms of cost and AIC score. As subset *4/4* contains fewer parameters, it is computationally more attractive. For the Sobol and relative local sensitivity ranking methods, SCM and OSM seems to give very similar results, both better than the combined subset, and the two best if only considering the AIC. For Morris, OSM is superior, giving a just slightly worse fit than the best Sobol SCM and OSM subsets, but with 2 parameters fewer, and a very small condition number. It is also worth noting that the Morris-OSM set is almost a subset of the Sobol-OSM set, with the only non-shared parameter being β_m.

8.2 Optimization

8.2.1 Data set with respiration

Using the subsets Sobol SCM, Sobol OSM, Morris OSM, Local SCM and Local OSM the model is fitted against the data set for which respiratory input is available. The algorithm used is *Nelder-Mead* from the python library `lmfit` (`http://cars9.uchicago.edu/software/python/lmfit/`). The resulting χ_v^2-value, AIC and parameter values are given in Table 8.15, while the corresponding heart rate plots are shown in Figure 8.4. All found parameter configurations satisfied the parameter constraint put forward in Chapter 4, and did not lead to negative neuron firing frequency. To see the effect of the respiratory input the optimization was repeated for the same subset, with the parameters fixed $\alpha_m = 1, \alpha_M = 1, \beta_m = 0, \beta_M = 0$, to reflect the model with no respiratory input and constant full weight of the baroreceptor input. Again parameter estimates satisfied constraints and didn't lead to negative neuron firing frequency. Results from this simulation are printed in Table 8.16 and the graphs of the calculated heart rate are in Figure 8.5.

With respiratory input the subset selected using the Morris method for filtering non-influential parameters, combined with OSM gave the best fit to data, both in terms of χ^2 and AIC, while it gave comparable results for the same data set with no respiratory input. The methods based on Sobol indices provided good fits as well, but with larger parameter sets and slightly larger computational cost. Based on these results, Morris-OSM is selected for further analysis.

While Morris-OSM gave a reasonable fit there are still challenges to be addressed. Considering the fit in Figure 8.4, the model output does not show the same degree of dynamics as the data. This observation is in agreement with the parameter estimates hitting upper bounds, indicating that the solver has not converged, but stopped when it was violating the boundaries. Especially, parameters related to the midpoint of Hill type equations, such as f_s and $f_{t,r}$ appears to be problematic. If the range of input for such functions is far removed from the set midpoint, the output of the Hill function will be near constant.

To remedy this problem the parameters prescribing the midpoint for the Hill function describing the parasympathetic and sympathetic signal in response to afferent firing is fixed. Another option would be to add a penalty to the cost function that increases as f_s, f_p and $f_{r,t}$ deviates from their nominal values.

Fixed f_s and f_p

Calculating the Morris indices with $f_s = 0.35$ and $f_p = 0.65$ fixed gives the ordering shown in Figure 8.6. Setting the cutoff after α_2 results in the subset

$$\theta_{\text{Morris}} = \left\{ k, A_{M0}, \alpha_2, \beta_2, s_1, s_2, \alpha_m, \alpha_M, \beta_m, \beta_M, \mu, h_0, h_m, h_M, f_{r,t} \right\}.$$

Table 8.15: Parameter fits to data with respiration.

Name	4/4	Sobol SCM	Sobol OSM	Morris OSM	Local SCM	Local OSM
χ^2_v	90.55	42.48	42.48	40.53	61.69	61.69
Size	7	9	10	8	8	10
AIC	1,949.97	1,625.72	1,626.69	1,604.48	1,785.54	1,787.49
k	2.54	–	2.47	–	–	–
A_{M0}	–	2.49	2.51	2.51	2.52	2.52
β_1	1	1	–	–	–	–
β_2	–	0.43	–	–	–	–
s_2	–	0.24	–	–	–	–
η	–	1	–	–	–	–
f_s	–	0.65	0.75	0.74	–	–
α_M	1.2	1.2	0.94	0.61	1.02	1.02
β_m	–	–	–	0.47	–	–
β_M	1.06	0.65	0.65	–	0.65	0.65
q_p	–	–	–	–	5.58	5.58
μ	0.3	–	0.9	0.93	0.82	0.82
h_0	76.7	–	60	61.35	69.81	69.81
h_m	–	–	49.66	50.37	–	–
h_M	110.37	–	110.95	–	111.38	111.38
$f_{r,t}$	–	0.36	0.6	0.6	0.6	0.6

Table 8.16: Parameter fits to data without respiratory input.

Name	4/4	Sobol SCM	Sobol OSM	Morris OSM	Local SCM	Local OSM
χ^2_v	86.48	70.41	70.41	72.41	85.54	85.54
Size	8	6	7	5	5	7
AIC	1,931.13	1,840.56	1,841.54	1,851.65	1,923.47	1,925.44
k	2.39	–	2.5	–	–	–
A_{M0}	–	2.49	2.48	2.44	1.59	1.59
β_1	1	1	–	–	–	–
β_2	–	0.25	–	–	–	–
s_2	–	0.32	–	–	–	–
η	–	15	–	–	–	–
f_s	–	0.67	0.75	0.75	–	–
q_p	–	–	–	–	8.9	8.9
μ	0.3	–	0.3	0.7	0.3	0.3
h_0	67.44	–	60	60	75.12	75.12
h_m	–	–	58.28	44.96	–	–
h_M	110.16	–	109.65	–	99.79	99.79

Analysing this subset using OSM results in the ordering shown in Table 8.17 the identifiability falls with almost a factor $^1/_3$ after the 8th parameter h_m, and the final subset

$$\theta_{\text{Morris-OSM}} = \left\{ k, s_1, s_2, \alpha_M, \beta_m, \mu, h_0, h_m, f_{r,t} \right\}$$

with condition number of the corresponding FIM 7.2×10^2.

Using these two subsets for fitting to the data with respiration results in the parameter values shown in Table 8.18 and the model output plotted in Figure 8.7. The obtained χ^2_v are 38.71 and 38.56 for Morris and Morris-OSM respectively, while the AIC are 1,591 and 1,584. Both sets have lower cost and AIC than the Morris-OSM subset where f_s and f_p was allowed to vary, $\chi^2_v = 40.53$, AIC $= 1,604$. None of the parameters with constraints was chosen for optimization, and the values therefore satisfies the conditions. It is worth noting that the optimization algorithm has still not converged, as some of the estimated values are on the boundary. Namely s_2 and $f_{r,t}$ for Morris-OSM, and α_m, α_M, h_0 are at or very near the interval limits.

Table 8.17:   OSM ranking after noninfluential parameters have been removed by Morris ranking, for $f_s = 0.35$ and $f_p = 0.65$. The horizontal line indicates the largest dip identifiability, and the cutoff for which parameters are deemed identifiable.

<div align="center">

OSM

Rank	Par	d	E	I
1	h_0	0	0.63	0
2	$f_{r,t}$	0.43	0.3	0.13
3	s_2	0.28	0.26	$7.37 \cdot 10^{-2}$
4	s_1	0.12	0.24	$2.88 \cdot 10^{-2}$
5	α_M	0.24	0.11	$2.56 \cdot 10^{-2}$
6	β_m	0.33	$6.08 \cdot 10^{-2}$	$2 \cdot 10^{-2}$
7	μ	0.12	0.15	$1.74 \cdot 10^{-2}$
8	h_m	$3.65 \cdot 10^{-2}$	0.41	$1.5 \cdot 10^{-2}$
9	β_M	$6.2 \cdot 10^{-2}$	$9.13 \cdot 10^{-2}$	$5.66 \cdot 10^{-3}$
10	α_m	$6.34 \cdot 10^{-2}$	$6.79 \cdot 10^{-2}$	$4.31 \cdot 10^{-3}$
11	h_M	$1.19 \cdot 10^{-2}$	0.22	$2.61 \cdot 10^{-3}$
12	A_{M0}	$6.99 \cdot 10^{-3}$	0.28	$1.98 \cdot 10^{-3}$
13	k	$1.67 \cdot 10^{-2}$	$5.97 \cdot 10^{-2}$	$9.97 \cdot 10^{-4}$
14	α_2	$2.16 \cdot 10^{-2}$	$3.31 \cdot 10^{-2}$	$7.15 \cdot 10^{-4}$
15	β_2	$9.02 \cdot 10^{-3}$	$3.33 \cdot 10^{-2}$	$3 \cdot 10^{-4}$

</div>

Table 8.18: Parameter values obtained for the two subsets found for f_s, f_p fixed for the dataset with respiration.

Par	Morris	Morris-OSM	Min	Max
χ_v^2	38.71	38.56	–	–
AIC	1,591.47	1,583.99	–	–
k	2.52	2.56	1	4
A_{M0}	2.5	–	1	4
α_2	$6.97 \cdot 10^{-2}$	–	$5 \cdot 10^{-2}$	0.2
β_2	0.87	–	0.25	1
s_1	1.1	3.89	1	4
s_2	0.5	0.5	0.15	0.5
α_m	0.22	0.48	0.2	0.8
α_M	1.17	–	0.3	1.2
β_m	0.67	0.48	0.3	1.2
β_M	1.46	–	0.65	2.7
μ	0.6	0.87	0.3	0.95
h_0	61.6	72.47	60	120
h_m	59.16	68.07	20	80
h_M	110.5	–	80	140
$f_{r,t}$	0.6	0.6	0.15	0.6

8.2.2 Data set without respiration

The model was also fitted to the other data set for which respiratory data is not available. To account for the missing respiratory input the model parameters describing the weighting of the respiratory input was fixed at $\alpha_m = \alpha_M = 1, \beta_m = \beta_M = 0$. The model was fitted thrice using the Nelder-Mead algorithm. The estimated parameter values, χ_v^2 and AIC are shown in Table 8.19. For the first fit, all parameters were allowed to vary, including f_s and f_p. This fit is referred to as *All*. For the other two fits, f_s and f_p was fixed to ensure appropriate behavior of Hill functions. First, all parameters selected by the Morris ranking is estimated, next, the one left after the subsequent OSM analysis is outlined in Section 8.2.1. All parameter configurations satisfies constraints and produced positive neuron firing. Model output for the estimated parameters sets are plotted against data in Figure 8.8.

Table 8.19: Parameter values obtained with f_s, f_p fixed optimizing all parameters as well as the parameters chosen for the identifiable subset by Morris-OSM. Parameter values has been set to ignore respiratory input, and give full weight to baroreceptor regulation, $\alpha_m = \alpha_M = 1, \beta_m = \beta_M = 0$.

| Par	All	Morris	Morris-OSM	Min	Max
χ_ν^2	31.79	45.11	41.6	–	–
AIC	1,601.85	1,652.58	1,613.75	–	–
k	2.52	2.52	2.4	1	4
A_{M0}	2.5	2.5	–	1	4
α_1	0.7	–	–	0.35	1.25
α_2	0.17	0.18	–	$5 \cdot 10^{-2}$	0.2
β_1	3.68	–	–	1	4
β_2	0.29	0.66	–	0.25	1
s_1	2.66	2.44	3.71	1	4
s_2	0.21	0.32	0.15	0.15	0.5
T_{pm}	0.12	–	–	0.1	0.4
ξ	4.8	–	–	1	15
f_p	0.62	–	–	0.25	0.75
T_{sm}	0.18	–	–	0.1	0.5
η	12.89	–	–	1	15
f_s	0.72	–	–	0.25	0.75
τ_A	0.39	–	–	0.1	0.4
q_p	2.62	–	–	2.5	10
k_{iN}	0.72	–	–	0.25	1
τ_N	18.44	–	–	4	20
q_s	0.19	–	–	$5 \cdot 10^{-2}$	0.25
μ	0.56	0.85	0.44	0.3	0.95
τ_{AS}	1.09	–	–	1	4
τ_{NS}	3.21	–	–	1.2	5
h_0	60.25	60	60	60	120
h_m	53.25	62.37	79.95	20	80
h_M	110.17	109.97	–	80	140
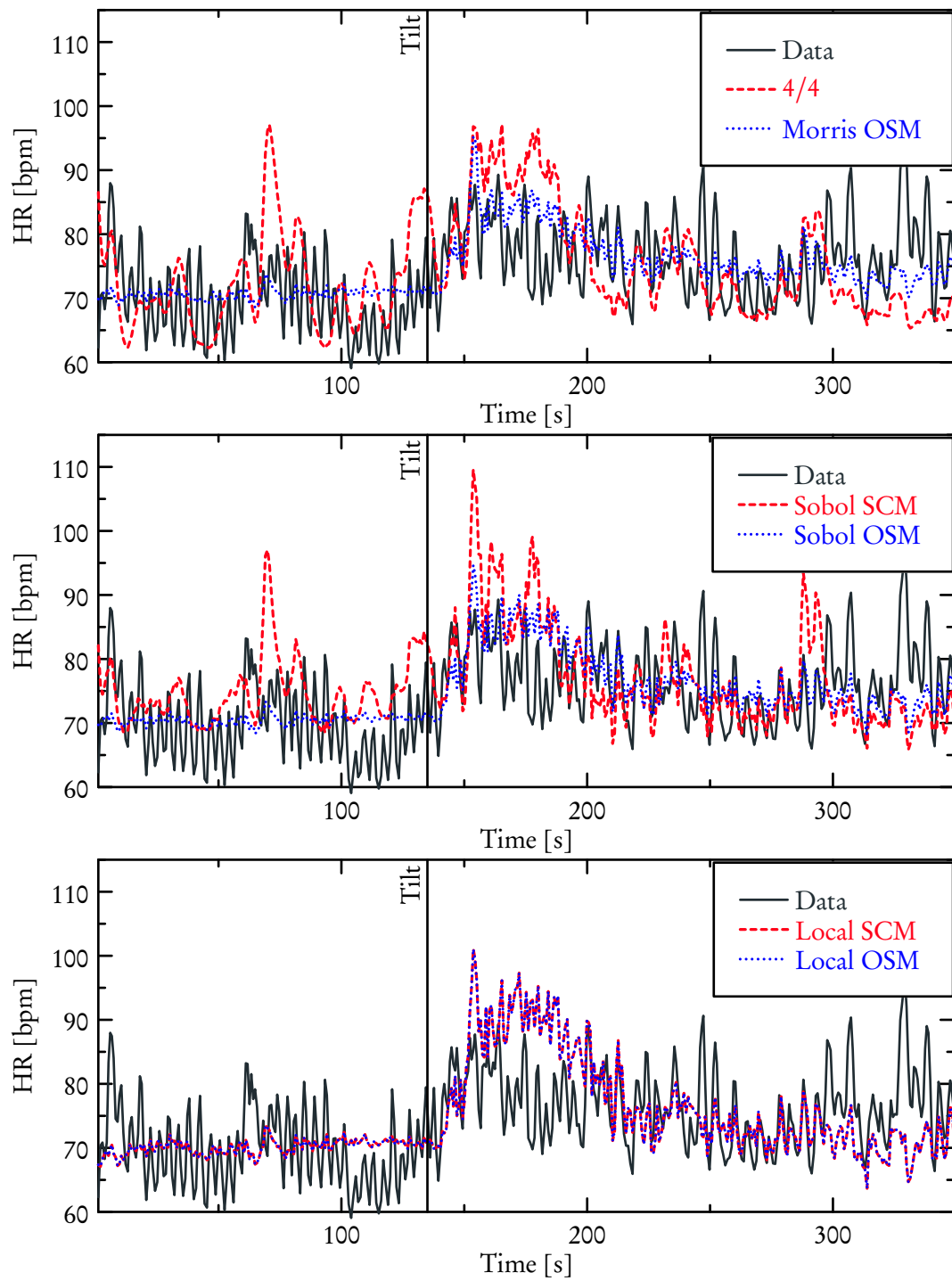
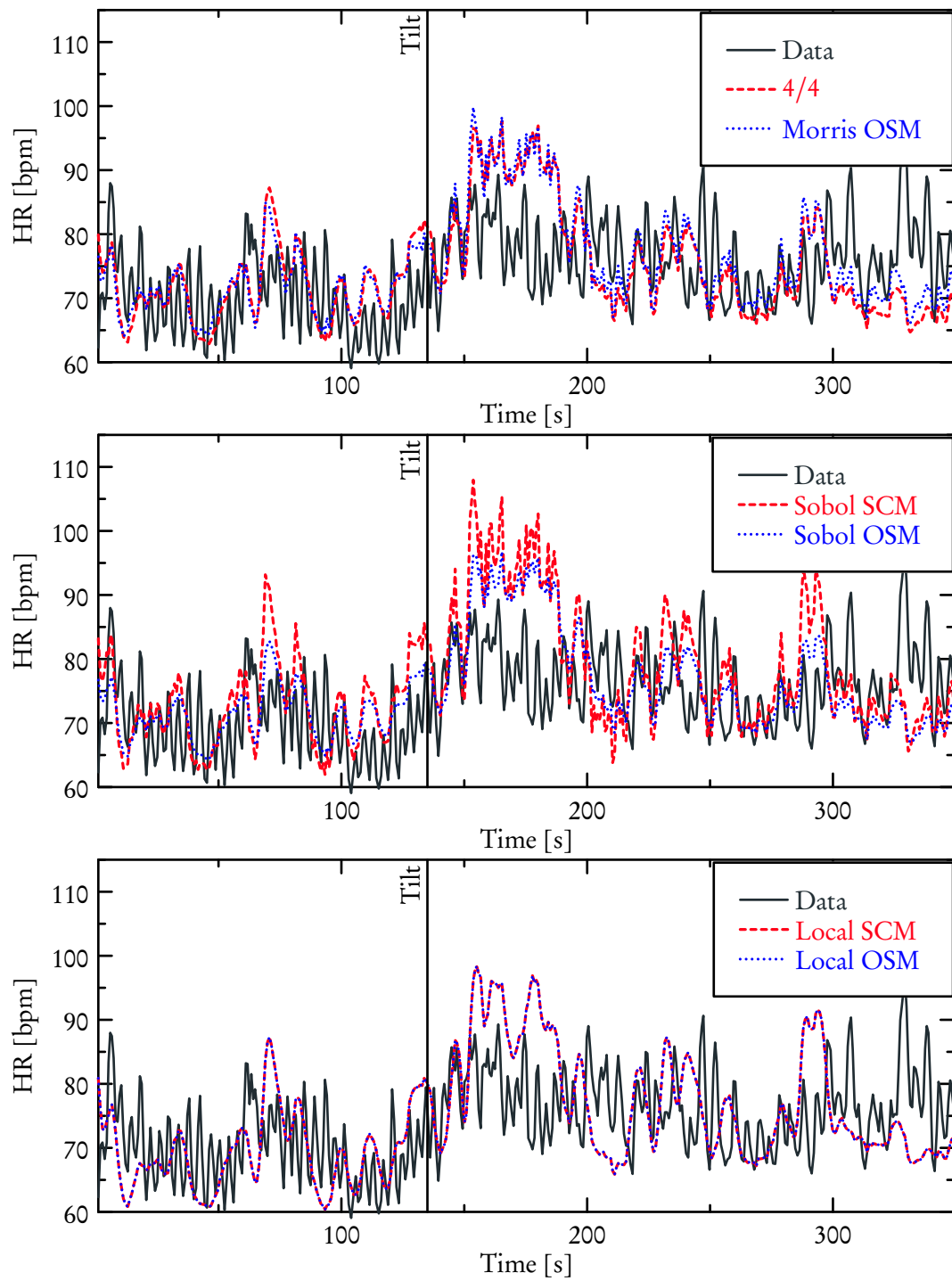Figure 8.4: Optimized model fits to data using respiratory input.

Figure 8.5: Optimized model fits to data without using respiratory input.
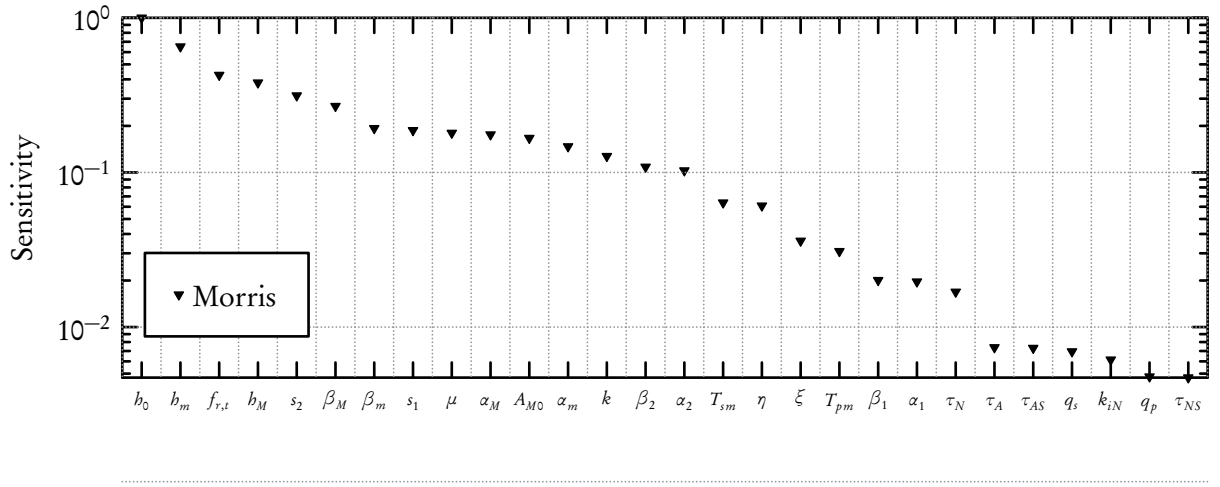
Figure 8.6: Ordering using two norm of Morris indices for the subset with f_s and f_p fixed.
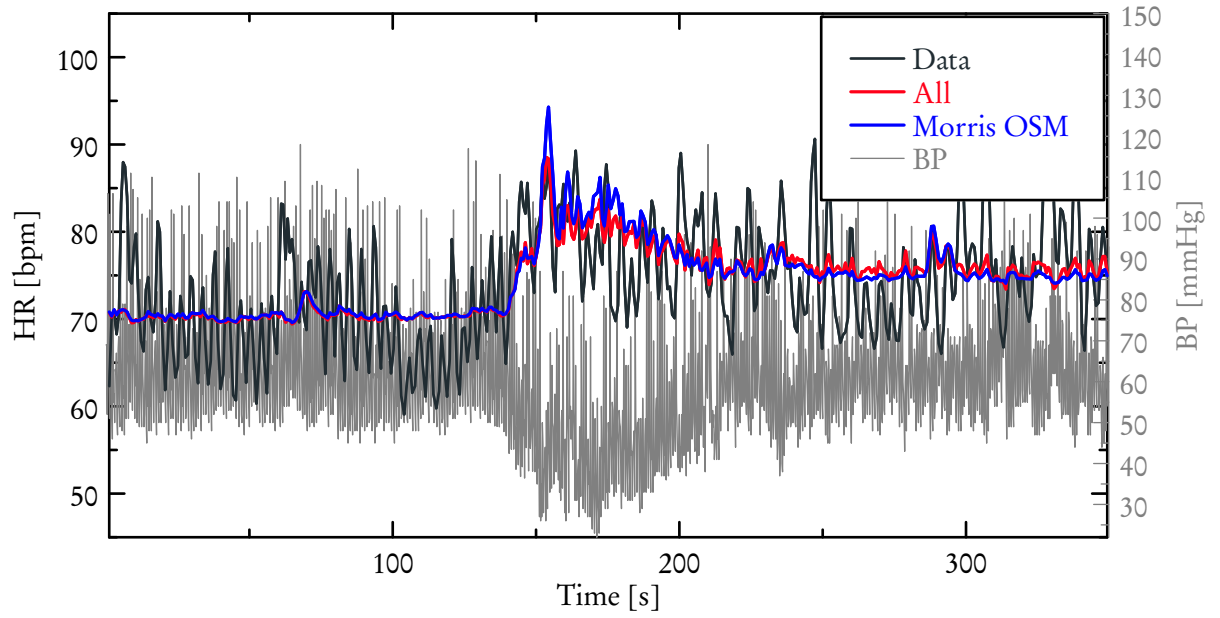

Figure 8.7: Model output fit to experimental data set with respiratory input.
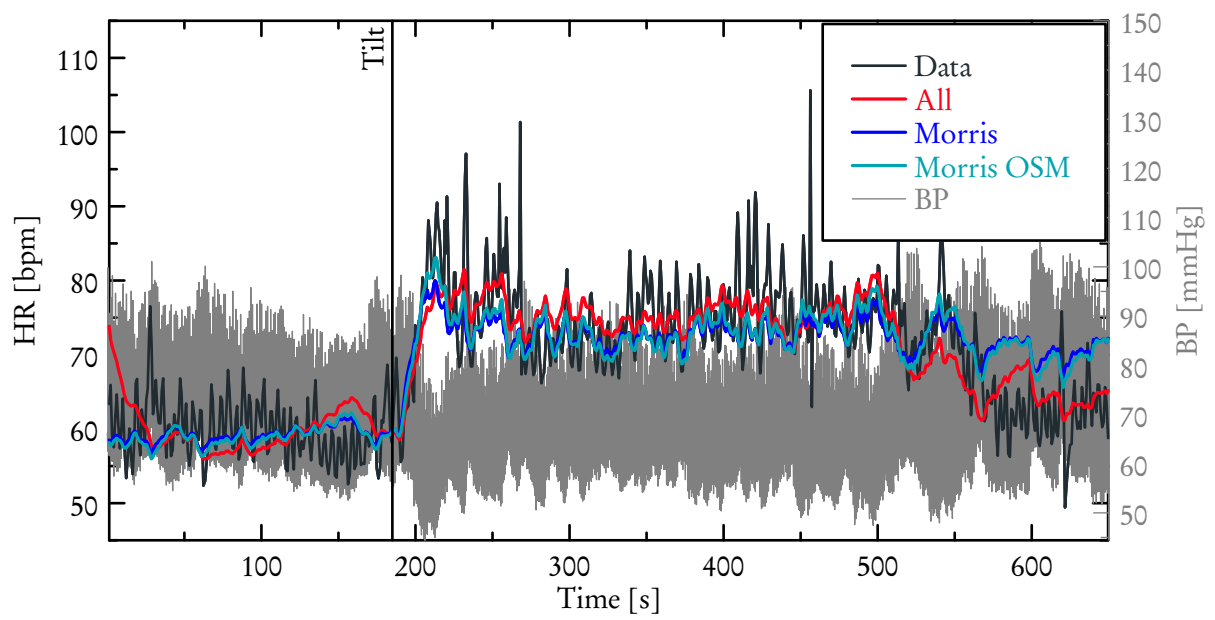
Figure 8.8:   Model output fit to experimental data set with no respiratory signal available.

8.3 Uncertainty quantification

DRAM was used to predict parameter uncertainties for both data sets. All parameters was bounded by 0 from below. The parameters T_{pm}, T_{sm} and μ was bounded by 1 from above, while the remaining parameters was unbounded from above. The initial parameter configurations was those found through optimization in Section 8.2.

8.3.1 Synthetic data

The optimized values for the Morris-OSM subset was used as initial parameter configuration for DRAM with 50,000 iterations. The resulting parameter chains are shown in Figure 8.9. Considering the panel showing the chain for μ, there is a transient initially, but after 2,000 iterations the chains appears to be sampling from the posterior distribution.

Considering the first 10,000 iterations as the burn in period the sampled points from the remainder of the chain gives rise to the parameter densities in Figure 8.10 and the pair wise correlations in Figure 8.11. The correlation between h_0 and h_m might give rise to identifiability issues, but for this data set it appears that both are identifiable judging from their densities. Sampling from the found densities and propagating through the model gives a median prediction and prediction interval describing where next measurement are expected. Median solution and 95% prediction intervals are shown in Figure 8.12. The variance predicted by DRAM is $s^2_{\text{DRAM}} = 25.4871$, which is in good agreement with the variance of the added noise of $\sigma^2 = 25$. For the synthetic data it is clear that the model dynamics are well described by the analysed subset, despite the remaining parameters are locked at 85% of the value used to generate synthetic data.

8.3.2 Dataset without respiration

All parameters

For the first run all parameters were allowed to vary. All parameters was bounded from 0 from below. The parameters T_{pm}, T_{sm}, and μ was bounded by 1 from above, while the remaining parameters was unbounded from above. A chain was generated with 50,000 points, as shown in Figure 8.13. The top panel shows the chains in their entire lengths, while the bottom panel shows only the last 10,000 points. The corresponding densities are shown in Figure 8.14, scatter plots of the most correlated parameters are shown in Figure 8.15 and solution and prediction intervals are shown in Figure 8.16. Considering first the scatter plots of correlated parameters it is clear that there exists rather strong correlations between some parameters. In addition several of the graphs shows clear trajectories, suggesting that the chain has not converged to sampling from a distribution. The same story is told by considering the chains plot in Figure 8.13. The jumps in the top panel, suggests that mixing is not well within the first 40,000 iterations, and the bottom panel does not look like points sampled
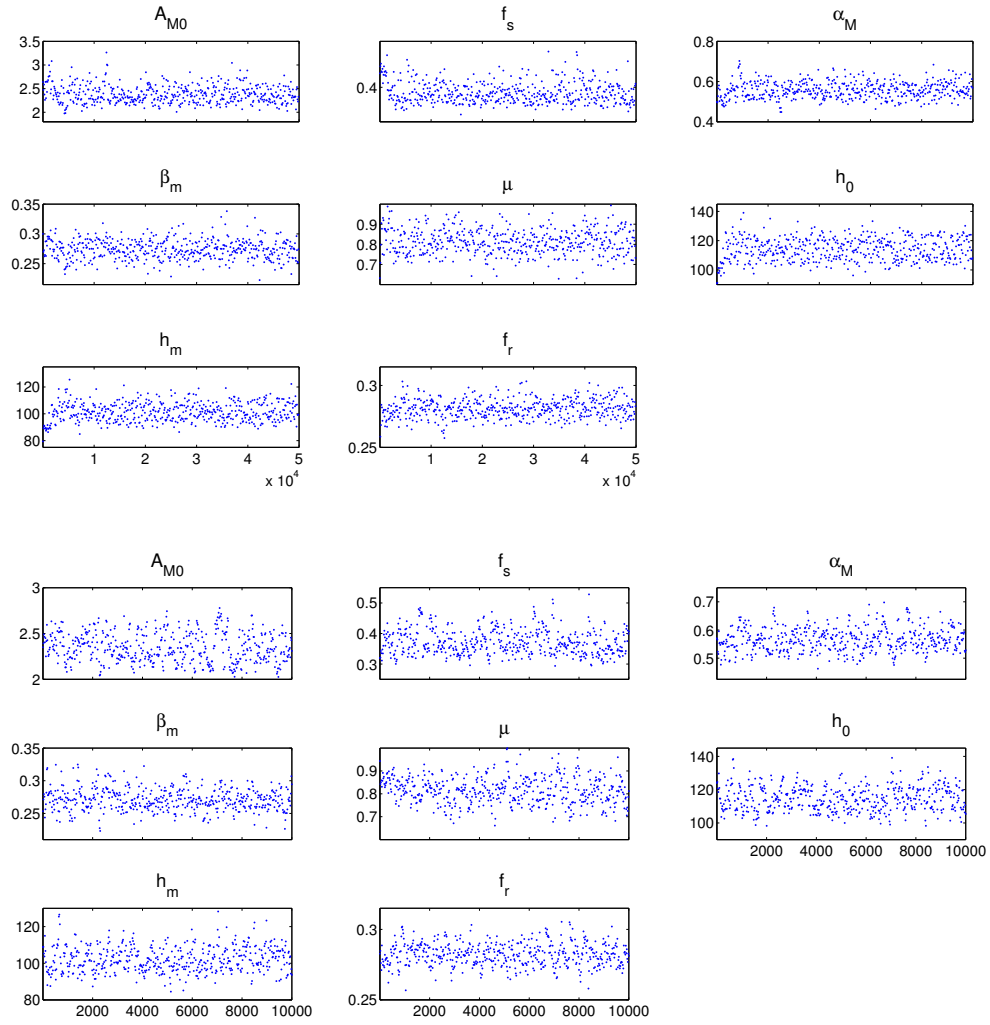
Figure 8.9: Parameter chains obtained from DRAM for fit to synthetic data. Top: entire chain with 50,000 points. It appears that there is a short transient at the beginning which appears to last less than 5,000 iterations. Bottom: last 10,000 points of the chain. The chain appears to be well mixed, and the samples appears to be random samples from a distribution.

randomly from a distribution. While the sum of squares shown in Figure 8.17 decreases for the chain, the number of correlated parameters makes it unlikely that running the chain longer would result in sampling from the posterior distribution. Since a reduced subset has already been found using Morris and OSM, the continued analysis will be performed for that subset.
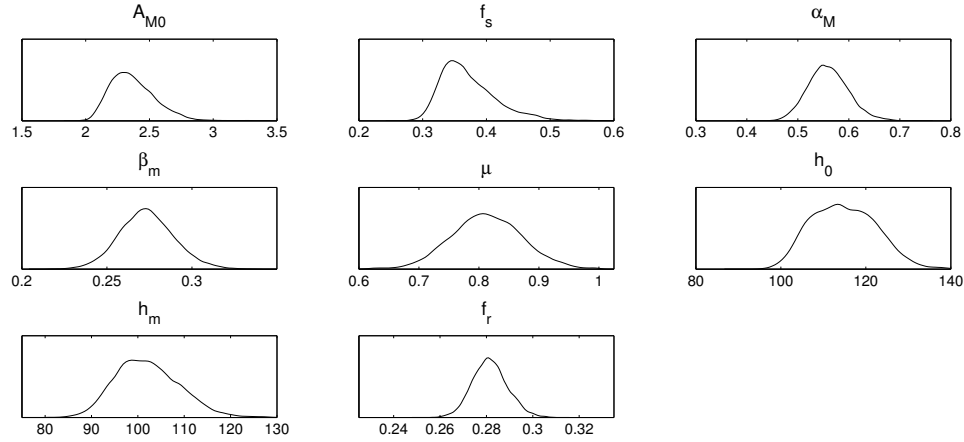
151

Figure 8.10: Parameter densities obtained from DRAM for fit to synthetic data, ignoring the first 10,000 points of the chain.

Morris-OSM subset

Limiting the subsets to the Morris-OSM subset and creating a chain with $50{,}000$ points leads to a very large correlation between the parameters h_0 and h_m, as seen in Figure 8.18. This correlation was also consistently identified by SCM as correlated for the data set with respiration, as shown in Table 8.5, 8.9, and 8.11. As information is more easily obtainable physiologically for h_0 than for h_m, h_0 is fixed for the subsequent analysis.

With h_0 fixed, DRAM produces the parameters chains shown in Figure 8.19 with $50{,}000$ iterations. Transients are observed within the first couple of thousand iterations, but the chain is well mixed and burned in for the remaining iterations. As a result the first $5{,}000$ points are ignored for the generation of the parameter densities in Figure 8.20 and the correlations in Figure 8.21. For this new chain some correlation is observed for the pairs s_1 and s_2, as well as for μ and h_m, but none of them are so strong that they cause problems with identifiability. This is confirmed by the parameter densities which indicate no multi-modal behavior.

Propagating the estimated parameter densities using $1{,}000$ points results in the solution and prediction interval shown in Figure 8.22.

The residual obtained for the median of parameter densities are plotted in Figure 8.23. It is clear that the errors are not iid., and that the model, with this configuration, is missing some dynamics of the data.
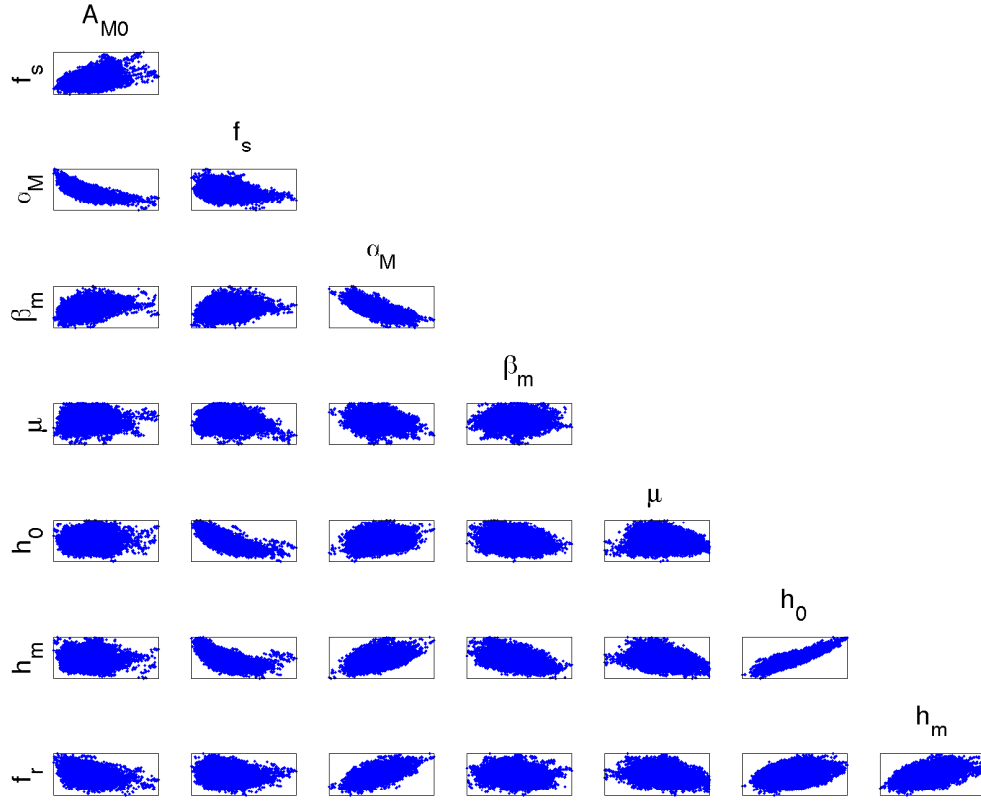
Figure 8.11:   Scatter plot for pairs of sampled parameter values for model fit to synthetic data using DRAM, ignoring the first 10,000 points of the chain.

8.3.3   Data set with respiration

This data set was only run for the parameter set determined by Morris-OSM. Using 50,000 points initially leads to very strong correlations between the parameters α_m and β_m, as well as between h_0 and h_m as shown in Figure 8.24. As α_m ranks lower in sensitivity from the Morris method in Table 8.7, α_m is locked together with h_0 for subsequent analysis.

New chains with 50,000 are generated after α_m and h_0 have been fixed. Again the first 5,000 iterations are ignored as burn in. The rusulting chains is shown in Figure 8.25. The sampled points resembles white noise, and the chain is therefore considered well mixed and burned-in. The resulting parameter densities are shown in Figure 8.26, while the scatter plots for parameter pairs are shown in
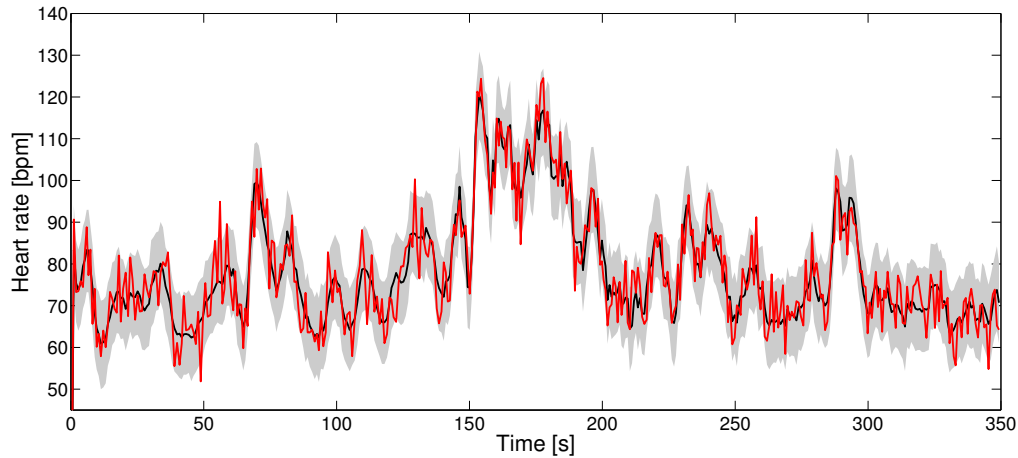
Figure 8.12: Synthetic data (red), median parameter density solution (black) and 95% prediction intervals (grey) for fit to synthetic data using DRAM.

Figure 8.27. While the scatter plots idicate some correlations, they do not appear to be single valued, just as the densities show no sign of multi-modal behavior that would indicate identifiability problems.

In addition it should be noted how the value of $f_{r,t}$, describing the set point for the Hill function of respiratory input, is estimated to be close to its upper boundary both by Nelders-Mead and DRAM. A set point so removed from the typical range of the respiratory signal ~ 0.3Hz, means that the resulting respiratory effect will be near constant.

Propagating the found parameter densities through the model, using 1,000 sampled points, results in the model output prediction intervals shown in Figure 8.28. The prediction intervals generated by DRAM contain 406 out of 431 data points, corresponding to 94.2%, indicating that the prediction intervals are correctly estimated. It is clear that the fit is not great, and that appears to produce a fit worse than that for the data set without respiration. On the other hand the residuals shown in Figure 8.29 appear to be closer to iid, than those presented for the fit to the data without respiration in Figure 8.23.
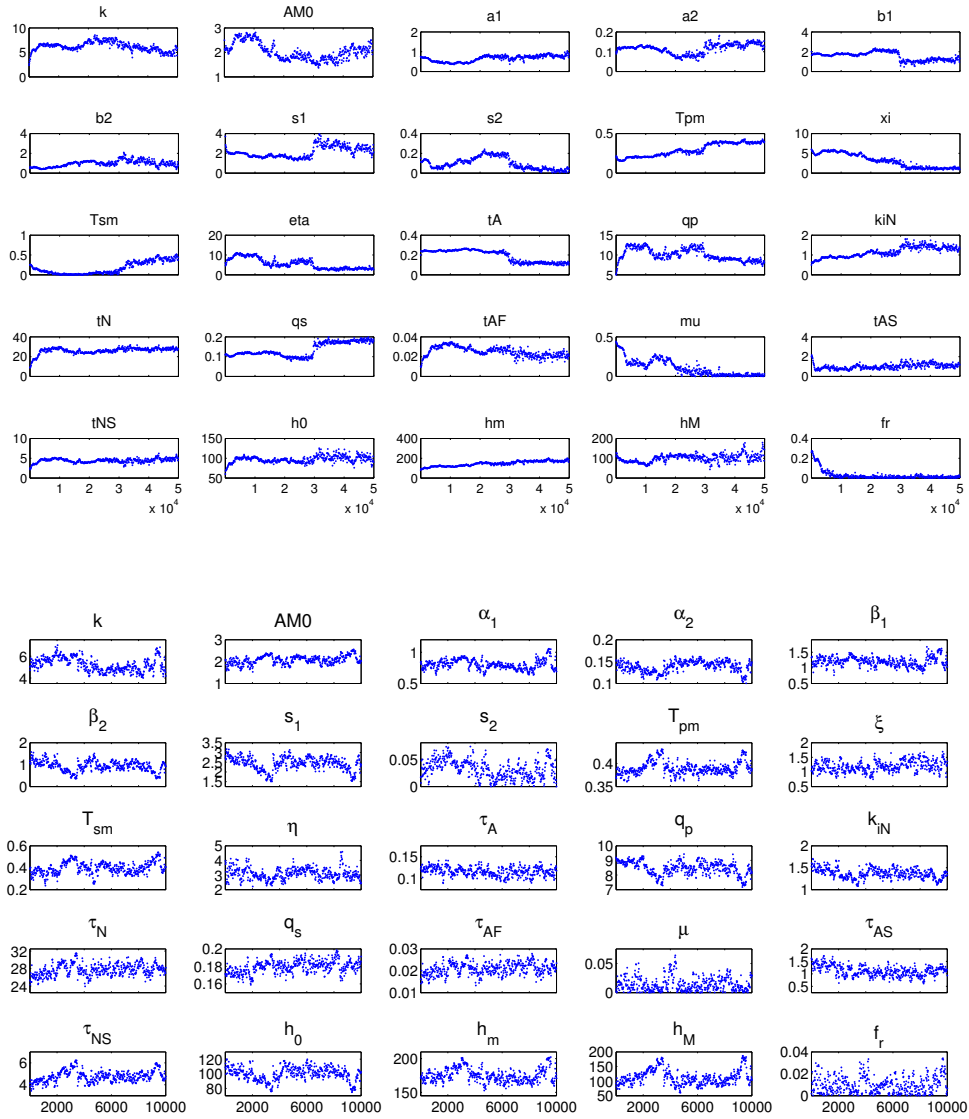
Figure 8.13: The chains of parameter values obtained for the dataset without respiration when all parameters are allowed to vary from DRAM using 50,000 iterations. Top: all 50,000 points. Bottom: last 10,000 points. Notice how even after 40,000 iterations the chains have not reached a fixed state, but are still moving around. It cannot be determined that the chain has reached a point where it is sampling from the posterior distribution.
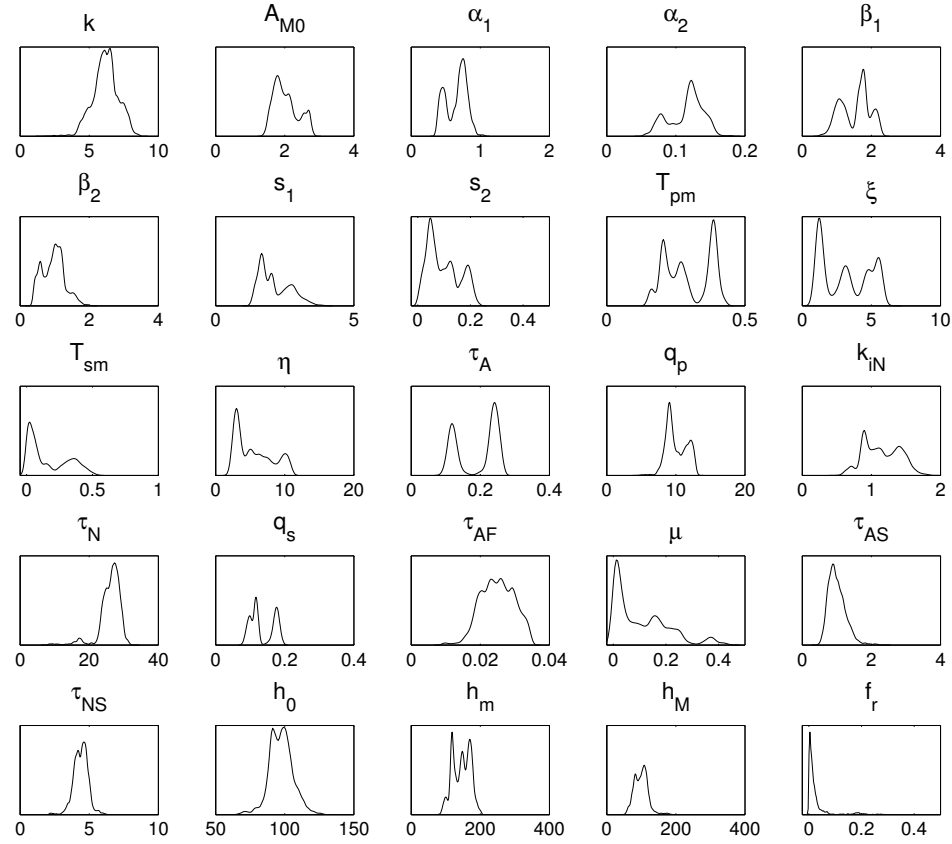
Figure 8.14: Parameter densities obtained for the dataset without respiration when all parameters are allowed to vary. The last 10,000 points of the chain has been used for these densities. It is clear that there is some bi-modal behavior for some of the parameters, probably due to interactions between parameters causing unidentifiability.
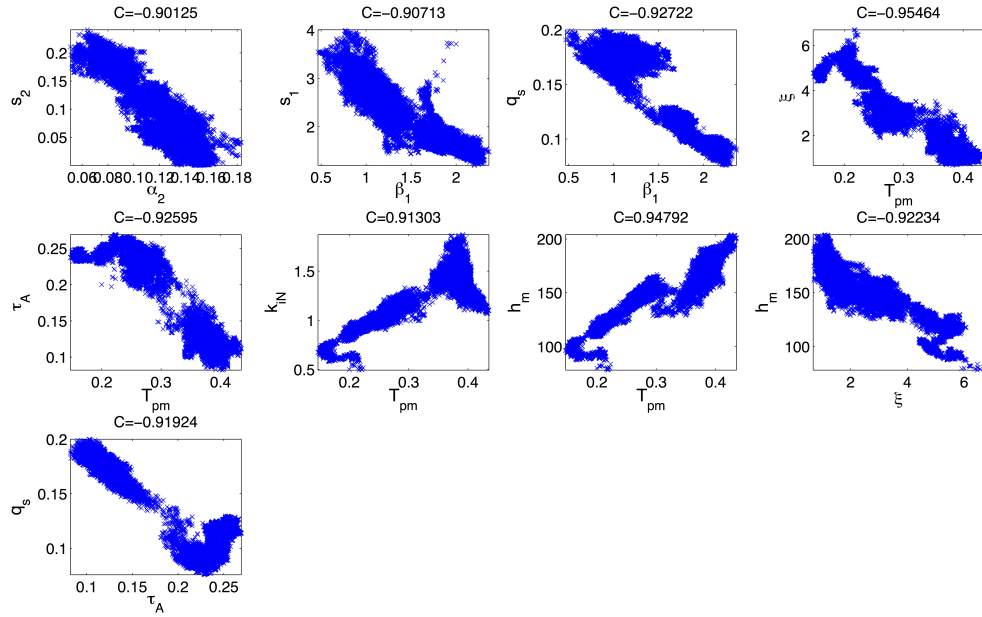
Figure 8.15: Scatter plots of parameters with absolute correlation larger than 0.9 for the last 10,000 points of the chain.
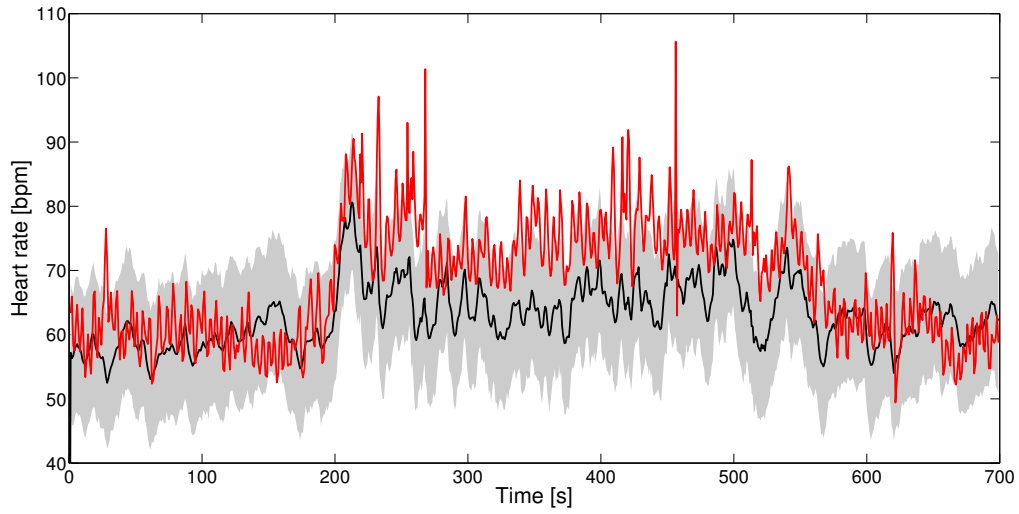
Figure 8.16: Experimental heart rate (red), model output heart rate (black) and prediction intervals (grey) obtained with parameter densities estimated by DRAM using last 10,000 samples from 50,000 iterations chain, where all parameters vary.
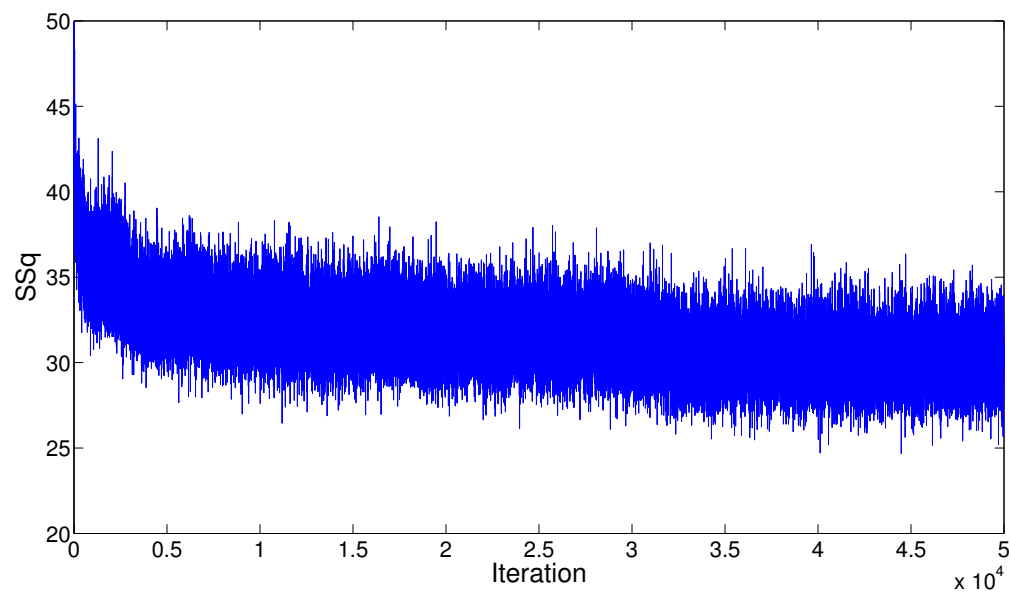
Figure 8.17: Chain of sum of residual squares Markov Chain when all parameters are allowed to vary for the data set with no respiration.
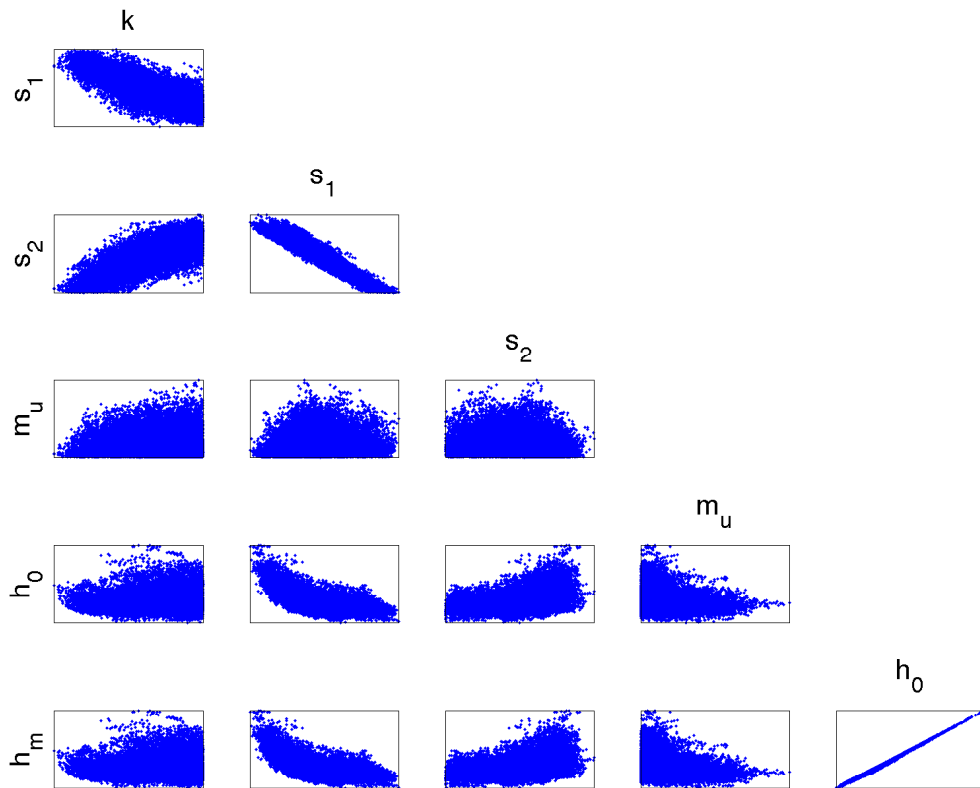
Figure 8.18: Correlations obtained for the Morris-OSM subset. A very clear observation is seen between parameters h_0 and h_m. Since knowledge is more easily obatined about h_0 than h_m, h_0 is fixed for subsequent analysis.

Figure 8.19: The chains of parameter values obtained for the dataset without respiration when only parameters selected by the Morris-OSM subset are allowed to vary from DRAM using 50,000 iterations. The signals looks like white noise indicating that the chain is well mixed and burned in.

Figure 8.20: Parameter densities obtained for the dataset without respiration when only the parameters selected by Morris-OSM are allowed to vary. There are very clear distribution for each, and no multi-modal behavior.
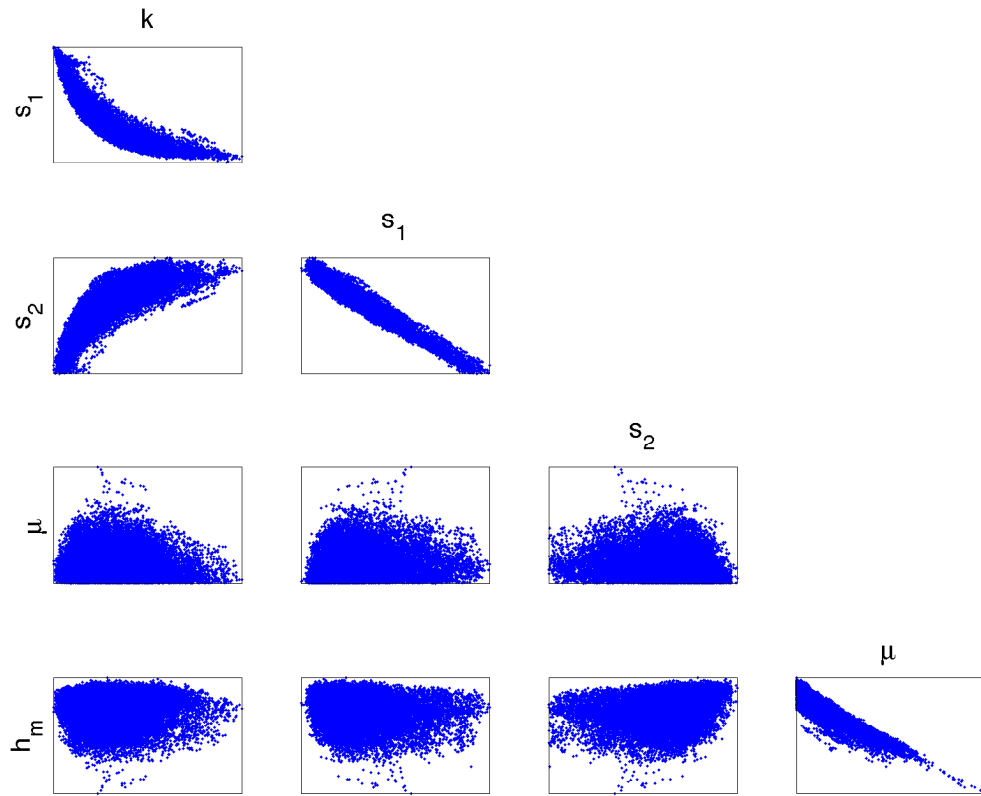
Figure 8.21: Relationship between parameter samples for the Morris-OSM subset with h_0 fixed. Several correlations are present, but none so single-valued they lead to identifiability issues.
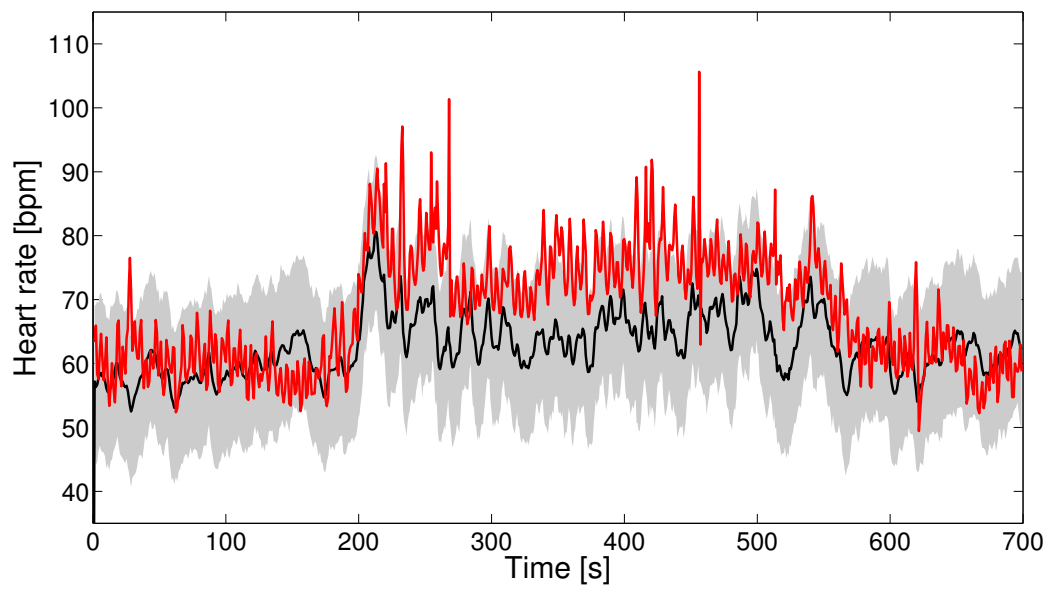
Figure 8.22: Solution (black) and prediction intervals (grey) obtained using DRAM using 50,000 iterations, letting all parameters vary, along with experimental data (red).

Figure 8.23: Plotting the residuals from the solution obtained by the mean value of the DRAM chain for each parameter reveal that the errors are not iid. There seems to be some dynamics that is currently not being reflected by the model.
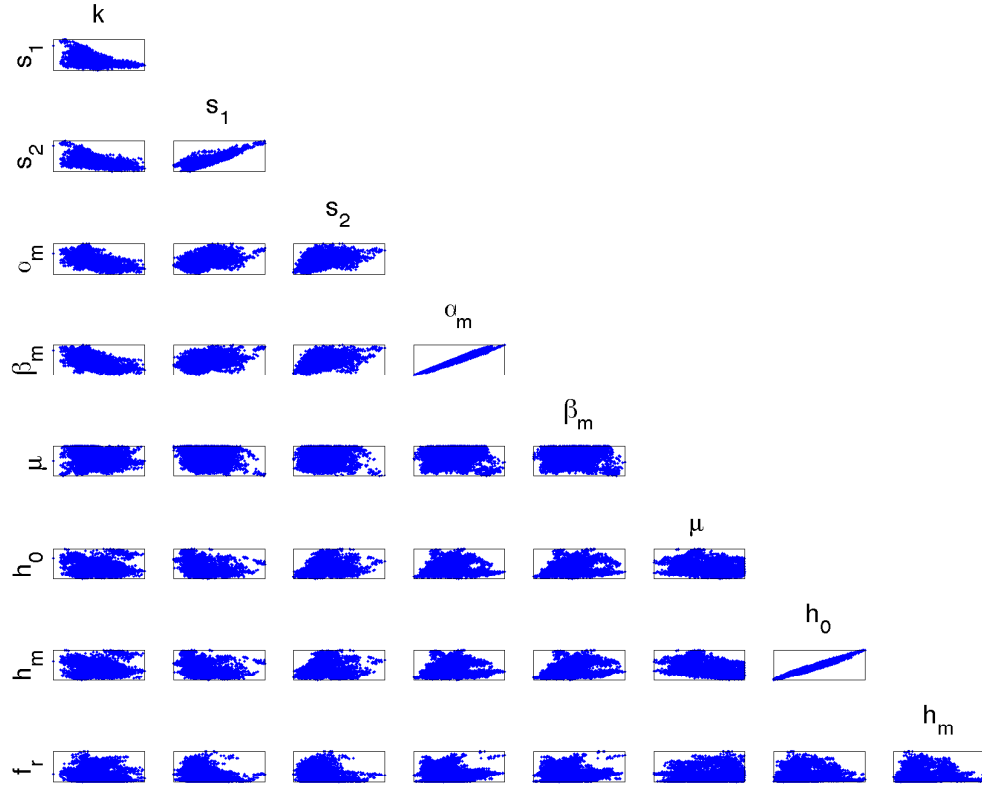
Figure 8.24: Scatter plots for parameter pairs. Strong correlations are observed between α_m and β_m and between h_0 and h_m. Parameters α_m and h_0 are fixed for subsequent analysis.
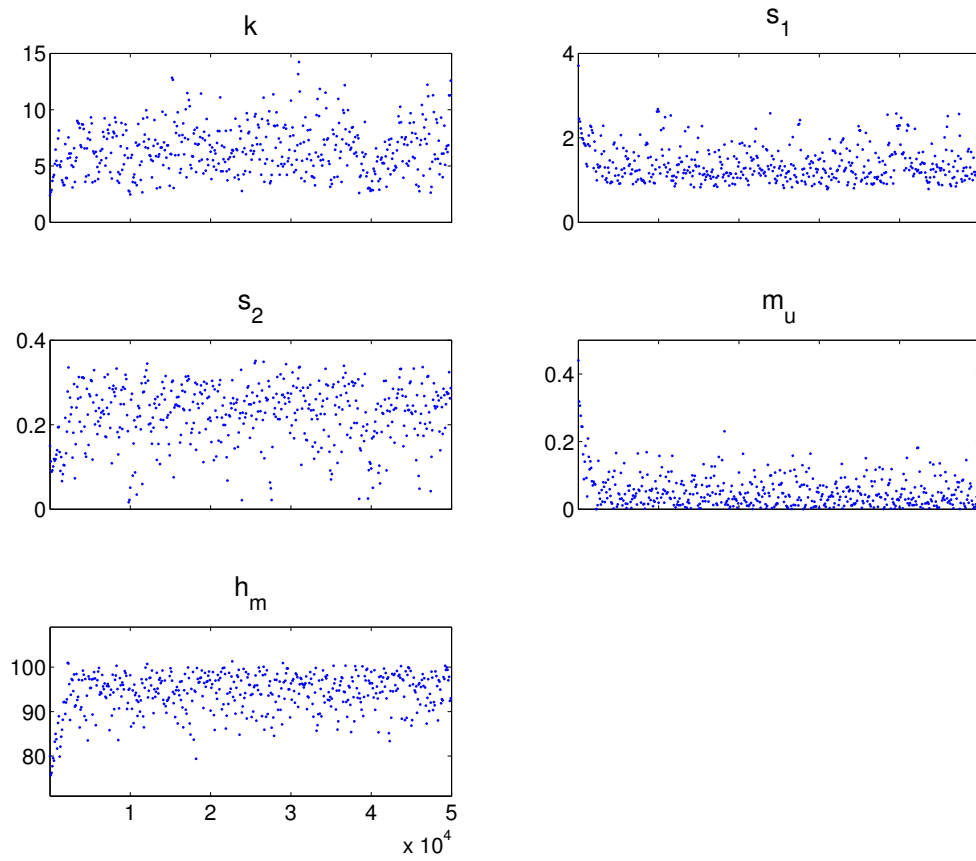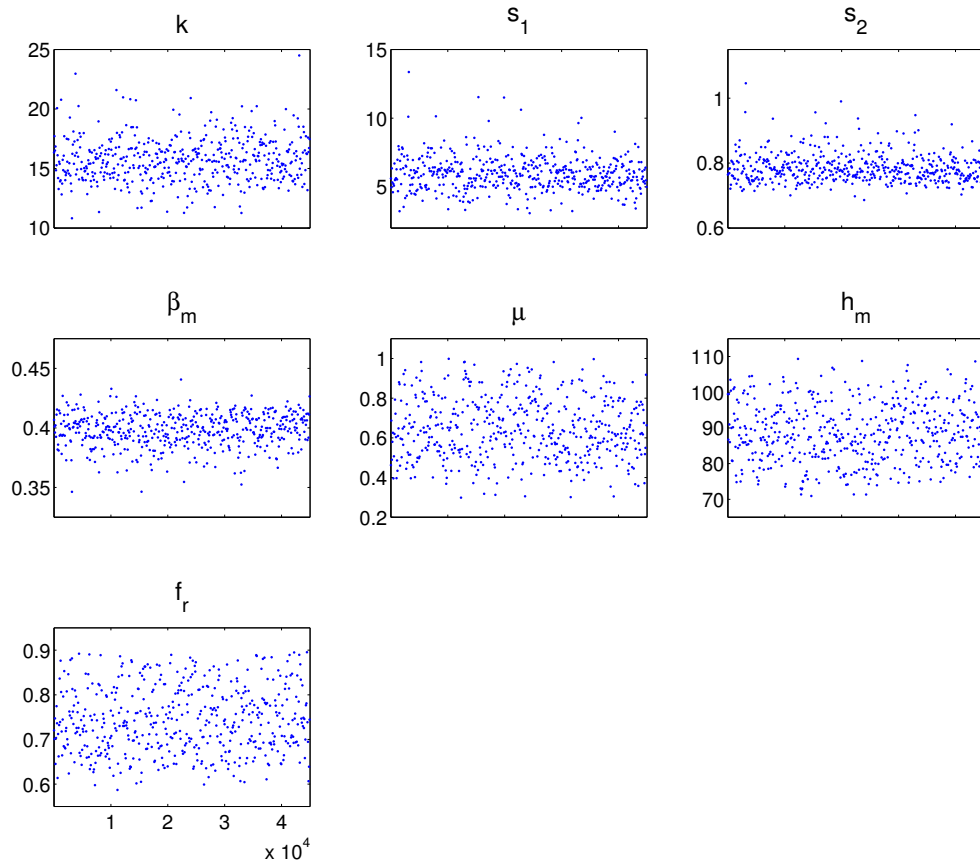
Figure 8.25: The chains of parameter values obtained for the dataset with respiration when only parameters selected by the Morris-OSM subset are allowed to vary. The points plotted here are samples after the burn-in period, and their stationary behavior indicate that the chain has converged.
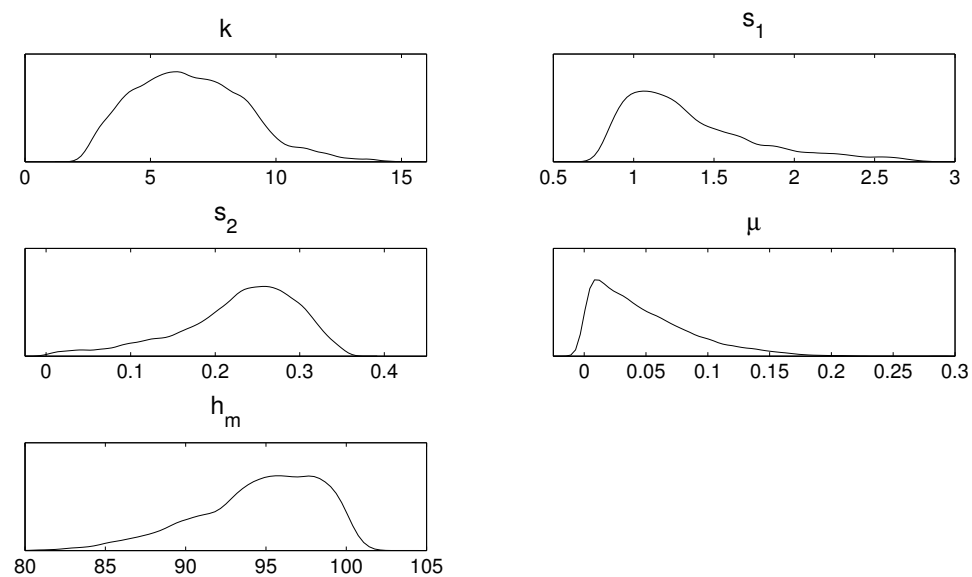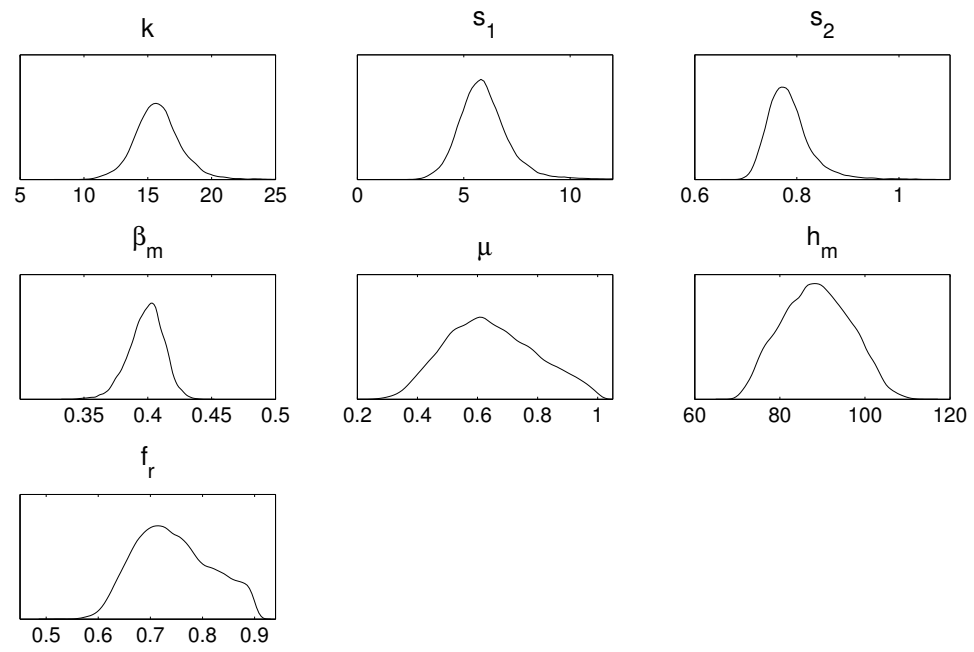
Figure 8.26: Parameter densities obtained for the dataset with respiration when only the parameters selected by Morris-OSM are allowed to vary. There are very clear distribution for each, and no bi-modal behavior.
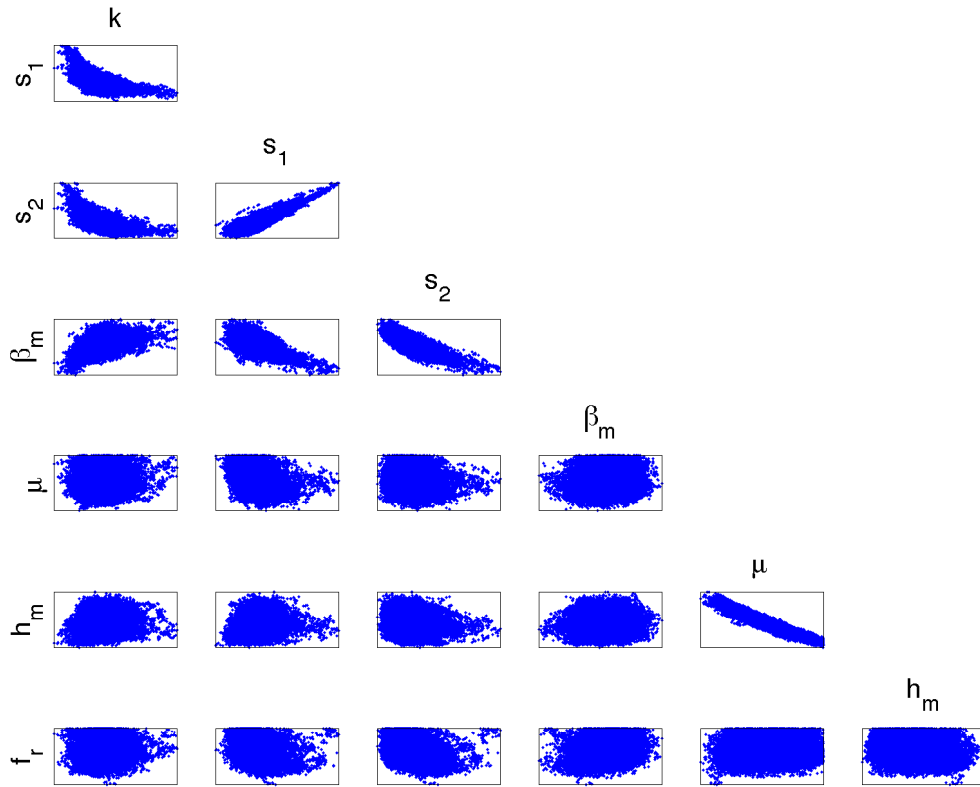
Figure 8.27: Parameter scatter plots for the Morris-OSM subset for data set with respiration. No transients are seen, indicating that the chain has converged. Some correlations are observed between α_m and β_m and between h_0 and h_m.
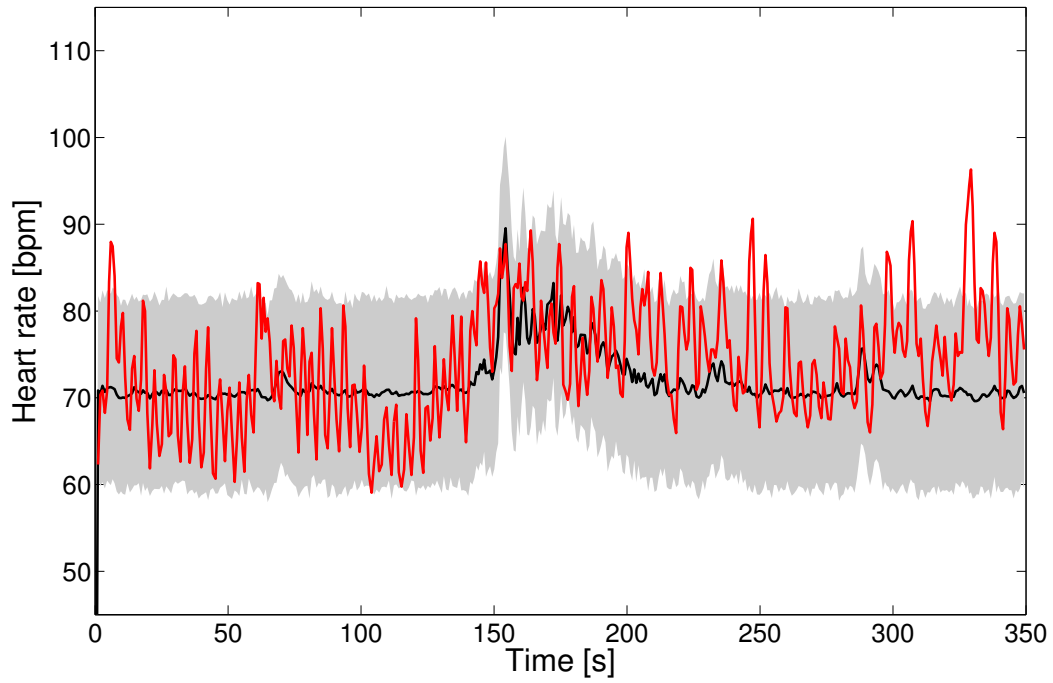
Figure 8.28: Experimental data (red), and Solution (black) and prediction intervals (grey) obtained for the model with respiration using DRAM with 50,000 iterations, fixing parameters α_m and h_0 but letting the remainder of Morris-OSM subset of parameters vary.
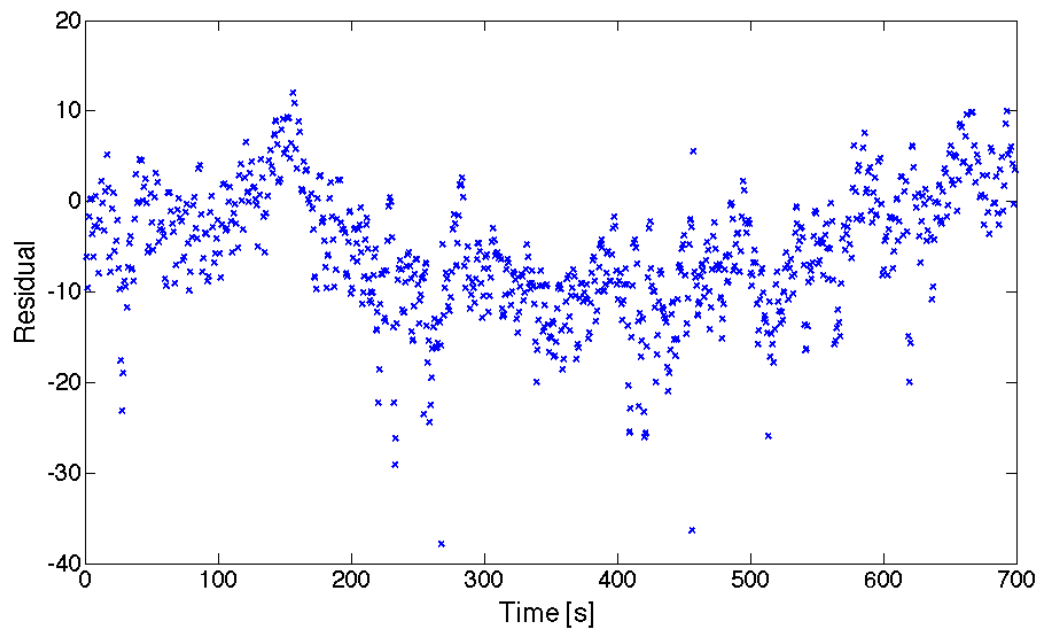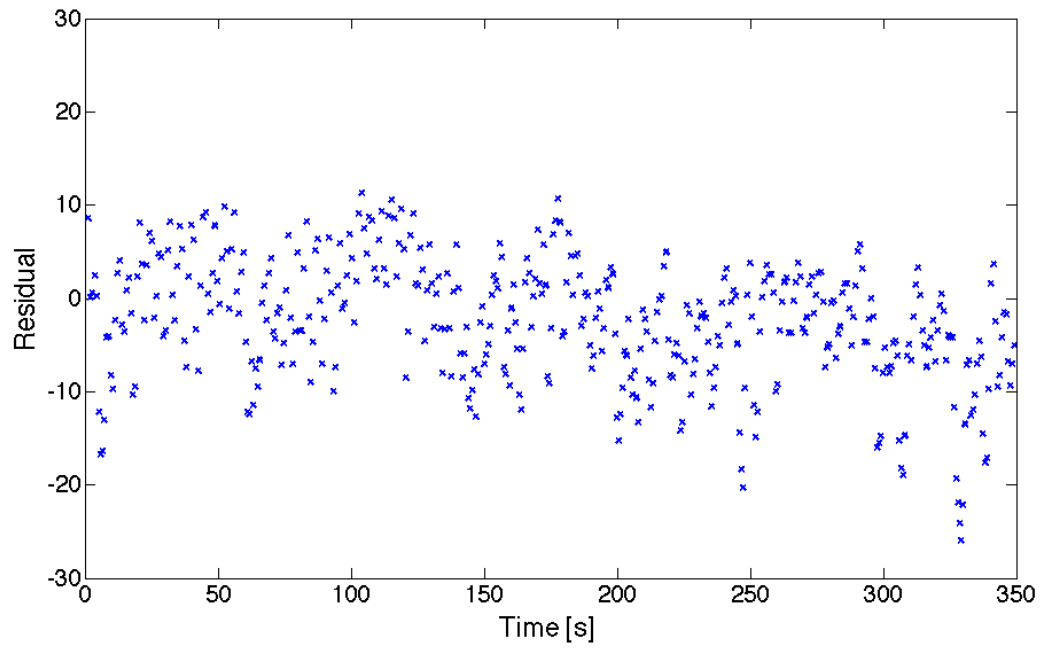
Figure 8.29: Plotting the residuals from the solution obtained by the mean value of the DRAM chain for each parameter reveal that the errors are not completely iid, but better than for the fit to experimental data without respiration.

8.4 Discussion

It was shown that different methods can be used for constructing subsets of parameters that are able to provide reasonable fits to data. The analysis with synthetic data revealed that even small subsets allowed for fitting constructed data, even though the remaining parameter values had been fixed at 85% of the "true" value. For the analysis against experimental data it was revealed that the methods based on global analysis of sensitivities were superior in providing a good fit. Morris-OSM ($\chi_v^2 = 41, \text{AIC} = 1604$) provided the best fit, with Sobol-SCM ($\chi_v^2 = 42, \text{AIC} = 1626$) and Sobol-OSM ($\chi_v^2 = 42, \text{AIC} = 1627$) being nearly as good, while local-SCM ($\chi_v^2 = 62, \text{AIC} = 1786$) and local-OSM ($\chi_v^2 = 62, \text{AIC} = 1787$) was significantly worse. Because the Morris method provided similar quality fit to Sobol, but has a signficant lower cost, OSM-Morris was favored in the subsequent analysis. Why the OSM method proved more efficient than SCM when using for parameters found sensitive by the Morris method is not clear however. A possible explanation is that it consistently produced subsets for which the condition number of the FIM was lower when the subsets were of equal size. Something that can likely be explained by how it considers linear independence between the model sensitivity to parameters, while SCM considers estimates of pair-wise correlations between parameters estimates.

The lower efficiency of the local methods can most likely be ascribed to the parameter configuration used for calculation was far from the optimum configurations. While this is an inherent disadvantage of local methods, one could consider running an initial optimization to close in on the optimum before calculating local sensitivities. For gradient based optimization algorithms, one might also consider the subset selection and optimization as an iterative process, where a new sensitivity analysis and subset selection is performed at each found optimum, before starting the optimization process again.

Fixation of parameters f_s and f_p for the Hill functions involved in modeling the autonomic nervous system response to afferent firing increased the quality of the fit for the OSM-Morris subset ($\chi_v^2 = 39, \text{AIC} = 1584$). Some of the estimated parameter values were still found at or very near the limits of the allowed intervals. Especially it seemed that the dynamics of the respiration was hard to encapsulate, suggesting that the respiratory input part of the model might need some reconsideration.

While the model fit to the data set with respiration was acceptable but didn't show the desired dynamics, the model fit to the data set without respiration was better. Three different optimizations was done. One without subset selection ($\chi_v^2 = 32, \text{AIC} = 1602$), one with non-influential parameters removed by Morris ($\chi_v^2 = 45, \text{AIC} = 1652$), and finally one for the Morris-OSM subset ($\chi_v^2 = 42, \text{AIC} = 1614$). While the parameter describing the base depolarization rate of the pacemaker cells, h_0, hit the limit of the allowed interval, all other parameter estimates was in the interior of the allowed intervals. It was mentioned earlier that fixing parameter values introduces a bias into the model and effectively changes the model. This is very clearly illustrated in the parameter estimates obtained for the data set without respiration. Table 8.19 shows that the obtained fits are somewhat similar in χ_v^2

values (41.6 for Morris-OSM and 45.11 for Morris) and Figure 8.8 show that the obtained solutions are quite similar, yet the parameter estimates are very different. This may also be interpreted as there being identifiability issues for the non-reduced model. Hence in addition to increasing the chance of producing unique optimum, the reduced subset also have the advantage that it allows the use of gradient based optimization methods that are favorable in computational cost.

For all optimized parameter configurations constraints set up to guarantee positivity of relevant physiological states was met eventhough they were not enforced during the optimization. The only model states not guaranteed to remain positive was those describing distribution of strain in the arterial wall, but the resulting neuron firing was positive.

The parameter estimates obtained with Morris-OSM for the two methods were used to calculate parameter densities and prediction intervals for model output. Here the parameter boundaries are ignored for parameters where no strict physiological boundaries are present. DRAM is run for four different problems: synthetic data with OSM-morris subset, experimental data without respiration with all parameters, experimental data without respiration with Morris-OSM subset and experimental data with respiration with Morris-OSM subset.

For the synthetic data set DRAM reproduces the experimental data with very tight predictions intervals, as expected. Parameter interactions shows no signs of identifiability issues, despite some correlations existing. For the full parameter set for experimental data without respiration DRAM is not able to converge within $50,000$ iterations. In addition correlations between parameters and the behavior of parameter chains strongly suggests that there is identifiability issues, and that the chain should not be expected to converge. For Morris-OSM without respiration parameters h_0 and h_m are found to be highly correlated. Since h_0 can most easily be determined physiologically, it is fixed at its nominal value and the analysis repeated. The result leads to some correlations between parameters that are closely related in the mathematical description of the model such as s_1 and s_2. None of these correlations have the form of a clear functional relationship, and as such poses no issus for identifiability. For Morris-OSM with respiration the near single-valued correlation between h_0 and h_m is seen again, but in addition the correlation between α_m and β_m is seen as well. h_0 and α_m are fixed and the analysis repeated.

The results from DRAM suggests that the method converges for each data set with the Morris-OSM parameter subset. The resulting fits however, seems to be missing some of the dynamics. For the fit to the data set without respiration, it appears that the heart rate does not stay at the level it should after the tilt. This is possible due to parasympathetic activity increasing or sympathetic activity decreasing too early after the tilt.

This is clearly indicated in the residual plot in 8.23. For the fit to the data set with respiration the missing dynamics seems to be less clear, except that the difference between model and data is becoming more negative towards the end.

While the subset selection based on Morris-OSM is still prefered due to the quality of produced

fits over the local methods and the higher computational efficiency than Sobol, the restrictive course chosen towards subset size might not be optimal.

Chapter 9

Concluding remarks

9.1 Conclusion

The mathematical model developed in this study is based on physiological descriptions of the mechanisms involved in the baroreceptor reflex mechanism. The model contains elements predicting firing rate in afferent neurons, sympathetic and parasympathetic outflow, concentrations of neurotransmitters acetylcholine and noradrenaline, from which heart rate is predicted. The detail level of the model is high enough to assert physiological meaning to each parameter, while simple enough that the effect of each subsystem can be understood and discussed.

A few things should be noted about the model. Nominal parameter values are in large set to match descriptions from other authors, or are based on simple assumptions about the expected behavior. To reproduce behavior known from literature, the model for stimulus of the baroreceptors assumes that the arterial wall distends elastically, and that the baroreceptors are strained viscoelastically. In reality the distention of the arterial wall is viscoelastic, just as the mechanism for initiating action potentials in the baroreceptor neuron also plays a role in the viscoelastic response. Likewise, the description of the intracellular pathways of the pacemaker cells on the heart are not based on the actual mechanisms, but formulated to describe the expected effect. Simulations using the mathematical model showed that the inclusion of a distributed sympathetic delay did not change the heart rate regulation significantly. While this suggests that the sympathetic delay does not greatly affect heart rate regulation in the physiological system, it is result for the mathematical model with that specific configuration. A preliminary analysis of the effect of respiration using simulations showed that the implementation can produce an increase in fast oscillations of model output heart rate, and a decrease in parasympathetic activity following a change in posture. This is in line with the goal of including respiration of predicting faster oscillations, and the physiological knowledge of parasympathetic activity following tilt.

The mathematical formulation of the model has been shown to guarantee positivity of solution for relevant state variables under certain restrictions on parameter configurations. The model is able to describe the mean behavior of heart rate regulation during head-up-tilt (HUT) experiment. While the tilt itself takes only 14 seconds, the model predicts the behavior over a period starting 3 minutes before HUT and ending 8 minutes after. Implementation of respiration input has been found to facilitate an increase in fast oscillations in model output heart rate, and to reflect physiological understanding of decreased parasympathetic activity following HUT.

While the model was able to correctly predict mean heart rate behavior, it was unable to match fast oscillations in the experimental data. It is hypothesised that these fast oscillations is due to respiration, and primarily affected by the respiration frequency. It is impossible to conclude if the shortcoming of the model is due to wrong description of the respiration effect or to errors in respiration data extracted from ECG. However, the absence of oscillations in respiration frequency, suggests that perhaps the signal considered should not be the frequency as done in this study, but rather the more dynamic respiration signal itself.

Sensitivity and identifiability analysis was performed for the model, using different strategies in terms of combining results from local and global methods. No clear common tendencies were found for these methods, which all produced different subsets. To test both the optimization algorithm implementation, and the ability of the subset to reflect required dynamics, the subsets were tested against synthetic data. Next, the subsets were tested by fitting the model to experimental data with respiration, allowing only the parameters of the subset to vary. Here the subset based on the Morris method, with subsequent analysis of parameter interactions by OSM, produced the best result.

It was found that parameters describing set-points for Hill-functions may pose extra difficulties in the optimization process. These parameters were fixed and a new subset was produced using Morris-OSM. Optimization was repeated for this new subset, as well as a subset consisting of parameters deemed sensitive by the Morris method, and a subset consisting of all parameters. In general the larger subsets produced better fits.

Parameter densities and model output prediction intervals were estimated using DRAM. When including all parameters in the analysis for the data set without respiration, the Markov chain did not converge in 50,000 iterations, but did continue to improve on the residual cost. Using the parameter set produced by the subset selection strategy Morris-OSM lead to fixation of the parameter h_0 describing the base depolarization rate of the pacemaker cells due to a correlation with the parameter h_m describing the pacemaker sensitivity to acetylcholine. Subsequent analysis with h_0 fixed resulted in reasonable parameter densities, suggesting that all remaining parameters are identifiable using this subset. For the data set where respiration was included parameter densities were estimated as well. Here two near single-valued correlations was found and parameters h_0 and α_m was fixed. α_m describes the weighting of the baroreceptor contribution to the parasympathetic tone before the tilt, and was correlated to β_m which describes the weighting of the respiration contribution to parasympathetic

tone after the tilt. For this data set it was especially interesting that the set point parameter for the Hill function describing respiratory input, $f_{r,t}$, was found to be close to it's largest allowed value. This suggests that the algorithm prefers a near constant respiratory input, and that the current inclusion of the respiration frequency does not increase the descriptive power of the model. For both data sets, the results produced by DRAM suggests that it is possible to produce better fits by increasing the size of the parameter subsets.

Future work

While the simulation results presented here are promising, additional research will surely increase the predictive power of the model. One area of interest is the size of parameter subset used for optimization. Following optimization and UQ results it is clear that the used subset selection strategies was used too restrictively. In relation to this, it would be relevant to analyse the impact of fixing physiologically (relatively) well known parameters such as h_0 prior to the subset selection procedures.

In terms of respiration it was hypothesized that the signal used to reflect the influence of respiration should be the respiration signal itself, in favor of the respiration frequency used here. As the respiration frequency is usually around 0.3Hz, this should include oscillations on this time scale in the model output heart rate. Another, but perhaps more laborious, option would be to include a mechanism generating oscillations in parasympathetic tone based on the respiration frequency. Either way, the respiration signal should induce oscillations of a frequency around 0.3Hz in the model.

BIBLIOGRAPHY

"2003 Dual System of Human Circulation" by OpenStax College - Anatomy & Physiology. Connexions Web site. `http://cnx.org/content/col11496/1.6/`, Jun 19, 2013, Licensed under Creative Commons Attribution 3.0 via Wikimedia Commons - `https://commons.wikimedia.org/wiki/File:2003_Dual_System_of_Human_Circulation.jpg#mediaviewer/File:2003_Dual_System_of_Human_Circulation.jpg` (cit. on p. 7).

Abbott, L.F. (1999). "Lapicques introduction of the integrate-and-fire model neuron (1907)". In: *Brain Research Bulletin* 50.5, pp. 303–304 (cit. on p. 46).

Abe, H., D.G. Benditt, W.W. Decker, B.P. Grubb, R. Sheldon, and W.K. Shen (2009). "Guidelines for the diagnosis and management of syncope (version 2009)". In: *European Heart Journal* 30, pp. 2631–2671 (cit. on pp. 1, 2).

Akaike, H. (1974). "A new look at the statistical model identfication". In: *IEEE Trans. Autom. Control* AC-19.6, pp. 716–723 (cit. on p. 138).

Alfrey, K.D. (1997). "Model of the aortic baroreceptor in rat". PhD thesis. MS thesis. Houston: Rice University (cit. on p. 44).

Allen, L.S. (2007). *An Introduction to Mathematical Biology*. London: Pearson Education (cit. on p. 63).

Arndt, J.O., J. Klauske, and F. Mersch (1968). "The diameter of the intact carotid artery in man and its change with pulse pressure". English. In: *Pflüger's Archiv für die gesamte Physiologie des Menschen und der Tiere* 301.3, pp. 230–240. DOI: 10.1007/BF00363770. URL: `http://dx.doi.org/10.1007/BF00363770` (cit. on pp. 41, 42, 44).

Atienza, J.M., G.V. Guinea, F.J. Rojo, R.J. Burgos, C. García-Montero, F.J. Goicolea, P. Aragoncillo, and M. Elicesa (2007). "The influence of pressure and temperature on the behavior of the human aorta and carotid arteries". In: *Revista Española de Cardiología (English Edition)* 60.3, pp. 259–267 (cit. on p. 41).

Bannister, R (1993). "Multiple system atrophy and pure autonomic failure". In: *Clinical autonomic disorders: evaluation and management*. Ed. by Low PA. Boston: Little, Brown, pp. 517–525 (cit. on p. 38).

Beard, D.A. and M.J. Kushmerick (2009). "Strong inference for systems biology". In: *PLoS comp biol* 5.8, e1000459 (cit. on p. 2).

Belia, S., F. Fidler, J. Williams, and G. Cumming (2005). "Researchers misunderstand confidence intervals and standard error bars." In: *Psychological methods* 10.4, p. 389 (cit. on p. 112).

Boron, W.F. and E.L. Boulpaep (2012). *Medical Physiology, 2e Updated Edition: with STUDENT CONSULT Online Access*. Elsevier Health Sciences (cit. on pp. 5, 24).

Bugenhagen, S.M., A.W. Cowley, and D.A. Beard (2010). "Identifying physiological origins of baroreflex dysfunction in salt-sensitive hypertension in the Dahl SS rat". In: *Physiol Genomics* 42, pp. 23–41 (cit. on pp. 38, 44, 46).

Bungartz, H.J. and M. Griebel (2004). "Sparse grids". In: *Acta numerica* 13, pp. 147–269 (cit. on p. 113).

Burnham, K.P. and D.R. Anderson (2004). "Multimodel Inference: Understanding AIC and BIC in Model Selection". In: *Sociological Methods & Research* 33.2, pp. 261–304 (cit. on p. 138).

Burton, A.C. (1966). *Physiology and biophysics of the circulation. An introductionary text.* 35 East Wacker Drive, Chicago: Year book medical publishers incorporated (cit. on pp. 1, 2, 5, 8, 9, 15, 17, 22, 41).

Coleridge, H.M., J.C. Coleridge, M.P. Kaufman, and A. Dangel (1981). "Operational sensitivity and acute resetting of aortic baroreceptors in dogs." In: *Circulation research* 48.5, pp. 676–684 (cit. on p. 40).

Daun, S., J. Rubin, Y. Vodovotz, A. Roy, R. Parker, and G. Clermont (2008). "An ensemble of models of the acute inflammatory response to bacterial lipopolysaccharide in rats: Results from parameter space reduction". In: *Journal of Theoretical Biology* 253.4, pp. 843–853 (cit. on p. 97).

Fung, Y.C. (1990). *Biomechanics*. Springer (cit. on p. 44).

Griewank, A. et al. (1989). "On automatic differentiation". In: *Mathematical Programming: recent developments and applications* 6, pp. 83–107 (cit. on p. 80).

Guyton, A.C. (1971). *Textbook of medical physiology*. Saunders. URL: http://books.google.com/books?id=U8ZqAAAAMAAJ (cit. on pp. 10, 11, 14).

Guyton, A.C and J.W. Harris (1951). "Pressoreceptor-autonomic oscillation: A probable cause of vasomotor waves". In: *American Journal of Physiology–Legacy Content* 165.1, pp. 158–166 (cit. on p. 53).

Haario, H., M. Laine, A. Mira, and E. Saksman (2006). "DRAM: Efficient adaptive MCMC". In: *Stat. Comput* 16, pp. 339–354 (cit. on pp. 115, 117, 118).

Hall, J.E. (2011). *Guyton and Hall textbook of medical physiology*. Philadelphia, PA: Saunders/Elsevier (cit. on pp. 2, 5, 18, 19, 22, 23, 25, 26, 28, 57).

Hallock, P. (1934). "Arterial elasticity in man in relation to age as evaluated by the pulse wave velocity method". In: *Archives of Internal Medicine* 54.5, pp. 770–798 (cit. on p. 17).

Halton, J.H. (1960). "On the efficiency of certain quasi-random sequences of points in evaluating multi-dimensional integrals". In: *Numerische Mathematik* 2.1, pp. 84–90 (cit. on p. 113).

Hammer, P.E. and J.P. Saul (2005). "Resonance in a mathematical model of baroreflex control: arterial blood pressure waves accompanying postural stress". In: *American Journal of Physiology-Regulatory, Integrative and Comparative Physiology* 288.6, R1637–R1648 (cit. on p. 53).

Harvey, W.D. and M.L. Ginsberg (1995). "Limited discrepancy search". In: *IJCAI (1)*, pp. 607–615 (cit. on p. 2).

Heusden, K. van, J. Gisolf, Wim J Stok, S. Dijkstra, and J.M. Karemaker (2006). "Mathematical modeling of gravitational effects on the circulation: importance of the time course of venous pooling and blood volume changes in the lungs". In: *Am J Physiol* 291, H2152–H2165 (cit. on p. 38).

Jacquez, J.A. (1985). *Compartmental analysis in biology and medicine*. Vol. 2. Ann Arbor, Michigan (cit. on p. 94).

Jansen, M.J.W. (1999). "Analysis of variance designs for model output". In: *Computer Physics Communications* 117.1, pp. 35–43 (cit. on pp. 81, 82).

Joe, S. and F.Y. Kuo (2003). "Remark on algorithm 659: Implementing Sobol's quasirandom sequence generator". In: *ACM Transactions on Mathematical Software (TOMS)* 29.1, pp. 49–57 (cit. on p. 113).

Jones, E., T. Oliphant, Peterson. P., et al. (2001–). *SciPy: Open source scientific tools for Python*. [Online; accessed 2014-10-01]. URL: http://www.scipy.org/ (cit. on p. 88).

Katona, P.G. and G. Barnett (1969). "Central origin of asymmetry in the carotid sinus reflex*". In: *Annals of the New York Academy of Sciences* 156.2, pp. 779–786 (cit. on p. 40).

Kobayashi, H. (1996). "Postural effect on respiratory sinus arrhythmia with various respiratory frequencies." In: *Applied human science: journal of physiological anthropology* 15.2, p. 87 (cit. on p. 50).

Koch, C. and I. Segev (1998). *Methods in neuronal modeling: from ions to networks*. MIT press (cit. on p. 46).

Landgren, S. (1952). "The baroreceptor activity in the carotid sinus nerve and the distensibility of the sinus wall". In: *Acta. Physiol. Scand.* 26, pp. 35–56 (cit. on p. 3).

Lapicque, L. (1907). "Recherches quantitatives sur l'excitation électrique des nerfs traitée comme une polarisation". In: *J. Physiol. Pathol. Gen* 9.1, pp. 620–635 (cit. on p. 46).

Laurent, S., B. Caviezel, L. Beck, X. Girerd, E. Billaud, P. Boutouyrie, A. Hoeks, and M. Safar (1994). "Carotid artery distensibility and distending pressure in hypertensive humans." In: *Hypertension* 23.6 Pt 2, pp. 878–883 (cit. on p. 41).

Li, R, M.A. Henson, and M.J. Kurtz (2004). "Selection of model parameters for off-line parameter estimation". In: *IEEE Transaction on control systems technology* 12.3 (cit. on pp. 94, 97).

Linzer, M., M. Pontinen, D.T. Gold, G.W. Divine, A. Felder, and W. Blair Brooks (1991). "Impairment of physical and psychosocial function in recurrent syncope". In: *Journal of clinical epidemiology* 44.10, pp. 1037–1043 (cit. on p. 1).

Ljung, L. (1987). "System identification: theoryfor the user". In: *Englewood Cliffs* (cit. on p. 3).

Ljung, L. and T. Glad (1994). "On global identifiability for arbitrary model parametrizations". In: *Automatica* 30.2, pp. 265–276. DOI: http://dx.doi.org/10.1016/0005-1098(94)90029-9. URL: http://www.sciencedirect.com/science/article/pii/0005109894900299 (cit. on p. 77).

MacDonald, N. (1978). *Time lags in biological models*. Berlin: Springer-Verlag Heidelberg (cit. on p. 52).

Mahdi, A., N. Meshkat, and S. Sullivant (2014). "Structural identifiability of viscoelastic mechanical systems". In: *PloS one* 9.2, e86411 (cit. on p. 110).

Mahdi, A., J. Sturdy, J.T. Ottesen, and M.S. Olufsen (2013). "Modeling the afferent dynamics of the baroreflex control system". In: *PLoS computational biology* 9.12, e1003384 (cit. on pp. 44, 46).

Mehlsen, J., K. Pagh, J.S. Nielsen, L. Sestoft, and S.L. Nielsen (1987). "Heart rate response to breathing: dependency upon breathing pattern". In: *Clinical Physiology* 7.2, pp. 115–124 (cit. on p. 50).

Metropolis, N., A.W. Rosenbluth, M.N. Rosenbluth, A.H. Teller, and E. Teller (1953). "Equation of state calculations by fast computing machines". In: *The journal of chemical physics* 21.6, pp. 1087–1092 (cit. on p. 114).

Miao, H., X. Xia, A.S. Perelson, and H. Wu (2011). "On identifiability of nonlinear ode models and applications in viral dynamics". In: *SIAM Rev.* 53, pp. 3–39 (cit. on pp. 3, 77, 94, 96, 97, 102).

Morris, M.D. (1991). "Factorial sampling plans for preliminary computational experiments". In: *Technometrics* 33.2, pp. 161–174 (cit. on p. 84).

Mosqueda-Garcia, R., R. Furlan, J. Tank, and R. Fernandez-Violante (2000). "The elusive pathophysiology of neurally mediated syncope". In: *Circulation* 102, pp. 2898–2906 (cit. on p. 38).

Oliphant, T.E. (2007). "Python for scientific computing". In: *Computing in Science & Engineering* 9.3, pp. 10–20 (cit. on p. 88).

Olsen, C.H., P. Gøtze, and T. Mosegaard (2011). "Acetylcholine influence on the baroreflex: Investigating a model of the baroreflex control mechanism on HUT-experiment data". MA thesis. Dept of Science, Systems, and Models, Roskilde Universitet, Denmark (cit. on p. 58).

Olufsen, M.S. and J.T. Ottesen (2013). "A practical approach to parameter estimation applied to model predicting heart rate regulation". English. In: *J Math Biol* 67.1, pp. 39–68. DOI: 10.1007/s00285-012-0535-8 (cit. on pp. 50, 58, 97).

Olufsen, M.S., H.T. Tran, J.T. Ottesen, L.A. Lipsitz, and V. Novak (2006). "Modeling baroreflex regulation of heart rate during orthostatic stress". In: *Am J Physiol* 291, R1355–R1368 (cit. on pp. 3, 38, 48, 50).

Ottesen, J.T. (1997a). "Modelling of the baroreflex-feedback mechanism with time-delay". English. In: *J Math Biol* 36 (1), pp. 41–63. DOI: 10.1007/s002850050089 (cit. on pp. 3, 58).

— (1997b). "Non-linearity of baroreceptor nerves". In: *Surv Math Ind Springer-Verlag* 7, pp. 187–201 (cit. on pp. 3, 53, 58).

— (2011). "The mathematical microscope–making the inaccessible accessible". In: *BetaSys*. Springer, pp. 97–118 (cit. on p. 2).

Ottesen, J.T. and M.S. Olufsen (2011). "Functionality of the baroreceptor nerves in heart rate regulation". In: *Comp Math Prog Biomed* 101, pp. 208–219 (cit. on pp. 38, 58).

— (2013). "Structural correlation method for model reduction and practical estimation of patient specific parameters illustrated on heart rate regulation". In: *PREPRINT* (cit. on pp. 3, 53–56, 94).

Pope, S.R., L.M. Ellwein, C.L. Zapata, V. Novak, C.T. Kelley, and M.S. Olufsen (2009). "Estimation and identification of parameters in a lumped cerebrovascular model". In: *Math Biosci Eng* 6.1, pp. 93–115 (cit. on p. 80).

Saltelli, A., P. Annoni, I. Azzini, F. Campolongo, M. Ratto, and S. Tarantola (2010). "Variance based sensitivity analysis of model output. Design and estimator for the total sensitivity index". In: *Computer Physics Communications* 181.2, pp. 259–270 (cit. on pp. 81, 82, 111).

Saltelli, A., M. Ratto, T. Andres, F. Campolongo, J. Cariboni, D. Gatelli, M. Saisana, and S. Tarantola (2008). *Global sensitivity analysis: the primer*. Chichester, England: John Wiley (cit. on p. 3).

Schild, J.H., J.W. Clark, M. Hay, D. Mendelowitz, M.C. Andresen, and D.L. Kunze (1994). "A-and C-type rat nodose sensory neurons: model interpretations of dynamic discharge characteristics". In: *Journal of Neurophysiology* 71.6, pp. 2338–2358 (cit. on p. 46).

Serban, R. and A.C Hindmarsh (2005). "CVODES, the sensitivity-enabled ODE solver in SUNDIALS". In: *Proc ASME Int Design Eng Techl Conf* (cit. on p. 81).

Smith, H. (2010). "An Introduction to Delay Differential Equations with Applications to the Life Sciences". In: ed. by J.E. Marsden, L. Sirovich, and S.S. Antman. Texts in Applied Mathematics. Springer Science+Business Media, LLC. URL: http://link.springer.com/book/10.1007/978-1-4419-7646-8/page/1 (cit. on p. 52).

Smith, R. C. (2014). *Uncertainty Quantification: Theory, Implementation, and Applications*. Computational Science and Engineering. Philadelphia: SIAM (cit. on pp. 3, 81, 82, 84–87, 103, 112, 115).

Smolyak, S.A. (1963). "Quadrature and interpolation formulas for tensor products of certain classes of functions". In: *Dokl. Akad. Nauk SSSR*. Vol. 4. 240-243, p. 123 (cit. on p. 113).

Smyth, H.S., P. Sleight, and G.W. Pickering (1969). "Reflex regulation of arterial pressure during sleep in man A quantitative method of assessing baroreflex sensitivity". In: *Circulation research* 24.1, pp. 109–121 (cit. on p. 3).

Sobol, I.M. (1993). "Sensitivity estimates for nonlinear mathematical models". In: *Math Modeling Comput Experiment* 1.4, pp. 407–414 (cit. on p. 81).

— (2001). "Global sensitivity indices for nonlinear mathematical models and their Monte Carlo estimates". In: *Math Comput Simulation* 55, pp. 271–280 (cit. on pp. 81, 86).

Sobol, I.M. and Y.L. Levitan (1999). "On the use of variance reducing multipliers in Monte Carlo computations of a global sensitivity index". In: *Computer Physics Communications* 117.1, pp. 52–61 (cit. on p. 84).

Strogatz, S.H. (1994). *Nonlinear dynamics and chaos. With applications to physics, biology, chemistry and engineering*. Reading, Massachusetts: Perseus Books (cit. on pp. 64, 65).

Sun, B.C., J.A. Emond, and C.A. Camargo Jr (2005). "Direct medical costs of syncope-related hospitalizations in the United States". In: *The American journal of cardiology* 95.5, pp. 668–671 (cit. on p. 1).

Taher, M.F., A.B.P. Cecchini, M.A. Allen, S.R. Gobran, R.C. Gorman, B.L. Guthrie, K.A. Lingenfelter, S.Y. Rabbany, P.M. Rolchigo, J. Melbin, et al. (1988). "Baroreceptor responses derived from a fundamental concept". In: *Annals of biomedical engineering* 16.5, pp. 429–443 (cit. on p. 3).

Tanaka, H., K.D. Monahan, and D.R. Seals (2001). "Age-predicted maximal heart rate revisited". In: *Journal of the American College of Cardiology* 37.1, pp. 153–156 (cit. on p. 57).

Tarantola, A. (2005). *Inverse problem theory and methods for model parameter estimation*. siam (cit. on p. 3).

Thomas, R.J., J.E. Mietus, C. Peng, A.L. Goldberger, et al. (2005). "An electrocardiogram-based technique to assess cardiopulmonary coupling during sleep". In: *Sleep-New York Then Westchester-* 28.9, p. 1151 (cit. on p. 35).

Thompson, A. and B.N. Taylor (2008). "Guide for the Use of the International System of Units (SI)". In: (cit. on p. 33).

Ursino, M. (1998). "Interaction between carotid baroregulation and the pulsating heart: a mathematical model". In: *American Journal of Physiology-Heart and Circulatory Physiology* 275.5, H1733–H1747 (cit. on p. 3).

Valdez-Jasso, D. (2011). *Modeling and Identification of Vascular Biomechanical Properties in Large Arteries*. North Carolina State University (cit. on p. 66).

Valdez-Jasso, D., D. Bia, Y. Zocalo, R.L. Armentano, M.A. Haider, and M.S. Olufsen (2011). "Linear and nonlinear viscoelastic modeling of aorta and carotid pressure-area." In: *Ann Biomed Eng* 39, pp. 1438–1456 (cit. on p. 40).

Van Dijk, N., M.A. Sprangers, N. Colman, K.R. Boer, W. Wieling, and M. Linzer (2006). "Clinical factors associated with quality of life in patients with transient loss of consciousness". In: *Journal of cardiovascular electrophysiology* 17.9, pp. 998–1003 (cit. on p. 1).

Vandewoestyne, B. and R. Cools (2006). "Good permutations for deterministic scrambled Halton sequences in terms of L2-discrepancy". In: *J comp appl math* 189.1, pp. 341–361 (cit. on p. 113).

Warner, H.R. et al. (1969). "Effect of combined sympathetic and vagal stimulation on heart rate in the dog". In: *Circulation Research* 24.4, pp. 567–573 (cit. on p. 53).

Warner, H.R. and A. Cox (1962). "A mathematical model of heart rate control by sympathetic and vagus efferent information". In: *J Appl Physiol* 17.suppL 2, p. 349 (cit. on p. 3).

Widjaja, D., J. Taelman, S. Vandeput, M.A.K.A. Braeken, R.A. Otte, B.R.H. Van den Bergh, and S. Van Huffel (2010). "Ecg-derived respiration: Comparison and new measures for respiratory variability". In: *Computing in Cardiology, 2010*. IEEE, pp. 149–152 (cit. on pp. 35, 36).

Williams, N.D., Ø. Wind-Willassen, A.A. Wright, J. Mehlsen, J.T. Ottesen, M.S. Olufsen, et al. (2013). "Patient-specific modelling of head-up tilt". In: *Mathematical Medicine and Biology*, dqt004 (cit. on p. 33).

Wolfram (2013). *Gauss-Newton Methods*. http://reference.wolfram.com/mathematica/tutorial/UnconstrainedOptimizationGaussNewtonMethods.html (cit. on p. 95).

Yasuma, F. and J. Hayano (2004). "Respiratory Sinus ArrhythmiaWhy Does the Heartbeat Synchronize With Respiratory Rhythm?" In: *Chest Journal* 125.2, pp. 683–690 (cit. on p. 38).